Fall 12-15-2018

Non-classical Plate Models Incorporating Microstructure and Surface Energy Effects: Their Variational Formulations and Applications

Gongye Zhang
Southern Methodist University, gongyezhangz@smu.edu

Recommended Citation

Zhang, Gongye, "Non-classical Plate Models Incorporating Microstructure and Surface Energy Effects: Their Variational Formulations and Applications" (2018). *Mechanical Engineering Research Theses and Dissertations*. 12.
https://scholar.smu.edu/engineering_mechanical_etds/12

NON-CLASSICAL PLATE MODELS INCORPORATING MICROSTRUCTURE AND SURFACE ENERGY EFFECTS: THEIR VARIATIONAL FORMULATIONS AND APPLICATIONS

Approved by:

Professor Xin-Lin Gao

Professor Wei Tong

Professor Tindaro Ioppolo

Professor Xu Nie

Professor Usama El Shamy

NON-CLASSICAL PLATE MODELS INCORPORATING MICROSTRUCTURE AND SURFACE ENERGY EFFECTS: THEIR VARIATIONAL FORMULATIONS AND APPLICATIONS

A Dissertation Presented to the Graduate Faculty of

Bobby B. Lyle School of Engineering

Southern Methodist University

in

Partial Fulfillment of the Requirements

for the degree of

Doctor of Philosophy

with a

Major in Mechanical Engineering

by

Gongye Zhang

(B.S., Nanjing Tech University, China, 2012)
(M.S., University of Texas at Dallas, USA, 2014)

December 15, 2018

ACKNOWLEDGMENTS

I would like to express my special thanks to my advisor, Prof. Xin-Lin Gao for his guidance during my Ph.D. study. His rich knowledge, painstaking advice and attitude toward conducting research are very helpful for me.

I am also thankful to Prof. Tindaro Ioppolo, Prof. Xu Nie, Prof. Usama El Shamy and Prof. Wei Tong for serving on my committee.

In addition, I thank my group members Ahmad Gad, Li Ai and Yongqiang Li and roommate Ningyuan Sun for their help and friendship.

Finally, I wish to thank my parents for their love, encouragement and support.

Gongye Zhang B.S., Nanjing Tech University, China, 2012
M.S., University of Texas at Dallas, USA, 2014

Non-classical Plate Models Incorporating Microstructure and Surface Energy Effects: Their Variational Formulations and Applications

Advisor: Professor Xin-Lin Gao

Doctor of Philosophy conferred on December 15, 2018

Dissertation completed on December 3, 2018

In this dissertation research, new non-classical models for Kirchhoff and Mindlin plates are developed and applied to study band gaps for flexural wave propagation in composite plate structures.

In Chapter 2, a new non-classical model for a Kirchhoff plate resting on an elastic foundation is developed using a modified couple stress theory, a surface elasticity theory and a two-parameter elastic foundation model. A variational formulation based on Hamilton's principle is employed, which leads to the simultaneous determination of the equations of motion and the complete boundary conditions and provides a unified treatment of the microstructure, surface energy and foundation effects. The new plate model contains a material length scale parameter to account for the microstructure effect, three surface elastic constants to describe the surface energy effect, and two foundation moduli to represent the foundation effect. The current non-classical plate model reduces to its classical elasticity-based counterpart when the microstructure, surface energy and foundation effects are all suppressed. In addition, the newly developed plate model includes the models considering the microstructure dependence or the surface energy effect or the foundation influence alone as special cases and recovers the Bernoulli–Euler beam

model incorporating the microstructure, surface energy and foundation effects. To illustrate the new model, the static bending and free vibration problems of a simply supported rectangular plate are analytically solved.

In Chapter 3, a new non-classical model for circular Kirchhoff plates subjected to axisymmetric loading is presented based on the same modified couple stress theory and surface elasticity theory but using cylindrical polar coordinates. The new non-classical plate model includes the circular plate models considering the microstructure influence or the surface energy effect alone as special cases and recovers the classical elasticity-based Kirchhoff plate model when both the microstructure and surface energy effects are suppressed. To demonstrate the new model, the static bending problem of a clamped solid circular Kirchhoff plate subjected to a uniform normal load is analytically solved.

In Chapter 4, a new non-classical model for a Mindlin plate resting on an elastic foundation is developed in a general form using the modified couple stress theory, the surface elasticity theory and the two-parameter Winkler–Pasternak foundation model, which are the same as those employed in Chapter 2. It includes all five kinematic variables possible for a Mindlin plate and treats the microstructure, surface energy and foundation effects in a unified manner. The current non-classical plate model reduces to its classical elasticity-based counterpart when the microstructure, surface energy and foundation effects are all neglected. In addition, the new model includes the Mindlin plate models considering the microstructure dependence or the surface energy effect or the foundation influence alone as special cases, and it degenerates to the Timoshenko beam model including the microstructure effect. To illustrate the new Mindlin plate model, the static bending and free vibration problems of a simply supported rectangular plate are analytically solved by directly applying the general formulae derived.

In Chapter 5, a new non-classical model for circular Mindlin plates is furnished using the modified couple stress theory, the surface elasticity theory, Hamilton’s principle, and cylindrical polar coordinates, as was done in Chapter 3. The non-classical model includes the circular plate models considering the microstructure influence only and the surface energy effect alone as special cases, and it recovers the classical elasticity-based circular Mindlin plate model when both the microstructure and surface energy effects are not considered. To illustrate the new model, the static bending problem of a clamped circular Mindlin plate under a uniform normal load is analytically solved.

In Chapter 6, a new model for determining band gaps for flexural elastic wave propagation in a periodic composite plate structure with square inclusions is developed by directly using the non-classical model for Kirchhoff plates presented in Chapter 2. The band gaps predicted by the newly developed model depend on the microstructure and surface elasticity of each constituent material, the elastic foundation moduli, the unit cell size, and the volume fraction of the inclusion phase. To quantitatively illustrate the effects of these factors, a parametric study is conducted.

In Chapter 7, a new model for predicting band gaps for flexural elastic wave propagation in a periodic composite plate structure with square or cruciform inclusions is provided by using the non-classical model for Mindlin plates proposed in Chapter 4. The band gaps predicted by the new model depend on the microstructure and surface elasticity of each consitituent material, the unit cell size, and the volume fraction. To quantitatively

illustrate the effects of these factors, a parametric study is conducted for periodic composite plate structures containing square and cruciform inclusions.

TABLE OF CONTENTS

LIST OF FIGURES

LIST OF TABLES

DEDICATION

This dissertation is dedicated to my grandfather.

Chapter

1. INTRODUCTION

Thin plates (such as those used in MEMS and NEMS devices as sensors and probes) often exhibit size effects, which cannot be captured by models based on classical continuum mechanics due to a lack of any material length scale parameter (e.g., Miller and Shenoy, 2000; Lam et al., 2003; Lim and He, 2004; McFarland and Colton, 2005; Li et al., 2009).

As atomistic models can be prohibitively expensive, continuum models remain to be essential in studying deformations of structural components at the micron scale. Higher-order continuum theories can capture microstructure effects resulting from non-local interactions of material particles at the micron scale. In such a theory, either a continuum embedded with microstructures or a non-local medium including long-range material interactions is employed. Surface elasticity theories can describe surface energy effects arising from the atom arrangements and material properties on a surface that are different from those in the bulk. In such a surface elasticity theory, a surface is regarded as a membrane or film with a negligible thickness that is perfectly bonded to the bulk material. However, very few plate models have been developed by considering both the microstructure and surface energy effects. These motivated the current dissertation research.

In Chapter 2, a new non-classical model for a Kirchhoff plate resting on an elastic foundation is provided. In Chapter 3, a new non-classical model for circular Kirchhoff plates subjected to axisymmetric loading is presented by using cylindrical polar coordinates. In Chapter 4, a new non-classical model for a Mindlin plate resting on an elastic foundation is developed. In Chapter 5, a new non-classical model for circular Mindlin plates is furnished using cylindrical polar coordinates. In Chapter 6, a new model for determining band gaps for flexural elastic wave propagation in a periodic composite plate structure is proposed based on the non-classical Kirchhoff plate model presented in Chapter 2. In Chapter 7, a new model for predicting band gaps for flexural elastic wave propagation in a periodic composite plate structure is developed by employing the non-classical Mindlin plate model formulated in Chapter 4.

Chapter

2. A NON-CLASSICAL KIRCHHOFF PLATE MODEL INCORPORATING MICROSTRUCTURE, SURFACE ENERGY AND FOUNDATION EFFECTS

2.1 Introduction

Thin beams and plates widely used in MEMS and NEMS often exhibit microstructure- and surface energy-dependent size effects (e.g., Miller and Shenoy, 2000; Lim and He, 2004; McFarland and Colton, 2005). Classical continuum mechanics cannot be used to interpret such size effects because of a lack of any material length scale parameter. Hence, models based on higher-order (non-classical) continuum theories that contain microstructure-dependent material parameters and can account for surface energy effects need to be developed.

Several higher-order elasticity theories have been applied to develop non-classical plate models. Lazopoulos (2004) provided a non-classical von Karman plate model based on a simplified strain gradient elasticity theory (SSGET) (e.g., Gao and Park, 2007; Gao and Zhou, 2013). This SSGET, which contains only one material length scale parameter, was also employed by Papargyri-Beskou and Beskos (2008) and Papargyri-Beskou et al. (2010) to derive non-classical equations of motion for Kirchhoff plates of strain gradient materials. By using a constitutive relation in non-local elasticity suggested in Eringen (1983), Lu et al. (2007) proposed a Kirchhoff plate model and a Mindlin plate model without using a variational formulation. Based on a modified couple stress theory that involves one additional material length scale parameter (Yang et al., 2002; Park and Gao, 2008), three Kirchhoff plate models were suggested in Tsiatas (2009), Jomehzadeh et al. (2011) and Akgöz and Civalek (2013), respectively.

On the other hand, for solids with a large surface layer to bulk volume ratio, surface effects, which cannot be described using classical elasticity, become important (e.g., Miller and Shenoy, 2000). Such surface effects can be interpreted using a surface elasticity theory, in which the surface of a solid, where the atom arrangements and material properties differ from those in the bulk (e.g., Cammarata, 1994), is regarded as a membrane or film with a negligible thickness (e.g., Steigmann and Ogden, 1997, 1999).

The surface elasticity theory (e.g., Gurtin and Murdoch, 1975, 1978) has been used to analyze thin plates involving surface effects. For example, Miller and Shenoy (2000) developed a model to describe the size dependency of the effective stiffness of a nano-sized structural element (a bar, beam or plate). Lim and He (2004) presented a geometrically nonlinear plate model for nano-scale films based on the Kirchhoff hypothesis and the von Karman strains. Lu et al. (2006) constructed a size-dependent thin plate model by including the normal stress on and inside the surface of the bulk substrate. Lü et al. (2011) developed a non-linear plate model for functionally graded films using the Kirchhoff kinematic relations and the von Karman non-linear strains for the bulk material. Wang and Wang (2012) provided a model for non-linear free vibrations of a Kirchhoff plate and a Mindlin plate using the von Karman strains.

However, very few models have been developed for thin plates by considering both the microstructure and surface energy effects. One non-classical model for Kirchhoff thin plates was provided in Lazopoulos (2009) by employing a strain gradient elasticity theory that contains two additional length scale parameters – one related to the bulk strain energy and the other linked to the surface energy. Another non-classical Kirchhoff plate model, which is based on a modified couple stress theory and a surface elasticity theory, was presented in Shaat et al. (2014) without using a variational formulation. The elastic foundation effect was not considered in either of these two studies.

The objective of the this chapter is to develop a non-classical model for a Kirchhoff plate resting on a two-parameter elastic foundation characterized by the Winkler and Pasternak foundation moduli using the modified couple stress theory (Yang et al., 2002; Park and Gao, 2008), the surface elasticity theory (Gurtin and Murdoch, 1975, 1978) and Hamilton's principle. This variational formulation leads to the simultaneous determination of the equations of motion and complete boundary conditions and provides a unified treatment of the microstructure, surface energy and foundation effects.

The rest of the Chapter 2 is organized as follows. In Section 2.2, a new non-classical model for a Kirchhoff plate on a two-parameter elastic foundation is developed using a variational formulation based on Hamilton's principle. The newly obtained Kirchhoff plate model includes the models incorporating the microstructure dependence or the surface energy effect or the elastic foundation influence alone as special cases and recovers the model for Bernoulli-Euler beams based on the same modified couple stress theory and surface elasticity theory. Also, the new plate model reduces to its classical elasticity-based counterpart when the microstructure, surface energy and foundation effects are all suppressed. In Section 2.3, static bending and free vibration problems of a simply supported rectangular plate are analytically solved by directly applying the new model. The numerical results are also presented there to quantitatively show the differences between the current non-classical Kirchhoff plate model and its classical counterpart. The chapter concludes in Section 2.4 with a summary.

2.2 Formulation

The Kirchhoff plate theory, also known as the classical plate theory, is the simplest theory for analyzing plates. It can be viewed as an extension of the Bernoulli-Euler beam theory to three-dimensional deformations.

Consider a Kirchhoff plate resting on an elastic foundation that can be characterized by a two-parameter model including the Winkler foundation modulus k_w to represent the spring elements and the Pasternak foundation modulus k_p to describe the shear layer which is incompressible and deforms in transverse shear only (e.g., Selvadurai, 1979; Yokoyama, 1996), as schematically shown in Fig 2.1. The effect of this two-parameter elastic foundation on the plate deformation can be equivalently represented as a vertical body force q (in N/m^2) given by (Selvadurai, 1979):

$$q(x,y,t) = k_w w(x,y,t) - k_p \nabla^2 w(x,y,t), \tag{2.1}$$

where ∇^2 is the Laplacian, and w is the displacement of point (x, y, 0) on the mid-plane of the plate at time t.

By using the Cartesian coordinate system (x, y, z) shown in Fig 2.2, the displacement field in a Kirchhoff plate of uniform thickness h can be written as (e.g., Reddy, 2002)

$$u_1 = u(x,y,t) - z\frac{\partial w}{\partial x}, \quad u_2 = v(x,y,t) - z\frac{\partial w}{\partial y}, \quad u_3 = w(x,y,t), \tag{2.2a-c}$$

where u_1, u_2 and u_3 are, respectively, the x-, y- and z-components of the displacement vector $\boldsymbol{u}$ of a point (x, y, z) in the plate at time t, and u, v and w are, respectively, the x-, y- and z-

components of the displacement vector of the corresponding point (*x, y*, 0) on the plate mid-plane at time *t*.

In Fig 2.2, S^+ and S^- denote, respectively, the lower and upper surface layers (with zero-thickness) of the Kirchhoff plate. These two surface layers are taken to be perfectly bonded to the bulk plate material at $z = \pm h/2$, respectively. The bulk material satisfies the modified couple stress theory (Yang et al., 2002; Park and Gao, 2008), while the surface layers have distinct material properties and are governed by the surface elasticity theory (Gurtin and Murdoch, 1975, 1978).

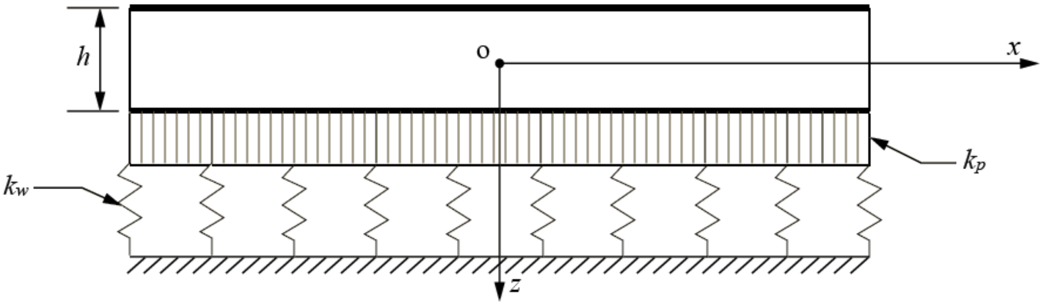

Fig. 2.1 Plate on a two-parameter elastic foundation

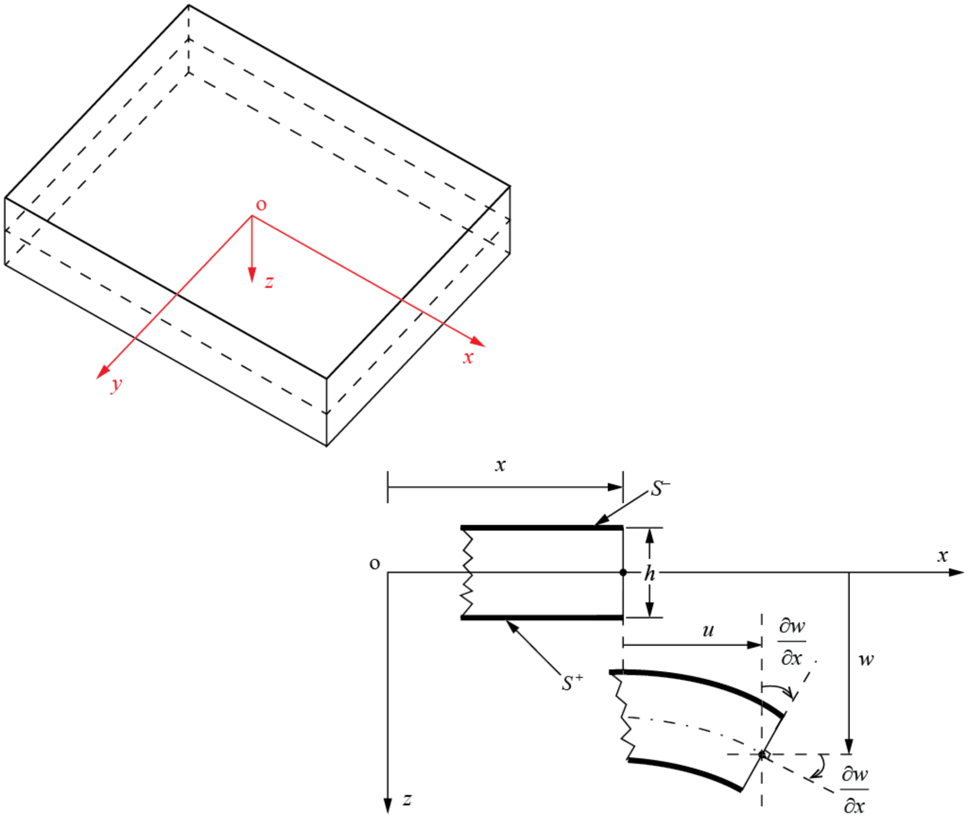

Fig. 2.2 Plate configuration and coordinate system

According to the modified couple stress theory (Yang et al., 2002; Park and Gao, 2008), the constitutive equations for an isotropic linear elastic material read

$$\sigma_{ij} = \lambda \varepsilon_{kk} \delta_{ij} + 2\mu \varepsilon_{ij}, \tag{2.3}$$

$$m_{ij} = 2 l^2 \mu \chi_{ij}, \tag{2.4}$$

where σ_{ij} are the components of the Cauchy stress tensor, m_{ij} are the components of the deviatoric part of the couple stress tensor, δ_{ij} is the Kronecker delta, λ and μ are the Lamé constants in classical elasticity, l is a material length scale parameter measuring the couple stress effect (e.g., Mindlin, 1963; Park and Gao, 2006), and ε_{ij} and χ_{ij} are, respectively, the components of the infinitesimal strain tensor and the symmetric curvature tensor defined by

$$\varepsilon_{ij} = \frac{1}{2}\left(u_{i,j} + u_{j,i}\right), \tag{2.5}$$

$$\chi_{ij} = \frac{1}{2}\left(\theta_{i,j} + \theta_{j,i}\right), \tag{2.6}$$

with u_i being the displacement components and θ_i being the components of the rotation vector defined as

$$\theta_i = \frac{1}{2}\varepsilon_{ijk}u_{k,j}. \tag{2.7}$$

According to the surface elasticity theory (e.g., Gurtin and Murdoch, 1975, 1978; Steigmann and Ogden, 1997, 1999), the surface layer of a bulk elastic material satisfies distinct constitutive equations involving surface elastic constants. The governing equations for the surface layer of zero thickness are given by (e.g., Gurtin and Murdoch, 1978; Ru, 2010; Zhou and Gao, 2013, 2015):

$$\sigma_{ij}n_j = \tau_{i\alpha,\alpha}, \quad \sigma_{ij}n_in_j = \tau_{\alpha\beta}\kappa_{\alpha\beta}, \tag{2.8a,b}$$

where $\kappa_{\alpha\beta}$ are the components of the surface curvature tensor, n_i are the components of the outward-pointing unit normal $\mathbf{n}$ ($= n_i\mathbf{e}_i$) to the surface, and $\tau_{\alpha\beta}$ are the in-plane components of the surface stress tensor expressed as (Gurtin and Murdoch, 1975, 1978)

$$\tau_{\alpha\beta} = \left[\tau_0 + (\lambda_0 + \tau_0)u_{\gamma,\gamma}\right]\delta_{\alpha\beta} + \mu_0\left(u_{\alpha,\beta} + u_{\beta,\alpha}\right) - \tau_0 u_{\beta,\alpha}, \tag{2.9}$$

where μ_0 and λ_0 are the surface elastic constants, and τ_0 is the residual surface stress (i.e., the surface stress at zero strain). These three constants μ_0, λ_0 and τ_0 can be determined from atomistic simulations (e.g., Miller and Shenoy, 2000; Shenoy, 2005) or experimental measurements (e.g., Jing et al., 2006; Zhang et al., 2013). Clearly, Eq. (2.9) shows that $\tau_{\alpha\beta}$ is not symmetric.

The out-of-plane components of the surface stress tensor read (Gurtin and Murdoch, 1978)

$$\tau_{3\beta} = \tau_0 u_{3,\beta}. \tag{2.10}$$

Note that in Eqs. (2.3)–(2.10) and throughout the Chapter 2, the summation convention and standard index notation are used, with the Greek indices running from 1 to 2 and the Latin indices from 1 to 3 unless otherwise indicated.

It follows from Eqs. (2.2a-c) and (2.5)–(2.7) that in the bulk of the current Kirchhoff plate,

$$\varepsilon_{xx} = \frac{\partial u}{\partial x} - z\frac{\partial^2 w}{\partial x^2},\ \varepsilon_{xy} = \frac{1}{2}(\frac{\partial u}{\partial y} + \frac{\partial v}{\partial x} - 2z\frac{\partial^2 w}{\partial x \partial y}),\ \varepsilon_{yy} = \frac{\partial v}{\partial y} - z\frac{\partial^2 w}{\partial y^2},\ \varepsilon_{xz} = \varepsilon_{yz} = \varepsilon_{zz} = 0, \tag{2.11}$$

$$\theta_1 = \frac{\partial w}{\partial y},\ \theta_2 = -\frac{\partial w}{\partial x},\ \theta_3 = \frac{1}{2}(\frac{\partial v}{\partial x} - \frac{\partial u}{\partial y}), \tag{2.12}$$

$$\begin{aligned} \chi_{xx} &= \frac{\partial^2 w}{\partial x \partial y},\ \chi_{xy} = \frac{1}{2}(\frac{\partial^2 w}{\partial y^2} - \frac{\partial^2 w}{\partial x^2}),\ \chi_{yy} = -\frac{\partial^2 w}{\partial x \partial y}, \\ \chi_{xz} &= \frac{1}{4}(\frac{\partial^2 v}{\partial x^2} - \frac{\partial^2 u}{\partial x \partial y}),\ \chi_{yz} = \frac{1}{4}(\frac{\partial^2 v}{\partial x \partial y} - \frac{\partial^2 u}{\partial y^2}),\ \chi_{zz} = 0. \end{aligned} \tag{2.13}$$

The total strain energy in the elastically deformed Kirchhoff plate is given by

$$\begin{aligned} U_T = U_B + U_S + U_F &= \frac{1}{2}\int_\Omega \left(\sigma_{ij}\varepsilon_{ij} + m_{ij}\chi_{ij}\right)\mathrm{d}V + \frac{1}{2}\int_{S^+} \tau_{\alpha\beta}\varepsilon_{\alpha\beta}\mathrm{d}A + \frac{1}{2}\int_{S^-} \tau_{\alpha\beta}\varepsilon_{\alpha\beta}\mathrm{d}A \\ &+ \frac{1}{2}\int_R k_w w^2 \mathrm{d}A + \frac{1}{2}\int_R k_p (\frac{\partial w}{\partial x})^2 \mathrm{d}A + \frac{1}{2}\int_R k_p (\frac{\partial w}{\partial y})^2 \mathrm{d}A, \end{aligned} \tag{2.14}$$

where Ω is the region occupied by the plate, S^- and S^+ represent, respectively, the top and bottom surface layers of the plate (see Fig 2.2), R denotes the area occupied by the mid-plane of the plate, dV is the volume element, and dA is the area element. In Eq. (2.14), U_B is the strain energy in the bulk of the plate, which is governed by the modified couple stress theory, U_S is the strain energy in the surface layers S^- and S^+ satisfying the surface elasticity theory, and U_F is the strain energy representing the effect of the two-parameter elastic foundation. Note that only the first part of U_B is considered in the classical Kirchhoff plate theory as the total strain energy (i.e., $U_T^C = \frac{1}{2}\int_\Omega \sigma_{ij}\varepsilon_{ij}\mathrm{d}V$) in the plate.

From Eqs. (2.9)–(2.14), the first variation of the total strain energy in the plate on the time interval [0, T] can be obtained as

$$\begin{aligned}\delta\int_0^T U_T\mathrm{d}t = {} & \int_0^T\int_\Omega\left(\sigma_{ij}\delta\varepsilon_{ij} + m_{ij}\delta\chi_{ij}\right)\mathrm{d}V\mathrm{d}t + \int_0^T\int_{S^+}(\tau^+_{\alpha\beta} - \frac{1}{2}\tau_0\delta_{\alpha\beta})\delta\varepsilon^+_{\alpha\beta}\mathrm{d}A\mathrm{d}t \\ & + \int_0^T\int_{S^-}(\tau^-_{\alpha\beta} - \frac{1}{2}\tau_0\delta_{\alpha\beta})\delta\varepsilon^-_{\alpha\beta}\mathrm{d}A\mathrm{d}t + \int_0^T\int_R k_w w\delta w\mathrm{d}A\mathrm{d}t - \int_0^T\int_R k_p\left(\frac{\partial^2 w}{\partial x^2} + \frac{\partial^2 w}{\partial y^2}\right)\delta w\mathrm{d}A\mathrm{d}t \\ & + \int_0^T\oint_{\partial R} k_p\left(\frac{\partial w}{\partial x}n_x + \frac{\partial w}{\partial y}n_y\right)\delta w\mathrm{d}s\mathrm{d}t,\end{aligned} \tag{2.15}$$

where ∂R is the boundary curve enclosing the area R, ds is the differential element of arc length along ∂R, $\tau^+_{\alpha\beta}$ and $\tau^-_{\alpha\beta}$ represent, respectively, the surface stress components on the plate bottom (S^+) and top (S^-) surfaces. In reaching Eq. (2.15), use has been made of Green's theorem and the fact that $\tau_{\alpha\beta}$ is non-symmetric. This fact has been overlooked in other variational studies employing the surface elasticity theory of Gurtin and Murdoch (1975, 1978).

Note that the volume integral of a sufficiently smooth function D (x, y, z, t) over the region Ω occupied by a uniform-thickness plate can be represented by

$$\int_{\Omega} D(x,\, y,\, z,\, t)\mathrm{d}V = \int_{R}\int_{-h/2}^{h/2} D(x,\, y,\, z,\, t)\mathrm{d}z\mathrm{d}A, \tag{2.16}$$

where h is the plate thickness, and R is the plate mid-plane area.

Using Eqs. (2.11), (2.13) and (2.16) in Eq. (2.15) gives, with the help of Green's theorem,

$$\begin{aligned}
\delta\int_0^T U_T\mathrm{d}t = &-\int_0^T\int_R \bigg\{\bigg[N_{xx,x} + N_{xy,y} + \frac{1}{2}\left(Y_{xz,xy} + Y_{yz,yy}\right) + \tau^{+}_{xx,x} + \tau^{-}_{xx,x} + \frac{1}{2}\left(\tau^{+}_{xy,y} + \tau^{-}_{xy,y}\right) \\
&+ \frac{1}{2}\left(\tau^{+}_{yx,y} + \tau^{-}_{yx,y}\right)\bigg]\delta u + \bigg[N_{yy,y} + N_{xy,x} - \frac{1}{2}\left(Y_{xz,xx} + Y_{yz,xy}\right) + \tau^{+}_{yy,y} + \tau^{-}_{yy,y} + \frac{1}{2}\left(\tau^{+}_{xy,x} + \tau^{-}_{xy,x}\right) \\
&+ \frac{1}{2}\left(\tau^{+}_{yx,x} + \tau^{-}_{yx,x}\right)\bigg]\delta v + \Big[M_{xx,xx} + 2M_{xy,xy} + M_{yy,yy} - Y_{xx,xy} + Y_{xy,xx} - Y_{xy,yy} + Y_{yy,xy} \\
&+ \frac{h}{2}\left(\tau^{+}_{\alpha\beta} - \tau^{-}_{\alpha\beta}\right)_{,\alpha\beta} - k_w w + k_p\left(\frac{\partial^2 w}{\partial x^2} + \frac{\partial^2 w}{\partial y^2}\right)\bigg]\delta w\bigg\}\mathrm{d}A\mathrm{d}t + \frac{1}{2}\int_0^T\oint_{\partial R}\Big\{\Big[2N_{xx}n_x + 2N_{xy}n_y \\
&+ \frac{1}{2}\left(Y_{xz,x}n_y + Y_{xz,y}n_x\right) + Y_{yz,y}n_y + 2\left(\tau^{+}_{xx} + \tau^{-}_{xx} - \tau_0\right)n_x + \left(\tau^{+}_{xy} + \tau^{-}_{xy} + \tau^{+}_{yx} + \tau^{-}_{yx}\right)n_y\bigg]\delta u \\
&+ \bigg[2N_{xy}n_x + 2N_{yy}n_y - Y_{xz,x}n_x - \frac{1}{2}\left(Y_{yz,x}n_y + Y_{yz,y}n_x\right) + 2\left(\tau^{+}_{yy} + \tau^{-}_{yy} - \tau_0\right)n_y \\
&+ \left(\tau^{+}_{xy} + \tau^{-}_{xy} + \tau^{+}_{yx} + \tau^{-}_{yx}\right)n_x\Big]\delta v + \Big[2\left(M_{xx,x} + M_{xy,y}\right)n_x + 2\left(M_{xy,x} + M_{yy,y}\right)n_y \\
&- \frac{1}{2}\left(Y_{xx} - Y_{yy}\right)_{,x}n_y - \frac{1}{2}\left(Y_{xx} - Y_{yy}\right)_{,y}n_x - \left(Y_{xx,x} + Y_{xy,y}\right)n_y + Y_{xy,x}n_x - Y_{xy,y}n_y + \left(Y_{xy,x} + Y_{yy,y}\right)n_x \\
&+ h\left(\tau^{+}_{\alpha\beta,\beta} - \tau^{-}_{\alpha\beta,\beta}\right)n_\alpha + 2k_p\left(\frac{\partial w}{\partial x}n_x + \frac{\partial w}{\partial y}n_y\right)\bigg]\delta w - \bigg[2M_{xx}n_x + 2M_{xy}n_y - \frac{1}{2}\left(Y_{xx} - 3Y_{yy}\right)n_y \\
&+ 2Y_{xy}n_x + h\left(\tau^{+}_{xx} - \tau^{-}_{xx}\right)n_x + h\left(\tau^{+}_{xy} - \tau^{-}_{xy}\right)n_y\Big]\delta w_{,x} - \bigg[2M_{xy}n_x + 2M_{yy}n_y - \frac{1}{2}\left(3Y_{xx} - Y_{yy}\right)n_x \\
&- 2Y_{xy}n_y + h\left(\tau^{+}_{yx} - \tau^{-}_{yx}\right)n_x + h\left(\tau^{+}_{yy} - \tau^{-}_{yy}\right)n_y\Big]\delta w_{,y} - \frac{1}{2}Y_{xz}n_y\delta u_{,x} - \left(\frac{1}{2}Y_{xz}n_x + Y_{yz}n_y\right)\delta u_{,y} \\
&+ \frac{1}{2}\left(2Y_{xz}n_x + Y_{yz}n_y\right)\delta v_{,x} + \frac{1}{2}Y_{yz}n_x\delta v_{,y}\bigg\}\mathrm{d}s\mathrm{d}t,
\end{aligned} \tag{2.17}$$

where

$$
\begin{aligned}
&N_{xx} \equiv \int_{-h/2}^{h/2} \sigma_{xx} \mathrm{d}z, \quad N_{yy} \equiv \int_{-h/2}^{h/2} \sigma_{yy} \mathrm{d}z, \quad N_{xy} \equiv \int_{-h/2}^{h/2} \sigma_{xy} \mathrm{d}z, \\
&M_{xx} \equiv \int_{-h/2}^{h/2} \sigma_{xx} z \mathrm{d}z, \quad M_{yy} \equiv \int_{-h/2}^{h/2} \sigma_{yy} z \mathrm{d}z, \quad M_{xy} \equiv \int_{-h/2}^{h/2} \sigma_{xy} z \mathrm{d}z, \\
&Y_{xx} \equiv \int_{-h/2}^{h/2} m_{xx} \mathrm{d}z, \quad Y_{yy} \equiv \int_{-h/2}^{h/2} m_{yy} \mathrm{d}z, \quad Y_{xy} \equiv \int_{-h/2}^{h/2} m_{xy} \mathrm{d}z, \quad Y_{xz} \equiv \int_{-h/2}^{h/2} m_{xz} \mathrm{d}z, \quad Y_{yz} \equiv \int_{-h/2}^{h/2} m_{yz} \mathrm{d}z
\end{aligned}
\tag{2.18}
$$

are the Cauchy stress and couple stress resultants through the plate thickness. Note that in reaching Eq. (2.17) use has been made of the relations $S^+ = R = S^-$, $\partial S^+ = \partial R = \partial S^-$ for the uniform-thickness plate under consideration in order to facilitate the integral evaluations.

The kinetic energy of the plate has the form (e.g., Ma et al., 2011; Gao et al., 2013)

$$K = \frac{1}{2}\int_{\Omega} \rho\left[\left(\dot{u}_1\right)^2 + \left(\dot{u}_2\right)^2 + \left(\dot{u}_3\right)^2\right] \mathrm{d}V \tag{2.19}$$

where ρ is the mass density of the plate material. Note that here and in the sequel the overhead "·" and "··" denote, respectively, the first and second time derivatives (e.g., $\dot{u}_1 = \partial u_1 / \partial t,\ \ddot{u}_1 = \partial^2 u_1 / \partial t^2$).

From Eqs. (2.2a-c), (2.16) and (2.19), the first variation of the kinetic energy, on the time interval [0, T], can be obtained as

$$\delta\int_0^T K \mathrm{d}t = -\int_0^T \int_R (m_0 \ddot{u}\delta u + m_0 \ddot{v}\delta v + m_0 \ddot{w}\delta w + m_2 \ddot{w}_{,x}\delta w_{,x} + m_2 \ddot{w}_{,y}\delta w_{,y}) \mathrm{d}A \mathrm{d}t, \tag{2.20}$$

where

$$m_0 \equiv \int_{-h/2}^{h/2} \rho \mathrm{d}z = \rho h, \quad m_2 \equiv \int_{-h/2}^{h/2} \rho z^2 \mathrm{d}z = \frac{\rho h^3}{12}. \tag{2.21}$$

In reaching Eq. (2.20), it has been assumed that the initial (t = 0) and final (t = T) configurations of the plate are prescribed so that the virtual displacements vanish at t = 0 and $t = T$. In addition, ρ is taken to be constant along the plate thickness and over the time interval [0, T] such that $\dot{m}_0 = 0,\ \dot{m}_2 = 0$.

From the general expression of the work done by external forces in the modified couple stress theory (Park and Gao, 2008) and in the surface elasticity theory (Gurtin and Murdoch, 1975, 1978), the virtual work done by the forces applied on the current plate over the time interval [0, T] can be written as

$$\delta\int_0^T W\mathrm{d}t = \int_0^T\int_R\left(\mathbf{f}\cdot\delta\mathbf{u}+\mathbf{c}\cdot\delta\boldsymbol{\theta}\right)\mathrm{d}A\mathrm{d}t+\int_0^T\oint_{\partial R}\left(\overline{\mathbf{t}}\cdot\delta\mathbf{u}+\overline{\mathbf{s}}\cdot\delta\boldsymbol{\theta}\right)\mathrm{d}s\mathrm{d}t+\int_0^T\int_S\mathbf{t}^s\cdot\delta(u_3\mathbf{e}_3)\mathrm{d}A\mathrm{d}t, \tag{2.22}$$

where $\mathbf{f}$ and $\mathbf{c}$ are, respectively, the body force resultant (force per unit area), body couple resultant (moment per unit area) through the plate thickness acting in the area R (i.e., the plate mid-plane), $\overline{\mathbf{t}}$ and $\overline{\mathbf{s}}$ are, respectively, the Cauchy traction resultant (force per unit length) and the surface couple resultant (moment per unit length) through the plate thickness acting on ∂R (i.e., the boundary of R), S represents the top and bottom surfaces of the plate (with $S = S^+ \cup S^-$), and $\mathbf{t}^s$ is the surface traction that is related to the surface stress $\boldsymbol{\tau}$ through $\mathbf{t}^s = \nabla_s\cdot\boldsymbol{\tau} = \tau_{i\alpha,\alpha}\mathbf{e}_i$ (e.g., Gurtin and Murdoch, 1978; Altenbach et al., 2010). Note that the last term in the virtual work expression in Eq. (2.22) accounts for the contribution of the normal stress on the top and bottom plate surfaces $\sigma_{33}^{\pm}$ (= $\pm\tau_{3\alpha,\alpha}^{\pm}$ from the equilibrium equations in Eq. (2.8a)), which is neglected in the classical Kirchhoff plate theory that does not consider the surface energy effect.

Using Eqs. (2.2a-c), (2.8a) and (2.12) in Eq. (2.22) leads to, with the help of Green's theorem,

$$\begin{aligned}\delta\int_0^T W\mathrm{d}t &= \int_0^T\int_R\left[f_x\delta u + f_y\delta v + f_z\delta w + c_x\delta w_{,y} - c_y\delta w_{,x} + \frac{1}{2}c_z(\delta v_{,x} - \delta u_{,y})\right]\mathrm{d}A\mathrm{d}t\\
&+\int_0^T\oint_{\partial R}\left[\overline{t}_x\delta u + \overline{t}_y\delta v + \overline{t}_z\delta w - \overline{M}_x\delta w_{,x} - \overline{M}_y\delta w_{,y} + \overline{s}_x\delta w_{,y} - \overline{s}_y\delta w_{,x} + \frac{1}{2}\overline{s}_z(\delta v_{,x} - \delta u_{,y})\right]\mathrm{d}s\mathrm{d}t\\
&+\int_0^T\int_{S^+}\overset{+}{\tau}_{3\alpha,\alpha}\delta w\mathrm{d}A\mathrm{d}t + \int_0^T\int_{S^-}\overset{-}{\tau}_{3\alpha,\alpha}\delta w\mathrm{d}A\mathrm{d}t,\end{aligned}$$

(2.23)

where f_i, c_i, $\overline{t}_i$ and $\overline{s}_i$ $(i = x, y, z)$ are, respectively, the components of $\mathbf{f}$, $\mathbf{c}$, $\overline{\mathbf{t}}$ and $\overline{\mathbf{s}}$, and $\overline{M}_x$ and $\overline{M}_y$ are, respectively, the applied moments per unit length about the *y*-axis and *x*-axis acting on ∂R. Note that the positive directions of $\overline{M}_x$ and $\overline{M}_y$ are, respectively, opposite to those of $\partial w/\partial x$ and $\partial w/\partial y$ (see Fig 2.2).

According to Hamilton's principle (e.g., Reddy, 2002; Ma et al., 2008, 2010, 2011; Gao et al. 2013),

$$\delta\int_0^T\left[K - \left(U_T - W\right)\right]\mathrm{d}t = 0. \tag{2.24}$$

Using Eqs. (2.17), (2.20) and (2.23) in Eq. (2.24) and applying the fundamental lemma of the calculus of variations (e.g., Steigmann, 1996, 2007; Gao and Mall, 2001) will result in, with the arbitrariness of δu, δv and δw and the relations $S^+ = R = S^-$, $\partial S^+ = \partial R = \partial S^-$ due to the uniform thickness of the plate,

$$\begin{aligned}&N_{xx,x} + N_{xy,y} + \frac{1}{2}\left(Y_{xz,xy} + Y_{yz,yy}\right) + \overset{+}{\tau}_{xx,x} + \overset{-}{\tau}_{xx,x} + \frac{1}{2}\left(\overset{+}{\tau}_{xy,y} + \overset{-}{\tau}_{xy,y}\right) + \frac{1}{2}\left(\overset{+}{\tau}_{yx,y} + \overset{-}{\tau}_{yx,y}\right)\\
&\quad + f_x + \frac{1}{2}c_{z,y} = m_0\ddot{u},\end{aligned} \tag{2.25a}$$

$$\begin{aligned}&N_{xy,x} + N_{yy,y} - \frac{1}{2}\left(Y_{xz,xx} + Y_{yz,xy}\right) + \overset{+}{\tau}_{yy,y} + \overset{-}{\tau}_{yy,y} + \frac{1}{2}\left(\overset{+}{\tau}_{xy,x} + \overset{-}{\tau}_{xy,x}\right) + \frac{1}{2}\left(\overset{+}{\tau}_{yx,x} + \overset{-}{\tau}_{yx,x}\right)\\
&\quad + f_y - \frac{1}{2}c_{z,x} = m_0\ddot{v},\end{aligned} \tag{2.25b}$$

$$
\begin{aligned}
&M_{xx,xx}+2M_{xy,xy}+M_{yy,yy}-Y_{xx,xy}+Y_{xy,xx}-Y_{xy,yy}+Y_{yy,xy}-k_w w+k_p\left(\frac{\partial^2 w}{\partial x^2}+\frac{\partial^2 w}{\partial y^2}\right)\\
&+\frac{h}{2}(\tau^+_{\alpha\beta}-\tau^-_{\alpha\beta})_{,\alpha\beta}+\tau^+_{3\alpha,\alpha}+\tau^-_{3\alpha,\alpha}+f_z-c_{x,y}+c_{y,x}=m_0\ddot{w}-m_2\frac{\partial^2\ddot{w}}{\partial x^2}-m_2\frac{\partial^2\ddot{w}}{\partial y^2}
\end{aligned}
\tag{2.25c}
$$

as the equations of motion of the Kirchhoff plate for any $(x, y) \in R$ and $t \in (0, T)$, and

$$
\begin{aligned}
&-\frac{1}{2}\int_0^T\oint_{\partial R}\Bigg\{\Big[2N_{xx}n_x+2N_{xy}n_y+\frac{1}{2}Y_{xz,x}n_y+\frac{1}{2}Y_{xz,y}n_x+Y_{yz,y}n_y+2(\tau^+_{xx}+\tau^-_{xx}-\tau_0)n_x\\
&+(\tau^+_{xy}+\tau^-_{xy}+\tau^+_{yx}+\tau^-_{yx})n_y+c_z n_y-2\overline{t}_x\Big]\delta u+\Big[2N_{xy}n_x+2N_{yy}n_y-Y_{xz,x}n_x-\frac{1}{2}Y_{yz,x}n_y\\
&-\frac{1}{2}Y_{yz,y}n_x+(\tau^+_{xy}+\tau^-_{xy}+\tau^+_{yx}+\tau^-_{yx})n_x+2(\tau^+_{yy}+\tau^-_{yy}-\tau_0)n_y-c_z n_x-2\overline{t}_y\Big]\delta v\\
&+\Big[2(M_{xx,x}+M_{xy,y})n_x+2(M_{xy,x}+M_{yy,y})n_y-\frac{1}{2}(Y_{xx}-Y_{yy})_{,x}n_y-\frac{1}{2}(Y_{xx}-Y_{yy})_{,y}n_x\\
&+Y_{xy,x}n_x-Y_{xy,y}n_y+(Y_{xy,x}+Y_{yy,y})n_x-(Y_{xx,x}+Y_{xy,y})n_y+2k_p\left(\frac{\partial w}{\partial x}n_x+\frac{\partial w}{\partial y}n_y\right)\\
&+h(\tau^+_{\alpha\beta,\beta}-\tau^-_{\alpha\beta,\beta})n_\alpha-2c_x n_y+2c_y n_x-2\overline{t}_z+2m_2(\ddot{w}_{,x}n_x+\ddot{w}_{,y}n_y)\Big]\delta w-\Big[2M_{xx}n_x+2M_{xy}n_y\\
&-\frac{1}{2}(Y_{xx}-3Y_{yy})n_y+2Y_{xy}n_x+h(\tau^+_{xx}-\tau^-_{xx})n_x+h(\tau^+_{xy}-\tau^-_{xy})n_y-2\overline{M}_x-2\overline{s}_y\Big]\delta w_{,x}-\Big[2M_{xy}n_x\\
&+2M_{yy}n_y-\frac{1}{2}(3Y_{xx}-Y_{yy})n_x-2Y_{xy}n_y+h(\tau^+_{yx}-\tau^-_{yx})n_x+h(\tau^+_{yy}-\tau^-_{yy})n_y-2\overline{M}_y+2\overline{s}_x\Big]\delta w_{,y}\\
&-\frac{1}{2}Y_{xz}n_y\delta u_{,x}-(\frac{1}{2}Y_{xz}n_x+Y_{yz}n_y-\overline{s}_z)\delta u_{,y}+(Y_{xz}n_x+\frac{1}{2}Y_{yz}n_y-\overline{s}_z)\delta v_{,x}+\frac{1}{2}Y_{yz}n_x\delta v_{,y}\Bigg\}\mathrm{d}s\mathrm{d}t=0,
\end{aligned}
\tag{2.26}
$$

which can be further simplified to obtain the boundary conditions.

Note that the integrand of the line integral in Eq. (2.26) is expressed in terms of the Cartesian components of the resultants and displacements that are functions of the Cartesian coordinates (x, y, z) with the unit base vectors $\{\mathbf{e}_1, \mathbf{e}_2, \mathbf{e}_3\}$. This is convenient for a rectangular plate whose edges are parallel to the x- and y-axes. However, for a more general case of a plate whose boundary is not aligned with the x- or y-axis, as shown in Fig 2.3, it is more convenient to use a Cartesian coordinate system $(n,\ s,\ z)$ with the unit base vectors $\{\mathbf{e}_n, \mathbf{e}_s, \mathbf{e}_3\}$, where $\mathbf{e}_n$ $(= n_x\mathbf{e}_1 + n_y\mathbf{e}_2)$ and $\mathbf{e}_s$ $(= -n_y\mathbf{e}_1 + n_x\mathbf{e}_2)$ are, respectively, the unit normal and tangent vectors on the plate boundary ∂R.

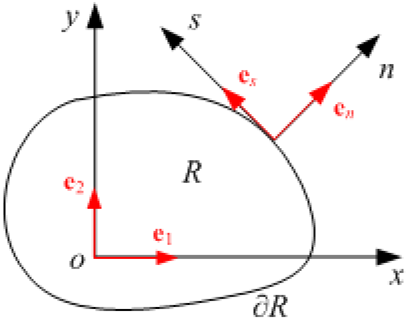

Fig. 2.3 Two coordinate systems

It can be shown that the components in the coordinate system (x, y, z) are related to those in the coordinate system (n, s, z) through the following transformation expressions:

$$\{u, v\}^T = [R_1]\{u_n, v_s\}^T, \ \{w_{,x}, w_{,y}\}^T = [R_1]\{w_{,n}, w_{,s}\}^T,$$

$$\{\bar{t}_x, \bar{t}_y\}^T = [R_1]\{\bar{t}_n, \bar{t}_s\}^T, \ \{\bar{s}_x, \bar{s}_y\}^T = [R_1]\{\bar{s}_n, \bar{s}_s\}^T, \ \{c_x, c_y\}^T = [R_1]\{c_n, c_s\}^T,$$

$$\{\bar{M}_x, \bar{M}_y\}^T = [R_1]\{\bar{M}_n, \bar{M}_s\}^T, \ \{Y_{xz}, Y_{yz}\}^T = [R_1]\{Y_{nz}, Y_{sz}\}^T,$$

$$\begin{bmatrix} N_{xx} & N_{xy} \\ N_{xy} & N_{yy} \end{bmatrix} = [R_1]\begin{bmatrix} N_{nn} & N_{ns} \\ N_{ns} & N_{ss} \end{bmatrix}[R_1]^T, \ \begin{bmatrix} Y_{xx} & Y_{xy} \\ Y_{xy} & Y_{yy} \end{bmatrix} = [R_1]\begin{bmatrix} Y_{nn} & Y_{ns} \\ Y_{ns} & Y_{ss} \end{bmatrix}[R_1]^T,$$

$$\begin{bmatrix} M_{xx} & M_{xy} \\ M_{xy} & M_{yy} \end{bmatrix} = [R_1]\begin{bmatrix} M_{nn} & M_{ns} \\ M_{ns} & M_{ss} \end{bmatrix}[R_1]^T, \ \begin{bmatrix} Y_{xz,x} & Y_{xz,y} \\ Y_{yz,x} & Y_{yz,y} \end{bmatrix} = [R_1]\begin{bmatrix} Y_{nz,n} & Y_{nz,s} \\ Y_{sz,n} & Y_{sz,s} \end{bmatrix}[R_1]^T, \quad (2.27)$$

$$\begin{bmatrix} \tau^{\pm}_{xx} & \tau^{\pm}_{xy} \\ \tau^{\pm}_{yx} & \tau^{\pm}_{yy} \end{bmatrix} = [R_1]\begin{bmatrix} \tau^{\pm}_{nn} & \tau^{\pm}_{ns} \\ \tau^{\pm}_{sn} & \tau^{\pm}_{ss} \end{bmatrix}[R_1]^T, \ \begin{bmatrix} u_{,x} & u_{,y} \\ v_{,x} & v_{,y} \end{bmatrix} = [R_1]\begin{bmatrix} u_{n,n} & u_{n,s} \\ v_{s,n} & v_{s,s} \end{bmatrix}[R_1]^T,$$

$$\{M_{xx,x}, M_{xx,y}, M_{xy,x}, M_{xy,y}, M_{yy,x}, M_{yy,y}\}^T = [R_3]\{M_{nn,n}, M_{nn,s}, M_{ns,n}, M_{ns,s}, M_{ss,n}, M_{ss,s}\}^T,$$

$$\{Y_{xx,x}, Y_{xx,y}, Y_{xy,x}, Y_{xy,y}, Y_{yy,x}, Y_{yy,y}\}^T = [R_3]\{Y_{nn,n}, Y_{nn,s}, Y_{ns,n}, Y_{ns,s}, Y_{ss,n}, Y_{ss,s}\}^T,$$

$$\left\{\tau^{\pm}_{xx,x},\ \tau^{\pm}_{xy,y},\ \tau^{\pm}_{yx,x},\ \tau^{\pm}_{yy,y}\right\}^{T} = \left[R_4\right]\left\{\tau^{\pm}_{nn,n},\ \tau^{\pm}_{nn,s},\ \tau^{\pm}_{ns,n},\ \tau^{\pm}_{sn,n},\ \tau^{\pm}_{ns,s},\ \tau^{\pm}_{sn,s},\ \tau^{\pm}_{ss,n},\ \tau^{\pm}_{ss,s}\right\}^{T},$$

where

$$\left[R_1\right] \equiv \begin{bmatrix} n_x & -n_y \\ n_y & n_x \end{bmatrix},$$

$$\left[R_3\right] \equiv \begin{bmatrix} n_x^3 & -n_x^2 n_y & -2n_x^2 n_y & 2n_x n_y^2 & n_x n_y^2 & -n_y^3 \\ n_x^2 n_y & n_x^3 & -2n_x n_y^2 & -2n_x^2 n_y & n_y^3 & n_x n_y^2 \\ n_x^2 n_y & -n_x n_y^2 & n_x^3 - n_x n_y^2 & -n_x^2 n_y + n_y^3 & -n_x^2 n_y & n_x n_y^2 \\ n_x n_y^2 & n_x^2 n_y & n_x^2 n_y - n_y^3 & n_x^3 - n_x n_y^2 & -n_x n_y^2 & -n_x^2 n_y \\ n_x n_y^2 & -n_y^3 & 2n_x^2 n_y & -2n_x n_y^2 & n_x^3 & -n_x^2 n_y \\ n_y^3 & n_x n_y^2 & 2n_x n_y^2 & 2n_x^2 n_y & n_x^2 n_y & n_x^3 \end{bmatrix}, \qquad (2.28a\text{-}c)$$

$$\left[R_4\right] \equiv \begin{bmatrix} n_x^3 & -n_x^2 n_y & -n_x^2 n_y & -n_x^2 n_y & n_x n_y^2 & n_x n_y^2 & n_x n_y^2 & -n_y^3 \\ n_x n_y^2 & n_x^2 n_y & n_x^2 n_y & -n_y^3 & n_x^3 & -n_x n_y^2 & -n_x n_y^2 & -n_x^2 n_y \\ n_x^2 n_y & -n_x n_y^2 & -n_x n_y^2 & n_x^3 & n_y^3 & -n_x^2 n_y & -n_x^2 n_y & n_x n_y^2 \\ n_y^3 & n_x n_y^2 & n_x n_y^2 & n_x n_y^2 & n_x^2 n_y & n_x^2 n_y & n_x^2 n_y & n_x^3 \end{bmatrix},$$

with $n_x^2 + n_y^2 = 1$.

Using Eqs. (2.27) and (2.28a-c) in Eq. (2.26) yields, after some lengthy algebra,

$$\begin{aligned} &\int_0^T \oint_{\partial R} \Bigg\{ 2\left(N_{nn} + \frac{1}{4} Y_{nz,s} + \tau^{+}_{nn} + \tau^{-}_{nn} - \tau_0 - \bar{t}_n \right)\delta u_n - \Bigg(-2N_{ns} + Y_{nz,n} + \frac{1}{2} Y_{sz,s} - \tau^{+}_{ns} - \tau^{-}_{ns} \\ &- \tau^{+}_{sn} - \tau^{-}_{sn} + c_z + 2\bar{t}_s \Bigg)\delta v_s + \Big[2M_{nn,n} + 2M_{ns,s} + h\left(\tau^{+}_{nn,n} - \tau^{-}_{nn,n} + \tau^{+}_{ns,s} - \tau^{-}_{ns,s} \right) - \frac{1}{2} Y_{nn,s} + 2Y_{ns,n} \\ &+ \frac{3}{2} Y_{ss,s} + 2c_s - 2\bar{t}_z + 2m_2 \ddot{w}_{,n} + 2k_p w_{,n} \Big]\delta w + \left(-2Y_{ns} - 2M_{nn} - h\tau^{+}_{nn} + h\tau^{-}_{nn} + 2\overline{M}_n + 2\bar{s}_s \right)\delta w_{,n} \\ &+ \left(-2M_{ns} + \frac{3}{2} Y_{nn} - \frac{1}{2} Y_{ss} - h\tau^{+}_{sn} + h\tau^{-}_{sn} + 2\overline{M}_s - 2\bar{s}_n \right)\delta w_{,s} + \left(-\frac{1}{2} Y_{nz} + \bar{s}_z\right)\delta u_{n,s} \\ &+ (Y_{nz} - \bar{s}_z)\delta v_{s,n} + \frac{1}{2} Y_{sz}\delta v_{s,s} \Bigg\} \mathrm{d}s\mathrm{d}t = 0. \end{aligned}$$

$$(2.29)$$

Note that on the closed boundary ∂R, the following identity:

$$\oint_{\partial R} D\delta g_{,s}\mathrm{d}s = -\oint_{\partial R} D_{,s}\delta g\mathrm{d}s \tag{2.30}$$

holds, where *D*, *g* are two smooth functions. Using Eq. (2.30) in Eq. (2.29) leads to

$$\int_0^T \oint_{\partial R}\left(\widehat{N}_{nn}\delta u_n + \widehat{N}_{ss}\delta v_s + \widehat{N}_{zz}\delta w + \widehat{T}_z\delta w_{,n} + \widehat{T}_s\delta v_{s,n}\right)\mathrm{d}s\mathrm{d}t = 0, \tag{2.31}$$

where

$$\begin{aligned}
\widehat{N}_{nn} &\equiv 2(N_{nn} + \frac{1}{2}Y_{nz,s} + \tau_{nn}^{+} + \tau_{nn}^{-} - \tau_0 - \frac{1}{2}\bar{s}_{z,s} - \bar{t}_n),\\
\widehat{N}_{ss} &\equiv 2N_{ns} - Y_{nz,n} - Y_{sz,s} + \tau_{ns}^{+} + \tau_{ns}^{-} + \tau_{sn}^{+} + \tau_{sn}^{-} - c_z - 2\bar{t}_s,\\
\widehat{N}_{zz} &\equiv 2M_{nn,n} + 4M_{ns,s} - 2Y_{nn,s} + 2Y_{ns,n} + 2Y_{ss,s} + h(\tau_{nn,n}^{+} - \tau_{nn,n}^{-} + \tau_{ns,s}^{+} - \tau_{ns,s}^{-}\\
&\quad + \tau_{sn,s}^{+} - \tau_{sn,s}^{-}) + 2c_s - 2\overline{M}_{s,s} + 2\bar{s}_{n,s} - 2\bar{t}_z + 2m_2\ddot{w}_{,n} + 2k_p w_{,n},\\
\widehat{T}_z &\equiv -2Y_{ns} - 2M_{nn} - h\tau_{nn}^{+} + h\tau_{nn}^{-} + 2\overline{M}_n + 2\bar{s}_s,\\
\widehat{T}_s &\equiv Y_{nz} - \bar{s}_z.
\end{aligned} \tag{2.32a-e}$$

The use of the fundamental lemma of the calculus of variations in Eq. (2.31) gives

$$\begin{aligned}
\widehat{N}_{nn} &= 0 \quad \text{or} \quad u_n = \bar{u}_n,\\
\widehat{N}_{ss} &= 0 \quad \text{or} \quad v_s = \bar{v}_s,\\
\widehat{N}_{zz} &= 0 \quad \text{or} \quad w = \bar{w},\\
\widehat{T}_z &= 0 \quad \text{or} \quad w_{,n} = \bar{w}_{,n},\\
\widehat{T}_s &= 0 \quad \text{or} \quad v_{s,n} = \bar{v}_{s,n}
\end{aligned} \tag{2.33a-e}$$

as the boundary conditions for any $(x, y) \in \partial R$ and $t \in (0, T)$, where the overhead bar defines the prescribed value.

From Eqs. (2.3), (2.4), (2.11), (2.13) and (2.18), the Cauchy stress and couple stress resultants can be expressed in terms of *u*, *v* and *w* as

$$N_{xx} = h[(\lambda + 2\mu)\frac{\partial u}{\partial x} + \lambda\frac{\partial v}{\partial y}],$$

$$N_{yy} = h[(\lambda + 2\mu)\frac{\partial v}{\partial y} + \lambda\frac{\partial u}{\partial x}],$$

$$N_{xy} = \mu h(\frac{\partial u}{\partial y} + \frac{\partial v}{\partial x}),$$

$$M_{xx} = -\frac{1}{12}h^3[(\lambda + 2\mu)\frac{\partial^2 w}{\partial x^2} + \lambda\frac{\partial^2 w}{\partial y^2}],$$

$$M_{yy} = -\frac{1}{12}h^3[(\lambda + 2\mu)\frac{\partial^2 w}{\partial y^2} + \lambda\frac{\partial^2 w}{\partial x^2}],$$

$$M_{xy} = -\frac{1}{6}\mu h^3 \frac{\partial^2 w}{\partial x \partial y},$$

$$Y_{xx} = 2\mu l^2 h\frac{\partial^2 w}{\partial x \partial y},$$

$$Y_{yy} = -2\mu l^2 h\frac{\partial^2 w}{\partial x \partial y},$$

$$Y_{xy} = \mu l^2 h(\frac{\partial^2 w}{\partial y^2} - \frac{\partial^2 w}{\partial x^2}),$$

$$Y_{xz} = \frac{1}{2}\mu l^2 h(\frac{\partial^2 v}{\partial x^2} - \frac{\partial^2 u}{\partial x \partial y}),$$

$$Y_{yz} = \frac{1}{2}\mu l^2 h(\frac{\partial^2 v}{\partial x \partial y} - \frac{\partial^2 u}{\partial y^2}). \qquad (2.34a\text{-}k)$$

From Eqs. (2.9), (2.10) and (2.2a-c), it follows that the surface stress components are given by

$$\tau_{xx}^{\pm} = \tau_0 + (\lambda_0 + \tau_0)(\frac{\partial v}{\partial y} \mp \frac{h}{2}\frac{\partial^2 w}{\partial y^2}) + (\lambda_0 + 2\mu_0)(\frac{\partial u}{\partial x} \mp \frac{h}{2}\frac{\partial^2 w}{\partial x^2}),$$

$$\tau_{yy}^{\pm} = \tau_0 + (\lambda_0 + \tau_0)(\frac{\partial u}{\partial x} \mp \frac{h}{2}\frac{\partial^2 w}{\partial x^2}) + (\lambda_0 + 2\mu_0)(\frac{\partial v}{\partial y} \mp \frac{h}{2}\frac{\partial^2 w}{\partial y^2}),$$

$$\tau_{xy}^{\pm} = \mu_0(\frac{\partial u}{\partial y} + \frac{\partial v}{\partial x}) - \tau_0\frac{\partial v}{\partial x} \mp \frac{1}{2}(2\mu_0 - \tau_0)h\frac{\partial^2 w}{\partial x \partial y},$$

$$
\begin{aligned}
&\tau_{yx}^{\pm} = \mu_0\left(\frac{\partial u}{\partial y} + \frac{\partial v}{\partial x}\right) - \tau_0 \frac{\partial u}{\partial y} \mp \frac{1}{2}(2\mu_0 - \tau_0) h \frac{\partial^2 w}{\partial x \partial y}, \\
&\tau_{3x}^{+} = \tau_{3x}^{-} = \tau_0 \frac{\partial w}{\partial x}, \\
&\tau_{3y}^{+} = \tau_{3y}^{-} = \tau_0 \frac{\partial w}{\partial y}.
\end{aligned} \tag{2.35a-f}
$$

Using Eqs. (2.34a-k) and (2.35a-f) in Eqs. (2.25a-c) then yields the equations of motion of the Kirchhoff plate in terms of *u*, *v* and *w* as

$$
\begin{aligned}
&(\lambda + 2\mu) h u_{,xx} + \mu h u_{,yy} + (\lambda + \mu) h v_{,xy} + \frac{1}{4}\mu l^2 h(-u_{,xxyy} - u_{,yyyy} + v_{,xxxy} + v_{,xyyy}) \\
&\quad + 2(\mu_0 + \lambda_0)(u_{,xx} + v_{,xy}) + (2\mu_0 - \tau_0)(2u_{,xx} + u_{,yy} + v_{,xy}) + f_x + \frac{1}{2} c_{z,y} = m_0 \ddot{u},
\end{aligned} \tag{2.36a}
$$

$$
\begin{aligned}
&(\lambda + 2\mu) h v_{,yy} + \mu h v_{,xx} + (\lambda + \mu) h u_{,xy} + \frac{1}{4}\mu l^2 h(u_{,xxxy} + u_{,xyyy} - v_{,xxxx} - v_{,xxyy}) \\
&\quad + 2(\mu_0 + \lambda_0)(u_{,xy} + v_{,yy}) + (2\mu_0 - \tau_0)(u_{,xy} + v_{,xx} + 2v_{,yy}) + f_y - \frac{1}{2} c_{z,x} = m_0 \ddot{v},
\end{aligned} \tag{2.36b}
$$

$$
\begin{aligned}
&-\left[\frac{1}{12}(\lambda + 2\mu) h^3 + \mu l^2 h + \frac{1}{2}(\lambda_0 + 2\mu_0) h^2\right](w_{,xxxx} + 2w_{,xxyy} + w_{,yyyy}) \\
&\quad + (2\tau_0 + k_p)(w_{,xx} + w_{,yy}) - k_w w + f_z - c_{x,y} + c_{y,x} = m_0 \ddot{w} - m_2 \frac{\partial^2 \ddot{w}}{\partial x^2} - m_2 \frac{\partial^2 \ddot{w}}{\partial y^2}.
\end{aligned} \tag{2.36c}
$$

The boundary-initial value problem for determining *u, v* and *w* is defined by the differential equations in Eqs. (2.36a–c), the boundary conditions in Eqs. (2.33a–e), and given initial conditions at $t = 0$ and $t = T$. It is seen from Eqs. (2.36a-c) that the in-plane displacements *u* and *v* are uncoupled with the out-of-plane displacement *w* and can therefore be obtained separately from solving Eqs. (2.36a,b) subject to prescribed boundary conditions of the form in Eqs. (2.33a,b,e) and suitable initial conditions.

When $l = 0$, $c_i = 0$, Eqs. (2.36a-c) will reduce to the governing equations for the Kirchhoff plate in the absence of the microstructure (or couple stress) effect.

When $\lambda_0 = \mu_0 = \tau_0 = 0$, Eqs. (2.36a-c) will become the governing equations for the Kirchhoff plate without the surface energy effect.

When $l = 0$, $c_i = 0$, and $\lambda_0 = \mu_0 = \tau_0 = 0$, Eqs. (2.36a-c) will degenerate to the classical elasticity-based governing equations for the Kirchhoff plate resting on the two-parameter elastic foundation.

When $l = 0$, $c_i = 0$, $\lambda_0 = \mu_0 = \tau_0 = 0$, and $k_w = k_p = 0$, Eqs. (2.36a-c) reduce to

$$(\lambda + 2\mu)hu_{,xx} + \mu hu_{,yy} + (\lambda + \mu)hv_{,xy} + f_x = m_0\ddot{u}, \tag{2.37a}$$

$$(\lambda + 2\mu)hv_{,yy} + \mu hv_{,xx} + (\lambda + \mu)hu_{,xy} + f_y = m_0\ddot{v}, \tag{2.37b}$$

$$-\frac{1}{12}(\lambda + 2\mu)h^3(w_{,xxxx} + 2w_{,xxyy} + w_{,yyyy}) + f_z = m_0\ddot{w} - m_2\frac{\partial^2\ddot{w}}{\partial x^2} - m_2\frac{\partial^2\ddot{w}}{\partial y^2}, \tag{2.37c}$$

which are the governing equations for the Kirchhoff plate based on classical elasticity.

When $u = v = 0$, $w = w(x, t)$, $f_x = f_y = 0$, and $c_x = c_z = 0$, the Kirchhoff plate considered here becomes a Bernoulli-Euler beam with a unit width and a height h undergoing only bending deformations. For this case, Eqs. (2.36a–c) are simplified as

$$\begin{aligned}&-\left[\frac{1}{12}(\lambda + 2\mu)h^3 + \mu l^2 h + \frac{1}{2}(\lambda_0 + 2\mu_0)h^2\right]w_{,xxxx} + (2\tau_0 + k_p)w_{,xx} - k_w w + f_z + c_{y,x}\\ &= m_0\ddot{w} - m_2\frac{\partial^2\ddot{w}}{\partial x^2}\end{aligned} \tag{2.38}$$

for any $x \in (0, L)$ and $t \in (0, T)$, where L is the length of the beam (plate). When the elastic foundation is not present (i.e., $k_w = k_p = 0$), the governing equation in Eq. (2.38) reduces to that for the Bernoulli-Euler beam with a unit width and a height h without considering axial loading and the surface energy effect on the two side surfaces of the beam (Gao, 2015; Gao and Zhang, 2015). That is, the current Kirchhoff plate model recovers the non-classical Bernoulli-Euler beam model based on the same modified couple stress theory and surface elasticity theory. For static bending, $w = w(x)$, and Eq. (2.38) further reduce to the static equilibrium equation for a Bernoulli-Euler beam without the elastic foundation derived in Gao and Mahmoud (2014).

2.3 Examples

To demonstrate the new Kirchhoff model developed in Section 2.2, static bending and free vibration problems of a simply supported rectangular plate (see Fig 2.4) are analytically solved herein by directly applying the new model.

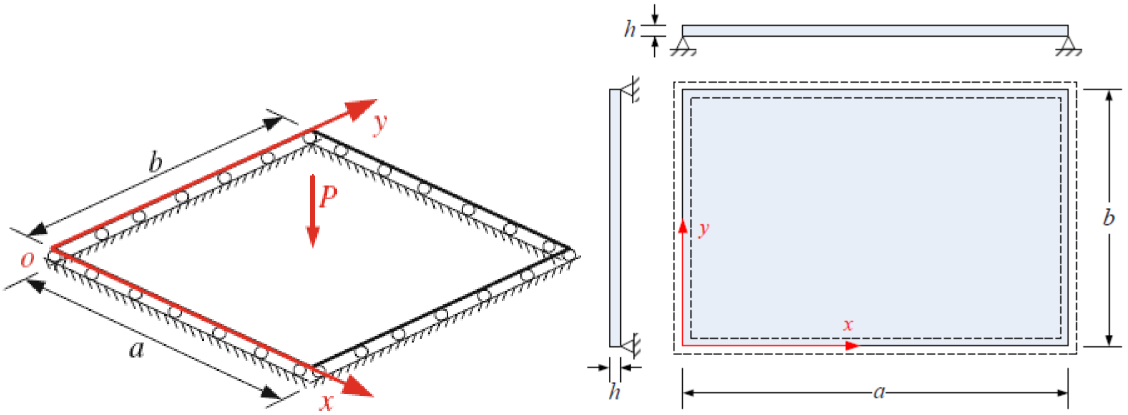

Fig. 2.4 Simply supported plate

In view of the general form of the boundary conditions (BCs) in Eqs. (2.33a–e), the BCs for this simply supported plate can be identified as

$$u_n = 0, \;\; \widehat{N}_{ss} = 0, \;\; w = 0, \;\; \hat{T}_z = 0, \;\; \hat{T}_s = 0 \tag{2.39}$$

for all (*x, y*) on the boundaries $x = 0$, a and $y = 0$, b. Also, the following applied traction resultants vanish on these boundaries:

$$\bar{s}_s = \bar{s}_z = 0, \;\; \overline{M}_n = 0, \;\; \bar{t}_s = 0. \tag{2.40}$$

For the boundaries $x = 0$, a, $n_y = 0$ and $n_x = -1$ (on $x = 0$) or $n_x = 1$ (on $x = a$), and Eq. (2.39) becomes, with the help of Eqs. (2.27), (2.28a), (2.32b,d,e) and (2.40),

$$u(0,y)=u(a,y)=0,$$

$$w(0,y)=w(a,y)=0,$$

$$N_{xy}-\frac{1}{2}Y_{xz,x}-\frac{1}{2}Y_{yz,y}+\frac{1}{2}(\tau_{xy}^{+}+\tau_{xy}^{-}+\tau_{yx}^{+}+\tau_{yx}^{-})-\frac{1}{2}c_z=0 \text{ on } x=0 \text{ and } x=a,$$

$$M_{xx}+Y_{xy}+\frac{h}{2}(\tau_{xx}^{+}-\tau_{xx}^{-})=0 \text{ on } x=0 \text{ and } x=a,$$

$$Y_{xz}=0 \text{ on } x=0 \text{ and } x=a. \tag{2.41a-e}$$

Using Eqs. (2.34c,d,i-k) and (2.35a,c,d) in Eqs. (2.41c-e) gives

$$\mu h(u_{,y}+v_{,x})+\frac{1}{4}\mu l^2 h(u_{,xyy}-v_{,xxx})+\frac{1}{4}\mu l^2 h(u_{,yyy}-v_{,xyy})+(2\mu_0-\tau_0)(u_{,y}+v_{,x})-\frac{1}{2}c_z=0,$$
$$\mu l^2 h(-w_{,xx}+w_{,yy})-\frac{1}{12}h^3[(\lambda+2\mu)w_{,xx}+\lambda w_{,yy}]-\frac{1}{2}h^2(\lambda_0+2\mu_0)w_{,xx}-\frac{1}{2}h^2(\lambda_0+\tau_0)w_{,yy}=0,$$
$$-u_{,xy}+v_{,xx}=0 \tag{2.42a-c}$$

on $x = 0$ and $x = a$.

For the boundaries $y = 0$, b, $n_x = 0$ and $n_y = -1$ (on $y = 0$) or $n_y = 1$ (on $y = b$), and Eq. (2.39) now becomes, with the help of Eqs. (2.27), (2.28a), (2.32b,d,e) and (2.40),

$$v(x,0)=v(x,b)=0,$$

$$w(x,0)=w(x,b)=0,$$

$$-N_{xy}-\frac{1}{2}(Y_{xz,x}+Y_{yz,y})-\frac{1}{2}(\tau_{xy}^{+}+\tau_{xy}^{-}+\tau_{yx}^{+}+\tau_{yx}^{-})-\frac{1}{2}c_z=0 \text{ on } y=0 \text{ and } y=b, \tag{2.43a-e}$$

$$M_{yy}-Y_{xy}+\frac{h}{2}(\tau_{yy}^{+}-\tau_{yy}^{-})=0 \text{ on } y=0 \text{ and } y=b,$$

$$Y_{yz}=0 \text{ on } y=0 \text{ and } y=b.$$

Using Eqs. (2.34c,e,i-k) and (2.35b-d) in Eqs. (2.43c-e) results in

$$\mu h(u_{,y}+v_{,x})-\frac{1}{4}\mu l^2 h(u_{,yyy}-v_{,xyy})-\frac{1}{4}\mu l^2 h(u_{,xxy}-v_{,xxx})+(2\mu_0-\tau_0)(u_{,y}+v_{,x})+\frac{1}{2}c_z=0,$$

$$\mu l^2 h(w_{,xx}-w_{,yy})-\frac{1}{12}h^3[\lambda w_{,xx}+(\lambda+2\mu)w_{,yy}]-\frac{1}{2}h^2[(\lambda_0+\tau_0)w_{,xx}+(\lambda_0+2\mu_0)w_{,yy}]=0,$$

$$u_{,yy}-v_{,xy}=0$$

(2.44a-c)

on $y = 0$ and $y = b$.

2.3.1 Static bending

For static bending problems, u, v and w are independent of time t so that all of the time derivatives involved in Eqs. (2.36a–c) vanish.

The boundary value problem (BVP) for the static bending of the simply supported plate shown in Fig 2.4 is defined by Eqs. (2.36a–c) and the boundary conditions in Eqs. (2.41a,b), (2.42a-c), (2.43a,b) and (2.44a-c), with $u = u(x, y)$, $v = v(x, y)$ and $w = w(x, y)$.

As mentioned in Section 2.2, the in-plane displacements u and v are uncoupled with w. They can be obtained from solving the BVP defined by Eqs. (2.36a), (2.36b), (2.41a), (2.42a,c), (2.43a) and (2.44a,c). For the current case with $f_x = f_y = 0$ and $c_z = 0$, the solution of this BVP gives $u = v = 0$ for any $(x, y) \in R$.

The out-of-plane displacement w can be obtained from solving the BVP defined by Eqs. (2.36c), (2.41b), (2.42b), (2.43b) and (2.44b).

Consider the following Fourier series solution for w:

$$w=\sum_{m=1}^{\infty}\sum_{n=1}^{\infty}W_{mn}\sin(\frac{m\pi x}{a})\sin(\frac{n\pi y}{b}), \tag{2.45}$$

where W_{mn} is the Fourier coefficient to be determined for each pair of m and n. It can be readily shown that w in Eq. (2.45) satisfies the boundary conditions in Eqs. (2.41b), (2.42b) at $x = 0$, a and in Eqs. (2.43b), (2.44b) at $y = 0$, b for any W_{mn}.

The force $f_z\,(x, y)$ involved in Eq. (2.36c) can also be expanded in a Fourier series as

$$f_z(x,y) = \sum_{m=1}^{\infty}\sum_{n=1}^{\infty} Q_{mn}\sin(\frac{m\pi x}{a})\sin(\frac{n\pi y}{b}), \tag{2.46}$$

where the Fourier coefficient Q_{mn} is given by

$$Q_{mn} = \frac{4}{ab}\int_0^a\int_0^b f_z(x,y)\sin(\frac{m\pi x}{a})\sin(\frac{n\pi y}{b})\mathrm{d}x\mathrm{d}y. \tag{2.47}$$

In the current case (see Fig 2.4), $f_z(x,y) = P\delta(x-\frac{a}{2})\delta(y-\frac{b}{2}),$ where $\delta(\cdot)$ is the Dirac delta function. Using this f_z in Eq. (2.47) yields

$$Q_{mn} = \frac{4P}{ab}\sin(\frac{m\pi}{2})\sin(\frac{n\pi}{2}). \tag{2.48}$$

Using Eqs. (2.45) and (2.46) in Eq. (2.36c) results in, with $c_x = c_y = 0,$

$$W_{mn} = \frac{Q_{mn}}{\Delta} \tag{2.49}$$

where

$$\Delta \equiv \Big[\frac{h^3}{12}(\lambda+2\mu)+\mu l^2 h+\frac{h^2}{2}(\lambda_0+2\mu_0)\Big](\frac{m^2\pi^2}{a^2}+\frac{n^2\pi^2}{b^2})^2+(2\tau_0+k_p)(\frac{m^2\pi^2}{a^2}+\frac{n^2\pi^2}{b^2})+k_w. \tag{2.50}$$

Substituting this W_{mn} into Eq. (2.45) will give the exact solution w based on the current non-classical Kirchhoff plate model for the simply supported plate subjected to the concentrated force at the center of the plate shown in Fig 2.4.

Clearly, Eqs. (2.49) and (2.50) show that the incorporation of the microstructure effect (i.e., with $l \neq 0$) will always lead to increased plate stiffness (thus reduced deflections), while the inclusion of the surface energy effect (i.e., with any of $\{\mu_0, \lambda_0, \tau_0\}$ not being zero) can result in either increased or decreased plate stiffness, depending on the signs of $2\mu_0 + \lambda_0$ and τ_0. It is also seen from Eqs. (2.49) and (2.50) that the presence of the elastic foundation (i.e., with $k_w > 0$ and/or $k_p > 0$) will always lead to reduced plate deflection.

Figure 2.5 displays the variations of the plate deflection w along the line $y = b/2$ predicted by the current non-classical Kirchhoff plate model and by its classical elasticity-based counterpart. The numerical results predicted by the new model are directly obtained from Eqs. (2.45) and (2.48)-(2.50), while those by the classical model are computed using the same equations but with $l = 0$, $\lambda_0 = \mu_0 = \tau_0 = 0$, and $k_w = k_p = 0$. In generating the numerical results shown in Fig 2.5, the shape of the plate is fixed by letting $a = b = 20h$, while the plate thickness h is varying. The plate material is taken to be aluminum with the following properties (Liu and Rajapakse, 2010; Gao and Mahmoud, 2014): $E = 90$ GPa, $v = 0.23$, $l = 6.58$ μm for the bulk properties, and $\mu_0 = -5.4251$ N/m, $\lambda_0 = 3.4939$ N/m, $\tau_0 = 0.5689$ N/m for the surface layers, where Young's modulus E and Poisson's ratio v are related to the Lamé constants λ and μ through (e.g., Timoshenko and Goodier, 1970):

$$\lambda = \frac{Ev}{(1+v)(1-2v)}, \quad \mu = \frac{E}{2(1+v)}. \tag{2.51}$$

The foundation moduli are non-dimensionalized and taken to be $\bar{K}_w = 100$, $\bar{K}_p = 10$, where $\bar{K}_w \equiv k_w a^4 / D$, $\bar{K}_p \equiv k_p a^2 / D$, with $D = Eh^3/[12(1-v^2)]$ being the plate flexural rigidity. The number of terms included in Eq. (2.45) is controlled by adjusting m and n. The numerical results for the plate deflection w obtained with $m = 30$ and $n = 30$ are found to be the same as those computed with larger m and n values (up to $m = 90$, $n = 90$) to the fourth decimal place. This indicates that using $m = 30$, $n = 30$ in the expansion is sufficient for the convergent numerical solution of w displayed in Fig 2.5.

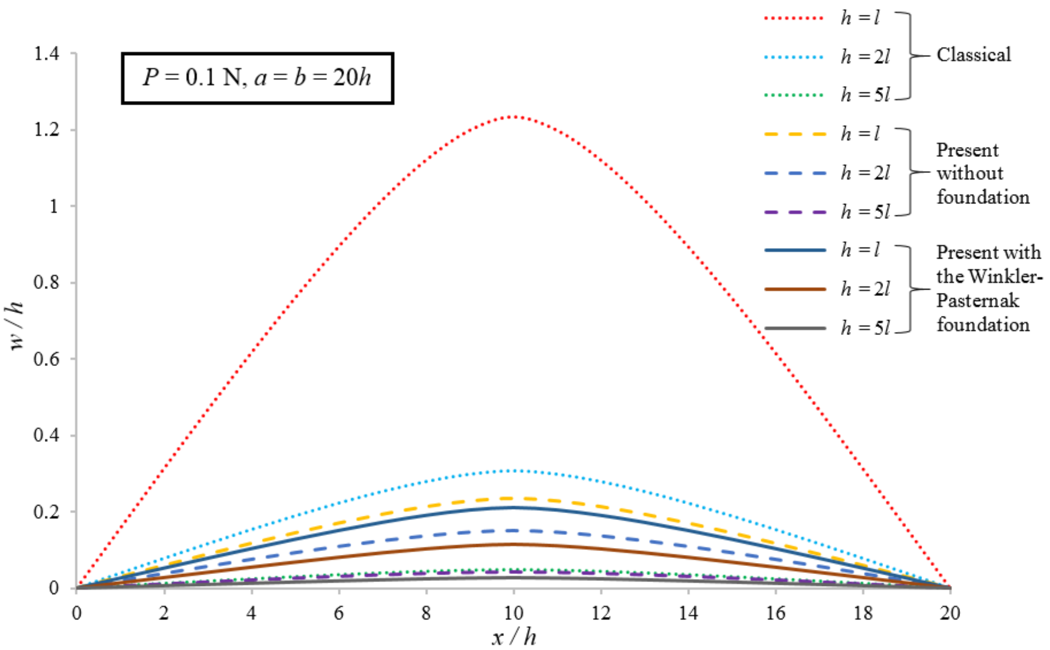

Fig. 2.5 Deflection of the simply supported Kirchhoff plate on $y = b/2$ with $\bar{K}_w = 100,\ \bar{K}_p = 10$

From Fig 2.5, it is clearly seen that the deflection w predicted by the current Kirchhoff model with or without the foundation is always lower than that predicted by the classical model in all cases considered. It also shows that the differences between the values predicted by the new model and the classical model are very large when the thickness of the plate h is small (with $h = l = 6.58$ μm here), but the differences are diminishing when the thickness of the plate h becomes large (with $h = 5l = 32.9$ μm here). This predicted size effect agrees with the general trend observed experimentally (e.g., McFarland and Colton, 2005). In addition, it is observed from Fig 2.5 that the presence of the elastic foundation does reduce the plate deflection, as expected (and noted earlier from Eqs. (2.49) and

(2.50)). This is further shown in Fig 2.6, where more cases with different values of k_w and k_p are compared, including the case without the foundation (as the top curve with $k_w = k_p = 0$). Note that the values of the other parameters are the same as those used in obtaining the numerical results shown in Fig 2.5.

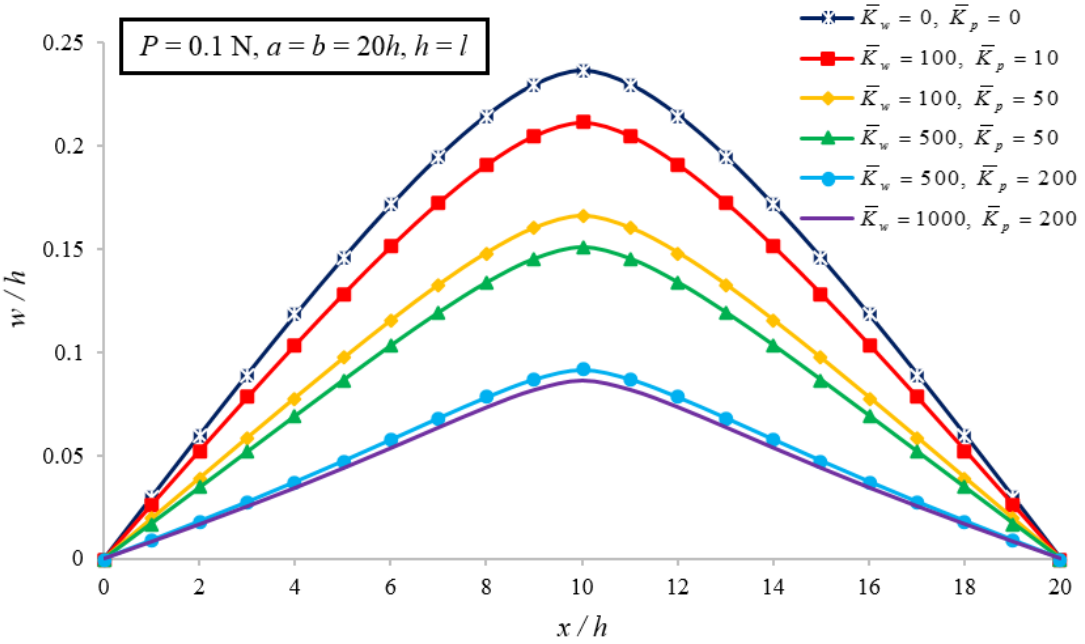

Fig. 2.6 Deflection of the plate with different values of k_w and k_p

Both the microstructure and surface energy effects are included in the numerical results shown in Figs 2.5 and 2.6. To illustrate the surface energy effect, additional numerical results are presented in Fig 2.7 for the deflection of the simply supported plate shown in Fig 2.4, which are obtained from Eqs. (2.45) and (2.48)-(2.50) by letting $l = 0$. For comparison purposes, the results predicted by the classical elasticity-based Kirchhoff plate model are also plotted in Fig 2.7, which are computed using (2.45) and (2.48)-(2.50) with $l = 0$ and $\lambda_0 = \mu_0 = \tau_0 = 0$. The plate material in this case is taken to be iron with the following properties (Gurtin and Murdoch, 1978): $E = 177.33$ GPa, $\nu = 0.27$ for the bulk, and $\mu_0 = 2.5$ N/m, $\lambda_0 = -8$ N/m, $\tau_0 = 1.7$ N/m for the surface layers. The cross-sectional shape is kept to be the same by letting $a = b = 20h$ (see Fig 2.4) for all cases. In addition, the foundation moduli are set to be $k_w = k_p = 0$ to examine only the surface energy effect.

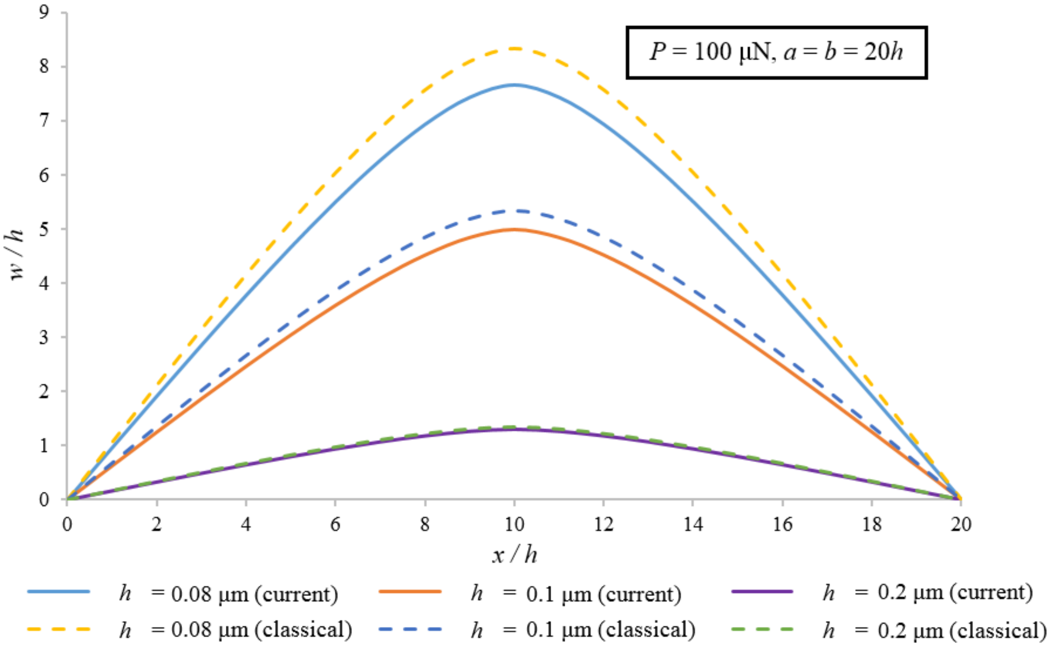

Fig. 2.7 Deflection of the simply supported plate predicted by the new model considering the surface energy effect alone (i.e., with $l = k_w = k_p = 0$) and by the classical model

From Fig 2.7, it is observed that the plate deflection predicted by the current model including the surface energy effect alone is always smaller than those predicted by the classical model in all cases considered here for the iron plate. Figure 2.7 also shows that the differences between the two sets of predicted values are significant only when the plate thickness h is very small, but they are diminishing as h increases. This indicates that the surface effect is important only when the plate is sufficiently thin.

2.3.2 Free vibration

For free vibration problems, the BVP for the simply supported plate shown in Fig 2.4 is defined by Eqs. (2.36a–c), (2.41a,b), (2.42a-c), (2.43a,b) and (2.44a-c), with all external forces vanished (i.e., $f_x = f_y = f_z = 0$ and $c_x = c_y = c_z = 0$).

For the current case with $f_x = f_y = 0$ and $c_z = 0$, Eqs. (2.36a,b), (2.41a), (2.42a,c), (2.43a) and (2.44a,c) give $u = u(x, y, t) = 0$, $v = v(x, y, t) = 0$ for any $(x, y) \in R$ and $t \in [0, T]$.

For $w = w(x, y, t)$, consider the following Fourier series expansion:

$$w(x,\ y,\ t) = \sum_{m=1}^{\infty}\sum_{n=1}^{\infty} W_{mn}^{V} \sin(\frac{m\pi x}{a}) \sin(\frac{n\pi y}{b}) e^{i\omega_n t}, \tag{2.52}$$

where ω_n is the nth natural frequency of vibration of the plate, W_{mn}^{V} is the Fourier coefficient, and i is the imaginary unit satisfying $i^2 = -1$. It can be readily shown that w in Eq. (2.52) satisfies the boundary conditions in Eqs. (2.41b), (2.42b), (2.43b) and (2.44b) for any $t \in [0, T]$.

Using Eq. (2.52) in Eq. (2.36c) gives, for a non-trivial solution with $W_{mn}^{V} \neq 0$,

$$\omega_n = \sqrt{\frac{k_w + \left\{2\tau_0 + k_p + \left[\frac{h^3}{12}(\lambda + 2\mu) + \mu l^2 h + \frac{h^2}{2}(\lambda_0 + 2\mu_0)\right]\left(\frac{m^2\pi^2}{a^2} + \frac{n^2\pi^2}{b^2}\right)\right\}\left(\frac{m^2\pi^2}{a^2} + \frac{n^2\pi^2}{b^2}\right)}{\rho h + \frac{1}{12}\rho h^3\left(\frac{m^2\pi^2}{a^2} + \frac{n^2\pi^2}{b^2}\right)}}, \tag{2.53}$$

where use has been made of Eq. (2.21). From Eq. (2.53), it is seen that the inclusion of the microstructure effect (with $l \neq 0$) and the presence of the foundation (with $k_w > 0$ and/or $k_p > 0$) will always lead to increased values of ω_n, while the incorporation of the surface energy effect may result in increased or decreased values of ω_n, depending on the signs of $\lambda_0 + 2\mu_0$ and τ_0.

Figure 2.8 shows the variation of the first natural frequency ω_1 obtained from Eq. (2.53) (with $m = 1$, $n = 1$) with the plate thickness predicted by the current Kirchhoff plate model and by the classical model. The results for the current plate model with the Winkler-Pasternak ($\bar{K}_w = 1000,\ \bar{K}_p = 100$) or Winkler ($\bar{K}_w = 1000,\ k_p = 0$) or no foundation ($k_w = k_p = 0$) shown in Fig 2.8 are obtained from Eq. (2.53), while those for the classical plate model are computed from the same equation but with $l = 0$, $\lambda_0 = \mu_0 = \tau_0 = 0$, and $k_w = k_p = 0$. The material properties and geometry of the aluminum plate used here are the same as those employed earlier to obtain the numerical results displayed in Figs 2.5 and 2.6. In addition, the density for the aluminum plate is taken to be $\rho = 2.7 \times 10^3\,\text{kg/m}^3$, which is needed in Eq. (2.53).

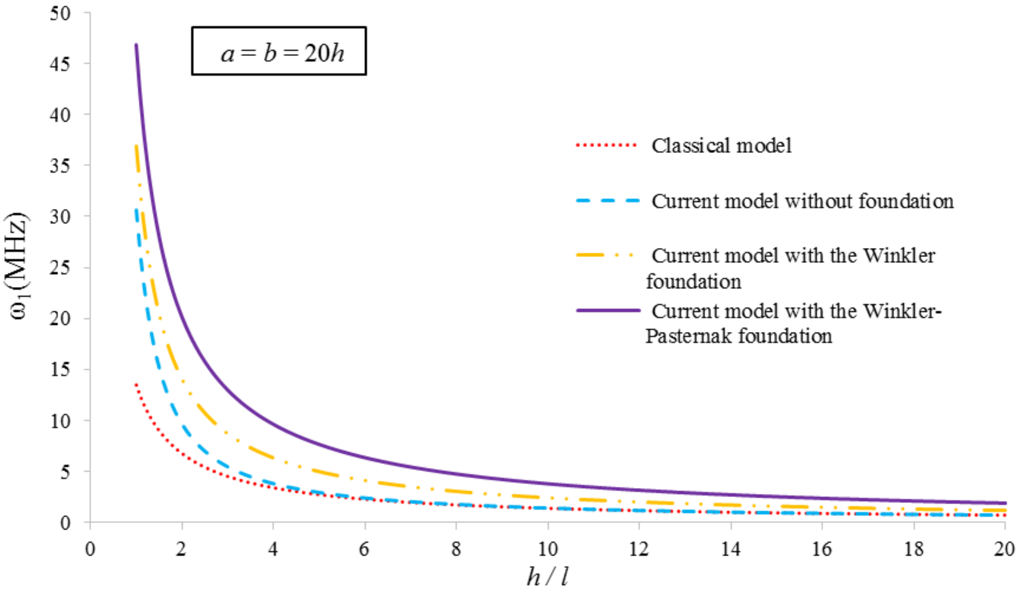

Fig. 2.8 Natural frequency varying with the plate thickness

From Fig 2.8, it is clearly seen that the natural frequency predicted by the current model with or without the foundation is always higher than that predicted by the classical elasticity-based model. The difference between the predictions by the current model (with the microstructure and surface energy effects) and the classical model is significant when the plate thickness h is very small (with $h < 2l = 13.16$ μm here if excluding the foundation effect). However, the difference is diminishing as h becomes large (with $h > 6l = 39.48$ μm here for the case with $k_w = k_p = 0$). This shows that the size effect on the natural frequency is important only when the plate thickness is very small. In addition, it is observed from Fig 2.8 that the presence of the elastic foundation indeed increases the natural frequency and this effect can be significant when the plate thickness is small but diminishes as the thickness becomes large.

2.4 Summary

A new non-classical Kirchhoff plate model is developed using a modified couple stress theory, a surface elasticity theory and a two-parameter elastic foundation model via a variational formulation based on Hamilton's principle. The equations of motion and the complete boundary conditions are determined simultaneously, and the microstructure, surface energy and foundation effects are treated in a unified manner. The new model contains a material length scale parameter to describe the microstructure effect, three surface elastic constants to account for the surface energy effect, and two foundation moduli to represent the foundation effect. The inclusion of the additional material constants enables the new model to capture the microstructure- and surface energy-dependent size effects.

It is shown that when the microstructure, surface energy, and foundation effects are all ignored, the new plate model recovers its classical elasticity-based counterpart as a limiting case. Also, it is seen that the newly developed plate model includes the models considering the microstructure dependence or the surface energy effect or the foundation effect alone as special cases and reduces to the Bernoulli–Euler beam model incorporating the microstructure, surface energy and foundation effects.

As direct applications of the new model, the static bending and free vibration problems of a simply supported rectangular plate are analytically solved, with the solutions compared to those based on the classical Kirchhoff plate theory. The numerical results show that the deflection of the simply supported plate with or without the elastic foundation predicted by the current model is smaller than that predicted by the classical model. Also, it is observed that the difference in the deflection predicted by the two plate models is very large when the plate thickness is sufficiently small, but it is diminishing with the increase of the plate thickness. In addition, it is found that the natural frequency predicted by the new plate model with or without the foundation is higher than that predicted by the classical plate model, and the difference is significant for very thin plates. These predicted size effects at the micron scale agree with the general trends observed in experiments. Finally, both the analytical formulas and the numerical results show that the plate deflection is reduced and the plate natural frequency is increased in the presence of the elastic foundation, as expected.

Chapter

3. A NON-CLASSICAL MODEL FOR CIRCULAR KIRCHHOFF PLATES INCORPORATING MICROSTRUCTURE AND SURFACE ENERGY EFFECTS

3.1 Introduction

Thin plates have been experimentally observed to exhibit microstructure-dependent size effects at the micron and nanometer scales (e.g., Lam et al., 2003; McFarland and Colton, 2005; Li et al., 2009). Such size effects cannot be interpreted using classical elasticity due to the lack of a material length scale parameter. This motivated the development of non-classical plate models based on higher-order elasticity and surface elasticity theories that contain microstructure- and/or surface energy-dependent material length scale parameters.

Several higher-order elasticity theories have been applied to develop non-classical plate models. Based on a modified couple stress theory that involves one additional material length scale parameter (Yang et al., 2002; Park and Gao, 2008), Reddy and Berry (2012) studied axisymmetric bending of functionally graded circular plates employing the modified couple stress theory. Recently, three new models for Mindlin plates and third-order shear deformation plates have been developed by Ma et al. (2011), Gao et al. (2013) and Zhou and Gao (2014) using the modified couple stress theory and Hamilton's principle.

The surface elasticity theory (e.g., Gurtin and Murdoch, 1975, 1978) has been used to analyze thin plates involving surface effects. For example, Miller and Shenoy (2000) developed a model to describe the size dependency of the effective stiffness of a nano-sized structural element (a bar, beam or plate. Lu et al. (2006) constructed a size-dependent thin plate model by including the normal stress on and inside the surface of the bulk substrate. Wang and Wang (2012) provided a model for non-linear free vibrations of a Kirchhoff plate and a Mindlin plate using the von Karman strains. Liu and Rajapakse (2013) presented a size-dependent continuum model for thin and thick circular plates.

However, very few models have been developed for thin plates by considering both the microstructure and surface energy effects. One non-classical model for Kirchhoff thin plates was provided in Lazopoulos (2009) by employing a strain gradient elasticity theory that contains two additional length scale parameters – one related to the bulk strain energy and the other linked to the surface energy. Another non-classical Kirchhoff plate model, which is based on a modified couple stress theory and a surface elasticity theory, was presented in Shaat et al. (2014) without using a variational formulation. Recently, a non-classical model for Kirchhoff plates was developed by Gao and Zhang (2016) using Cartesian coordinates and a variational formulation based on Hamilton’s principle, a modified couple stress theory and a surface elasticity theory.

This chapter aims is to develop a non-classical model for circular Kirchhoff plates using cylindrical polar coordinates. Circular plates are widely used in various industries as key components, which include cover plates for cylindrical pressure vessels, thrust-bearing plates, speaker diaphragms, piston heads, and compact discs for data storage.

The rest of the Chapter 3 is organized as follows. In Section 3.2, the new non-classical model for a circular Kirchhoff plate subjected to axisymmetric loading is developed using a variational formulation based on Hamilton's principle. This leads to the simultaneous determination of the equations of motion and complete boundary conditions and provides a unified treatment of the microstructure and surface energy effects. It is shown that the newly obtained model includes the models considering the microstructure influence or the surface energy effect alone as special cases and recovers the Kirchhoff plate model based on classical elasticity. In Section 3.3, the static bending problem of a clamped solid circular plate subjected to a uniform normal load is analytically solved by directly applying the general formulas derived. The numerical results are also presented there to quantitatively illustrate the differences between the current non-classical plate model and its classical counterpart. The chapter concludes in Section 3.4 with a summary.

3.2 Formulation

Consider a flat thin circular plate of inner radius *a*, outer radius *b* and uniform thickness *h*, as shown in Fig 3.1, where the cylindrical coordinate system (*r*, *θ*, *z*) is adopted, with the *rθ*-plane being coincident with the geometrical mid-plane of the undeformed plate.

According to the Kirchhoff plate theory (also known as the classical plate theory), the displacement field in a thin circular plate undergoing axisymmetric deformations can be written as (e.g., Reddy, 2002; Zhou and Gao, 2014)

$$u_r(r,\theta,z,t) = u(r,t) - z\frac{\partial w(r,t)}{\partial r}, \quad u_\theta(r,\theta,z,t) = 0, \quad u_z(r,\theta,z,t) = w(r,t), \qquad \text{(3.1a-c)}$$

where u_r, u_θ and u_z are, respectively, the radial, tangential and transverse components of the displacement vector **u** of a point (*r*, *θ*, *z*) in the plate at time *t*, *u* and *w* are, respectively, the radial and transverse components of the displacement vector of the corresponding point (r, θ, 0) on the plate mid-plane at time t.

In Fig 3.1, S^+ and S^- denote, respectively, the upper and lower surface layers of the circular Kirchhoff plate. These two surface layers are of zero-thickness and are perfectly bonded to the bulk plate material at $z = \pm h/2$, which have distinct material properties from the bulk material. The bulk material satisfies the modified couple stress theory (Yang et al., 2002; Park and Gao, 2008), while the surface layers are governed by the surface elasticity theory (Gurtin and Murdoch, 1975, 1978).

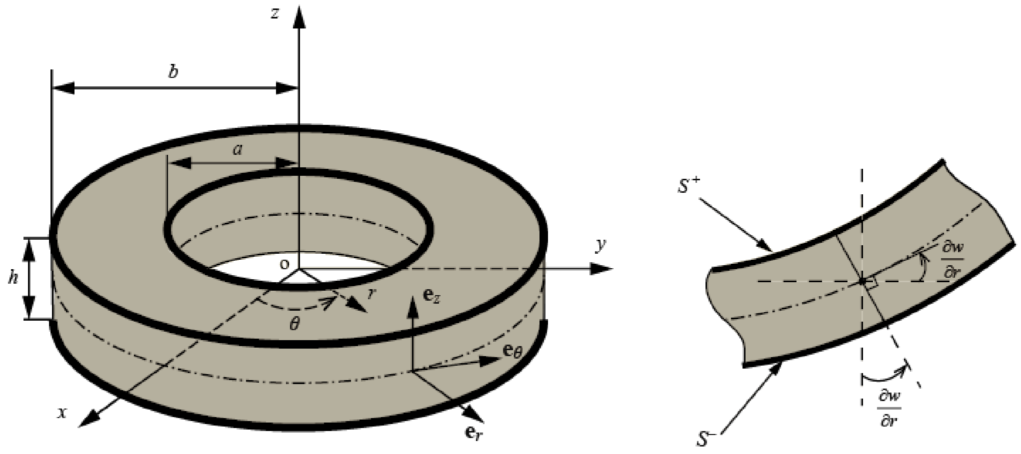

Fig. 3.1 Plate geometry and coordinate system

According to the modified couple stress theory (Yang et al., 2002; Park and Gao, 2008), the constitutive equations and geometrical equations are given by

$$\boldsymbol{\sigma} = \lambda\,\mathrm{tr}(\boldsymbol{\varepsilon})\mathbf{I} + 2\mu\boldsymbol{\varepsilon}, \quad \mathbf{m} = 2l^2\mu\boldsymbol{\chi}, \tag{3.2a,b}$$

$$\boldsymbol{\varepsilon} = \frac{1}{2}\left[\nabla\mathbf{u} + \left(\nabla\mathbf{u}\right)^T\right], \ \ \boldsymbol{\chi} = \frac{1}{2}\left[\nabla\boldsymbol{\psi} + \left(\nabla\boldsymbol{\psi}\right)^T\right], \tag{3.3a,b}$$

where $\boldsymbol{\sigma}$ is the Cauchy stress tensor, $\boldsymbol{\varepsilon}$ is the infinitesimal strain tensor, $\mathbf{m}$ is the deviatoric part of the couple stress tensor, $\boldsymbol{\chi}$ is the symmetric curvature tensor, $\mathbf{I}$ is the second-order identity tensor, λ and μ are the Lamé constants in classical elasticity, l is a material length scale parameter measuring the couple stress effect (e.g., Mindlin, 1963; Park and Gao, 2006), ∇ denotes the gradient, the superscript T represents the transpose, $\mathbf{u}$ is the displacement vector, and $\boldsymbol{\psi}$ is the rotation vector defined by

$$\boldsymbol{\psi} = \frac{1}{2} curl \mathbf{u} . \tag{3.4}$$

According to the surface elasticity theory (e.g., Gurtin and Murdoch, 1975, 1978), the surface layer of a bulk elastic material satisfies distinct constitutive equations involving surface elastic constants, and the equilibrium equations for the surface layer of zero thickness read

$$div_S \boldsymbol{\tau} = \boldsymbol{\sigma}\mathbf{n}, \tag{3.5}$$

where $\mathbf{n}$ is the outward-pointing unit normal vector to the surface, div_S represents the surface divergence, and $\boldsymbol{\tau}$ is the in-plane surface stress tensor given by (Gurtin and Murdoch, 1978; Zhou and Gao, 2015)

$$\boldsymbol{\tau} = \left[\tau_0 + (\lambda_0 + \tau_0)(\mathrm{tr}\,\boldsymbol{\varepsilon}^s)\right]\mathbf{I}_S + \mu_0\left[\boldsymbol{\nabla}_S\mathbf{u} + \left(\boldsymbol{\nabla}_S\mathbf{u}\right)^T\right] - \tau_0\left(\boldsymbol{\nabla}_S\mathbf{u}\right)^T , \tag{3.6}$$

where μ_0 and λ_0 are the surface elastic constants, τ_0 is the residual surface stress (i.e., the surface stress at zero strain), $\mathbf{I}^S$ is the projection tensor with $\mathbf{I}^S = \mathbf{I} - \mathbf{n} \otimes \mathbf{n}$, $\boldsymbol{\nabla}_S$ is the surface gradient operator defined by $\boldsymbol{\nabla}_S(\bullet) = (\mathbf{I} - \mathbf{n} \otimes \mathbf{n})\boldsymbol{\nabla}(\bullet)$, and $\boldsymbol{\varepsilon}^S$ is the surface strain tensor given by

$$\boldsymbol{\varepsilon}^S = \frac{1}{2}\left[\nabla_S\mathbf{u} + (\nabla_S\mathbf{u})^T\right] = \frac{1}{2}\left(\mathbf{I} - \mathbf{n} \otimes \mathbf{n}\right)\left[\nabla\mathbf{u} + (\nabla\mathbf{u})^T\right], \tag{3.7}$$

in which $\mathbf{I}$ is the second-order identity tensor. Note that the three surface elastic constants μ_0, λ_0 and τ_0 introduced in Eq. (3.6) can be obtained from atomistic simulations or experimental measurements (e.g., Shenoy, 2005; Zhang et al., 2013). Clearly, Eq. (3.6) indicates that $\boldsymbol{\tau}$ is not a symmetric tensor.

The out-of-plane components of the surface stress tensor read (Gurtin and Murdoch, 1978)

$$\tau_{3\beta} = \tau_0 u_{3,\beta}. \tag{3.8}$$

It follows from Eqs. (3.1a-c), (3.3a,b) and (3.4) that the geometrical equations in the bulk of the current axisymmetric circular Kirchhoff plate are given by

$$\varepsilon_{rr} = \frac{\partial u}{\partial r} - z\frac{\partial^2 w}{\partial r^2}, \quad \varepsilon_{\theta\theta} = \frac{1}{r}(u - z\frac{\partial w}{\partial r}), \quad \varepsilon_{zz} = \varepsilon_{r\theta} = \varepsilon_{\theta z} = \varepsilon_{zr} = 0, \tag{3.9}$$

$$\psi_\theta = -\frac{\partial w}{\partial r}, \quad \psi_r = \psi_z = 0, \tag{3.10}$$

$$\chi_{r\theta} = -\frac{1}{2}r\frac{\partial}{\partial r}\left(\frac{1}{r}\frac{\partial w}{\partial r}\right) = \chi_{\theta r}, \quad \chi_{rr} = \chi_{\theta\theta} = \chi_{zz} = \chi_{rz} = \chi_{\theta z} = 0. \tag{3.11}$$

The total strain energy in the elastically deformed circular Kirchhoff plate, U_T, can be expressed as

$$U_T = U_B + U_S = \frac{1}{2}\int_\Omega \left(\sigma_{ij}\varepsilon_{ij} + m_{ij}\chi_{ij}\right)\mathrm{d}V + \frac{1}{2}\int_{S^+} \tau_{\alpha\beta}\varepsilon_{\alpha\beta}\mathrm{d}A + \frac{1}{2}\int_{S^-} \tau_{\alpha\beta}\varepsilon_{\alpha\beta}\mathrm{d}A, \tag{3.12}$$

where $\boldsymbol{\Omega}$ is the region occupied by the plate, dV is the volume element, and dA is the area element. In Eq. (3.12), U_B is the strain energy in the bulk of the plate, which is governed by the modified couple stress theory, and U_S is the strain energy in the surface layers S^+ and S^- satisfying the surface elasticity theory. It should be mentioned that only the first part of U_B is considered in the classical Kirchhoff plate theory as the total strain energy (i.e., $U_T^C = \frac{1}{2}\int_\Omega \sigma_{ij}\varepsilon_{ij}\mathrm{d}V$) in the plate.

Note that in Eq (3.12) and throughout the Chapter 3 the summation convention and standard index notation are used, with the Greek indices taking r or θ (i.e., $\alpha \in \{ r, \theta\}$) and the Latin indices taking r, θ or z (i.e., $i \in \{ r, \theta, z\}$) unless otherwise indicated.

From Eqs. (3.6), (3.7), (3.9), (3.11) and (3.12), the first variation of the total strain energy in the circular Kirchhoff plate over the time interval [0, T] can be obtained as (Zhou and Gao, 2014; Gao and Zhang, 2015)

$$\begin{aligned}\delta\int_0^T U\mathrm{d}t = &\int_0^T\int_\Omega(\sigma_{rr}\delta\varepsilon_{rr}+\sigma_{\theta\theta}\delta\varepsilon_{\theta\theta}+2m_{r\theta}\delta\chi_{r\theta})\mathrm{d}V\mathrm{d}t\\ &+\int_0^T\int_{S^+}\left[(\tau_{rr}^+-\frac{1}{2}\tau_0)\delta\varepsilon_{rr}^+ +(\tau_{\theta\theta}^+-\frac{1}{2}\tau_0)\delta\varepsilon_{\theta\theta}^+\right]\mathrm{d}A\mathrm{d}t\\ &+\int_0^T\int_{S^-}\left[(\tau_{rr}^- -\frac{1}{2}\tau_0)\delta\varepsilon_{rr}^- +(\tau_{\theta\theta}^- -\frac{1}{2}\tau_0)\delta\varepsilon_{\theta\theta}^-\right]\mathrm{d}A\mathrm{d}t,\end{aligned} \tag{3.13}$$

where $\tau_{\alpha\beta}^+$ and $\tau_{\alpha\beta}^-$ represent, respectively, the surface stress components on the plate top (S^+) and bottom (S^-) surfaces. In reaching Eq. (3.13) use has been made of the fact that $\tau_{\alpha\beta}$ is non-symmetric. This fact has been overlooked in some variational studies employing the surface elasticity theory of Gurtin and Murdoch (1975, 1978).

Note that the volume integral of a sufficiently smooth function F (x, y, z, t) over the region Ω occupied by a uniform-thickness plate can be represented by

$$\int_\Omega F(x,\ y,\ z,\ t)\mathrm{d}V=\int_R\int_{-h/2}^{h/2}F(x,\ y,\ z,\ t)\mathrm{d}z\mathrm{d}A, \tag{3.14}$$

where h is the plate thickness, and R is the plate mid-plane area.

Using Eqs. (3.9), (3.11) and (3.14) in Eq. (3.13) yields, with the help of Green's theorem,

$$
\begin{aligned}
\delta\int_0^T U\mathrm{d}t = \int_0^T\int_0^{2\pi}\int_a^b \Bigg\{ & \left[N_{\theta\theta} - \frac{\partial(rN_{rr})}{\partial r} + \tau_{\theta\theta}^{+} - \frac{\partial(r\tau_{rr}^{+})}{\partial r} + \tau_{\theta\theta}^{-} - \frac{\partial(r\tau_{rr}^{-})}{\partial r} \right]\delta u \\
& - \left[\frac{\partial^2(rM_{rr})}{\partial r^2} - \frac{\partial M_{\theta\theta}}{\partial r} + 3\frac{\partial Y_{r\theta}}{\partial r} + r\frac{\partial^2 Y_{r\theta}}{\partial r^2} + \frac{h}{2}\frac{\partial^2(r\tau_{rr}^{+})}{\partial r^2} - \frac{h}{2}\frac{\partial^2(r\tau_{rr}^{-})}{\partial r^2} - \frac{h}{2}\frac{\partial \tau_{\theta\theta}^{+}}{\partial r} \right. \\
& \left. + \frac{h}{2}\frac{\partial \tau_{\theta\theta}^{-}}{\partial r} \right]\delta w \Bigg\} \mathrm{d}r\mathrm{d}\theta\mathrm{d}t + \int_0^T\int_0^{2\pi} \Bigg\{ (rN_{rr} + r\tau_{rr}^{+} + r\tau_{rr}^{-} - r\tau_0)\delta u \\
& + \left[\frac{\partial(rM_{rr})}{\partial r} - M_{\theta\theta} + 2Y_{r\theta} + r\frac{\partial Y_{r\theta}}{\partial r} + \frac{h}{2}\frac{\partial(r\tau_{rr}^{+})}{\partial r} - \frac{h}{2}\frac{\partial(r\tau_{rr}^{-})}{\partial r} - \frac{h}{2}\tau_{\theta\theta}^{+} + \frac{h}{2}\tau_{\theta\theta}^{-} \right]\delta w \\
& - \left(rM_{rr} + rY_{r\theta} + \frac{h}{2}r\tau_{rr}^{+} - \frac{h}{2}r\tau_{rr}^{-} \right)\delta\left(\frac{\partial w}{\partial r}\right) \Bigg\} \Bigg|_{r=a}^{r=b} \mathrm{d}\theta\mathrm{d}t,
\end{aligned}
\tag{3.15}
$$

where

$$
\begin{gathered}
N_{rr} = \int_{-h/2}^{h/2}\sigma_{rr}\mathrm{d}z, \quad N_{\theta\theta} = \int_{-h/2}^{h/2}\sigma_{\theta\theta}\mathrm{d}z, \quad M_{rr} = \int_{-h/2}^{h/2}\sigma_{rr}z\mathrm{d}z, \\
M_{\theta\theta} = \int_{-h/2}^{h/2}\sigma_{\theta\theta}z\mathrm{d}z, \quad Y_{r\theta} = \int_{-h/2}^{h/2}m_{r\theta}\mathrm{d}z
\end{gathered}
\tag{3.16}
$$

are the Cauchy stress and couple stress resultants through the plate thickness. Note that in reaching Eq. (3.15) use has been made of the relations $S^{+} = R = S^{-}$, $\partial S^{+} = \partial R = \partial S^{-}$ for the uniform-thickness plate under consideration in order to facilitate the integral evaluations.

The kinetic energy of the plate has the form (e.g., Ma et al., 2011; Gao et al., 2013)

$$
K = \frac{1}{2}\int_{\Omega}\rho\left[(\dot{u}_1)^2 + (\dot{u}_2)^2 + (\dot{u}_3)^2\right]\mathrm{d}V,
\tag{3.17}
$$

where ρ is the mass density of the plate material. Here and in the sequel the overhead "·" and "··" denote, respectively, the first and second time derivatives (e.g., $\dot{u}_1 = \partial u_1/\partial t,\ \ddot{u}_1 = \partial^2 u_1/\partial t^2$).

From Eqs. (3.1a-c), (3.14) and (3.17), the first variation of the kinetic energy for the axisymmetric plate, over the time interval [0, T], can be obtained as (e.g., Ma et al., 2011; Zhou and Gao, 2014)

$$\delta\int_0^T K\mathrm{d}t = -\int_0^T\int_0^{2\pi}\int_a^b \left[m_0(\ddot{u}\delta u + \ddot{w}\delta w) - m_2\frac{1}{r}\left(\frac{\partial \ddot{w}}{\partial r} + r\frac{\partial^2 \ddot{w}}{\partial r^2}\right)\delta w \right] r\mathrm{d}r\mathrm{d}\theta\mathrm{d}t, \tag{3.18}$$

where

$$m_0 \equiv \int_{-h/2}^{h/2}\rho\mathrm{d}z = \rho h, \quad m_2 \equiv \int_{-h/2}^{h/2}\rho z^2\mathrm{d}z = \frac{\rho h^3}{12}. \tag{3.19}$$

In reaching Eq. (3.18), it has been assumed that the initial (t = 0) and final (t = T) configurations of the plate are prescribed so that the virtual displacements vanish at t = 0 and t = T. In addition, ρ is taken to be constant along the plate thickness and over the time interval [0, T] such that $\dot{m}_0 = 0,\ \dot{m}_2 = 0$.

From the general expression of the work done by external forces in the modified couple stress theory (Park and Gao, 2008) and in the surface elasticity theory (Gurtin and Murdoch, 1975, 1978), the virtual work done by the forces applied on the current circular plate over the time interval [0, T] can be written as (e.g., Zhou and Gao, 2014; Gao and Zhang, 2016)

$$\delta\int_0^T W\mathrm{d}t = \int_0^T\int_R \left(\mathbf{f}\cdot\delta\mathbf{u} + \mathbf{c}\cdot\delta\boldsymbol{\psi}\right)\mathrm{d}A\mathrm{d}t + \int_0^T\oint_{\partial R}\left(\overline{\mathbf{t}}\cdot\delta\mathbf{u} + \overline{\mathbf{s}}\cdot\delta\boldsymbol{\psi}\right)\mathrm{d}s\mathrm{d}t + \int_0^T\int_S \mathbf{t}^s\cdot\delta(u_3\mathbf{e}_3)\mathrm{d}A\mathrm{d}t, \tag{3.20}$$

where $\mathbf{f}$ and $\mathbf{c}$ are, respectively, the body force resultant (force per unit area), body couple resultant (moment per unit area) through the plate thickness acting in the area R (i.e., the plate mid-plane), $\overline{\mathbf{t}}$ and $\overline{\mathbf{s}}$ are, respectively, the Cauchy traction resultant (force per unit length) and the surface couple resultant (moment per unit length) through the plate thickness acting on ∂R (i.e., the boundary of R), S represents the top and bottom surfaces of the plate (with S = $S^+ \cup S^-$), and $\mathbf{t}^s$ is the surface traction that is related to the surface stress $\boldsymbol{\tau}$ through $\mathbf{t}^s = \nabla_s \cdot \boldsymbol{\tau} = \tau_{i\alpha,\alpha}\mathbf{e}_i$ (e.g., Gurtin and Murdoch, 1978; Altenbach et al., 2010). Note that the last term in the virtual work expression in Eq. (3.20) accounts for the contribution of the normal stress on the top and bottom plate surfaces $\sigma_{33}^{\pm}$ ($= \pm\tau_{3\alpha,\alpha}^{\pm}$ from the equilibrium equations in Eq. (3.5)), which is neglected in the classical Kirchhoff plate theory that does not consider the surface energy effect.

Using Eqs. (3.1a-c), (3.5) and (3.10) in Eq. (3.20) leads to, with the help of Green's theorem,

$$\begin{aligned}\delta\int_0^T W\mathrm{d}t &= \int_0^T\int_0^{2\pi}\int_a^b \left\{ rf_r\delta u + \left[\frac{\partial(rc_\theta)}{\partial r} + rf_z\right]\delta w \right\}\mathrm{d}r\mathrm{d}\theta\mathrm{d}t \\ &\quad + \int_0^T\int_0^{2\pi}\left[r\bar{t}_r\delta u - (rc_\theta - r\bar{t}_z)\delta w - (r\bar{s}_\theta + r\bar{M}_\theta)\delta\left(\frac{\partial w}{\partial r}\right)\right]\Bigg|_{r=a}^{r=b}\mathrm{d}\theta\mathrm{d}t \\ &\quad + \int_0^T\int_{S^+}\frac{1}{r}\frac{\partial(r\tau_{3r}^+)}{\partial r}\delta w\mathrm{d}A\mathrm{d}t + \int_0^T\int_{S^-}\frac{1}{r}\frac{\partial(r\tau_{3r}^-)}{\partial r}\delta w\mathrm{d}A\mathrm{d}t,\end{aligned} \tag{3.21}$$

where f_i, c_i, $\bar{t}_i$ and $\bar{s}_i$ ($i \in \{r, \theta, z\}$) are, respectively, the components of $\mathbf{f}$, $\mathbf{c}$, $\bar{\mathbf{t}}$ and $\bar{\mathbf{s}}$, and $\bar{M}_\theta$ is the applied moment per unit arc length along the circular boundary. Note that the positive directions of $\bar{M}_\theta$, which is along the $\mathbf{e}_\theta$-direction, is opposite to that of $\partial w/\partial r$ (see Fig 3.1).

According to Hamilton's principle (e.g., Reddy, 2002; Ma et al., 2008; Gao et al. 2013),

$$\delta\int_0^T\left[K - (U - W)\right]\mathrm{d}t = 0. \tag{3.22}$$

Using Eqs. (3.15), (3.18) and (3.21) in Eq. (3.22) gives

$$
\begin{aligned}
&\int_0^T\int_0^{2\pi}\int_a^b\left\{\left[N_{\theta\theta}-\frac{\partial(rN_{rr})}{\partial r}+\tau_{\theta\theta}^{+}-\frac{\partial(r\tau_{rr}^{+})}{\partial r}+\tau_{\theta\theta}^{-}-\frac{\partial(r\tau_{rr}^{-})}{\partial r}-rf_r+m_0r\ddot{u}\right]\delta u\right.\\
&-\left[\frac{\partial^2(rM_{rr})}{\partial r^2}-\frac{\partial M_{\theta\theta}}{\partial r}+3\frac{\partial Y_{r\theta}}{\partial r}+r\frac{\partial^2 Y_{r\theta}}{\partial r^2}+\frac{h}{2}\frac{\partial^2(r\tau_{rr}^{+})}{\partial r^2}-\frac{h}{2}\frac{\partial^2(r\tau_{rr}^{-})}{\partial r^2}-\frac{h}{2}\frac{\partial\tau_{\theta\theta}^{+}}{\partial r}\right.\\
&\left.\left.+\frac{h}{2}\frac{\partial\tau_{\theta\theta}^{-}}{\partial r}+\frac{\partial(rc_\theta)}{\partial r}+\frac{\partial(r\tau_{3r}^{+})}{\partial r}+\frac{\partial(r\tau_{3r}^{-})}{\partial r}+rf_z-m_0r\ddot{w}+m_2\frac{\partial\ddot{w}}{\partial r}+m_2r\frac{\partial^2\ddot{w}}{\partial r^2}\right]\delta w\right\}\mathrm{d}r\mathrm{d}\theta\mathrm{d}t\\
&+\int_0^T\int_0^{2\pi}\left\{(rN_{rr}+r\tau_{rr}^{+}+r\tau_{rr}^{-}-r\tau_0-r\bar{t}_r)\delta u+\left[\frac{\partial(rM_{rr})}{\partial r}-M_{\theta\theta}+2Y_{r\theta}+r\frac{\partial Y_{r\theta}}{\partial r}+\frac{h}{2}\frac{\partial(r\tau_{rr}^{+})}{\partial r}\right.\right.\\
&\left.-\frac{h}{2}\frac{\partial(r\tau_{rr}^{-})}{\partial r}-\frac{h}{2}\tau_{\theta\theta}^{+}+\frac{h}{2}\tau_{\theta\theta}^{-}+rc_\theta-r\bar{t}_z\right]\delta w-(rM_{rr}+rY_{r\theta}+\frac{h}{2}r\tau_{rr}^{+}-\frac{h}{2}r\tau_{rr}^{-}-r\bar{s}_\theta\\
&\left.\left.-r\bar{M}_\theta)\delta\left(\frac{\partial w}{\partial r}\right)\right\}\right|_{r=a}^{r=b}\mathrm{d}\theta\mathrm{d}t=0.
\end{aligned}
\tag{3.23}
$$

Applying the fundamental lemma of the calculus of variations to Eq. (3.23) results in, with the arbitrariness of δu and δw (e.g., Gao and Mall, 2001; Ma et al., 2010),

$$
-\frac{N_{\theta\theta}}{r}+\frac{1}{r}\frac{\partial(rN_{rr})}{\partial r}-\frac{\tau_{\theta\theta}^{+}+\tau_{\theta\theta}^{-}}{r}+\frac{1}{r}\frac{\partial(r\tau_{rr}^{+})}{\partial r}+\frac{1}{r}\frac{\partial(r\tau_{rr}^{-})}{\partial r}+f_r=m_0\ddot{u},
\tag{3.24a}
$$

$$
\begin{aligned}
&\frac{1}{r}\frac{\partial^2(rM_{rr})}{\partial r^2}-\frac{1}{r}\frac{\partial M_{\theta\theta}}{\partial r}+\frac{3}{r}\frac{\partial Y_{r\theta}}{\partial r}+\frac{\partial^2 Y_{r\theta}}{\partial r^2}+\frac{h}{2r}\frac{\partial^2(r\tau_{rr}^{+})}{\partial r^2}-\frac{h}{2r}\frac{\partial^2(r\tau_{rr}^{-})}{\partial r^2}-\frac{h}{2r}\left(\frac{\partial\tau_{\theta\theta}^{+}}{\partial r}-\frac{\partial\tau_{\theta\theta}^{-}}{\partial r}\right)\\
&+\frac{1}{r}\frac{\partial(r\tau_{3r}^{+})}{\partial r}+\frac{1}{r}\frac{\partial(r\tau_{3r}^{-})}{\partial r}+\frac{1}{r}\frac{\partial(rc_\theta)}{\partial r}+f_z=m_0\ddot{w}-m_2\left(\frac{1}{r}\frac{\partial\ddot{w}}{\partial r}+\frac{\partial^2\ddot{w}}{\partial r^2}\right)
\end{aligned}
\tag{3.24b}
$$

as the equations of motion of the circular Kirchhoff plate for any $(r, \theta) \in R$ and $t \in (0, T)$, and

$$
N_{rr}+\tau_{rr}^{+}+\tau_{rr}^{-}-\tau_0=\bar{t}_r \quad \text{or} \quad u=\bar{u} \quad \text{at} \quad r=a \quad \text{and} \quad r=b,
\tag{3.25a}
$$

$$
\begin{aligned}
&\frac{1}{r}\frac{\partial(rM_{rr})}{\partial r}-\frac{M_{\theta\theta}}{r}+\frac{2Y_{r\theta}}{r}+\frac{\partial Y_{r\theta}}{\partial r}+\frac{h}{2r}\frac{\partial(r\tau_{rr}^{+})}{\partial r}-\frac{h}{2r}\frac{\partial(r\tau_{rr}^{-})}{\partial r}-\frac{h}{2r}\left(\tau_{\theta\theta}^{+}-\tau_{\theta\theta}^{-}\right)+c_\theta=\bar{t}_z\\
&\quad \text{or} \quad w=\bar{w} \quad \text{at} \quad r=a \quad \text{and} \quad r=b,
\end{aligned}
\tag{3.25b}
$$

$$
M_{rr}+Y_{r\theta}+\frac{h}{2}\tau_{rr}^{+}-\frac{h}{2}\tau_{rr}^{-}=\overline{s_\theta}+\overline{M_\theta} \quad \text{or} \quad \frac{\partial w}{\partial r}=\overline{\frac{\partial w}{\partial r}} \quad \text{at} \quad r=a \quad \text{and} \quad r=b
\tag{3.25c}
$$

as the boundary conditions.

From Eqs. (3.2a), (3.9) and (3.16), the Cauchy stress resultants can be expressed in terms of u and w as

$$N_{rr} = h(\lambda + 2\mu)\frac{\partial u}{\partial r} + \lambda h \frac{u}{r}, \tag{3.26a}$$

$$N_{\theta\theta} = \lambda h \frac{\partial u}{\partial r} + h(\lambda + 2\mu)\frac{u}{r}, \tag{3.26b}$$

$$M_{rr} = -\frac{(\lambda + 2\mu)h^3}{12}\frac{\partial^2 w}{\partial r^2} - \frac{\lambda h^3}{12}\frac{1}{r}\frac{\partial w}{\partial r}, \tag{3.26c}$$

$$M_{\theta\theta} = -\frac{\lambda h^3}{12}\frac{\partial^2 w}{\partial r^2} - \frac{(\lambda + 2\mu)h^3}{12}\frac{1}{r}\frac{\partial w}{\partial r}. \tag{3.26d}$$

From Eqs. (3.2b), (3.11) and (3.16), the couple stress resultant can be written in terms of w as

$$Y_{r\theta} = -\mu l^2 h \left(\frac{\partial^2 w}{\partial r^2} - \frac{1}{r}\frac{\partial w}{\partial r} \right). \tag{3.27}$$

From Eqs. (3.1a-c) and (3.6)–(3.8), it follows that the surface stress components are given by

$$\tau_{rr}^{\pm} = \tau_0 + (\lambda_0 + 2\mu_0)\left(\frac{\partial u}{\partial r} \mp \frac{h}{2}\frac{\partial^2 w}{\partial r^2} \right) + (\lambda_0 + \tau_0)\left(\frac{u}{r} \mp \frac{h}{2r}\frac{\partial w}{\partial r} \right), \tag{3.28a}$$

$$\tau_{\theta\theta}^{\pm} = \tau_0 + (\lambda_0 + 2\mu_0)\left(\frac{u}{r} \mp \frac{h}{2r}\frac{\partial w}{\partial r} \right) + (\lambda_0 + \tau_0)\left(\frac{\partial u}{\partial r} \mp \frac{h}{2}\frac{\partial^2 w}{\partial r^2} \right), \tag{3.28b}$$

$$\tau_{3r}^{+} = \tau_{3r}^{-} = \tau_0 \frac{\partial w}{\partial r}. \tag{3.28c}$$

Substituting Eqs. (3.26a-d), (3.27) and (3.28a-c) into Eqs. (3.24a,b) then leads to the equations of motion for the circular Kirchhoff plate in terms of u and w as

$$\left[(\lambda + 2\mu)h + 2(\lambda_0 + 2\mu_0)\right]\left(-\frac{u}{r^2} + \frac{1}{r}\frac{\partial u}{\partial r} + \frac{\partial^2 u}{\partial r^2} \right) + f_r = m_0 \ddot{u}, \tag{3.29a}$$

$$\begin{aligned}&-\left[\frac{(\lambda+2\mu)h^3}{12}+\mu l^2 h+\frac{(\lambda_0+2\mu_0)h^2}{2}\right]\frac{1}{r}\frac{\partial}{\partial r}\left\{r\frac{\partial}{\partial r}\left[\frac{1}{r}\frac{\partial}{\partial r}\left(r\frac{\partial w}{\partial r}\right)\right]\right\}\\&+2\tau_0\frac{1}{r}\frac{\partial}{\partial r}\left(r\frac{\partial w}{\partial r}\right)+\frac{1}{r}\frac{\partial(rc_\theta)}{\partial r}+f_z=m_0\ddot{w}-m_2\left(\frac{1}{r}\frac{\partial\ddot{w}}{\partial r}+\frac{\partial^2\ddot{w}}{\partial r^2}\right).\end{aligned}\tag{3.29b}$$

From Eqs. (3.29a, b), it can be seen that the radial displacement (stretching) $u(r, t)$ is uncoupled with the deflection $w(r, t)$. Therefore, $u(r, t)$ can be obtained from solving Eq. (3.29a) subject to prescribed boundary conditions of the form in Eqs. (3.25a) and suitable initial conditions. Note that the material length scale parameter l is not involved in Eq. (3.29a) or (3.25a). As a result, the radial displacement $u(r, t)$ will not be affected by the microstructure of the plate material. The deflection $w(r, t)$ can be determined from solving the boundary-initial value problem defined by the differential equation in Eq. (3.29b), the boundary conditions in Eqs. (3.25b,c) and given initial conditions at $t = 0$ and $t = T$.

When $l = 0$ and $c_\theta = 0$ (i.e., with the microstructure effect ignored), Eqs. (3.29a,b) reduce to

$$\left[(\lambda+2\mu)h+2(\lambda_0+2\mu_0)\right]\left(-\frac{u}{r^2}+\frac{1}{r}\frac{\partial u}{\partial r}+\frac{\partial^2 u}{\partial r^2}\right)+f_r=m_0\ddot{u},\tag{3.30a}$$

$$\begin{aligned}&-\left[\frac{(\lambda+2\mu)h^3}{12}+\frac{(\lambda_0+2\mu_0)h^2}{2}\right]\frac{1}{r}\frac{\partial}{\partial r}\left\{r\frac{\partial}{\partial r}\left[\frac{1}{r}\frac{\partial}{\partial r}\left(r\frac{\partial w}{\partial r}\right)\right]\right\}+2\tau_0\frac{1}{r}\frac{\partial}{\partial r}\left(r\frac{\partial w}{\partial r}\right)+f_z\\&=m_0\ddot{w}-m_2\left(\frac{1}{r}\frac{\partial\ddot{w}}{\partial r}+\frac{\partial^2\ddot{w}}{\partial r^2}\right),\end{aligned}\tag{3.30b}$$

which are the governing equations for the circular Kirchhoff plate that incorporate the surface energy effect alone. Note that Eq. (3.30a) is the same as Eq. (3.29a) because of the microstructure-independence of $u(r, t)$, as observed earlier.

When $\lambda_0 = \mu_0 = \tau_0 = 0$ (i.e., with the surface energy effect neglected), Eqs. (3.29a,b) become

$$(\lambda + 2\mu)h\frac{\partial}{\partial r}\left[\frac{1}{r}\frac{\partial(ru)}{\partial r}\right] + f_r = m_0\ddot{u}, \tag{3.31a}$$

$$-\left[D(1-v) + \mu l^2 h\right]\nabla^4 w + \frac{1}{r}\frac{\partial(rc_\theta)}{\partial r} + f_z = m_0\ddot{w} - m_2\nabla^2\ddot{w}, \tag{3.31b}$$

where

$$D \equiv \frac{Eh^3}{12(1-2v)(1+v)}, \tag{3.32a}$$

$$\nabla^2 = \frac{1}{r}\frac{\partial}{\partial r}\left(r\frac{\partial}{\partial r}\right), \tag{3.32b}$$

$$\nabla^4 = \frac{1}{r}\frac{\partial}{\partial r}\left\{r\frac{\partial}{\partial r}\left[\frac{1}{r}\frac{\partial}{\partial r}\left(r\frac{\partial}{\partial r}\right)\right]\right\}. \tag{3.32c}$$

Equations (3.31a) and (3.31b) are the governing equations for the circular Kirchhoff plate incorporating the microstructure effect alone, which are identical to those derived in Zhou and Gao (2014) using the modified couple stress theory. Note that the Young's modulus E and Poisson's ratio v in Eq. (3.32a) are related to the Lamé constants λ and μ through (e.g., Timoshenko and Goodier, 1970):

$$\lambda = \frac{Ev}{(1+v)(1-2v)}, \quad \mu = \frac{E}{2(1+v)}. \tag{3.33}$$

Furthermore, when $l = 0$, $c_\theta = 0$ and $\lambda_0 = \mu_0 = \tau_0 = 0$ (i.e., with both the microstructure and surface energy effects suppressed), Eqs. (3.29a,b) reduce to, with the help of Eqs. (3.32a-c),

$$(\lambda + 2\mu)h\frac{\partial}{\partial r}\left[\frac{1}{r}\frac{\partial(ru)}{\partial r}\right] + f_r = m_0\ddot{u}, \tag{3.34a}$$

$$D(1-v)\nabla^4 w - f_z = \frac{\partial^2}{\partial t^2}\left(m_2\nabla^2 w - m_0 w\right), \tag{3.34b}$$

which are the same as the equations of motion for the circular Kirchhoff plate subjected to axisymmetric loading based on classical elasticity (e.g., Reddy, 2002; Zhou and Gao, 2014). That is, the classical Kirchhoff plate model is included in the current model as a special case.

3.3 Example

To further demonstrate the new circular Kirchhoff plate model developed in Section 3.2, the static bending problem of a solid circular plate (with $a = 0$) clamped at its edge $r = b$ and subjected to a uniformly distributed normal load $f_z = -q =$ constant (with the negative sign here indicating that the normal load q (> 0) is pointing downward) is analytically solved herein by directly applying the new model.

In view of the general boundary conditions (BCs) in Eqs. (3.25a–c), the BCs for the current solid circular Kirchhoff plate clamped at its edge $r = b$ can be identified as

$$u\Big|_{r=b} = 0, \quad w\Big|_{r=b} = 0, \quad \left.\frac{\partial w}{\partial r}\right|_{r=b} = 0. \tag{3.35a-c}$$

In addition, the following symmetry conditions need to be satisfied

$$u\Big|_{r=0} = 0, \quad w\Big|_{r=0} < \infty, \quad \left.\frac{\partial w}{\partial r}\right|_{r=0} = 0. \tag{3.36a-c}$$

Note that Eq. (3.36b) indicates that the plate deflection is finite at $r = 0$.

For static bending problems, u and w are independent of time t so that all of the time derivatives involved in Eqs. (3.29a,b) vanish. As a result, the governing equations for static problems with $f_r = 0 = c_\theta$ are given by

$$\left[(\lambda + 2\mu)h + 2(\lambda_0 + 2\mu_0)\right]\left(-\frac{u}{r^2} + \frac{1}{r}\frac{\partial u}{\partial r} + \frac{\partial^2 u}{\partial r^2}\right) = 0, \tag{3.37a}$$

$$-\left[\frac{(\lambda+2\mu)h^3}{12}+\mu l^2 h+\frac{(\lambda_0+2\mu_0)h^2}{2}\right]\frac{1}{r}\frac{\partial}{\partial r}\left\{r\frac{\partial}{\partial r}\left[\frac{1}{r}\frac{\partial}{\partial r}\left(r\frac{\partial w}{\partial r}\right)\right]\right\}+2\tau_0\frac{1}{r}\frac{\partial}{\partial r}\left(r\frac{\partial w}{\partial r}\right)+f_z=0. \tag{3.37b}$$

The radial displacement u, which is uncoupled with w, can be obtained from solving the boundary value problem (BVP) defined by Eqs. (3.35a), (3.36a) and (3.37a). It can be readily shown that the solution of this BVP gives $u(r) = 0$ for any $(r, \theta) \in R$.

The deflection w can be obtained from solving the BVP defined by Eqs. (3.35b,c), (3.36b,c) and (3.37b). Note that Eq. (3.37b) can be rewritten as

$$-L\nabla^4 w+2\tau_0\nabla^2 w+f_z=0, \tag{3.38}$$

where ∇^2 and ∇^4 are, respectively, the operators given in Eqs. (3.32b) and (3.32c), and L is defined as

$$L\equiv\frac{(\lambda+2\mu)h^3}{12}+\mu l^2 h+\frac{(\lambda_0+2\mu_0)h^2}{2}, \tag{3.39}$$

which is the plate bending stiffness accounting for both the microstructure (through l) and surface energy effects (via λ_0 and μ_0). When $l = 0$ and $\lambda_0 = \mu_0 = 0$ (i.e., in the absence of both the microstructure and surface energy effects), L reduces to the bending stiffness D in the classical plate theory defined in Eq. (3.32a). Equation (3.38) can be expressed in a non-dimensional form as

$$\nabla^4\overline{w}(\overline{r})-\omega^2\nabla^2\overline{w}(\overline{r})-\frac{f_z b^3}{L}=0, \tag{3.40}$$

where

$$\overline{w}\equiv\frac{w}{b},\quad \overline{r}\equiv\frac{r}{b},\quad \omega^2\equiv\frac{2b^2\tau_0}{L}. \tag{3.41a-c}$$

When $\omega \neq 0$ (i.e., $\tau_0 \neq 0$) and $f_z = -q$ = constant, the general solution of Eq. (3.40) can be analytically obtained as

$$\overline{w}(\overline{r}) = c_1 I_0(\omega\overline{r}) + c_2 K_0(\omega\overline{r}) + \frac{1}{\omega^2}(c_3 \ln\overline{r} + c_4) + \frac{qb\overline{r}^2}{8\tau_0}, \tag{3.42}$$

where I_0 and K_0 are, respectively, the modified Bessel functions of the first and second kind of the zeroth order, and c_1~c_4 are four constants to be determined from the boundary conditions.

When $\omega = 0$ (i.e., $\tau_0 = 0$) and $f_z = -q$ = constant, the general solution of Eq. (3.40) can be readily shown to be

$$\overline{w}(\overline{r}) = d_1\overline{r}^2 \ln\overline{r} + d_2\overline{r}^2 + d_3 \ln\overline{r} + d_4 - \frac{qb^3\overline{r}^4}{64L}, \tag{3.43}$$

where d_1~d_4 are four integration constants.

The boundary and symmetry conditions listed in Eqs. (3.35b,c) and (3.36b,c) can be expressed in non-dimensional forms as

$$\overline{w}\Big|_{\overline{r}=1} = 0, \quad \frac{\partial\overline{w}}{\partial\overline{r}}\Big|_{\overline{r}=1} = 0, \quad \overline{w}\Big|_{\overline{r}=0} < \infty, \quad \frac{\partial\overline{w}}{\partial\overline{r}}\Big|_{\overline{r}=0} = 0. \tag{3.44a-d}$$

Using Eq. (3.42) in Eqs. (3.44a-d) leads to

$$c_1 = -\frac{qb}{4\tau_0\omega I_1(\omega)}, \quad c_2 = 0, \quad c_3 = 0, \quad c_4 = \frac{qb\omega^2 I_0(\omega)}{4\tau_0\omega I_1(\omega)} - \frac{qb\omega^2}{8\tau_0}. \tag{3.45a-d}$$

Substituting Eqs. (3.45a-d) into Eq. (3.42) then yields

$$\overline{w}(\overline{r}) = -\frac{qb}{4\tau_0\omega I_1(\omega)}\left[I_0(\omega\overline{r}) - I_0(\omega)\right] - \frac{qb}{8\tau_0}(1-\overline{r}^2), \tag{3.46}$$

which can be converted to the dimensional form as, with the help of Eqs. (3.41a,b),

$$w(r) = -\frac{qb^2}{4\tau_0 \omega I_1(\omega)}\left[I_0(\frac{\omega r}{b}) - I_0(\omega) \right] - \frac{qb^2}{8\tau_0}\left[1 - \left(\frac{r}{b}\right)^2 \right], \tag{3.47}$$

where ω is defined in Eq. (3.41c). Equation (3.47) gives the exact solution of the clamped solid circular Kirchhoff plate subjected to a uniform normal load $-q$ when $\omega \neq 0$ (i.e., $\tau_0 \neq 0$).

For the case with $\omega = 0$ (i.e., $\tau_0 = 0$) and $f_z = -q =$ constant, the solution for the deflection of the clamped solid circular Kirchhoff plate under consideration can be readily obtained from Eqs. (3.43) and (3.44a-d) as

$$w(r) = -\frac{qb^4}{64L}\left[1 - \left(\frac{r}{b}\right)^2 \right]^2, \tag{3.48}$$

where use has been made of Eqs. (3.41a,b).

When both the microstructure and surface energy effects are suppressed by setting $l = 0$ and $\lambda_0 = \mu_0 = \tau_0 = 0$, Eq. (3.48) reduces to, with the help of Eqs. (3.32a), (3.33) and (3.39),

$$w^C(r) = -\frac{qb^4}{64D(1-\nu)}\left[1 - \left(\frac{r}{b}\right)^2 \right]^2, \tag{3.49}$$

which is the classical elasticity-based exact solution for the solid circular Kirchhoff plate under the uniformly distributed load $-q$. It can be readily shown that the deflection obtained in Eq. (3.49) will be the same as that based on classical elasticity for a clamped solid circular Kirchhoff plate under a uniform normal load $-q$ (e.g., Reddy, 2002) if the two-dimensional plane stress Hooke's law is used (so that $D(1-\nu)$ here will be replaced by $Eh^3/[12(1-\nu^2)]$) (Zhou and Gao, 2014). That is, the current solution for the clamped solid circular Kirchhoff plate includes the classical solution as a special case.

Finally, it should be mentioned that the example problem considered here can also be analytically solved by using the Fourier-Bessel series method, as was done in Zhou and Gao (2014).

To illustrate the newly derived solution for the clamped solid circular Kirchhoff plate, some numerical results are obtained and shown in Figs 3.2 and 3.3. Figure 3.2 displays the variation of the plate deflection w along the radial direction. The numerical results predicted by the new model are directly obtained from Eq. (3.47), while those by the classical model are determined using Eq. (3.49). In generating the numerical results shown in Fig 3.2, the radius of the circular plate is fixed at $b = 20h$, while the plate thickness h is varying. The circular plate material is taken to be aluminum with the following properties (e.g., Liu and Rajapakse, 2010; Gao and Mahmoud, 2014; Gao, 2015): $E = 90$ GPa, $\nu = 0.23$, $l = 6.58$ μm for the bulk properties, and $\mu_0 = -5.4251$ N/m, $\lambda_0 = 3.4939$ N/m, $\tau_0 = 0.5689$ N/m for the surface layers. In addition, the circular plate is subjected to a uniform, downward-pointing normal load of $q = 1$ MPa.

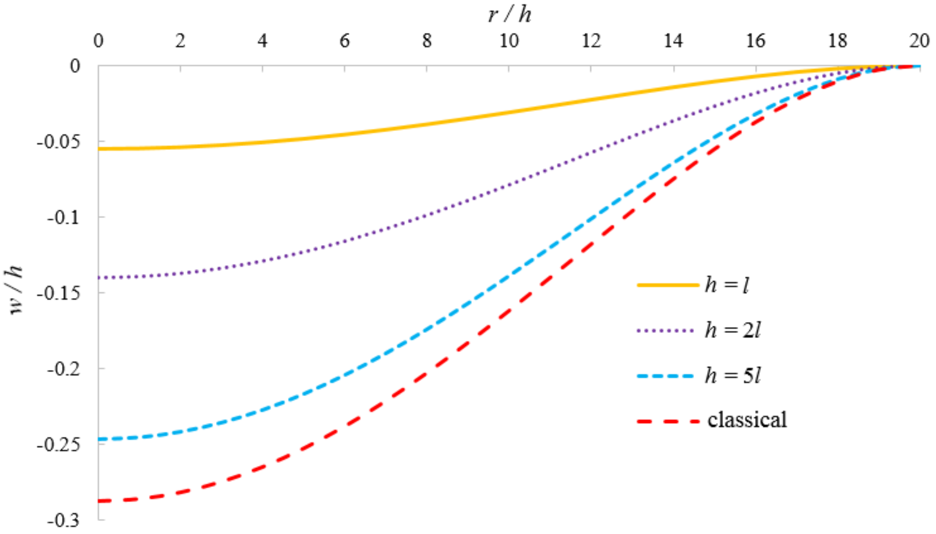

Fig. 3.2 Deflection of the clamped circular Kirchhoff plate

From Fig 3.2, it is clearly seen that the deflection w (magnitude) predicted by the new circular Kirchhoff plate model is always smaller than that predicted by the classical model in all cases considered. Figure 3.2 also shows that the differences between the deflection values predicted by the new model and those predicted by its classical counterpart are very large when the plate thickness h is small (with $h = l = 6.58$ μm here), but the differences are diminishing when h increases. This predicted size effect agrees with the general trend observed experimentally (e.g., McFarland and Colton, 2005).

As the numerical results shown in Fig 3.2 include both the microstructure and surface energy effects, one additional set of values are obtained for the deflection of the clamped solid circular plate to illustrate the surface energy effect alone. The numerical results displayed in Fig 3.3 are determined from Eq. (3.47) by letting $l = 0$ through Eqs. (3.41c) and (3.39). For comparison, the results predicted by the classical solid circular Kirchhoff plate model are also plotted in Fig 3.3, which are obtained from Eq. (3.49). The plate material in this case is taken to be iron with the following properties (Gurtin and Murdoch, 1978; Gao and Zhang, 2015): $E = 177.33$ GPa, $v = 0.27$ for the bulk, and $\mu_0 = 2.5$ N/m, $\lambda_0 = -8\,\text{N/m}$, $\tau_0 = 1.7$ N/m for the surface layers. The radius of the circular plate is fixed at $b = 20h$, and the uniform, downward-pointing normal load is taken to be $q = 1$ MPa, as was done in obtaining the numerical results shown in Fig 3.2.

From Fig 3.3, it is seen that the plate deflection (magnitude) predicted by the current model including the surface energy effect is always smaller than that predicted by the classical model in all cases considered here. Figure 3.3 also shows that the differences between the deflection values predicted by the current model including the surface energy effect and those predicted by the classical model are significant when the plate thickness *h* is very small. However, the differences are diminishing when the thickness *h* increases. This indicates that the surface energy effect is important only when the plate is very thin.

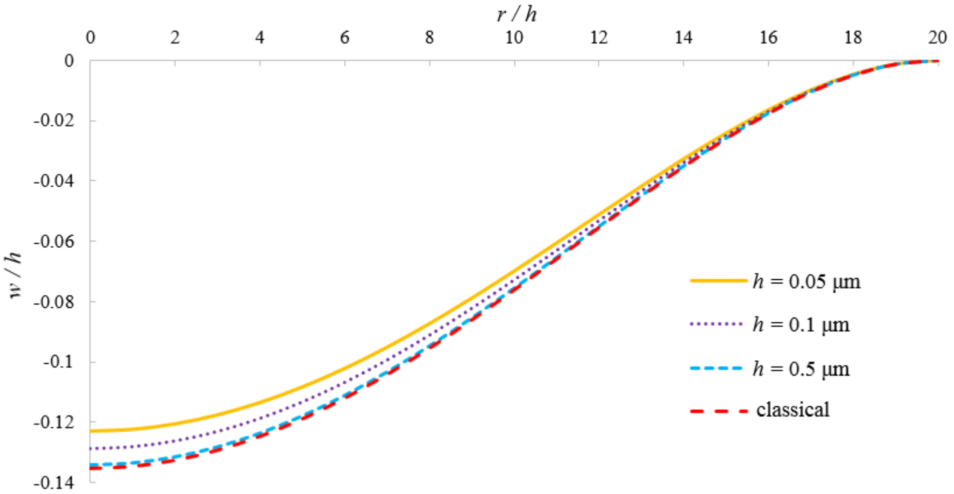

Fig. 3.3 Deflection of the clamped circular Kirchhoff plate predicted by the new model considering the surface energy effect alone.

3.4 Summary

A new non-classical model is developed for circular Kirchhoff plates subjected to axisymmetric loading by using a modified couple stress theory, a surface elasticity theory and Hamilton's principle. The equations of motion and boundary conditions are simultaneously obtained by employing a variational formulation. The new model contains a material length scale parameter to account for the microstructure effect and three surface elasticity constants to represent the surface energy effect.

It is shown that the newly obtained model degenerates to the Kirchhoff plate model considering the surface energy effect alone when the microstructure effect is ignored and reduces to the Kirchhoff plate model including the microstructure effect only when the surface energy effect is neglected. In addition, the new model recovers the classical elasticity-based model when both the microstructure and surface energy effects are not considered.

To illustrate the new model, the static bending problem of a clamped solid circular Kirchhoff plate subjected to a uniform normal load is analytically solved by directly applying the new model. The numerical results show that the deflection predicted by the new model is always smaller than that predicted by the classical model when the plate thickness is very small, but the former approaches the latter as the plate thickness increases. It is also observed that the difference between the plate deflection predicted by the model including the surface energy effect and that predicted by the classical model is significant when the plate thickness is sufficiently small. However, the difference is diminishing with the increase of the plate thickness. The trends of these predicted size effects are in agreement with experimental observations.

Chapter

4. A NON-CLASSICAL MINDLIN PLATE MODEL INCORPORATING MICROSTRUCTURE, SURFACE ENERGY AND FOUNDATION EFFECTS

4.1 Introduction

Thin plates resting on elastic foundations have been widely used in nano- and micro-scale devices and systems. As size effects play a significant role in nano- and micro-scale applications and classical continuum theories are unable to capture such effects, higher-order continuum theories, which contain material length-scale parameters and can account for the microstructure and surface energy effects, have recently been used to develop new models for thin beams and plates resting on elastic foundations.

Khajeansari et al. (2012) studied the bending deformation of an Euler-Bernoulli beam lying on a Winkler-Pasternak foundation by using a surface elasticity theory (e.g., Gurtin and Murdoch, 1978; Eremeyev and Lebedev, 2016) to incorporate the surface energy effect. Şimşek and Reddy (2013) proposed a model for a functionally graded micro-beam embedded in an elastic medium by applying a modified couple stress theory (e.g., Yang et al., 2002; Park and Gao, 2008) and the Winkler-Pasternak foundation model. Limkatanyu et al. (2014) provided a model for an Euler-Bernoulli beam resting on a Winkler-Pasternak foundation by including both the microstructure and surface energy effects, which extends the non-classical beam model of Gao and Mahmoud (2014).

However, very few models have been developed for thin plates that incorporates the elastic foundation effect in addition to the microstructure and surface energy effects. Recently, a general non-classical model that considers the microstructure, surface energy and foundation effects was provided by Gao and Zhang (2016) for Kirchhoff plates using a variational formulation.

The objective of the current chapter is to develop a new model for Mindlin plates in a most general form involving all five possible kinematic variables (rather than three for Kirchhoff plates) by including the microstructure, surface energy and foundation effects in a unified manner.

The rest of the Chapter 4 is organized as follows. In Section 4.2, a new non-classical model for a Mindlin plate resting on an elastic foundation is developed using a modified couple stress theory (Yang et al., 2002; Park and Gao, 2008), a surface elasticity theory (Gurtin and Murdoch, 1975, 1978) and a two-parameter Winkler-Pasternak foundation model (e.g., Selvadurai, 1979; Yokoyama, 1996) through a variational formulation based on Hamilton’s principle. It is shown that the new Mindlin plate model reduces to its classical elasticity-based counterpart when the microstructure, surface energy and foundation effects are all suppressed. In addition, the new model includes the Mindlin plate models considering the microstructure dependence or the surface energy effect or the foundation influence alone as special cases, recovers the counterpart non-classical model for Kirchhoff plates, and degenerates to the Timoshenko beam model incorporating the microstructure effect. In Section 4.3, the static bending and free vibration problems of a simply supported rectangular plate are analytically solved by directly applying the new model. The numerical results are also presented there to quantitatively show the differences between the current non-classical Mindlin plate model and its classical counterpart. The chapter concludes in Section 4.4 with a summary.

4.2 Formulation

The Mindlin plate theory, also known as the first-order shear deformation plate theory, is the simplest plate theory including transverse shear strains. By using the Cartesian coordinate system (x, y, z) shown in Fig 4.1, where the xy-plane is coincident with the geometrical mid-plane of the undeformed plate, the displacement field in a Mindlin plate of uniform thickness h can be written as (e.g., Reddy, 2002; Ma et al., 2011)

$$u_1(x,y,z,t) = u(x,y,t) - z\phi_x(x,y,t),\ u_2(x,y,z,t) = v(x,y,t) - z\phi_y(x,y,t),\ u_3(x,y,z,t) = w(x,y,t) \tag{4.1a-c}$$

where u_1, u_2 and u_3 are, respectively, the x-, y- and z-components of the displacement vector $\boldsymbol{u}$ of a point (x, y, z) in the plate at time t, u, v and w are, respectively, the x-, y- and z-components of the displacement vector of the corresponding point (x, y, 0) on the plate mid-plane at time t, and ϕ_x and ϕ_y are, respectively, the rotation angles of a transverse normal about the y-axis and x-axis (see Fig 4.1). Note that in Eqs. (4.1a-c) there are five independent kinematic variables, i.e., u, v, w, ϕ_x and ϕ_y, which will need to be determined in order to fully describe the displacement field in the Mindlin plate.

In Fig 4.1, S^+ and S^- are two surface layers of zero thickness that are taken to be perfectly bonded to the bulk plate material at $z = \pm h/2$, respectively. The bulk material satisfies a modified couple stress theory (Yang et al., 2002; Park and Gao, 2008), while the two surface layers are governed by a surface elasticity theory (Gurtin and Murdoch, 1975, 1978).

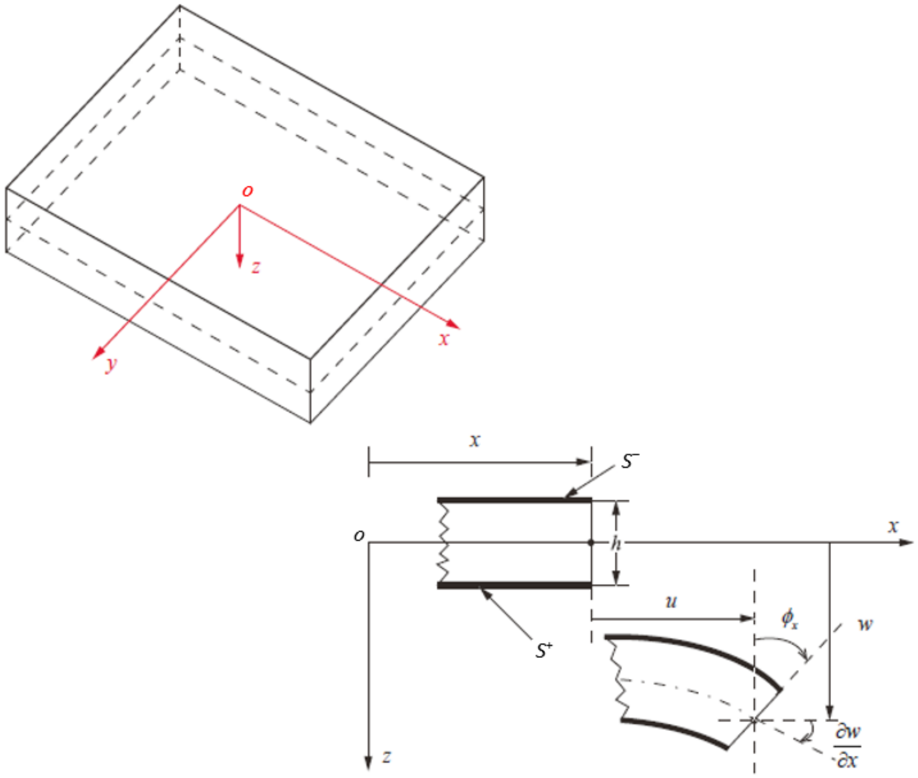

Fig. 4.1 Plate configuration and coordinate system

Figure 4.2 shows a Mindlin plate resting on a Winkler-Pasternak foundation. The Winkler-Pasternak foundation model contains two parameters, namely, the Winkler foundation modulus k_w for the spring elements and the Pasternak foundation modulus k_p for the shear layer (e.g., Selvadurai, 1979; Yokoyama, 1996). The effect of this two-parameter elastic foundation on the plate can be treated as a vertical body force q (in N/m^2) given by (Selvadurai, 1979):

$$q(x,y,t) = k_w w(x,y,t) - k_p \nabla^2 w(x,y,t), \tag{4.2}$$

where ∇^2 is the Laplacian, and w is the plate mid-plane deflection first introduced through Eq. (4.1c).

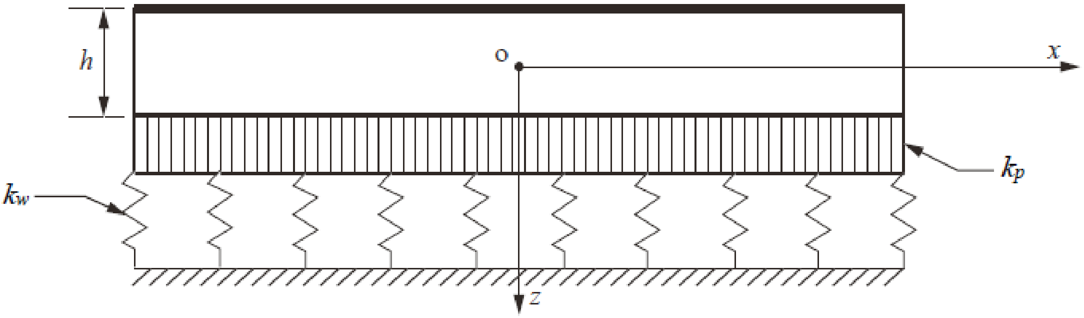

Fig. 4.2 Plate on a Winkler-Pasternak foundation

According to the modified couple stress theory (Yang et al., 2002; Park and Gao, 2008), the constitutive equations for an isotropic linear elastic material read

$$\sigma_{ij} = \lambda \varepsilon_{kk} \delta_{ij} + 2\mu \varepsilon_{ij}, \tag{4.3}$$

$$m_{ij} = 2 l^2 \mu \chi_{ij}, \tag{4.4}$$

where σ_{ij}, m_{ij} and δ_{ij} are, respectively, the components of the Cauchy stress tensor, the components of the deviatoric part of the couple stress tensor and the Kronecker delta, λ and μ are the Lamé constants in classical elasticity, l is a material length scale parameter measuring the couple stress effect (e.g., Mindlin, 1963; Park and Gao, 2006), and ε_{ij} and χ_{ij} are, respectively, the components of the infinitesimal strain tensor and the symmetric curvature tensor given by

$$\varepsilon_{ij} = \frac{1}{2}\left(u_{i,j} + u_{j,i}\right), \tag{4.5}$$

$$\chi_{ij} = \frac{1}{2}\left(\theta_{i,j} + \theta_{j,i}\right), \tag{4.6}$$

with u_i being the displacement components and θ_i being the components of the rotation vector defined by

$$\theta_i = \frac{1}{2} \varepsilon_{ijk} u_{k,j}. \tag{4.7}$$

According to the surface elasticity theory (e.g., Gurtin and Murdoch, 1975, 1978; Steigmann and Ogden, 1997, 1999; Altenbach et al., 2010; Eremeyev and Lebedev, 2016), the zero-thickness surface layer of a bulk elastic material has distinct elastic properties and satisfies the following governing equations (e.g., Gurtin and Murdoch, 1978; Zhou and Gao, 2013, 2015):

$$\sigma_{ij} n_j = \tau_{i\alpha,\alpha}, \quad \sigma_{ij} n_i n_j = \tau_{\alpha\beta} \kappa_{\alpha\beta}, \tag{4.8a,b}$$

where $\kappa_{\alpha\beta}$ are the components of the surface curvature tensor, n_i are the components of the outward-pointing unit normal $\mathbf{n}$ ($= n_i \mathbf{e}_i$) to the surface (with n_β being the two in-plane components of $\mathbf{n}$), $\tau_{\alpha\beta}$ are the in-plane components of the non-symmetric surface stress tensor given by (Gurtin and Murdoch, 1978)

$$\tau_{\alpha\beta} = \left[\tau_0 + (\lambda_0 + \tau_0) u_{\gamma,\gamma} \right] \delta_{\alpha\beta} + \mu_0 \left(u_{\alpha,\beta} + u_{\beta,\alpha} \right) - \tau_0 u_{\beta,\alpha}, \tag{4.9a}$$

and $\tau_{3\beta}$ are the out-of-plane components of the surface stress tensor expressed as (Gurtin and Murdoch, 1975, 1978)

$$\tau_{3\beta} = \tau_0 u_{3,\beta}, \tag{4.9b}$$

where μ_0 and λ_0 are the surface elastic constants, and τ_0 is the residual surface stress (i.e., the surface stress at zero strain). These three constants μ_0, λ_0 and τ_0 can be determined from either atomistic simulations or experimental measurements (e.g., Miller and Shenoy, 2000; Jing et al., 2006; Zhang et al., 2013).

Note that in Eqs. (4.3)–(4.9a,b) and throughout the Chapter 4, the summation convention and standard index notation are used, with the Greek indices running from 1 to 2 and the Latin indices from 1 to 3 unless otherwise indicated.

From Eqs. (4.1a-c) and (4.5)–(4.7), it follows that in the bulk of the current Mindlin plate,

$$\left.\begin{aligned}
&\varepsilon_{xx}=\frac{\partial u}{\partial x}-z\frac{\partial \phi_x}{\partial x},\ \varepsilon_{xy}=\frac{1}{2}(\frac{\partial u}{\partial y}+\frac{\partial v}{\partial x}-z\frac{\partial \phi_x}{\partial y}-z\frac{\partial \phi_y}{\partial x}),\ \varepsilon_{xz}=\frac{1}{2}(\frac{\partial w}{\partial x}-\phi_x),\\
&\qquad\qquad \varepsilon_{yy}=\frac{\partial v}{\partial y}-z\frac{\partial \phi_y}{\partial y},\ \varepsilon_{yz}=\frac{1}{2}(\frac{\partial w}{\partial y}-\phi_y),\ \varepsilon_{zz}=0,
\end{aligned}\right\} \tag{4.10}$$

$$\theta_1=\frac{1}{2}(\frac{\partial w}{\partial y}+\phi_y),\ \theta_2=-\frac{1}{2}(\frac{\partial w}{\partial x}+\phi_x),\ \theta_3=\frac{1}{2}(-\frac{\partial u}{\partial y}+\frac{\partial v}{\partial x}+z\frac{\partial \phi_x}{\partial y}-z\frac{\partial \phi_y}{\partial x}), \tag{4.11}$$

$$\left.\begin{aligned}
&\chi_{xx}=\frac{1}{2}(\frac{\partial^2 w}{\partial x\partial y}+\frac{\partial \phi_y}{\partial x}),\ \chi_{xy}=\frac{1}{4}(-\frac{\partial^2 w}{\partial x^2}+\frac{\partial^2 w}{\partial y^2}-\frac{\partial \phi_x}{\partial x}+\frac{\partial \phi_y}{\partial y}),\\
&\chi_{xz}=\frac{1}{4}(-\frac{\partial^2 u}{\partial x\partial y}+\frac{\partial^2 v}{\partial x^2}+z\frac{\partial^2 \phi_x}{\partial x\partial y}-z\frac{\partial^2 \phi_y}{\partial x^2}),\ \chi_{yy}=-\frac{1}{2}(\frac{\partial^2 w}{\partial x\partial y}+\frac{\partial \phi_x}{\partial y}),\\
&\chi_{yz}=\frac{1}{4}(-\frac{\partial^2 u}{\partial y^2}+\frac{\partial^2 v}{\partial x\partial y}+z\frac{\partial^2 \phi_x}{\partial y^2}-z\frac{\partial^2 \phi_y}{\partial x\partial y}),\ \chi_{zz}=\frac{1}{2}(\frac{\partial \phi_x}{\partial y}-\frac{\partial \phi_y}{\partial x}).
\end{aligned}\right\} \tag{4.12}$$

The total strain energy in the elastically deformed Mindlin plate is given by

$$\begin{aligned}
U_T&=U_B+U_S+U_F\\
&=\frac{1}{2}\int_{\Omega}\left(\sigma_{ij}\varepsilon_{ij}+m_{ij}\chi_{ij}\right)\mathrm{d}V+\frac{1}{2}\int_{S^+}\tau_{\alpha\beta}\varepsilon_{\alpha\beta}\mathrm{d}A+\frac{1}{2}\int_{S^-}\tau_{\alpha\beta}\varepsilon_{\alpha\beta}\mathrm{d}A+\frac{1}{2}\int_{R}k_w w^2\mathrm{d}A+\frac{1}{2}\int_{R}k_p w_{,\alpha}w_{,\alpha}\mathrm{d}A,
\end{aligned} \tag{4.13}$$

where Ω is the region occupied by the plate, S^+ and S^- represent, respectively, the bottom and top surface layers at $z = \pm h/2$ of the Mindlin plate (see Fig 4.1), R denotes the area occupied by the mid-plane of the plate, dV is the volume element, and dA is the area element. In Eq. (4.13), U_B is the strain energy in the bulk of the plate which is governed by the modified couple stress theory, U_S is the strain energy in the surface layers S^+ and S^- satisfying the surface elasticity theory, and U_F is the strain energy representing the effect of the two-parameter Winkler-Pasternak foundation.

The first variation of the total strain energy in the Mindlin plate over the time interval [0, *T*] can be obtained from Eqs. (4.9a,b)–(4.13) as

$$\begin{aligned}\delta\int_0^T U_T dt &= \int_0^T \int_\Omega \left(\sigma_{ij}\delta\varepsilon_{ij} + m_{ij}\delta\chi_{ij}\right)\mathrm{d}V\mathrm{d}t + \int_0^T \int_{S^+} (\tau^+_{\alpha\beta} - \frac{1}{2}\tau_0\delta_{\alpha\beta})\delta\varepsilon^+_{\alpha\beta}\mathrm{d}A\mathrm{d}t \\ &+ \int_0^T \int_{S^-} (\tau^-_{\alpha\beta} - \frac{1}{2}\tau_0\delta_{\alpha\beta})\delta\varepsilon^-_{\alpha\beta}\mathrm{d}A\mathrm{d}t + \int_0^T \int_R k_w w\delta w\mathrm{d}A\mathrm{d}t + \int_0^T \int_R k_p w_{,\alpha}\delta w_{,\alpha}\mathrm{d}A\mathrm{d}t,\end{aligned} \tag{4.14}$$

where ∂R is the boundary curve enclosing the area *R*, d*s* is the differential element of arc length along ∂R, and $\tau^+_{\alpha\beta}$ and $\tau^-_{\alpha\beta}$ represent, respectively, the surface stress components on the plate bottom (S^+) and top (S^-) surfaces.

Note that the volume integral of a sufficiently smooth function *D* (*x, y, z, t*) over the region Ω can be written as

$$\int_\Omega D(x,\ y,\ z,\ t)\mathrm{d}V = \int_R \int_{-h/2}^{h/2} D(x,\ y,\ z,\ t)\mathrm{d}z\mathrm{d}A, \tag{4.15}$$

where *h* is the (uniform) plate thickness, and *R* is the area occupied by the mid-plane of the plate.

From Eqs. (4.10) and (4.15), it follows that, with the help of Green's theorem,

$$\begin{aligned}\int_0^T \int_\Omega \sigma_{ij}\delta\varepsilon_{ij}\mathrm{d}V\mathrm{d}t = &-\int_0^T \int_R \Big[\left(N_{xx,x} + N_{xy,y}\right)\delta u + \left(N_{xy,x} + N_{yy,y}\right)\delta v + \left(N_{xz,x} + N_{yz,y}\right)\delta w \\ &- \left(-N_{xz} + M_{xx,x} + M_{xy,y}\right)\delta\phi_x - \left(-N_{yz} + M_{xy,x} + M_{yy,y}\right)\delta\phi_y\Big]\mathrm{d}A\mathrm{d}t \\ &+ \int_0^T \oint_{\partial R} \Big[\left(N_{xx}n_x + N_{xy}n_y\right)\delta u + \left(N_{xy}n_x + N_{yy}n_y\right)\delta v + \left(N_{xz}n_x + N_{yz}n_y\right)\delta w \\ &- \left(M_{xx}n_x + M_{xy}n_y\right)\delta\phi_x - \left(M_{xy}n_x + M_{yy}n_y\right)\delta\phi_y\Big]\mathrm{d}s\mathrm{d}t,\end{aligned} \tag{4.16}$$

where

$$\begin{aligned}&N_{xx} \equiv \int_{-h/2}^{h/2} \sigma_{xx}\mathrm{d}z,\quad N_{xy} \equiv \int_{-h/2}^{h/2} \sigma_{xy}\mathrm{d}z,\quad N_{xz} \equiv \int_{-h/2}^{h/2} \sigma_{xz}\mathrm{d}z,\quad N_{yy} \equiv \int_{-h/2}^{h/2} \sigma_{yy}\mathrm{d}z, \\ &N_{yz} \equiv \int_{-h/2}^{h/2} \sigma_{yz}\mathrm{d}z,\quad M_{xx} \equiv \int_{-h/2}^{h/2} \sigma_{xx}z\mathrm{d}z,\quad M_{xy} \equiv \int_{-h/2}^{h/2} \sigma_{xy}z\mathrm{d}z,\quad M_{yy} \equiv \int_{-h/2}^{h/2} \sigma_{yy}z\mathrm{d}z,\end{aligned} \tag{4.17}$$

are the Cauchy stress resultants through the plate thickness.

Similarly, the use of Eqs. (4.12) and (4.15) and Green’s theorem yields

$$
\begin{aligned}
&\int_0^T \int_\Omega m_{ij}\delta\chi_{ij}\mathrm{d}V\mathrm{d}t = -\frac{1}{2}\int_0^T \int_R \Big[\big(Y_{xz,xy} + Y_{yz,yy}\big)\delta u - \big(Y_{xz,xx} + Y_{yz,xy}\big)\delta v - \big(Y_{xx,xy} - Y_{xy,xx} + Y_{xy,yy} \\
&\quad - Y_{yy,xy}\big)\delta w - \big(Y_{xy,x} + Y_{yy,y} - Y_{zz,y} + H_{xz,xy} + H_{yz,yy}\big)\delta\phi_x - \big(-Y_{xx,x} - Y_{xy,y} + Y_{zz,x} - H_{xz,xx} \\
&\quad - H_{yz,xy}\big)\delta\phi_y\Big]\mathrm{d}A\mathrm{d}t + \frac{1}{2}\int_0^T \oint_{\partial R}\Bigg[\bigg(\frac{1}{2}Y_{xz,x}n_y + \frac{1}{2}Y_{xz,y}n_x + Y_{yz,y}n_y\bigg)\delta u - \bigg(Y_{xz,x}n_x + \frac{1}{2}Y_{yz,x}n_y \\
&\quad + \frac{1}{2}Y_{yz,y}n_x\bigg)\delta v - \bigg(\frac{1}{2}Y_{xx,x}n_y + \frac{1}{2}Y_{xx,y}n_x - Y_{xy,x}n_x + Y_{xy,y}n_y - \frac{1}{2}Y_{yy,x}n_y - \frac{1}{2}Y_{yy,y}n_x\bigg)\delta w \\
&\quad + \bigg(-Y_{xy}n_x - Y_{yy}n_y + Y_{zz}n_y - \frac{1}{2}H_{xz,x}n_y - \frac{1}{2}H_{xz,y}n_x - H_{yz,y}n_y\bigg)\delta\phi_x + \big(Y_{xx}n_x + Y_{xy}n_y - Y_{zz}n_x \\
&\quad + H_{xz,x}n_x + \frac{1}{2}H_{yz,x}n_y + \frac{1}{2}H_{yz,y}n_x\bigg)\delta\phi_y - \frac{1}{2}Y_{xz}n_y\delta u_{,x} - \bigg(\frac{1}{2}Y_{xz}n_x + Y_{yz}n_y\bigg)\delta u_{,y} + \big(Y_{xz}n_x \\
&\quad + \frac{1}{2}Y_{yz}n_y\bigg)\delta v_{,x} + \frac{1}{2}Y_{yz}n_x\delta v_{,y} + \bigg(\frac{1}{2}Y_{xx}n_y - Y_{xy}n_x - \frac{1}{2}Y_{yy}n_y\bigg)\delta w_{,x} + \bigg(\frac{1}{2}Y_{xx}n_x + Y_{xy}n_y - \frac{1}{2}Y_{yy}n_x\bigg)\delta w_{,y} \\
&\quad + \frac{1}{2}H_{xz}n_y\delta\phi_{x,x} + \bigg(\frac{1}{2}H_{xz}n_x + H_{yz}n_y\bigg)\delta\phi_{x,y} - \bigg(H_{xz}n_x + \frac{1}{2}H_{yz}n_y\bigg)\delta\phi_{y,x} - \frac{1}{2}H_{yz}n_x\delta\phi_{y,y}\Bigg]\mathrm{d}s\mathrm{d}t,
\end{aligned}
\tag{4.18}
$$

where

$$
\begin{aligned}
&Y_{xx} \equiv \int_{-h/2}^{h/2} m_{xx}\mathrm{d}z,\ \ Y_{xy} \equiv \int_{-h/2}^{h/2} m_{xy}\mathrm{d}z,\ \ Y_{xz} \equiv \int_{-h/2}^{h/2} m_{xz}\mathrm{d}z,\ \ Y_{yy} \equiv \int_{-h/2}^{h/2} m_{yy}\mathrm{d}z, \\
&Y_{yz} \equiv \int_{-h/2}^{h/2} m_{yz}\mathrm{d}z,\ \ Y_{zz} \equiv \int_{-h/2}^{h/2} m_{zz}\mathrm{d}z,\ \ H_{xz} \equiv \int_{-h/2}^{h/2} m_{xz}z\mathrm{d}z,\ \ H_{yz} \equiv \int_{-h/2}^{h/2} m_{yz}z\mathrm{d}z
\end{aligned}
\tag{4.19}
$$

are the couple stress resultants through the plate thickness.

Also, it follows from Eqs. (4.10) and (4.15) and Green’s theorem that

$$
\begin{aligned}
&\int_0^T\int_{S^+}(\tau^+_{\alpha\beta}-\frac{1}{2}\tau_0\delta_{\alpha\beta})\delta\varepsilon^+_{\alpha\beta}\mathrm{d}A\mathrm{d}t+\int_0^T\int_{S^-}(\tau^-_{\alpha\beta}-\frac{1}{2}\tau_0\delta_{\alpha\beta})\delta\varepsilon^-_{\alpha\beta}\mathrm{d}A\mathrm{d}t\\
&=-\int_0^T\int_R\bigg[\left(\tau^+_{xx,x}+\frac{1}{2}\tau^+_{xy,y}+\frac{1}{2}\tau^+_{yx,y}+\tau^-_{xx,x}+\frac{1}{2}\tau^-_{xy,y}+\frac{1}{2}\tau^-_{yx,y}\right)\delta u\\
&+\left(\frac{1}{2}\tau^+_{xy,x}+\frac{1}{2}\tau^+_{yx,x}+\tau^+_{yy,y}+\frac{1}{2}\tau^-_{xy,x}+\frac{1}{2}\tau^-_{yx,x}+\tau^-_{yy,y}\right)\delta v\\
&-\frac{h}{2}\left(\tau^+_{xx,x}+\frac{1}{2}\tau^+_{xy,y}+\frac{1}{2}\tau^+_{yx,y}-\tau^-_{xx,x}-\frac{1}{2}\tau^-_{xy,y}-\frac{1}{2}\tau^-_{yx,y}\right)\delta\phi_x\\
&-\frac{h}{2}\left(\frac{1}{2}\tau^+_{xy,x}+\frac{1}{2}\tau^+_{yx,x}+\tau^+_{yy,y}-\frac{1}{2}\tau^-_{xy,x}-\frac{1}{2}\tau^-_{yx,x}-\tau^-_{yy,y}\right)\delta\phi_y\bigg]\mathrm{d}A\mathrm{d}t\\
&+\frac{1}{2}\int_0^T\oint_{\partial R}\Big[\left(2\tau^+_{xx}n_x+\tau^+_{xy}n_y+\tau^+_{yx}n_y+2\tau^-_{xx}n_x+\tau^-_{xy}n_y+\tau^-_{yx}n_y-2\tau_0n_x\right)\delta u\\
&+\left(\tau^+_{xy}n_x+\tau^+_{yx}n_x+2\tau^+_{yy}n_y+\tau^-_{xy}n_x+\tau^-_{yx}n_x+2\tau^-_{yy}n_y-2\tau_0n_y\right)\delta v\\
&-h\left(\tau^+_{xx}n_x+\frac{1}{2}\tau^+_{xy}n_y+\frac{1}{2}\tau^+_{yx}n_y-\tau^-_{xx}n_x-\frac{1}{2}\tau^-_{xy}n_y-\frac{1}{2}\tau^-_{yx}n_y\right)\delta\phi_x\\
&-h\left(\frac{1}{2}\tau^+_{xy}n_x+\frac{1}{2}\tau^+_{yx}n_x+\tau^+_{yy}n_y-\frac{1}{2}\tau^-_{xy}n_x-\frac{1}{2}\tau^-_{yx}n_x-\tau^-_{yy}n_y\right)\delta\phi_y\Big]\mathrm{d}s\mathrm{d}t.
\end{aligned}
\tag{4.20}
$$

Note that in reaching Eq. (4.20) use has been made of the relations $S^+ = R = S^-$, $\partial S^+ = \partial R = \partial S^-$ for the uniform-thickness plate under consideration in order to facilitate the integral evaluations.

In addition, using Green's theorem gives

$$
\begin{aligned}
&\int_0^T\int_R k_w w\delta w\mathrm{d}A\mathrm{d}t+\int_0^T\int_R k_p w_{,\alpha}\delta w_{,\alpha}\mathrm{d}A\mathrm{d}t\\
&=\int_0^T\int_R k_w w\delta w\mathrm{d}A\mathrm{d}t-\int_0^T\int_R k_p\left(w_{,xx}+w_{,yy}\right)\delta w\mathrm{d}A\mathrm{d}t+\int_0^T\oint_{\partial R}k_p\left(w_{,x}n_x+w_{,y}n_y\right)\delta w\mathrm{d}s\mathrm{d}t.
\end{aligned}
\tag{4.21}
$$

The kinetic energy of the Mindlin plate can be written as (e.g., Ma et al., 2011)

$$
K=\frac{1}{2}\int_\Omega\rho\left[\left(\dot{u}_1\right)^2+\left(\dot{u}_2\right)^2+\left(\dot{u}_3\right)^2\right]\mathrm{d}V,
\tag{4.22}
$$

where ρ is the mass density of the plate material. Note that here and in the sequel, the overhead "·" and "··" denote, respectively, the first and second time derivatives (e.g., $\dot{u}_1 = \partial u_1 / \partial t,\ \ddot{u}_1 = \partial^2 u_1 / \partial t^2$).

The first variation of the kinetic energy, over the time interval [0, T], can be obtained from Eqs. (4.1a-c), (4.15) and (4.22) as

$$\delta\int_0^T K\mathrm{d}t = -\int_0^T \int_R (m_0\ddot{u}\delta u + m_0\ddot{v}\delta v + m_0\ddot{w}\delta w + m_2\ddot{\phi}_x\delta\phi_x + m_2\ddot{\phi}_y\delta\phi_y)\mathrm{d}A\mathrm{d}t, \tag{4.23}$$

where

$$m_0 \equiv \int_{-h/2}^{h/2} \rho \mathrm{d}z = \rho h, \quad m_2 \equiv \int_{-h/2}^{h/2} \rho z^2 \mathrm{d}z = \frac{\rho h^3}{12}. \tag{4.24}$$

In reaching Eq. (4.23), it has been assumed that the initial (t = 0) and final (t = T) configurations of the plate are prescribed so that the virtual displacements vanish at t = 0 and t = T. In addition, ρ is taken to be constant along the plate thickness and over the time interval [0, T] such that $\dot{m}_0 = 0, \dot{m}_2 = 0$.

From the general expression of the work done by external forces in the modified couple stress theory (e.g., Park and Gao, 2006, 2008) and in the surface elasticity theory (e.g., Gurtin and Murdoch, 1975, 1978), the virtual work done by the forces applied on the current Mindlin plate over the time interval [0, T] can be expressed as

$$\begin{aligned}\delta\int_0^T W\mathrm{d}t = &\int_0^T \int_R \Big[f_x\delta u + f_y\delta v + f_z\delta w + \frac{1}{2}c_x\delta(w_{,y} + \phi_y) - \frac{1}{2}c_y\delta(w_{,x} + \phi_x) \\ &- \frac{1}{2}c_z(\delta u_{,y} - \delta v_{,x}) \Big]\mathrm{d}A\mathrm{d}t + \int_0^T \oint_{\partial R} \Big[\overline{t}_x\delta u + \overline{t}_y\delta v + \overline{t}_z\delta w - \overline{M}_x\delta\phi_x - \overline{M}_y\delta\phi_y \\ &+ \frac{1}{2}\overline{s}_x\delta(w_{,y} + \phi_y) - \frac{1}{2}\overline{s}_y\delta(w_{,x} + \phi_x) - \frac{1}{2}\overline{s}_z(\delta u_{,y} - \delta v_{,x}) \Big]\mathrm{d}s\mathrm{d}t \\ &+ \int_0^T \int_{S^+} \tau^+_{3\alpha,\alpha}\delta w\mathrm{d}A\mathrm{d}t + \int_0^T \int_{S^-} \tau^-_{3\alpha,\alpha}\delta w\mathrm{d}A\mathrm{d}t,\end{aligned} \tag{4.25}$$

where f_i and c_i ($i = x, y, z$) are, respectively, the components of the body force resultant (force per unit area) and the body couple resultant (moment per unit area) through the plate thickness acting in the area R (i.e., the plate mid-plane), $\bar{t}_i$ and $\overline{s_i}$ ($i = x, y, z$) are, respectively, the components of the Cauchy traction resultant (force per unit length) and the surface couple resultant (moment per unit length) through the plate thickness acting on ∂R (i.e., the boundary of R), and $\overline{M_x}$ and $\overline{M_y}$ are, respectively, the applied moments per unit length about the y-axis and x-axis acting on ∂R. Note that the positive directions of $\overline{M_x}$ and $\overline{M_y}$ are, respectively, opposite to those of ϕ_x and ϕ_y (see Fig 4.1). Also, in reaching Eq. (4.25), use has been made of Green's theorem. It should be mentioned that the last two terms in the virtual work expression in Eq. (4.25) account for the contribution of the normal stress on the top and bottom plate surfaces $\sigma_{33}^{\pm}$ (= $\pm\tau_{3\alpha,\alpha}^{\pm}$ from the equilibrium equations in Eq. (4.8a)), which is neglected in the Mindlin plate models that do not consider the surface energy effect (e.g., Ma et al., 2011; Zhou and Gao, 2014).

According to Hamilton's principle (e.g., Reddy, 2002; Ma et al., 2008, 2010, 2011; Gao et al. 2013; Gao and Zhang, 2015, 2016),

$$\delta\int_0^T \left[K - \left(U_T - W\right)\right] \mathrm{d}t = 0. \tag{4.26}$$

Using Eqs. (4.14), (4.16), (4.18), (4.20), (4.21), (4.23) and (4.25) in Eq. (4.26) and applying the fundamental lemma of the calculus of variations (e.g., Gao and Mall, 2001; Steigmann, 2007; Gao, 2015) will lead to, with the arbitrariness of δu, δv, δw, $\delta\phi_x$ and $\delta\phi_y$ and the relations $S^+ = R = S^-$, $\partial S^+ = \partial R = \partial S^-$ due to the uniform thickness of the plate,

$$N_{xx,x}+N_{xy,y}+\frac{Y_{xz,xy}+Y_{yz,yy}}{2}+\tau^{+}_{xx,x}+\frac{1}{2}\tau^{+}_{xy,y}+\frac{1}{2}\tau^{+}_{yx,y}+\tau^{-}_{xx,x}+\frac{1}{2}\tau^{-}_{xy,y}+\frac{1}{2}\tau^{-}_{yx,y}+f_x+\frac{1}{2}c_{z,y}=m_0\ddot{u},$$

(4.27a)

$$N_{xy,x}+N_{yy,y}-\frac{Y_{xz,xx}+Y_{yz,xy}}{2}+\frac{1}{2}\tau^{+}_{xy,x}+\frac{1}{2}\tau^{+}_{yx,x}+\tau^{+}_{yy,y}+\frac{1}{2}\tau^{-}_{xy,x}+\frac{1}{2}\tau^{-}_{yx,x}+\tau^{-}_{yy,y}+f_y-\frac{1}{2}c_{z,x}=m_0\ddot{v},$$

(4.27b)

$$N_{xz,x}+N_{yz,y}-\frac{Y_{xx,xy}-Y_{xy,xx}+Y_{xy,yy}-Y_{yy,xy}}{2}+\tau^{+}_{3\alpha,\alpha}+\tau^{-}_{3\alpha,\alpha}-k_w w+k_p\nabla^2 w+f_z-\frac{1}{2}c_{x,y}+\frac{1}{2}c_{y,x}=m_0\ddot{w},$$

(4.27c)

$$-N_{xz}+M_{xx,x}+M_{xy,y}+\frac{Y_{xy,x}+Y_{yy,y}-Y_{zz,y}+H_{xz,xy}+H_{yz,yy}}{2}+\frac{h}{4}\Big(2\tau^{+}_{xx,x}+\tau^{+}_{xy,y}+\tau^{+}_{yx,y}-2\tau^{-}_{xx,x}$$
$$-\tau^{-}_{xy,y}-\tau^{-}_{yx,y}\Big)+\frac{1}{2}c_y=-m_2\ddot{\phi}_x,$$

(4.27d)

$$-N_{yz}+M_{xy,x}+M_{yy,y}+\frac{-Y_{xx,x}-Y_{xy,y}+Y_{zz,x}-H_{xz,xx}-H_{yz,xy}}{2}+\frac{h}{4}\Big(\tau^{+}_{xy,x}+\tau^{+}_{yx,x}+2\tau^{+}_{yy,y}-\tau^{-}_{xy,x}$$
$$-\tau^{-}_{yx,x}-2\tau^{-}_{yy,y}\Big)-\frac{1}{2}c_x=-m_2\ddot{\phi}_y$$

(4.27e)

as the equations of motion of the current Mindlin plate for any $(x, y) \in R$ and $t \in (0, T)$, and

$$\int_0^T\oint_{\partial R}\Big\{\Big[2N_{xx}n_x+2N_{xy}n_y+\frac{1}{2}Y_{xz,x}n_y+\frac{1}{2}Y_{xz,y}n_x+Y_{yz,y}n_y+2(\tau^{+}_{xx}+\tau^{-}_{xx}-\tau_0)n_x+(\tau^{+}_{xy}+\tau^{-}_{xy}$$
$$+\tau^{+}_{yx}+\tau^{-}_{yx})n_y+c_z n_y-2\overline{t}_x\Big]\delta u+\Big[2N_{xy}n_x+2N_{yy}n_y-Y_{xz,x}n_x-\frac{1}{2}Y_{yz,x}n_y-\frac{1}{2}Y_{yz,y}n_x+(\tau^{+}_{xy}$$
$$+\tau^{-}_{xy}+\tau^{+}_{yx}+\tau^{-}_{yx})n_x+2(\tau^{+}_{yy}+\tau^{-}_{yy}-\tau_0)n_y-c_z n_x-2\overline{t}_y\Big]\delta v+\Big[2N_{xz}n_x+2N_{yz}n_y-\frac{1}{2}(Y_{xx}-Y_{yy})_{,x}n_y$$
$$-\frac{1}{2}(Y_{xx}-Y_{yy})_{,y}n_x+Y_{xy,x}n_x-Y_{xy,y}n_y+2k_p\left(w_{,x}n_x+w_{,y}n_y\right)-c_x n_y+c_y n_x-2\overline{t}_z\Big]\delta w-\big[2M_{xx}n_x$$
$$+2M_{xy}n_y+Y_{xy}n_x+Y_{yy}n_y-Y_{zz}n_y+\frac{1}{2}H_{xz,x}n_y+\frac{1}{2}H_{xz,y}n_x+H_{yz,y}n_y+h(\tau^{+}_{xx}-\tau^{-}_{xx})n_x+\frac{h}{2}(\tau^{+}_{xy}$$
$$-\tau^{-}_{xy}+\tau^{+}_{yx}-\tau^{-}_{yx})n_y-2\overline{M}_x-\overline{s}_y\Big]\delta\phi_x-\big[2M_{xy}n_x+2M_{yy}n_y-Y_{xx}n_x-Y_{xy}n_y+Y_{zz}n_x$$

$$
\begin{aligned}
&-H_{xz,x}n_x-\frac{1}{2}H_{yz,x}n_y-\frac{1}{2}H_{yz,y}n_x+h(\tau_{yy}^{+}-\tau_{yy}^{-})n_y+\frac{h}{2}(\tau_{xy}^{+}-\tau_{xy}^{-}+\tau_{yx}^{+}-\tau_{yx}^{-})n_x\\
&-2\bar{M}_y+\bar{s}_x\Big]\delta\phi_y-\frac{1}{2}Y_{xz}n_y\delta u_{,x}-\left(\frac{1}{2}Y_{xz}n_x+Y_{yz}n_y-\bar{s}_z\right)\delta u_{,y}+\left(Y_{xz}n_x+\frac{1}{2}Y_{yz}n_y-\bar{s}_z\right)\delta v_{,x}\\
&+\frac{1}{2}Y_{yz}n_x\delta v_{,y}+\left[\frac{1}{2}(Y_{xx}-Y_{yy})n_y-Y_{xy}n_x+\bar{s}_y\right]\delta w_{,x}+\left[\frac{1}{2}(Y_{xx}-Y_{yy})n_x+Y_{xy}n_y-\bar{s}_x\right]\delta w_{,y}\\
&+\frac{1}{2}H_{xz}n_y\delta\phi_{x,x}+\left(\frac{1}{2}H_{xz}n_x+H_{yz}n_y\right)\delta\phi_{x,y}-\left(H_{xz}n_x+\frac{1}{2}H_{yz}n_y\right)\delta\phi_{y,x}-\frac{1}{2}H_{yz}n_x\delta\phi_{y,y}\Big\}\mathrm{d}s\mathrm{d}t=0,
\end{aligned}
\tag{4.28}
$$

which can be further simplified to obtain the boundary conditions.

Note that the integrand of the line integral in Eq. (4.28) is expressed in terms of the Cartesian components of the resultants and displacements that are functions of the Cartesian coordinates (x, y, z) with the unit base vectors $\{\mathbf{e}_1, \mathbf{e}_2, \mathbf{e}_3\}$. This is convenient for a rectangular plate whose edges are parallel to the *x*- and *y*-axes. However, for a more general case of a plate whose boundary is not aligned with the *x*- or *y*-axis, as shown in Fig 4.3, it is more convenient to use a Cartesian coordinate system $(n,\ s,\ z)$ with the unit base vectors $\{\mathbf{e}_n, \mathbf{e}_s, \mathbf{e}_3\}$, where $\mathbf{e}_n$ $(=n_x\mathbf{e}_1+n_y\mathbf{e}_2)$ and $\mathbf{e}_s$ $(=-n_y\mathbf{e}_1+n_x\mathbf{e}_2)$ are, respectively, the unit normal and tangent vectors on the plate boundary ∂R.

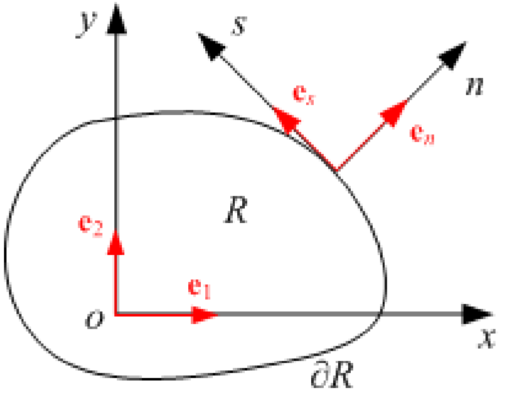

Fig. 4.3 Two coordinate systems

It can be shown that the components in the coordinate system $(x,\ y,\ z)$ are related to those in the coordinate system $(n,\ s,\ z)$ through the following transformation expressions:

$$
\begin{gathered}
\{u,\ v\}^T = [R_1]\{u_n,\ v_s\}^T,\ \{\phi_x,\ \phi_y\}^T = [R_1]\{\phi_n,\ \phi_s\}^T,\ \{w_{,x},\ w_{,y}\}^T = [R_1]\{w_{,n},\ w_{,s}\}^T, \\
\{\overline{t}_x,\ \overline{t}_y\}^T = [R_1]\{\overline{t}_n,\ \overline{t}_s\}^T,\ \{\overline{s}_x,\ \overline{s}_y\}^T = [R_1]\{\overline{s}_n,\ \overline{s}_s\}^T,\ \{c_x,\ c_y\}^T = [R_1]\{c_n,\ c_s\}^T, \\
\{N_{xz},\ N_{yz}\}^T = [R_1]\{N_{nz},\ N_{sz}\}^T,\ \{\overline{M}_x,\ \overline{M}_y\}^T = [R_1]\{\overline{M}_n,\ \overline{M}_s\}^T, \\
\{Y_{xz},\ Y_{yz}\}^T = [R_1]\{Y_{nz},\ Y_{sz}\}^T,\ \{H_{xz},\ H_{yz}\}^T = [R_1]\{H_{nz},\ H_{sz}\}^T, \\
\begin{bmatrix} N_{xx} & N_{xy} \\ N_{xy} & N_{yy} \end{bmatrix} = [R_1]\begin{bmatrix} N_{nn} & N_{ns} \\ N_{ns} & N_{ss} \end{bmatrix}[R_1]^T,\ \begin{bmatrix} Y_{xx} & Y_{xy} \\ Y_{xy} & Y_{yy} \end{bmatrix} = [R_1]\begin{bmatrix} Y_{nn} & Y_{ns} \\ Y_{ns} & Y_{ss} \end{bmatrix}[R_1]^T, \qquad (4.29) \\
\begin{bmatrix} M_{xx} & M_{xy} \\ M_{xy} & M_{yy} \end{bmatrix} = [R_1]\begin{bmatrix} M_{nn} & M_{ns} \\ M_{ns} & M_{ss} \end{bmatrix}[R_1]^T,\ \begin{bmatrix} Y_{xz,x} & Y_{xz,y} \\ Y_{yz,x} & Y_{yz,y} \end{bmatrix} = [R_1]\begin{bmatrix} Y_{nz,n} & Y_{nz,s} \\ Y_{sz,n} & Y_{sz,s} \end{bmatrix}[R_1]^T, \\
\begin{bmatrix} \phi_{x,x} & \phi_{x,y} \\ \phi_{y,x} & \phi_{y,y} \end{bmatrix} = [R_1]\begin{bmatrix} \phi_{n,n} & \phi_{n,s} \\ \phi_{s,n} & \phi_{s,s} \end{bmatrix}[R_1]^T,\ \begin{bmatrix} H_{xz,x} & H_{xz,y} \\ H_{yz,x} & H_{yz,y} \end{bmatrix} = [R_1]\begin{bmatrix} H_{nz,n} & H_{nz,s} \\ H_{sz,n} & H_{sz,s} \end{bmatrix}[R_1]^T, \\
\begin{bmatrix} \tau_{xx}^{\pm} & \tau_{xy}^{\pm} \\ \tau_{yx}^{\pm} & \tau_{yy}^{\pm} \end{bmatrix} = [R_1]\begin{bmatrix} \tau_{nn}^{\pm} & \tau_{ns}^{\pm} \\ \tau_{sn}^{\pm} & \tau_{ss}^{\pm} \end{bmatrix}[R_1]^T,\ \begin{bmatrix} u_{,x} & u_{,y} \\ v_{,x} & v_{,y} \end{bmatrix} = [R_1]\begin{bmatrix} u_{n,n} & u_{n,s} \\ v_{s,n} & v_{s,s} \end{bmatrix}[R_1]^T, \\
\{Y_{xx,x},\ Y_{xx,y},\ Y_{xy,x},\ Y_{xy,y},\ Y_{yy,x},\ Y_{yy,y}\}^T = [R_3]\{Y_{nn,n},\ Y_{nn,s},\ Y_{ns,n},\ Y_{ns,s},\ Y_{ss,n},\ Y_{ss,s}\}^T,
\end{gathered}
$$

where

$$[R_1] \equiv \begin{bmatrix} n_x & -n_y \\ n_y & n_x \end{bmatrix}, \qquad (4.30a)$$

$$[R_3] \equiv \begin{bmatrix} n_x^3 & -n_x^2 n_y & -2n_x^2 n_y & 2n_x n_y^2 & n_x n_y^2 & -n_y^3 \\ n_x^2 n_y & n_x^3 & -2n_x n_y^2 & -2n_x^2 n_y & n_y^3 & n_x n_y^2 \\ n_x^2 n_y & -n_x n_y^2 & n_x^3 - n_x n_y^2 & -n_x^2 n_y + n_y^3 & -n_x^2 n_y & n_x n_y^2 \\ n_x n_y^2 & n_x^2 n_y & n_x^2 n_y - n_y^3 & n_x^3 - n_x n_y^2 & -n_x n_y^2 & -n_x^2 n_y \\ n_x n_y^2 & -n_y^3 & 2n_x^2 n_y & -2n_x n_y^2 & n_x^3 & -n_x^2 n_y \\ n_y^3 & n_x n_y^2 & 2n_x n_y^2 & 2n_x^2 n_y & n_x^2 n_y & n_x^3 \end{bmatrix}, \qquad (4.30b)$$

with $n_x^2 + n_y^2 = 1$.

Using Eqs. (4.29) and (4.30a,b) in Eq. (4.28) yields, after some lengthy algebra,

$$\begin{aligned}
&\int_0^T \oint_{\partial R} \left[2\left(N_{nn} + \frac{1}{4} Y_{nz,s} + \tau_{nn}^{+} + \tau_{nn}^{-} - \tau_0 - \bar{t}_n \right) \delta u_n + \left(2N_{ns} - Y_{nz,n} - \frac{1}{2} Y_{sz,s} + \tau_{ns}^{+} + \tau_{ns}^{-} \right.\right. \\
&\left. + \tau_{sn}^{+} + \tau_{sn}^{-} - c_z - 2\bar{t}_s \right) \delta v_s + \left(2N_{nz} - \frac{Y_{nn,s} - Y_{ss,s}}{2} + Y_{ns,n} + 2k_p w_{,n} + c_s - 2\bar{t}_z \right) \delta w \\
&- (Y_{ns} - \bar{s}_s) \delta w_{,n} + \left(\frac{Y_{nn} - Y_{ss}}{2} - \bar{s}_n \right) \delta w_{,s} - \left(2M_{nn} + Y_{ns} + \frac{1}{2} H_{nz,s} + h\tau_{nn}^{+} - h\tau_{nn}^{-} \right. \\
&\left. - 2\bar{M}_n - \bar{s}_s \right) \delta \phi_n - \left(2M_{ns} - Y_{nn} + Y_{zz} - H_{nz,n} - \frac{H_{sz,s}}{2} + \frac{h}{2} \tau_{ns}^{+} - \frac{h}{2} \tau_{ns}^{-} + \frac{h}{2} \tau_{sn}^{+} - \frac{h}{2} \tau_{sn}^{-} \right. \\
&\left. - 2\bar{M}_s + \bar{s}_n \right) \delta \phi_s - \left(\frac{Y_{nz}}{2} - \bar{s}_z \right) \delta u_{n,s} + (Y_{nz} - \bar{s}_z) \delta v_{s,n} + \frac{Y_{sz}}{2} \delta v_{s,s} + \frac{H_{nz}}{2} \delta \phi_{n,s} - H_{nz} \delta \phi_{s,n} \\
&\left. - \frac{H_{sz}}{2} \delta \phi_{s,s} \right] \mathrm{d}s \mathrm{d}t = 0.
\end{aligned}$$

(4.31)

Note that on the closed boundary ∂R the following identity:

$$\oint_{\partial R} D \delta g_{,s} \mathrm{d}s = -\oint_{\partial R} D_{,s} \delta g \mathrm{d}s \tag{4.32}$$

holds, where D, g are two smooth functions. With the help of Eq. (4.32), Eq. (4.31) becomes

$$\int_0^T \oint_{\partial R} \left(\widehat{N}_{nn} \delta u_n + \widehat{N}_{ss} \delta v_s + \widehat{N}_{zz} \delta w + \widehat{M}_n \delta \phi_n + \widehat{M}_s \delta \phi_s + \hat{T}_z \delta w_{,n} + \hat{T}_s \delta v_{s,n} + \hat{Z}_s \delta \phi_{s,n} \right) \mathrm{d}s \mathrm{d}t = 0,$$

(4.33)

where

$$\begin{aligned}
&\widehat{N}_{nn} \equiv 2(N_{nn} + \frac{1}{2}Y_{nz,s} + \tau_{nn}^{+} + \tau_{nn}^{-} - \tau_0 - \frac{1}{2}\bar{s}_{z,s} - \bar{t}_n),\\
&\widehat{N}_{ss} \equiv 2N_{ns} - Y_{nz,n} - Y_{sz,s} + \tau_{ns}^{+} + \tau_{ns}^{-} + \tau_{sn}^{+} + \tau_{sn}^{-} - c_z - 2\bar{t}_s,\\
&\widehat{N}_{zz} \equiv 2N_{nz} - Y_{nn,s} + Y_{ns,n} + Y_{ss,s} + 2k_p w_{,n} + c_s + \bar{s}_{n,s} - 2\bar{t}_z,\\
&\widehat{M}_n \equiv -2M_{nn} - Y_{ns} - H_{nz,s} - h(\tau_{nn}^{+} - \tau_{nn}^{-}) + 2\bar{M}_n + \bar{s}_s,\\
&\widehat{M}_s \equiv -2M_{ns} + Y_{nn} - Y_{zz} + H_{nz,n} + H_{sz,s} - \frac{h}{2}(\tau_{ns}^{+} - \tau_{ns}^{-} + \tau_{sn}^{+} - \tau_{sn}^{-}) + 2\bar{M}_s - \bar{s}_n,\\
&\widehat{T}_z \equiv -Y_{ns} + \bar{s}_s,\\
&\widehat{T}_s \equiv Y_{nz} - \bar{s}_z,\\
&\widehat{Z}_s \equiv -H_{nz}.
\end{aligned} \tag{4.34a-h}$$

Using the fundamental lemma of the calculus of variations in Eq. (4.33) then gives

$$\begin{aligned}
&\widehat{N}_{nn} = 0 \quad \text{or} \quad u_n = \bar{u}_n,\\
&\widehat{N}_{ss} = 0 \quad \text{or} \quad v_s = \bar{v}_s,\\
&\widehat{N}_{zz} = 0 \quad \text{or} \quad w = \bar{w},\\
&\widehat{M}_n = 0 \quad \text{or} \quad \phi_n = \bar{\phi}_n,\\
&\widehat{M}_s = 0 \quad \text{or} \quad \phi_s = \bar{\phi}_s,\\
&\widehat{T}_z = 0 \quad \text{or} \quad w_{,n} = \bar{w}_{,n},\\
&\widehat{T}_s = 0 \quad \text{or} \quad v_{s,n} = \bar{v}_{s,n},\\
&\widehat{Z}_s = 0 \quad \text{or} \quad \phi_{s,n} = \bar{\phi}_{s,n}
\end{aligned} \tag{4.35a-h}$$

as the boundary conditions for any $(x, y) \in \partial R$ and $t \in (0, T)$, where the overhead bar indicates the prescribed value.

From Eqs. (4.3), (4.10) and (4.17), the Cauchy stress resultants can be expressed in terms of the five kinematic variables u, v, w, ϕ_x and ϕ_y as

$$N_{xx} = h\left[(\lambda + 2\mu)u_{,x} + \lambda v_{,y}\right],$$

$$N_{xy} = \mu h(u_{,y} + v_{,x}),$$

$$N_{xz} = k_s \mu h (w_{,x} - \phi_x),$$

$$N_{yy} = h\left[\lambda u_{,x} + (\lambda + 2\mu) v_{,y}\right],$$

$$N_{yz} = k_s \mu h (w_{,y} - \phi_y),$$

$$M_{xx} = -\frac{1}{12} h^3 \left[(\lambda + 2\mu)\phi_{x,x} + \lambda \phi_{y,y}\right],$$

$$M_{xy} = -\frac{1}{12} \mu h^3 (\phi_{x,y} + \phi_{y,x}),$$

$$M_{yy} = -\frac{1}{12} h^3 \left[\lambda \phi_{x,x} + (\lambda + 2\mu)\phi_{y,y}\right], \tag{4.36a-h}$$

where k_s is a shear correction factor introduced to account for the non-uniformity of the shear strain components ε_{xz} and ε_{yz} over the plate thickness (e.g., Wang et al., 2001; Liu and Soh, 2007).

From Eqs. (4.4), (4.12) and (4.19), the couple stress resultants through the plate thickness can be expressed in terms of u, v, w, ϕ_x and ϕ_y as

$$Y_{xx} = \mu l^2 h (w_{,xy} + \phi_{y,x}),$$

$$Y_{xy} = \frac{1}{2} \mu l^2 h (-w_{,xx} + w_{,yy} - \phi_{x,x} + \phi_{y,y}),$$

$$Y_{xz} = \frac{1}{2} \mu l^2 h (-u_{,xy} + v_{,xx}),$$

$$Y_{yy} = -\mu l^2 h (w_{,xy} + \phi_{x,y}),$$

$$Y_{yz} = \frac{1}{2} \mu l^2 h (-u_{,yy} + v_{,xy}),$$

$$Y_{zz} = \mu l^2 h (\phi_{x,y} - \phi_{y,x}),$$

$$H_{xz} = \frac{1}{24}\mu l^2 h^3 (\phi_{x,xy} - \phi_{y,xx}),$$

$$H_{yz} = \frac{1}{24}\mu l^2 h^3 (\phi_{x,yy} - \phi_{y,xy}). \tag{4.37a-h}$$

Also, from Eqs. (4.1a-c) and (4.9a,b), it follows that the surface stress components can be expressed in terms of u, v, w, ϕ_x and ϕ_y as

$$\tau_{xx}^{\pm} = \tau_0 + (\lambda_0 + 2\mu_0)(u_{,x} \mp \frac{h}{2}\phi_{x,x}) + (\lambda_0 + \tau_0)(v_{,y} \mp \frac{h}{2}\phi_{y,y}),$$

$$\tau_{xy}^{\pm} = \mu_0(u_{,y} + v_{,x}) - \tau_0 v_{,x} \mp \frac{1}{2}h\left(\mu_0\phi_{x,y} + \mu_0\phi_{y,x} - \tau_0\phi_{y,x}\right),$$

$$\tau_{yx}^{\pm} = \mu_0(u_{,y} + v_{,x}) - \tau_0 u_{,y} \mp \frac{1}{2}h\left(\mu_0\phi_{x,y} - \tau_0\phi_{x,y} + \mu_0\phi_{y,x}\right),$$

$$\tau_{yy}^{\pm} = \tau_0 + (\lambda_0 + \tau_0)(u_{,x} \mp \frac{h}{2}\phi_{x,x}) + (\lambda_0 + 2\mu_0)(v_{,y} \mp \frac{h}{2}\phi_{y,y}),$$

$$\tau_{3x}^{+} = \tau_{3x}^{-} = \tau_0 w_{,x},$$

$$\tau_{3y}^{+} = \tau_{3y}^{-} = \tau_0 w_{,y}. \tag{4.38a-f}$$

The equations of motion of the Mindlin plate in terms of the five kinematic variables u, v, w, ϕ_x and ϕ_y can then be obtained by using Eqs. (4.36a-h), (4.37a-h) and (4.38a-f) in Eqs. (4.27a-e) as

$$\begin{gathered}(\lambda + 2\mu)hu_{,xx} + \mu hu_{,yy} + (\lambda + \mu)hv_{,xy} + \frac{1}{4}\mu l^2 h(-u_{,xxyy} - u_{,yyyy} + v_{,xxxy} + v_{,xyyy}) \\ + 2(2\mu_0 + \lambda_0)u_{,xx} + (2\mu_0 - \tau_0)u_{,yy} + (2\mu_0 + 2\lambda_0 + \tau_0)v_{,xy} + f_x + \frac{1}{2}c_{z,y} = m_0\ddot{u},\end{gathered} \tag{4.39a}$$

$$\begin{gathered}(\lambda + \mu)hu_{,xy} + \mu hv_{,xx} + (\lambda + 2\mu)hv_{,yy} + \frac{1}{4}\mu l^2 h(u_{,xxxy} + u_{,xyyy} - v_{,xxxx} - v_{,xxyy}) \\ + (2\mu_0 + 2\lambda_0 + \tau_0)u_{,xy} + (2\mu_0 - \tau_0)v_{,xx} + 2(2\mu_0 + \lambda_0)v_{,yy} + f_y - \frac{1}{2}c_{z,x} = m_0\ddot{v},\end{gathered} \tag{4.39b}$$

$$
\begin{aligned}
&k_s \mu h(w_{,xx} + w_{,yy} - \phi_{x,x} - \phi_{y,y}) - \frac{1}{4}\mu l^2 h(w_{,xxxx} + 2w_{,xxyy} + w_{,yyyy} + \phi_{x,xxx} + \phi_{x,xyy} + \phi_{y,xxy} + \phi_{y,yyy}) \\
&\quad + 2\tau_0(w_{,xx} + w_{,yy}) - k_w w + k_p(w_{,xx} + w_{,yy}) + f_z - \frac{1}{2}c_{x,y} + \frac{1}{2}c_{y,x} = m_0 \ddot{w},
\end{aligned} \tag{4.39c}
$$

$$
\begin{aligned}
&-\frac{1}{12}(\lambda + 2\mu)h^3\phi_{x,xx} - \frac{1}{12}\mu h^3 \phi_{x,yy} - \frac{1}{12}(\lambda + \mu)h^3\phi_{y,xy} - k_s \mu h(w_{,x} - \phi_x) - \frac{1}{48}\mu l^2 h^3(-\phi_{x,xxyy} \\
&\quad - \phi_{x,yyyy} + \phi_{y,xxxy} + \phi_{y,xyyy}) + \frac{1}{4}\mu l^2 h(-w_{,xxx} - w_{,xyy} - \phi_{x,xx} - 4\phi_{x,yy} + 3\phi_{y,xy}) \\
&\quad - \frac{1}{4}h^2\left[2(\lambda_0 + 2\mu_0)\phi_{x,xx} + (2\mu_0 - \tau_0)\phi_{x,yy} + (2\lambda_0 + 2\mu_0 + \tau_0)\phi_{y,xy}\right] + \frac{1}{2}c_y = -m_2\ddot{\phi}_x,
\end{aligned} \tag{4.39d}
$$

$$
\begin{aligned}
&-\frac{1}{12}(\lambda + \mu)h^3\phi_{x,xy} - \frac{1}{12}\mu h^3 \phi_{y,xx} - \frac{1}{12}(\lambda + 2\mu)h^3\phi_{y,yy} - k_s \mu h(w_{,y} - \phi_y) - \frac{1}{48}\mu l^2 h^3(\phi_{x,xxxy} \\
&\quad + \phi_{x,xyyy} - \phi_{y,xxxx} - \phi_{y,xxyy}) + \frac{1}{4}\mu l^2 h(-w_{,xxy} - w_{,yyy} + 3\phi_{x,xy} - 4\phi_{y,xx} - \phi_{y,yy}) \\
&\quad - \frac{1}{4}h^2\left[(2\lambda_0 + 2\mu_0 + \tau_0)\phi_{x,xy} + (2\mu_0 - \tau_0)\phi_{y,xx} + 2(\lambda_0 + 2\mu_0)\phi_{y,yy}\right] - \frac{1}{2}c_x = -m_2\ddot{\phi}_y
\end{aligned} \tag{4.39e}
$$

for any $(x, y) \in R$ and $t \in (0,\ T)$.

The differential equations in Eqs. (4.39a–e), the boundary conditions in Eqs. (4.35a–h) (along with Eqs. (4.34a-h), (4.29) and (4.30a,b)), and the given initial conditions at $t = 0$ and $t = T$ define the boundary-initial value problem for determining u, v, w, ϕ_x and ϕ_y. It is seen from Eqs. (4.39a-e) that the in-plane displacements u and v are uncoupled with the out-of-plane displacement w and the rotations ϕ_x and ϕ_y. Therefore, u and v can be obtained separately from solving Eqs. (4.39a,b) subject to prescribed boundary conditions of the form in Eqs. (4.35a,b,g) and suitable initial conditions.

When $k_w = k_p = 0$, Eqs. (4.39a-e) will reduce to the governing equations for the Mindlin plate without the foundation (but incorporating the microstructure and surface energy effects).

When $l = 0$ and $c_i = 0$, Eqs. (4.39a-e) will become the governing equations for the Mindlin plate in the absence of the microstructure (or couple stress) effect (but including the surface energy and foundation effects).

When $\lambda_0 = \mu_0 = \tau_0 = 0$, Eqs. (4.39a-e) will degenerate to the governing equations for the Mindlin plate without considering the surface energy effect (but accounting for the microstructure and foundation effects).

When $l = 0$, $c_i = 0$ and $\lambda_0 = \mu_0 = \tau_0 = 0$, Eqs. (4.39a-e) will be simplified as the classical elasticity-based governing equations for the Mindlin plate resting on the two-parameter Winkler-Pasternak elastic foundation.

When $k_w = k_p = 0$ and $\lambda_0 = \mu_0 = \tau_0 = 0$, Eqs. (4.39a-e) become

$$(\lambda+2\mu)hu_{,xx}+\mu hu_{,yy}+(\lambda+\mu)hv_{,xy}+\frac{1}{4}\mu l^2h(-u_{,xxyy}-u_{,yyyy}+v_{,xxxy}+v_{,xyyy})+f_x+\frac{1}{2}c_{z,y}=m_0\ddot{u},$$

(4.40a)

$$(\lambda+\mu)hu_{,xy}+\mu hv_{,xx}+(\lambda+2\mu)hv_{,yy}+\frac{1}{4}\mu l^2h(u_{,xxxy}+u_{,xyyy}-v_{,xxxx}-v_{,xxyy})+f_y-\frac{1}{2}c_{z,x}=m_0\ddot{v},$$

(4.40b)

$$\begin{aligned}&k_s\mu h(w_{,xx}+w_{,yy}-\phi_{x,x}-\phi_{y,y})-\frac{1}{4}\mu l^2h(w_{,xxxx}+2w_{,xxyy}+w_{,yyyy}+\phi_{x,xxx}+\phi_{x,xyy}+\phi_{y,xxy}+\phi_{y,yyy})\\&\quad+f_z-\frac{1}{2}c_{x,y}+\frac{1}{2}c_{y,x}=m_0\ddot{w},\end{aligned}$$

(4.40c)

$$\begin{aligned}&-\frac{1}{12}(\lambda+2\mu)h^3\phi_{x,xx}-\frac{1}{12}\mu h^3\phi_{x,yy}-\frac{1}{12}(\lambda+\mu)h^3\phi_{y,xy}-k_s\mu h(w_{,x}-\phi_x)-\frac{1}{48}\mu l^2h^3(-\phi_{x,xxyy}\\&\quad-\phi_{x,yyyy}+\phi_{y,xxxy}+\phi_{y,xyyy})+\frac{1}{4}\mu l^2h(-w_{,xxx}-w_{,xyy}-\phi_{x,xx}-4\phi_{x,yy}+3\phi_{y,xy})+\frac{1}{2}c_y=-m_2\ddot{\phi}_x,\end{aligned}$$

(4.40d)

$$-\frac{1}{12}(\lambda+\mu)h^3\phi_{x,xy}-\frac{1}{12}\mu h^3\phi_{y,xx}-\frac{1}{12}(\lambda+2\mu)h^3\phi_{y,yy}-k_s\mu h(w_{,y}-\phi_y)-\frac{1}{48}\mu l^2h^3(\phi_{x,xxxy}$$
$$+\phi_{x,xyyy}-\phi_{y,xxxx}-\phi_{y,xxyy})+\frac{1}{4}\mu l^2h(-w_{,xxy}-w_{,yyy}+3\phi_{x,xy}-4\phi_{y,xx}-\phi_{y,yy})-\frac{1}{2}c_x=-m_2\ddot{\phi}_y,$$

(4.40e)

which are the governing equations for the Mindlin plate incorporating the microstructure effect alone. These equations are identical to those derived in Ma et al. (2011) using the same modified couple stress theory. By setting $l = 0$ and $c_i = 0$, Eqs. (4.40a-e) will be further reduced to the governing equations for the Mindlin plate based on classical elasticity, as shown in Ma et al. (2011).

When $\phi_x = \partial w/\partial x$ and $\phi_y = \partial w/\partial y$, Eqs. (4.39a-e) are simplified as

$$(\lambda+2\mu)hu_{,xx}+\mu hu_{,yy}+(\lambda+\mu)hv_{,xy}+\frac{1}{4}\mu l^2h(-u_{,xxyy}-u_{,yyyy}+v_{,xxxy}+v_{,xyyy})$$
$$+2(2\mu_0+\lambda_0)u_{,xx}+(2\mu_0-\tau_0)u_{,yy}+(2\mu_0+2\lambda_0+\tau_0)v_{,xy}+f_x+\frac{1}{2}c_{z,y}=m_0\ddot{u}, \tag{4.41a}$$

$$(\lambda+\mu)hu_{,xy}+\mu hv_{,xx}+(\lambda+2\mu)hv_{,yy}+\frac{1}{4}\mu l^2h(u_{,xxxy}+u_{,xyyy}-v_{,xxxx}-v_{,xxyy})$$
$$+(2\mu_0+2\lambda_0+\tau_0)u_{,xy}+(2\mu_0-\tau_0)v_{,xx}+2(2\mu_0+\lambda_0)v_{,yy}+f_y-\frac{1}{2}c_{z,x}=m_0\ddot{v}, \tag{4.41b}$$

$$-\left[\frac{1}{12}(\lambda+2\mu)h^3+\mu l^2h+\frac{1}{2}(\lambda_0+2\mu_0)h^2\right](w_{,xxxx}+2w_{,xxyy}+w_{,yyyy})$$
$$+\left(2\tau_0+k_p\right)(w_{,xx}+w_{,yy})-k_ww+f_z-c_{x,y}+c_{y,x}=m_0\ddot{w}-m_2\frac{\partial^2\ddot{w}}{\partial x^2}-m_2\frac{\partial^2\ddot{w}}{\partial y^2}, \tag{4.41c}$$

which are the same as the governing equations first derived in Gao and Zhang (2016) for the non-classical Kirchhoff plate model incorporating microstructure, surface energy and foundation effects and involving three independent kinematic variables *u*, *v* and *w*. That is, the newly developed Mindlin plate model reduces to the non-classical Kirchhoff plate model when the normality assumption is reinstated.

When $v = 0$, $\phi_y = 0$, $u = u(x, t)$, $w = w(x, t)$, $\phi_x = \phi_x(x, t)$, $f_y = 0$, $c_x = 0$ and $c_z = 0$, the Mindlin plate considered here becomes a Timoshenko beam. For this case, Eqs. (4.39a-e) reduce to, by setting $k_w = k_p = 0$ and $\lambda_0 = \mu_0 = \tau_0 = 0$ additionally,

$$(\lambda + 2\mu)hu_{,xx} + f_x = m_0\ddot{u}, \tag{4.42a}$$

$$k_s\mu h(w_{,xx} - \phi_{x,x}) - \frac{1}{4}\mu l^2 h(w_{,xxxx} + \phi_{x,xxx}) + f_z + \frac{1}{2}c_{y,x} = m_0\ddot{w}, \tag{4.42b}$$

$$\frac{1}{12}(\lambda + 2\mu)h^3\phi_{x,xx} + k_s\mu h(w_{,x} - \phi_x) + \frac{1}{4}\mu l^2 h(w_{,xxx} + \phi_{x,xx}) - \frac{1}{2}c_y = m_2\ddot{\phi}_x, \tag{4.42c}$$

which are identical to the equations of motion for a Timoshenko beam with a unit width and a height h derived in Ma et al. (2008). That is, the current Mindlin plate model recovers the non-classical Timoshenko beam model based on the same modified couple stress theory as a special case.

4.3 Examples

To further demonstrate the new non-classical Mindlin plate model developed in Section 4.2, the static bending and free vibration problems of a simply supported rectangular plate (see Fig 4.4) are analytically solved in this section by directly applying the general forms of the governing equations and boundary conditions of the new model.

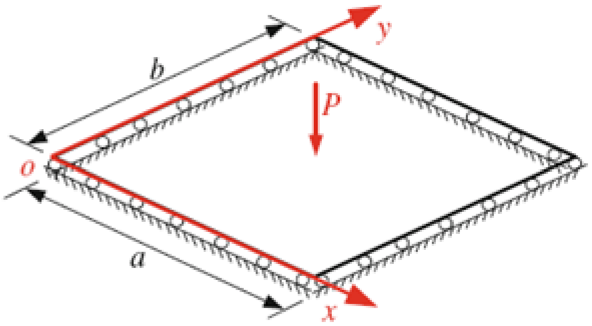

Fig. 4.4 Simply supported plate

In view of the general form of the boundary conditions (BCs) in Eqs. (4.35a–h), the BCs for this simply supported plate can be identified as

$$u_n = 0,\ \ w = 0,\ \ \phi_s = 0,\ \ \widehat{N}_{ss} = 0,\ \ \widehat{M}_n = 0,\ \ \hat{T}_z = 0,\ \ \hat{T}_s = 0,\ \ \hat{Z}_s = 0 \tag{4.43}$$

for all (x, y) on the boundaries $x = 0$, a and $y = 0$, b. Also, the following applied traction resultants vanish on these boundaries:

$$\bar{s}_n = \bar{s}_s = \bar{s}_z = 0,\ \ \overline{M}_n = 0,\ \ \bar{t}_s = 0. \tag{4.44}$$

For the boundaries $x = 0$ and $x = a$, $n_y = 0$ and $n_x = -1$ (on $x = 0$) or $n_x = 1$ (on $x = a$), and Eq. (4.43) becomes, with the help of Eqs. (4.29), (4.30a), (4.34b,d,f,g,h) and (4.44),

$$\begin{aligned}
&u(0,y) = u(a,y) = 0,\\
&w(0,y) = w(a,y) = 0,\\
&\phi_y(0,y) = \phi_y(a,y) = 0,\\
&N_{xy} - \frac{1}{2}Y_{xz,x} - \frac{1}{2}Y_{yz,y} + \frac{1}{2}(\tau_{xy}^{+} + \tau_{xy}^{-} + \tau_{yx}^{+} + \tau_{yx}^{-}) - \frac{1}{2}c_z = 0 \text{ on } x = 0 \text{ and } x = a,\\
&2M_{xx} + Y_{xy} + H_{xz,y} + h(\tau_{xx}^{+} - \tau_{xx}^{-}) = 0 \text{ on } x = 0 \text{ and } x = a,\\
&Y_{xy} = 0 \text{ on } x = 0 \text{ and } x = a,\\
&Y_{xz} = 0 \text{ on } x = 0 \text{ and } x = a,\\
&H_{xz} = 0 \text{ on } x = 0 \text{ and } x = a.
\end{aligned} \tag{4.45a-h}$$

Using Eqs. (4.36b,f), (4.37b,c,e,g) and (4.38a-c) in Eqs. (4.45d-h) yields

$$\begin{aligned}
&h\mu(u_{,y} + v_{,x}) - \frac{1}{4}\mu l^2 h(-u_{,xxy} - u_{,yyy} + v_{,xxx} + v_{,xyy}) + (2\mu_0 - \tau_0)(u_{,y} + v_{,x}) - \frac{1}{2}c_z = 0,\\
&\frac{h^3}{6}\left[(\lambda + 2\mu)\phi_{x,x} + \lambda\phi_{y,y}\right] - \frac{1}{24}\mu l^2 h^3(\phi_{x,xyy} - \phi_{y,xxy}) - \frac{1}{2}\mu l^2 h(-w_{,xx} + w_{,yy}\\
&-\phi_{x,x} + \phi_{y,y}) + h^2\left[(\lambda_0 + 2\mu_0)\phi_{x,x} + (\lambda_0 + \tau_0)\phi_{y,y}\right] = 0,\\
&w_{,xx} - w_{,yy} + \phi_{x,x} - \phi_{y,y} = 0,\\
&u_{,xy} - v_{,xx} = 0,\\
&\phi_{x,xy} - \phi_{y,xx} = 0,
\end{aligned} \tag{4.46a-e}$$

on $x = 0$ and $x = a$.

For the boundaries $y = 0$ and $y = b$, $n_x = 0$ and $n_y = -1$ (on $y = 0$) or $n_y = 1$ (on $y = b$), and Eq. (4.43) becomes, with the help of Eqs. (4.29), (4.30a), (4.34b,d,f,g,h) and (4.44),

$$\begin{aligned}
&v(x,0) = v(x,b) = 0,\\
&w(x,0) = w(x,b) = 0,\\
&\phi_x(x,0) = \phi_x(x,b) = 0,\\
&N_{yx} + \frac{1}{2}Y_{xz,x} + \frac{1}{2}Y_{yz,y} + \frac{1}{2}(\tau_{xy}^{+} + \tau_{xy}^{-} + \tau_{yx}^{+} + \tau_{yx}^{-}) + \frac{1}{2}c_z = 0 \text{ on } y = 0 \text{ and } y = b,\\
&2M_{yy} - Y_{yx} - H_{yz,x} + h(\tau_{yy}^{+} - \tau_{yy}^{-}) = 0 \text{ on } y = 0 \text{ and } y = b,\\
&Y_{yx} = 0 \text{ on } y = 0 \text{ and } y = b,\\
&Y_{yz} = 0 \text{ on } y = 0 \text{ and } y = b,\\
&H_{yz} = 0 \text{ on } y = 0 \text{ and } y = b.
\end{aligned} \tag{4.47a-h}$$

Using Eqs. (4.36b, h), (4.37b,c,e,h) and (4.38b-d) in Eqs. (4.47d-h) gives

$$\begin{aligned}
&\mu h(u_{,y} + v_{,x}) + \frac{1}{4}\mu l^2 h(-u_{,xxy} - u_{,yyy} + v_{,xxx} + v_{,xyy}) + (2\mu_0 - \tau_0)(u_{,y} + v_{,x}) + \frac{1}{2}c_z = 0,\\
&\frac{1}{6}h^3\left[\lambda\phi_{x,x} + (\lambda + 2\mu)\phi_{y,y}\right] + \frac{1}{24}\mu l^2 h^3(\phi_{x,xyy} - \phi_{y,xxy}) + \frac{1}{2}\mu l^2 h(-w_{,xx} + w_{,yy} - \phi_{x,x} + \phi_{y,y})\\
&\qquad + h^2\left[(\lambda_0 + \tau_0)\phi_{x,x} + (\lambda_0 + 2\mu_0)\phi_{y,y}\right] = 0,\\
&w_{,xx} - w_{,yy} + \phi_{x,x} - \phi_{y,y} = 0,\\
&u_{,yy} - v_{,xy} = 0,\\
&\phi_{x,yy} - \phi_{y,xy} = 0,
\end{aligned} \tag{4.48a-e}$$

on $y = 0$ and $y = b$.

4.3.1 Static bending

For static bending problems, u, v, w, ϕ_x and ϕ_y are independent of time t so that all of the time derivatives involved in Eqs. (4.39a–e) vanish.

The boundary value problem (BVP) for the static bending of the simply supported plate shown in Fig 4.4 is defined by the governing equations in Eqs. (4.39a–e) and the boundary conditions in Eqs. (4.45a-c), (4.46a-e), (4.47a-c) and (4.48a-e), with $u = u(x, y)$, $v = v(x, y)$, $w = w(x, y)$ $\phi_x = \phi_x(x, y)$ and $\phi_y = \phi_y(x, y)$.

As mentioned in Section 4.2, the in-plane displacements u and v are uncoupled with w, ϕ_x and ϕ_y. Therefore, u and v can be obtained from solving the BVP defined by Eqs. (4.39a,b), (4.45a), (4.46a,d), (4.47a) and (4.48a,d). For the current case with $f_x = f_y = 0$ and $c_z = 0$, the solution of this BVP gives $u = v = 0$ for any $(x, y) \in R$.

The out-of-plane displacement w and rotations ϕ_x and ϕ_y can be obtained from solving the BVP defined by Eqs. (4.39c-e), (4.45b,c), (4.46b,c,e), (4.47b,c) and (4.48b,c,e), as shown next.

Consider the following Fourier series solutions for w, ϕ_x and ϕ_y:

$$\begin{aligned} w &= \sum_{m=1}^{\infty}\sum_{n=1}^{\infty} W_{mn} \sin(\frac{m\pi x}{a})\sin(\frac{n\pi y}{b}), \\ \phi_x &= \sum_{m=1}^{\infty}\sum_{n=1}^{\infty} \Phi^x_{mn} \cos(\frac{m\pi x}{a})\sin(\frac{n\pi y}{b}), \\ \phi_y &= \sum_{m=1}^{\infty}\sum_{n=1}^{\infty} \Phi^y_{mn} \sin(\frac{m\pi x}{a})\cos(\frac{n\pi y}{b}), \end{aligned} \tag{4.49}$$

where W_{mn}, Φ^x_{mn} and Φ^y_{mn} are the Fourier coefficients to be determined for each pair of m and n. It can be readily shown that w, ϕ_x and ϕ_y in Eq. (4.49) satisfy the boundary conditions in Eqs. (4.45b,c), (4.46b,c,e) at $x = 0$, a and in Eqs. (4.47b,c), (4.48b,c,e) at $y = 0$, b for any W_{mn}, Φ^x_{mn} and Φ^y_{mn}.

The resultant force $f_z(x, y)$ can also be expanded as a Fourier series:

$$f_z(x, y) = \sum_{m=1}^{\infty}\sum_{n=1}^{\infty} Q_{mn} \sin(\frac{m\pi x}{a})\sin(\frac{n\pi y}{b}), \tag{4.50}$$

where the Fourier coefficient Q_{mn} is given by

$$Q_{mn} = \frac{4}{ab}\int_0^a \int_0^b f_z(x,y)\sin(\frac{m\pi x}{a})\sin(\frac{n\pi y}{b})\mathrm{d}x\mathrm{d}y. \tag{4.51}$$

In the current case (see Fig 4.4), $f_z(x,y) = P\delta(x-\frac{a}{2})\delta(y-\frac{b}{2}),$ where $\delta(\cdot)$ is the Dirac delta function. Using this f_z in Eq. (4.51) yields

$$Q_{mn} = \frac{4P}{ab}\sin(\frac{m\pi}{2})\sin(\frac{n\pi}{2}). \tag{4.52}$$

Substituting Eqs. (4.49) and (4.50) into Eq. (4.39c-e) results in, with $c_x = c_y = 0,$

$$[C][W_{mn}, \Phi_{mn}^x, \Phi_{mn}^y]^T = [-Q_{mn}, 0, 0]^T, \tag{4.53}$$

where $[C]$ is a 3-by-3 matrix whose components are

$$\begin{aligned}
C_{11} &= -(k_s\mu h + 2\tau_0 + k_p)(\frac{m^2\pi^2}{a^2} + \frac{n^2\pi^2}{b^2}) - \frac{\mu l^2 h}{4}(\frac{m^2\pi^2}{a^2} + \frac{n^2\pi^2}{b^2})^2 - k_w,\\
C_{12} &= k_s\mu h\frac{m\pi}{a} - \frac{\mu l^2 h}{4}(\frac{m^3\pi^3}{a^3} + \frac{mn^2\pi^3}{ab^2}),\\
C_{13} &= k_s\mu h\frac{n\pi}{b} - \frac{\mu l^2 h}{4}(\frac{m^2 n\pi^3}{a^2 b} + \frac{n^3\pi^3}{b^3}),\\
C_{22} &= k_s\mu h + \frac{(\lambda+2\mu)h^3}{12}\frac{m^2\pi^2}{a^2} + \frac{\mu h^3}{12}\frac{n^2\pi^2}{b^2} + \frac{\mu l^2 h^3}{48}(\frac{m^2 n^2\pi^4}{a^2 b^2} + \frac{n^4\pi^4}{b^4})\\
&\quad + \frac{\mu l^2 h}{4}(\frac{m^2\pi^2}{a^2} + \frac{4n^2\pi^2}{b^2}) + \frac{(2\mu_0+\lambda_0)h^2}{2}\frac{m^2\pi^2}{a^2} + \frac{(2\mu_0-\tau_0)h^2}{4}\frac{n^2\pi^2}{b^2},\\
C_{23} &= \frac{(\lambda+\mu)h^3}{12}\frac{mn\pi^2}{ab} - \frac{\mu l^2 h^3}{48}(\frac{m^3 n\pi^4}{a^3 b} + \frac{mn^3\pi^4}{ab^3}) - \frac{3\mu l^2 h}{4}\frac{mn\pi^2}{ab}\\
&\quad + \frac{(2\mu_0+2\lambda_0+\tau_0)h^2}{4}\frac{mn\pi^2}{ab},\\
C_{33} &= k_s\mu h + \frac{(\lambda+2\mu)h^3}{12}\frac{n^2\pi^2}{b^2} + \frac{\mu h^3}{12}\frac{m^2\pi^2}{a^2} + \frac{\mu l^2 h^3}{48}(\frac{m^2 n^2\pi^4}{a^2 b^2} + \frac{m^4\pi^4}{a^4})\\
&\quad + \frac{\mu l^2 h}{4}(\frac{4m^2\pi^2}{a^2} + \frac{n^2\pi^2}{b^2}) + \frac{(2\mu_0+\lambda_0)h^2}{2}\frac{n^2\pi^2}{b^2} + \frac{(2\mu_0-\tau_0)h^2}{4}\frac{m^2\pi^2}{a^2},\\
C_{21} &= -C_{12},\ C_{31} = -C_{13},\ C_{32} = C_{23}.
\end{aligned} \tag{4.54}$$

Solving the linear algebraic equation system in Eq. (4.53) will yield W_{mn}, Φ_{mn}^{x} and Φ_{mn}^{y}. Then, substituting them into Eq. (4.49) will give the exact solutions w, ϕ_x and ϕ_y based on the current non-classical Mindlin plate model for the simply supported plate subjected to the concentrated force at the center of the plate (see Fig 4.4).

Figures 4.5 and 4.6 display, respectively, the variations of the plate deflection w and the rotation ϕ_x along the line $y = b/2$ predicted by the newly developed Mindlin plate model (with or without the Winkler-Pasternak foundation) and by the classical Mindlin plate model. The numerical results for the plate with the Winkler-Pasternak foundation (solid lines) are directly obtained from Eqs. (4.49) and (4.52)-(4.54), while those for the plate without the foundation (dash lines) are computed using the same equations but with $k_w = k_p = 0$. The values for the classical Mindlin plate (dot lines) are determined from Eqs. (4.49) and (4.52)-(4.54) by setting $l = 0$, $\lambda_0 = \mu_0 = \tau_0 = 0$, and $k_w = k_p = 0$.

For illustration purposes, in the numerical analysis presented herein, the plate material is taken to be aluminum with the following properties (Liu and Rajapakse, 2010; Gao and Mahmoud, 2014): E = 90 GPa, v = 0.23, l = 6.58 μm for the bulk properties, and $\mu_0 = -5.4251$ N/m, λ_0 = 3.4939 N/m, τ_0 = 0.5689 N/m for the surface layers, where Young's modulus E and Poisson's ratio v are related to the Lamé constants λ and μ by (e.g., Timoshenko and Goodier, 1970):

$$E = \frac{\mu(3\lambda + 2\mu)}{\lambda + \mu}, \quad v = \frac{\lambda}{2(\lambda + \mu)}. \tag{4.55}$$

The shear correction factor k_s is taken to be 0.8 (e.g., Wang et al., 2001; Liu and Soh, 2007; Ma et al., 2011). In addition, the shape of the plate is fixed by letting $a = b = 20h$, while the plate thickness h is varying.

In Figs 4.5 and 4.6, the foundation moduli are non-dimensionalized and taken to be $\bar{K}_w = 100, \bar{K}_p = 10$, where $\bar{K}_w \equiv k_w a^4 / D, \bar{K}_p \equiv k_p a^2 / D$, with $D = Eh^3 / [12(1-\nu^2)]$ being the plate flexural rigidity. The number of terms included in Eq. (4.49) is controlled by adjusting m and n. The numerical results for w, ϕ_x and ϕ_y obtained with $m = 30$ and $n = 30$ are found to be the same as those computed with larger m and n values (up to $m = 60$, $n = 60$) to the third decimal place. This indicates that using $m = 30$, $n = 30$ in the expansions is sufficient for the convergent numerical solutions of w and ϕ_x displayed in Figs 4.5 and 4.6. Note that the values of ϕ_y along the line $x = a/2$ are the same as those of ϕ_x along the line $y = b/2$ due to the loading and geometrical symmetry of the square plate under consideration. Hence, ϕ_y is not plotted here.

From Figs 4.5 and 4.6, it is clearly seen that both the deflection w and the rotation ϕ_x predicted by the current Mindlin plate model with or without the foundation are always smaller than those predicted by the classical model in all cases considered. It is also observed that the differences between the values predicted by the new model (with or without the foundation) and those by the classical model are very large when the plate thickness h is small (with $h = l = 6.58$ μm here), but the differences are diminishing when h becomes large (with $h = 5l = 32.9$ μm here). This predicted size effect agrees with the general trend observed experimentally (e.g., McFarland and Colton, 2005). In addition, it is observed from Figs 4.5 and 4.6 that the presence of the elastic foundation does reduce the plate deflection and rotation, as expected. The foundation effect on the deflection of the simply supported plate (see Fig 4.4) is further shown in Fig 4.7, where more cases with different values of k_w and k_p, including the case without the foundation (as the top curve with $k_w = k_p = 0$) and the case with the Winkler foundation (as the red dash curve with $k_p = 0$), are compared. Note that the values of the other parameters remain the same as those used in obtaining the numerical results shown in Fig 4.5.

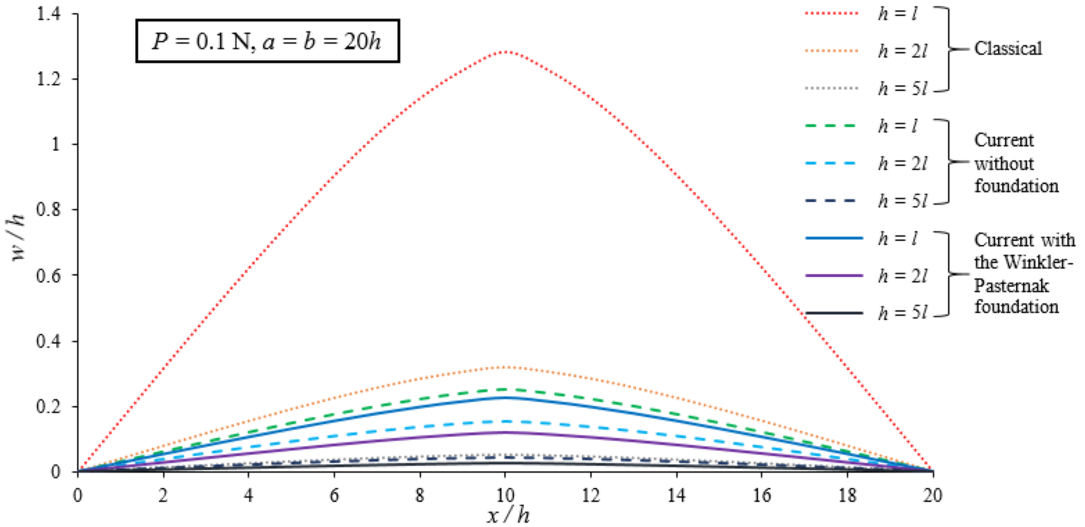

Fig. 4.5 Deflection of the simply supported Mindlin plate on $y = b/2$ with $\bar{K}_w = 100,\ \bar{K}_p = 10$

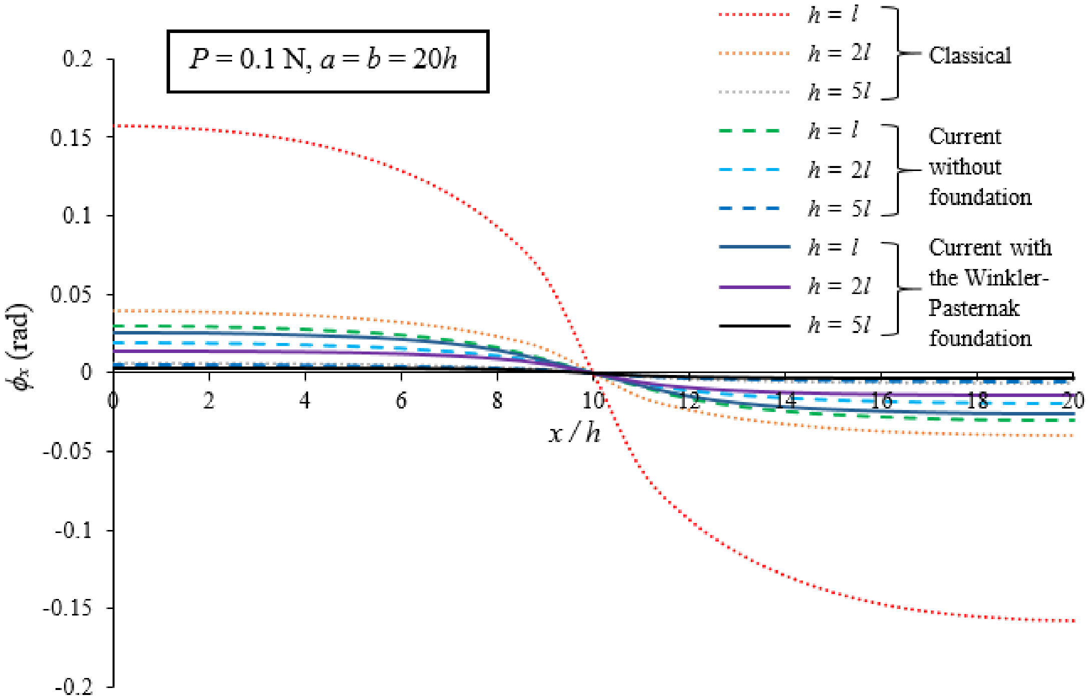

Fig. 4.6 Rotation of the simply supported Mindlin plate on $y = b/2$ with $\bar{K}_w = 100,\ \bar{K}_p = 10$

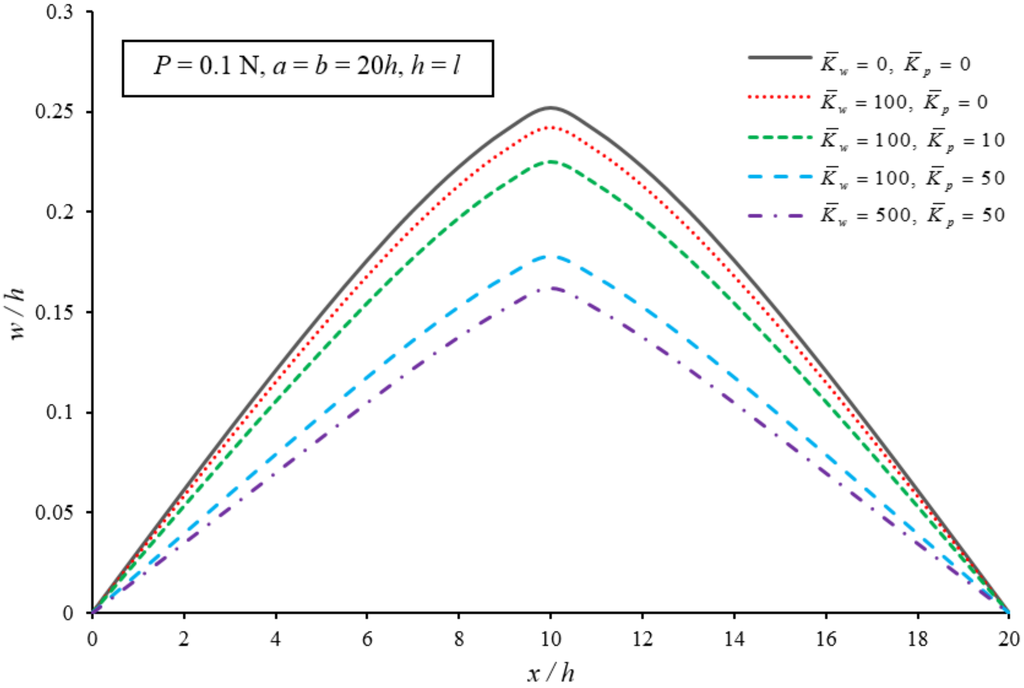

Fig. 4.7 Deflection of the plate with different values of k_w and k_p

Both the microstructure and surface energy effects are included in the numerical results shown in Figs 4.5–4.7. To illustrate the surface energy effect separately, additional numerical results are presented in Fig 4.8 for the deflection of the simply supported plate, which are obtained from Eqs. (4.49) and (4.52)-(4.54) by letting $l = 0$. For comparison purposes, the results predicted by the classical elasticity-based Mindlin plate model are also plotted in Fig 4.8, which are computed using Eqs. (4.49) and (4.52)-(4.54) with $l = 0$ and $\lambda_0 = \mu_0 = \tau_0 = 0$. In addition, the foundation moduli are set to be $k_w = k_p = 0$ to examine only the surface energy effect. Note that the plate material properties used here remain the same as those employed earlier, and the plate shape is kept to be the same by letting $a = b = 20h$ (see Fig 4.4) for all cases (with different values of h).

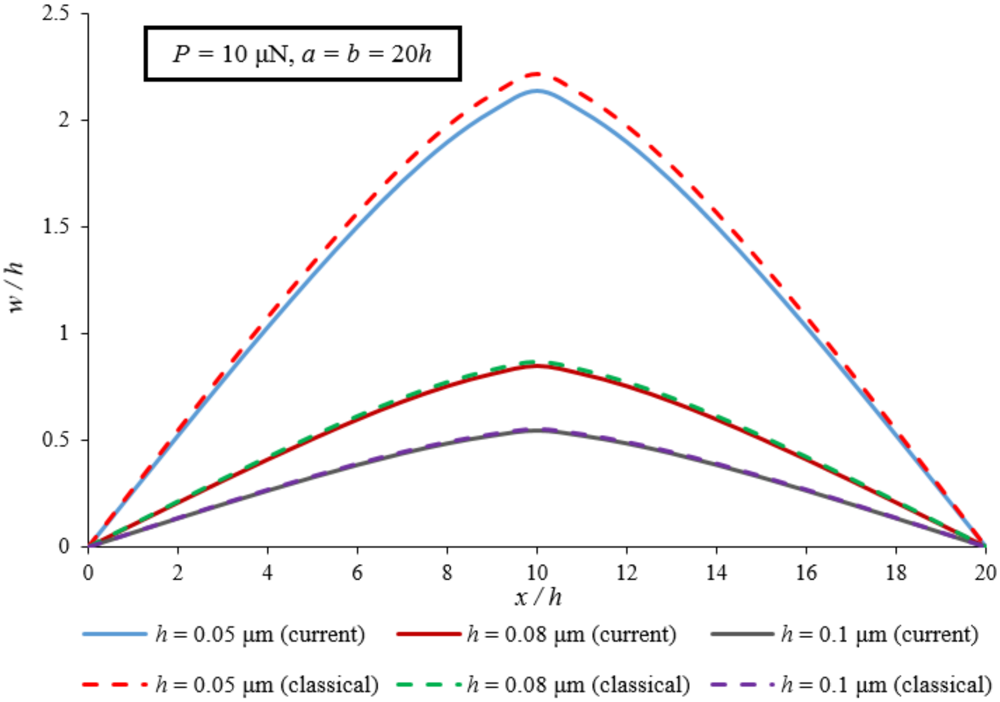

Fig. 4.8 Deflection of the simply supported plate predicted by the new model considering the surface energy effect alone (i.e., with $l = k_w = k_p = 0$) and by the classical model (with $l = k_w = k_p = 0$ and $\lambda_0 = \mu_0 = \tau_0 = 0$)

From Fig 4.8, it is clearly seen that the plate deflection predicted by the current model including the surface energy effect alone is always smaller than those predicted by the classical model in all cases considered here. Figure 4.8 also illustrates that the differences between the two sets of predicted values are significant only when the plate thickness h is very small, but they are diminishing as h increases. This indicates that the surface energy effect is important only when the plate is sufficiently thin.

4.3.2 Free vibration

For free vibration problems, the boundary-initial value problem for the simply supported plate shown in Fig. 4.4 is defined by Eqs. (4.39a-e), (4.45a-c), (4.46a-e), (4.47a-

c) and (4.48a-e), with all external forces vanished (i.e., $f_x = f_y = f_z = 0$ and $c_x = c_y = c_z = 0$).

For the current case with $f_x = f_y = 0$ and $c_z = 0$, Eqs. (4.39a,b), (4.45a), (4.46a,d), (4.47a) and (4.48a,d) give $u = u(x, y, t) = 0$, $v = v(x, y, t) = 0$ for any $(x, y) \in R$ and $t \in [0, T]$.

For w, ϕ_x and ϕ_y, consider the following Fourier series expansions:

$$\begin{aligned} w(x,\ y,\ t) &= \sum_{m=1}^{\infty}\sum_{n=1}^{\infty} W_{mn}^{V} \sin(\frac{m\pi x}{a})\sin(\frac{n\pi y}{b})e^{i\omega_n t}, \\ \phi_x(x,\ y,\ t) &= \sum_{m=1}^{\infty}\sum_{n=1}^{\infty} \Phi_{mn}^{x,V} \cos(\frac{m\pi x}{a})\sin(\frac{n\pi y}{b})e^{i\omega_n t}, \\ \phi_y(x,\ y,\ t) &= \sum_{m=1}^{\infty}\sum_{n=1}^{\infty} \Phi_{mn}^{y,V} \sin(\frac{m\pi x}{a})\cos(\frac{n\pi y}{b})e^{i\omega_n t}, \end{aligned} \tag{4.56}$$

where ω_n is the nth natural frequency of vibration of the plate, W_{mn}^{V}, $\Phi_{mn}^{x,V}$ and $\Phi_{mn}^{y,V}$ are the Fourier coefficients, and i is the imaginary unit satisfying $i^2 = -1$. It can be readily shown that the expressions of w, ϕ_x and ϕ_y in Eq. (4.56) satisfy the boundary conditions in Eqs. (4.45b,c), (4.46b,c,e) at $x = 0$, a and in Eqs. (4.47b,c), (4.48b,c,e) at $y = 0$, b for any $t \in [0, T]$.

Using Eq. (4.56) in Eq. (4.39c-e) gives, with the help of Eq. (4.24),

$$[C]\left[W_{mn}^{V}, \Phi_{mn}^{x,V}, \Phi_{mn}^{y,V}\right]^T + \begin{bmatrix} \rho h\omega_n^2 & 0 & 0 \\ 0 & -\frac{\rho h^3}{12}\omega_n^2 & 0 \\ 0 & 0 & -\frac{\rho h^3}{12}\omega_n^2 \end{bmatrix} \left[W_{mn}^{V}, \Phi_{mn}^{x,V}, \Phi_{mn}^{y,V}\right]^T = [0,\ 0,\ 0]^T, \tag{4.57}$$

where $[C]$ is the 3-by-3 matrix whose components are defined in Eq. (4.54).

Let

$$\begin{aligned}&D_{11}=\frac{1}{h}C_{11},\ D_{12}=\frac{1}{h}C_{12},\ D_{13}=\frac{1}{h}C_{13},\\&D_{21}=-\frac{12}{h^3}C_{21},\ D_{22}=-\frac{12}{h^3}C_{22},\ D_{23}=-\frac{12}{h^3}C_{23},\\&D_{31}=-\frac{12}{h^3}C_{31},\ D_{32}=-\frac{12}{h^3}C_{32},\ D_{33}=-\frac{12}{h^3}C_{33}.\end{aligned}\tag{4.58}$$

Using Eq. (4.58) in Eq. (4.57) yields

$$([D]+\rho\omega_n^2[I])\left[W_{mn}^V,\Phi_{mn}^{x,V},\Phi_{mn}^{y,V}\right]^T=[0,\ 0,\ 0]^T,\tag{4.59}$$

where [*I*] is the 3-by-3 identity matrix. For a non-trivial solution of $W_{mn}^V\neq 0$, $\Phi_{mn}^{x,V}\neq 0$ and $\Phi_{mn}^{y,V}\neq 0$ simultaneously, it is required that the determinant of the coefficient matrix of Eq. (4.59) vanish. That is,

$$\left|\ [D]+\rho\omega_n^2[I]\ \right|=0,\tag{4.60}$$

which can be expanded to obtain

$$(\rho\omega_n^2)^3+I_D(\rho\omega_n^2)^2+II_D(\rho\omega_n^2)+III_D=0,\tag{4.61}$$

where

$$\begin{aligned}&I_D\equiv D_{ii}=D_{11}+D_{22}+D_{33},\\&II_D\equiv\frac{1}{2}(D_{ii}D_{jj}-D_{ij}D_{ji})=D_{11}D_{22}+D_{22}D_{33}+D_{33}D_{11}-D_{12}D_{21}-D_{23}D_{32}-D_{13}D_{31},\\&III_D\equiv\varepsilon_{ijk}D_{i1}D_{j2}D_{k3}=D_{11}D_{22}D_{33}-D_{11}D_{23}D_{32}-D_{12}D_{21}D_{33}+D_{12}D_{23}D_{31}+D_{13}D_{21}D_{32}-D_{13}D_{31}D_{22},\end{aligned}\tag{4.62}$$

are the three invariants of the [*D*] matrix whose components D_{ij} are defined in Eq. (4.58).

Equation (4.61) is a cubic equation in ω_n^2. The smallest (positive) root of Eq. (4.61) gives the *n*th natural frequency, ω_n, for the free vibration of the plate.

With ω_n determined from Eq. (4.61), W_{mn}^V, $\Phi_{mn}^{x,V}$ and $\Phi_{mn}^{y,V}$ (with two being independent) can then be obtained from solving Eq. (4.59), which will then lead to the determination of $w(x, y, t)$, $\phi_x(x,y,t)$ and $\phi_y(x,y,t)$ through Eq. (4.56), and thereby completing the solution.

Figure 4.9 shows the variation of the first natural frequency ω_1, obtained from Eq. (4.61) (with $m = 1$, $n = 1$ in Eq. (4.54)), with the plate thickness, which is predicted by the current Mindlin plate model with the Winkler-Pasternak ($\bar{K}_w = 1000,\ \bar{K}_p = 100$) or Winkler ($\bar{K}_w = 1000,\ k_p = 0$) or no foundation ($k_w = k_p = 0$) and by the classical model (i.e., with $l = 0$, $\lambda_0 = \mu_0 = \tau_0 = 0$, and $k_w = k_p = 0$). The material properties and geometry of the aluminum plate used here are the same as those employed earlier to obtain the numerical results shown in Figs 4.5–4.8. In addition, the density for the aluminum plate is taken to be $\rho = 2.7\times10^3\,\text{kg/m}^3$, which is needed in Eq. (4.61).

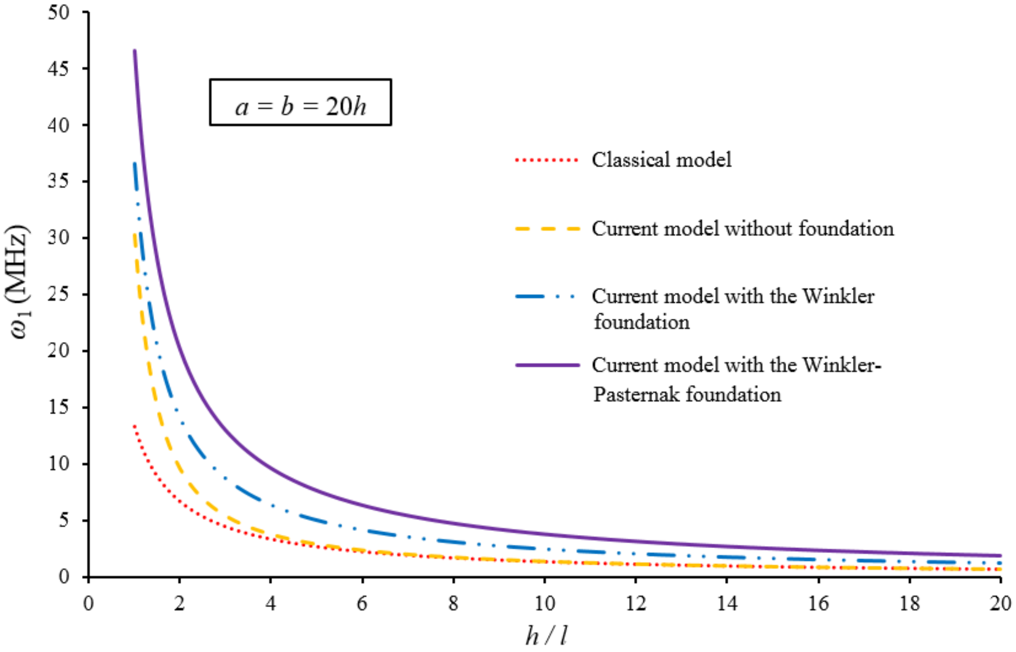

Fig. 4.9 Natural frequency varying with the plate thickness

From Fig. 4.9, it is clearly seen that the natural frequency predicted by the current model with or without the foundation is always higher than that predicted by the classical elasticity-based model. The difference between the predictions by the current model without the foundation and the classical model is significant when the plate thickness h is very small (with $h < 2l = 13.16$ μm here), while the difference is diminishing as h becomes large (with $h > 6l = 39.48$ μm here for the case with $k_w = k_p = 0$). This shows that the size effect on the natural frequency is important only when the plate thickness is very small. In addition, it is observed from Fig 4.9 that the presence of the elastic foundation indeed increases the natural frequency, and this effect can be significant when the plate thickness is small but diminishes as the thickness becomes large. The effect of the foundation on the natural frequency of the simply supported plate (see Fig 4.4) is further illustrated in Fig 4.10, where more cases with different values of k_w and k_p, including the case with the Winkler foundation (as the bottom curve with $k_p = 0$), are compared. Note that the values of the other parameters remain the same as those used in obtaining the numerical results shown in Fig 4.9.

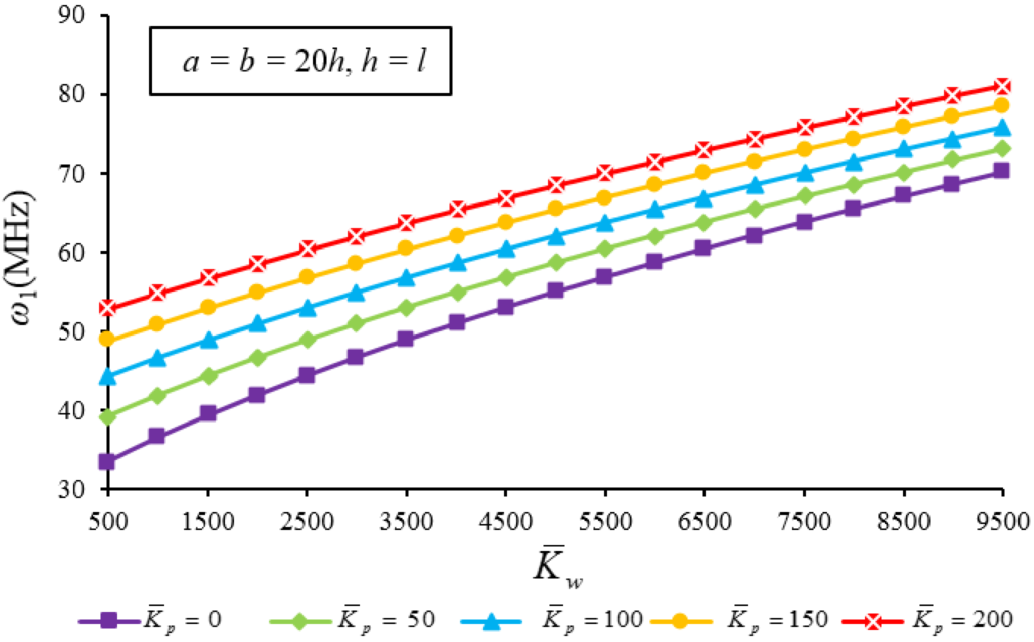

Fig. 4.10 Natural frequency of the plate with different values of k_w and k_p

Clearly, Fig 4.10 shows that the larger the value of k_w or k_p is, the larger the natural frequency ω_1 is, which supports what is observed from Fig 4.9.

4.4 Summary

A new non-classical Mindlin plate model is developed in a most general form by using a modified couple stress theory, a surface elasticity theory and a two-parameter Winkler-Pasternak elastic foundation model and by including all five kinematic variables possible for a Mindlin plate. The equations of motion and the complete boundary conditions are determined simultaneously through a variational formulation based on Hamilton's principle, and the microstructure, surface energy and foundation effects are treated in a unified manner. The inclusion of the additional material constants enables the new model to capture the microstructure- and surface energy-dependent size effects.

It is shown that when the microstructure, surface energy, and foundation effects are all ignored, the new plate model recovers the classical elasticity-based Mindlin plate model as a limiting case. Also, it is seen that the newly developed plate model includes the Mindlin plate models considering the microstructure dependence or the surface energy effect or the foundation effect alone as special cases. In addition, the new Mindlin plate model reduces to the non-classical Kirchhoff plate model incorporating the microstructure, surface energy and foundation effects and degenerates to the Timoshenko beam model including the microstructure effect.

As direct applications of the new Mindlin plate model, the static bending and free vibration problems of a simply supported rectangular plate are analytically solved, with the solutions compared to those based on the classical Mindlin plate theory. The numerical results show that the deflection and rotations predicted by the current Mindlin plate model with or without the elastic foundation are smaller than those predicted by the classical model. Also, it is observed that the difference in the deflection or rotation predicted by the two plate models is very large when the plate thickness is sufficiently small, but it is diminishing with the increase of the plate thickness. In addition, it is found that the natural frequency predicted by the new plate model with or without the Winkler-Pasternak foundation is higher than that predicted by the classical model, and the difference is significant for very thin plates. These predicted size effects at the micron scale agree with the general trends observed in experiments. Finally, the numerical results show quantitatively that the plate deflection is reduced and the plate natural frequency is increased in the presence of the elastic foundation, as expected.

Chapter

5. A NON-CLASSICAL MODEL FOR CIRCULAR MINDLIN PLATES INCORPORATING MICROSTRUCTURE AND SURFACE ENERGY EFFECTS

5.1 Introduction

Thin plates have been widely used in microelectromechanical systems and devices. It has been experimentally observed that these plates exhibit microstructure-dependent size effects at the micron scales (e.g., McFarland and Colton, 2005), which cannot be explained using classical elasticity due to the lack of a material length scale parameter. Hence, efforts have been made to develop non-classical plate models based on higher-order elasticity and surface elasticity theories.

Lazopoulos (2004) provided a non-classical von Karman plate model based on a simplified strain gradient elasticity theory (SSGET) (e.g., Gao and Park, 2007). This SSGET was also employed by Papargyri-Beskou and Beskos (2008) and Papargyri-Beskou et al. (2010) to derive non-classical equations of motion for Kirchhoff plates. By using a constitutive relation in non-local elasticity suggested in Eringen (1983), Lu et al. (2007) proposed a Kirchhoff plate model and a Mindlin plate model without using a variational formulation. Reddy and Berry (2012) studied axisymmetric bending of functionally graded circular plates employing the modified couple stress theory. Recently, three models for

Mindlin plates and third-order shear deformation plates have been developed by Ma et al. (2011), Gao et al. (2013) and Zhou and Gao (2014) using the modified couple stress theory and Hamilton's principle.

The surface elasticity theory (e.g., Gurtin and Murdoch, 1975, 1978; Steigmann and Ogden, 1997, 1999; Altenbach et al., 2010) has also been used to develop non-classical models for thin plates involving surface effects. For example, Lim and He (2004) presented a geometrically nonlinear plate model for nano-scale films based on the Kirchhoff hypothesis and the von Karman strains. Lu et al. (2006) constructed a size-dependent thin plate model by including the normal stress on and inside the surface of the bulk substrate. Wang and Wang (2012) provided a model for non-linear free vibrations of a Kirchhoff plate and a Mindlin plate using the von Karman strains. Liu and Rajapakse (2013) presented a size-dependent continuum model for thin and thick circular plates.

However, very few models have been developed for thin plates by considering both the microstructure and surface energy effects. A non-classical Kirchhoff plate model, which is based on a modified couple stress theory and a surface elasticity theory, was presented in Shaat et al. (2014) without using a variational formulation. Recently, non-classical models for Kirchhoff plates were developed by Zhang et al. (2015) and Gao and Zhang (2016) using a variational formulation, a modified couple stress theory and a surface elasticity theory.

In the Chapter 5, a non-classical model for circular Mindlin plates is provided by using the modified couple stress theory (Yang et al., 2002; Park and Gao, 2008), the surface elasticity theory (Gurtin and Murdoch, 1975, 1978), and the Hamilton's principle. The rest of the Chapter 5 is organized as follows. In Section 5.2, the new non-classical model for a circular Mindlin plate subjected to axisymmetric loading is developed using a variational formulation based on Hamilton's principle. In Section 5.3, the static bending problem of a clamped solid circular plate subjected to a uniform normal load is analytically solved by directly applying the general formulas derived. The chapter concludes in Section 5.4 with a summary.

5.2 Formulation

Consider a flat thin circular plate of inner radius *a*, outer radius *b* and uniform thickness *h*, as shown in Fig 5.1, where the cylindrical coordinate system (r, θ, z) is adopted, with the $r\theta$-plane being coincident with the geometrical mid-plane of the undeformed plate.

According to the Mindlin plate theory, the displacement field in a thin circular plate undergoing axisymmetric deformations can be written as (e.g., Reddy, 2002; Zhou and Gao, 2014)

$$u_r(r,\theta,z,t) = u\ (r,t) - z\phi_r(r,t),\ \ u_\theta(r,\theta,z,t) = 0,\ \ u_z(r,\theta,z,t) = w\ (r,t), \qquad (5.1\text{a-c})$$

where u_r, u_θ and u_z are, respectively, the radial, tangential and transverse components of the displacement vector **u** of a point (r, θ, z) in the plate at time t, u and w are, respectively, the radial and transverse components of the displacement vector of the corresponding point (r, θ, 0) on the plate midplane at time t, and ϕ_r is the rotation angle of a transverse normal line about the $\mathbf{e}_\theta$ direction (see Fig 5.1).

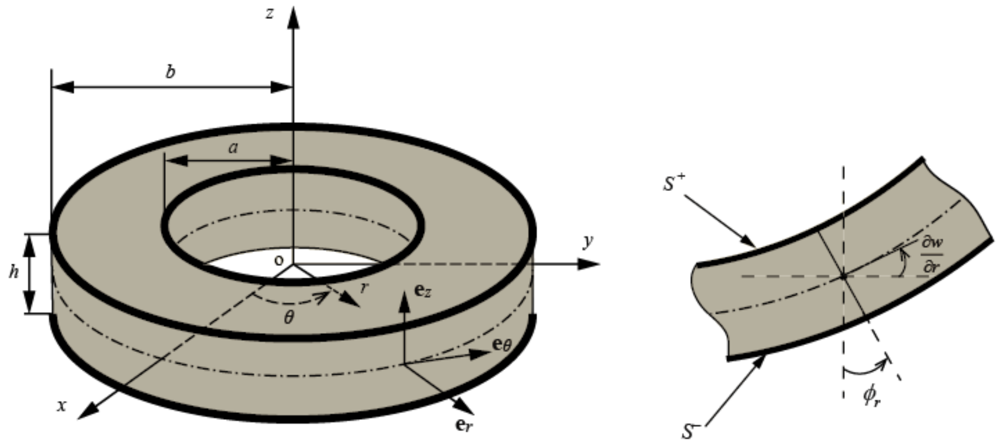

Fig. 5.1 Plate geometry and coordinate system

In Fig 5.1, S^+ and S^- denote, respectively, the upper and lower surface layers of the circular Mindlin plate. These two zero-thickness surface layers are perfectly bonded to the bulk plate material at $z = \pm h/2$ and have distinct material properties from the bulk material. The bulk material satisfies the modified couple stress theory (Yang et al., 2002; Park and Gao, 2008), while the surface layers are governed by the surface elasticity theory (Gurtin and Murdoch, 1975, 1978).

According to the modified couple stress theory (Yang et al., 2002; Park and Gao, 2008),

$$\boldsymbol{\sigma} = \lambda\,\mathrm{tr}(\boldsymbol{\varepsilon})\mathbf{I} + 2\mu\boldsymbol{\varepsilon}, \quad \mathbf{m} = 2l^2\mu\boldsymbol{\chi}, \tag{5.2a,b}$$

$$\boldsymbol{\varepsilon} = \frac{1}{2}\left[\nabla\mathbf{u} + \left(\nabla\mathbf{u}\right)^T\right], \quad \boldsymbol{\chi} = \frac{1}{2}\left[\nabla\boldsymbol{\psi} + \left(\nabla\boldsymbol{\psi}\right)^T\right], \tag{5.3a,b}$$

where $\boldsymbol{\sigma}$ is the Cauchy stress tensor, $\mathbf{m}$ is the deviatoric part of the couple stress tensor, $\mathbf{I}$ is the second-order identity tensor, λ and μ are the Lamé constants in classical elasticity, l is a material length scale parameter measuring the couple stress effect (e.g., Mindlin, 1963; Park and Gao, 2006), $\boldsymbol{\varepsilon}$ is the infinitesimal strain tensor, $\boldsymbol{\chi}$ is the symmetric curvature tensor,

∇ denotes the gradient, the superscript T represents the transpose, $\mathbf{u}$ is the displacement vector, and $\boldsymbol{\psi}$ is the rotation vector defined by

$$\boldsymbol{\psi} = \frac{1}{2} curl\mathbf{u}\,. \tag{5.4}$$

According to the surface elasticity theory (Gurtin and Murdoch, 1975, 1978), the zero-thickness surface layer of a bulk elastic material has distinct constitutive equations involving surface elastic constants and satisfies the governing equations given by

$$\mathrm{div}_S\, \boldsymbol{\tau} = \boldsymbol{\sigma}\mathbf{n}, \tag{5.5}$$

where $\mathbf{n}$ is the outward-pointing unit normal vector to the surface, div_S represents the surface divergence, and $\boldsymbol{\tau}$ is the in-plane surface stress tensor given by (e.g., Gurtin and Murdoch, 1975, 1978; Gao and Mahmoud, 2014; Gao, 2015)

$$\boldsymbol{\tau} = \left[\tau_0 + (\lambda_0 + \tau_0)(\mathrm{tr}\,\boldsymbol{\varepsilon}^s)\right]\mathbf{I}_S + 2\mu_0\boldsymbol{\varepsilon}^s - \tau_0\nabla_S\mathbf{u}, \tag{5.6}$$

where μ_0 and λ_0 are the surface elastic constants, τ_0 is the residual surface stress (i.e., the surface stress at zero strain), $\mathbf{I}_S$ is the projection tensor with $\mathbf{I}_S = \mathbf{I} - \mathbf{n}\otimes\mathbf{n}$, $\boldsymbol{\nabla}_S$ is the surface gradient operator defined by $\boldsymbol{\nabla}_S(\cdot) = (\mathbf{I} - \mathbf{n}\otimes\mathbf{n})\boldsymbol{\nabla}(\cdot)$, and $\boldsymbol{\varepsilon}^s$ is the surface strain tensor given by

$$\boldsymbol{\varepsilon}^s = \frac{1}{2}\left[\nabla_S\mathbf{u} + \left(\nabla_S\mathbf{u}\right)^T\right]. \tag{5.7}$$

Note that the three constants μ_0, λ_0 and τ_0 can be determined from atomistic simulations or experimental measurements (e.g., Shenoy, 2005; Jing et al., 2006; Zhang et al., 2013). Clearly, Eq. (5.6) indicates that $\boldsymbol{\tau}$ is not a symmetric tensor.

The out-of-plane components of the surface stress tensor read (Gurtin and Murdoch, 1978)

$$\tau_{3\beta} = \tau_0 u_{3,\beta}. \tag{5.8}$$

It follows from Eqs. (5.1a-c), (5.2a,b) and (5.4) that the geometrical equations in the bulk of the current axisymmetric circular Mindlin plate are given by

$$\varepsilon_{rr} = \frac{\partial u}{\partial r} - z\frac{\partial \phi_r}{\partial r},\ \varepsilon_{\theta\theta} = \frac{1}{r}(u - z\phi_r),\ \varepsilon_{zr} = \frac{1}{2}\left(\frac{\partial w}{\partial r} - \phi_r\right),\ \varepsilon_{zz} = \varepsilon_{r\theta} = \varepsilon_{\theta z} = 0, \tag{5.9}$$

$$\psi_\theta = -\frac{1}{2}\left(\frac{\partial w}{\partial r} + \phi_r\right),\ \psi_r = \psi_z = 0, \tag{5.10}$$

$$\chi_{r\theta} = -\frac{1}{4} r\frac{\partial}{\partial r}\left[\frac{1}{r}\left(\phi_r + \frac{\partial w}{\partial r}\right)\right] = \chi_{\theta r},\ \chi_{rr} = \chi_{\theta\theta} = \chi_{zz} = \chi_{rz} = \chi_{\theta z} = 0. \tag{5.11}$$

The total strain energy in the elastically deformed circular Kirchhoff plate, U_T, can be expressed as

$$U_T = U_B + U_S = \frac{1}{2}\int_\Omega \left(\sigma_{ij}\varepsilon_{ij} + m_{ij}\chi_{ij}\right)\mathrm{d}V + \frac{1}{2}\int_{S^+} \tau_{\alpha\beta}\varepsilon_{\alpha\beta}\mathrm{d}A + \frac{1}{2}\int_{S^-} \tau_{\alpha\beta}\varepsilon_{\alpha\beta}\mathrm{d}A, \tag{5.12}$$

where Ω is the region occupied by the plate, dV is a differential volume, and dA is a differential area. In Eq. (5.12), U_B is the strain energy in the bulk of the plate, which is governed by the modified couple stress theory, and U_S is the strain energy in the surface layers S^+ and S^- satisfying the surface elasticity theory. It should be mentioned that only the first part of U_B is considered in the classical Mindlin plate theory as the total strain energy (i.e., $U_T^C = \frac{1}{2}\int_\Omega \sigma_{ij}\varepsilon_{ij}\mathrm{d}V$) in the plate.

Note that in Eq. (5.12) and throughout the paper the summation convention and standard index notation are used, with the Greek indices taking r or θ (e.g., $\alpha \in \{r, \theta\}$) and the Latin indices taking r, θ or z (e.g., $i \in \{r, \theta, z\}$) unless otherwise indicated.

From Eqs. (5.6), (5.7) and (5.9)–(5.12), it follows that the first variation of the total strain energy in the circular Mindlin plate over the time interval [0, *T*] can be obtained as (e.g., Zhou and Gao, 2014; Zhang et al., 2015)

$$\begin{aligned}\delta\int_0^T U\mathrm{d}t &= \int_0^T\int_\Omega(\sigma_{rr}\delta\varepsilon_{rr}+\sigma_{\theta\theta}\delta\varepsilon_{\theta\theta}+2\sigma_{zr}\delta\varepsilon_{zr}+2m_{r\theta}\delta\chi_{r\theta})\mathrm{d}V\mathrm{d}t\\ &+\int_0^T\int_{S^+}\left[(\tau_{rr}^{+}-\frac{1}{2}\tau_0)\delta\varepsilon_{rr}^{+}+(\tau_{\theta\theta}^{+}-\frac{1}{2}\tau_0)\delta\varepsilon_{\theta\theta}^{+}\right]\mathrm{d}A\mathrm{d}t\\ &+\int_0^T\int_{S^-}\left[(\tau_{rr}^{-}-\frac{1}{2}\tau_0)\delta\varepsilon_{rr}^{-}+(\tau_{\theta\theta}^{-}-\frac{1}{2}\tau_0)\delta\varepsilon_{\theta\theta}^{-}\right]\mathrm{d}A\mathrm{d}t,\end{aligned} \tag{5.13}$$

where $\overset{+}{\tau}_{\alpha\beta}$ and $\overset{-}{\tau}_{\alpha\beta}$ represent, respectively, the surface stress components on the plate top (S^+) and bottom (S^-) surfaces. In reaching Eq. (5.13), use has been made of the fact that $\tau_{\alpha\beta}$ is non-symmetric. This fact has been overlooked in some variational studies employing the surface elasticity theory of Gurtin and Murdoch (1975, 1978).

Note that the volume integral of a sufficiently smooth function D (x, y, z, t) over the region Ω occupied by a uniform-thickness plate can be represented by

$$\int_\Omega D(x,\ y,\ z,\ t)\mathrm{d}V=\int_R\int_{-h/2}^{h/2}D(x,\ y,\ z,\ t)\mathrm{d}z\mathrm{d}A, \tag{5.14}$$

where h is the plate thickness, and R is the plate mid-plane area.

Using Eqs. (5.9), (5.11) and (5.14) in Eq. (5.13) yields, with the help of Green's theorem,

$$
\begin{aligned}
\delta\int_0^T U\mathrm{d}t = \int_0^T\int_0^{2\pi}\int_a^b \Bigg\{ & \left[N_{\theta\theta} - \frac{\partial(rN_{rr})}{\partial r} + \tau_{\theta\theta}^{+} - \frac{\partial(r\tau_{rr}^{+})}{\partial r} + \tau_{\theta\theta}^{-} - \frac{\partial(r\tau_{rr}^{-})}{\partial r} \right]\delta u \\
& - \left[\frac{\partial(rQ_{zr})}{\partial r} + \frac{1}{2}\frac{\partial^2(rY_{r\theta})}{\partial r^2} + \frac{1}{2}\frac{\partial Y_{r\theta}}{\partial r} \right]\delta w + \left[\frac{\partial(rM_{rr})}{\partial r} - M_{\theta\theta} + \frac{1}{2}\frac{\partial(rY_{r\theta})}{\partial r} + \frac{1}{2}Y_{r\theta} \right. \\
& \left. - rQ_{zr} + \frac{h}{2}\frac{\partial(r\tau_{rr}^{+})}{\partial r} - \frac{h}{2}\frac{\partial(r\tau_{rr}^{-})}{\partial r} - \frac{h}{2}\tau_{\theta\theta}^{+} + \frac{h}{2}\tau_{\theta\theta}^{-} \right]\delta\phi_r \Bigg\} \mathrm{d}r\mathrm{d}\theta\mathrm{d}t \\
+ \int_0^T\int_0^{2\pi} \Bigg\{ & (rN_{rr} + r\tau_{rr}^{+} + r\tau_{rr}^{-} - r\tau_0)\delta u + \left[rQ_{zr} + \frac{1}{2}\frac{\partial(rY_{r\theta})}{\partial r} + \frac{1}{2}Y_{r\theta} \right]\delta w \\
& - (rM_{rr} + \frac{1}{2}rY_{r\theta} + \frac{h}{2}r\tau_{rr}^{+} - \frac{h}{2}r\tau_{rr}^{-})\delta\phi_r - \frac{1}{2}rY_{r\theta}\delta(\frac{\partial w}{\partial r}) \Bigg\} \Bigg|_{r=a}^{r=b} \mathrm{d}\theta\mathrm{d}t,
\end{aligned}
\tag{5.15}
$$

where

$$
\begin{aligned}
N_{rr} &= \int_{-h/2}^{h/2}\sigma_{rr}\mathrm{d}z, \quad N_{\theta\theta} = \int_{-h/2}^{h/2}\sigma_{\theta\theta}\mathrm{d}z, \quad Q_{zr} = \int_{-h/2}^{h/2}\sigma_{zr}\mathrm{d}z, \\
M_{rr} &= \int_{-h/2}^{h/2}\sigma_{rr}z\mathrm{d}z, \quad M_{\theta\theta} = \int_{-h/2}^{h/2}\sigma_{\theta\theta}z\mathrm{d}z, \quad Y_{r\theta} = \int_{-h/2}^{h/2}m_{r\theta}\mathrm{d}z,
\end{aligned}
\tag{5.16}
$$

are the Cauchy stress and couple stress resultants through the plate thickness. Note that in reaching Eq. (5.15) use has been made of the relations $S^{+} = R = S^{-}$, $\partial S^{+} = \partial R = \partial S^{-}$ for the uniform-thickness plate under consideration in order to facilitate the integral evaluations.

The kinetic energy of the plate has the form (e.g., Ma et al., 2011; Gao et al., 2013)

$$
K = \frac{1}{2}\int_{\Omega}\rho\left[\left(\dot{u}_1\right)^2 + \left(\dot{u}_2\right)^2 + \left(\dot{u}_3\right)^2\right]\mathrm{d}V, \tag{5.17}
$$

where ρ is the mass density of the plate material. Here and in the sequel the overhead "·" and "··" denote, respectively, the first and second time derivatives (e.g., $\dot{u}_1 = \partial u_1 / \partial t$, $\ddot{u}_1 = \partial^2 u_1 / \partial t^2$).

From Eqs. (5.1a-c), (5.14) and (5.17), the first variation of the kinetic energy for the axisymmetric plate, over the time interval [0, T], can be obtained as (e.g., Zhou and Gao, 2014)

$$\delta\int_0^T K\mathrm{d}t = -\int_0^T\int_0^{2\pi}\int_a^b\left[m_0(\ddot{u}\delta u+\ddot{w}\delta w)+m_2\ddot{\phi}_r\delta\phi_r\right]r\mathrm{d}r\mathrm{d}\theta\mathrm{d}t, \tag{5.18}$$

where

$$m_0 \equiv \int_{-h/2}^{h/2}\rho\mathrm{d}z = \rho h, \quad m_2 \equiv \int_{-h/2}^{h/2}\rho z^2\mathrm{d}z = \frac{\rho h^3}{12}. \tag{5.19}$$

In reaching Eq. (5.18), it has been assumed that the initial (t = 0) and final (t = T) configurations of the plate are prescribed so that the virtual displacements vanish at t = 0 and t = T. In addition, ρ is taken to be constant along the plate thickness and over the time interval [0, T] such that $\dot{m}_0 = 0,\ \dot{m}_2 = 0$.

From the general expression of the work done by external forces in the modified couple stress theory (Park and Gao, 2008) and in the surface elasticity theory (Gurtin and Murdoch, 1975, 1978), the virtual work done by the forces applied on the current circular plate over the time interval [0, T] can be written as (e.g., Zhou and Gao, 2014; Gao and Zhang, 2016)

$$\begin{aligned}\delta\int_0^T W\mathrm{d}t = &\int_0^T\int_R\left(\mathbf{f}\cdot\delta\mathbf{u}+\mathbf{c}\cdot\delta\boldsymbol{\psi}\right)\mathrm{d}A\mathrm{d}t+\int_0^T\oint_{\partial R}\left(\bar{\mathbf{t}}\cdot\delta\mathbf{u}+\bar{\mathbf{s}}\cdot\delta\boldsymbol{\psi}\right)\mathrm{d}s\mathrm{d}t\\ &+\int_0^T\int_S\mathbf{t}^s\cdot\delta(u_3\mathbf{e}_3)\mathrm{d}A\mathrm{d}t,\end{aligned} \tag{5.20}$$

where $\mathbf{f}$ and $\mathbf{c}$ are, respectively, the body force resultant (force per unit area), body couple resultant (moment per unit area) through the plate thickness acting in the area R (i.e., the plate mid-plane), $\bar{\mathbf{t}}$ and $\bar{\mathbf{s}}$ are, respectively, the Cauchy traction resultant (force per unit length) and the surface couple resultant (moment per unit length) through the plate thickness acting on ∂R (i.e., the boundary of R), $\mathbf{t}^s$ is the surface traction that is related to the surface stress $\boldsymbol{\tau}$ through $\mathbf{t}^s = \nabla_s\cdot\boldsymbol{\tau} = \tau_{i\alpha,\alpha}\mathbf{e}_i$ (e.g., Gurtin and Murdoch, 1978; Altenbach et al., 2010), and ds is a differential arc length along ∂R,. Note that the last term in the virtual work expression in Eq. (5.20) accounts for the contribution of the normal stress on the top and bottom plate surfaces $\sigma_{33}^{\pm}$ ($=\pm\tau_{3\alpha,\alpha}^{\pm}$ from the equilibrium equations in Eq. (5.5)), which is neglected in the classical Mindlin plate theory that does not consider the surface energy effect.

Using Eqs. (5.1a-c), (5.5) and (5.10) in Eq. (5.20) leads to, with the help of Green's theorem,

$$\delta\int_0^T W\mathrm{d}t = \int_0^T\int_0^{2\pi}\int_a^b \left\{ rf_r\delta u + \left[\frac{1}{2}\frac{\partial(rc_\theta)}{\partial r} + rf_z + \frac{\partial(r\tau_{3r}^{+})}{\partial r} + \frac{\partial(r\tau_{3r}^{-})}{\partial r}\right]\delta w - \frac{1}{2}rc_\theta\delta\phi_r \right\}\mathrm{d}r\mathrm{d}\theta\mathrm{d}t$$
$$+\int_0^T\int_0^{2\pi}\left[r\bar{t}_r\delta u + (-\frac{1}{2}rc_\theta + r\bar{t}_z)\delta w - (r\bar{M}_\theta + \frac{1}{2}r\bar{s}_\theta)\delta\phi_r - \frac{1}{2}r\bar{s}_\theta\delta(\frac{\partial w}{\partial r})\right]\Big|_{r=a}^{r=b}\,\mathrm{d}\theta\mathrm{d}t, \tag{5.21}$$

where f_i, c_i, $\bar{t}_i$ and $\bar{s}_i$ ($i \in \{ r, \theta, z\}$) are, respectively, the components of $\mathbf{f}$, $\mathbf{c}$, $\bar{\mathbf{t}}$ and $\bar{\mathbf{s}}$, and $\bar{M}_\theta$ is the applied moment per unit arc length along the circular boundary. Note that the positive directions of $\bar{M}_\theta$, which is along the $\mathbf{e}_\theta$ direction, is opposite to the positive direction of ϕ_r (see Fig 5.1).

According to Hamilton's principle (e.g., Reddy, 2002; Ma et al., 2008),

$$\delta\int_0^T\left[K-\left(U-W\right)\right]\mathrm{d}t = 0. \tag{5.22}$$

Substituting Eqs. (5.15), (5.18) and (5.21) into Eq. (5.22) gives

$$
\begin{aligned}
&\int_0^T\int_0^{2\pi}\int_a^b\Bigg\{\left[N_{\theta\theta}-\frac{\partial(rN_{rr})}{\partial r}+\tau_{\theta\theta}^{+}-\frac{\partial(r\tau_{rr}^{+})}{\partial r}+\tau_{\theta\theta}^{-}-\frac{\partial(r\tau_{rr}^{-})}{\partial r}-rf_r+m_0r\ddot{u}\right]\delta u\\
&-\left[\frac{\partial(rQ_{zr})}{\partial r}+\frac{1}{2}\frac{\partial^2(rY_{r\theta})}{\partial r^2}+\frac{1}{2}\frac{\partial Y_{r\theta}}{\partial r}+\frac{1}{2}\frac{\partial(rc_\theta)}{\partial r}+\frac{\partial(r\tau_{3r}^{+})}{\partial r}+\frac{\partial(r\tau_{3r}^{-})}{\partial r}+rf_z-m_0r\ddot{w}\right]\delta w\\
&+\left[\frac{\partial(rM_{rr})}{\partial r}-M_{\theta\theta}+\frac{1}{2}\frac{\partial(rY_{r\theta})}{\partial r}+\frac{1}{2}Y_{r\theta}-rQ_{zr}+\frac{h}{2}\frac{\partial(r\tau_{rr}^{+})}{\partial r}-\frac{h}{2}\frac{\partial(r\tau_{rr}^{-})}{\partial r}-\frac{h}{2}\tau_{\theta\theta}^{+}\right.\\
&\left.+\frac{h}{2}\tau_{\theta\theta}^{-}+\frac{1}{2}rc_\theta+m_2r\ddot{\phi}_r\right]\delta\phi_r\Bigg\}\mathrm{d}r\mathrm{d}\theta\mathrm{d}t+\int_0^T\int_0^{2\pi}\Big\{(rN_{rr}+r\tau_{rr}^{+}+r\tau_{rr}^{-}-r\tau_0-r\overline{t}_r)\delta u\\
&+\left[rQ_{zr}+\frac{1}{2}\frac{\partial(rY_{r\theta})}{\partial r}+\frac{1}{2}Y_{r\theta}+\frac{1}{2}rc_\theta-r\overline{t}_z\right]\delta w-(rM_{rr}+\frac{1}{2}rY_{r\theta}+\frac{h}{2}r\tau_{rr}^{+}-\frac{h}{2}r\tau_{rr}^{-}\\
&-r\overline{M}_\theta-\frac{1}{2}r\overline{s}_\theta)\delta\phi_r-(\frac{1}{2}rY_{r\theta}-\frac{1}{2}r\overline{s}_\theta)\,\delta(\frac{\partial w}{\partial r})\Big\}\Big|_{r=a}^{r=b}\,\mathrm{d}\theta\mathrm{d}t=0.
\end{aligned}
\tag{5.23}
$$

Applying the fundamental lemma of the calculus of variations to Eq. (5.23) then yields, with the arbitrariness of δu, δw and $\delta\phi_r$ (e.g., Gao and Mall, 2001; Ma et al., 2008),

$$
-\frac{N_{\theta\theta}}{r}+\frac{1}{r}\frac{\partial(rN_{rr})}{\partial r}+\frac{1}{r}\frac{\partial(r\tau_{rr}^{+})}{\partial r}+\frac{1}{r}\frac{\partial(r\tau_{rr}^{-})}{\partial r}-\frac{\tau_{\theta\theta}^{+}}{r}-\frac{\tau_{\theta\theta}^{-}}{r}+f_r=m_0\ddot{u}, \tag{5.24a}
$$

$$
\frac{1}{r}\frac{\partial(rQ_{zr})}{\partial r}+\frac{1}{2r}\left[\frac{\partial Y_{r\theta}}{\partial r}+\frac{\partial^2(rY_{r\theta})}{\partial r^2}\right]+\frac{1}{r}\frac{\partial(r\tau_{3r}^{+})}{\partial r}+\frac{1}{r}\frac{\partial(r\tau_{3r}^{-})}{\partial r}+\frac{1}{2r}\frac{\partial(rc_\theta)}{\partial r}+f_z=m_0\ddot{w}, \tag{5.24b}
$$

$$
\begin{aligned}
&-\frac{1}{r}\frac{\partial(rM_{rr})}{\partial r}+\frac{1}{r}M_{\theta\theta}-\frac{1}{2r}\left[Y_{r\theta}+\frac{\partial(rY_{r\theta})}{\partial r}\right]+Q_{zr}-\frac{h}{2r}\frac{\partial(r\tau_{rr}^{+})}{\partial r}+\frac{h}{2r}\frac{\partial(r\tau_{rr}^{-})}{\partial r}\\
&\quad+\frac{h}{2r}\tau_{\theta\theta}^{+}-\frac{h}{2r}\tau_{\theta\theta}^{-}-\frac{1}{2}c_\theta=m_2\ddot{\phi}_r
\end{aligned}
\tag{5.24c}
$$

as the equations of motion of the circular Mindlin plate for any $(r, \theta) \in R$ and $t \in (0, T)$, and

$$
N_{rr}+\tau_{rr}^{+}+\tau_{rr}^{-}-\tau_0=\overline{t}_r \quad \text{or} \quad u=\overline{u} \quad \text{at} \quad r=a \quad \text{and} \quad r=b, \tag{5.25a}
$$

$$
Q_{zr}+\frac{1}{2r}\frac{\partial(rY_{r\theta})}{\partial r}+\frac{1}{2r}Y_{r\theta}+\frac{1}{2}c_\theta=\overline{t}_z \quad \text{or} \quad w=\overline{w} \quad \text{at} \quad r=a \quad \text{and} \quad r=b, \tag{5.25b}
$$

$$M_{rr} + \frac{1}{2}Y_{r\theta} + \frac{h}{2}\tau_{rr}^{+} - \frac{h}{2}\tau_{rr}^{-} = \overline{M}_{\theta} + \frac{1}{2}\overline{s}_{\theta} \quad \text{or} \quad \phi_r = \overline{\phi}_r \quad \text{at} \quad r = a \quad \text{and} \quad r = b, \tag{5.25c}$$

$$Y_{r\theta} = \overline{s}_{\theta} \quad \text{or} \quad \frac{\partial w}{\partial r} = \frac{\partial \overline{w}}{\partial r} \quad \text{at} \quad r = a \quad \text{and} \quad r = b \tag{5.25d}$$

as the boundary conditions.

From Eqs. (5.2a,b), (5.9), (5.11) and (5.16), the Cauchy stress and couple stress resultants can be expressed in terms of u, w and ϕ_r, the three kinematic variables, as

$$N_{rr} = h(\lambda + 2\mu)\frac{\partial u}{\partial r} + \lambda h \frac{u}{r}, \tag{5.26a}$$

$$N_{\theta\theta} = \lambda h \frac{\partial u}{\partial r} + h(\lambda + 2\mu)\frac{u}{r}, \tag{5.26b}$$

$$M_{rr} = -\frac{h^3}{12}(\lambda + 2\mu)\frac{\partial \phi_r}{\partial r} - \frac{h^3}{12}\lambda\frac{1}{r}\phi_r, \tag{5.26c}$$

$$M_{\theta\theta} = -\frac{h^3}{12}\lambda\frac{\partial \phi_r}{\partial r} - \frac{h^3}{12}(\lambda + 2\mu)\frac{1}{r}\phi_r, \tag{5.26d}$$

$$Q_{zr} = K_s \mu h(\frac{\partial w}{\partial r} - \phi_r), \tag{5.26e}$$

$$Y_{r\theta} = -\frac{1}{2}l^2 \mu h(\frac{\partial \phi_r}{\partial r} + \frac{\partial^2 w}{\partial r^2} - \frac{1}{r}\frac{\partial w}{\partial r} - \frac{1}{r}\phi_r), \tag{5.26f}$$

where K_s is the shear correction factor to account for the non-uniformity of the shear strain along the plate thickness.

From Eqs. (5.5)–(5.7) and (5.8a-c), the surface stress components can be written in terms of u, w and ϕ_r as

$$\tau_{rr}^{\pm} = \tau_0 + (2\mu_0 + \lambda_0)\left(\frac{\partial u}{\partial r} \mp \frac{h}{2}\frac{\partial \phi_r}{\partial r}\right) + (\lambda_0 + \tau_0)\left(\frac{u}{r} \mp \frac{h}{2r}\phi_r\right), \tag{5.27a}$$

$$\tau_{\theta\theta}^{\pm} = \tau_0 + (2\mu_0 + \lambda_0)\left(\frac{u}{r} \mp \frac{h}{2r}\phi_r\right) + (\lambda_0 + \tau_0)\left(\frac{\partial u}{\partial r} \mp \frac{h}{2}\frac{\partial \phi_r}{\partial r}\right), \tag{5.27b}$$

$$\tau_{3r}^{+} = \tau_{3r}^{-} = \tau_0 \frac{\partial w}{\partial r}. \tag{5.27c}$$

Using Eqs. (5.26a-f) and (5.27a-c) in Eqs. (5.24a-c) then leads to the equations of motion of the circular Mindlin plate in terms of *u*, *w* and ϕ_r as

$$\left[(\lambda + 2\mu)h + 2(\lambda_0 + 2\mu_0)\right](-\frac{u}{r^2} + \frac{1}{r}\frac{\partial u}{\partial r} + \frac{\partial^2 u}{\partial r^2}) + f_r = m_0 \ddot{u}, \tag{5.28a}$$

$$\begin{aligned} &K_s \mu h \frac{1}{r}\frac{\partial}{\partial r}\left[r\left(\frac{\partial w}{\partial r} - \phi_r\right)\right] - \frac{1}{4}l^2 \mu h \frac{1}{r}\frac{\partial}{\partial r}\left\{r\frac{\partial}{\partial r}\left[\frac{1}{r}\frac{\partial}{\partial r}\left(r\phi_r + r\frac{\partial w}{\partial r}\right)\right]\right\} \\ &+ 2\tau_0 \frac{1}{r}\frac{\partial}{\partial r}\left(r\frac{\partial w}{\partial r}\right) + \frac{1}{2r}\frac{\partial (r c_\theta)}{\partial r} + f_z = m_0 \ddot{w}, \end{aligned} \tag{5.28b}$$

$$\begin{aligned} &\frac{(\lambda + 2\mu)h^3}{12}\frac{\partial}{\partial r}\left[\frac{1}{r}\frac{\partial}{\partial r}(r\phi_r)\right] + K_s \mu h\left(\frac{\partial w}{\partial r} - \phi_r\right) + \frac{1}{4}l^2 \mu h \frac{\partial}{\partial r}\left\{\frac{1}{r}\frac{\partial}{\partial r}\left[r\left(\phi_r + \frac{\partial w}{\partial r}\right)\right]\right\} \\ &+ \frac{h^2}{2}(2\mu_0 + \lambda_0)\frac{\partial}{\partial r}\left[\frac{1}{r}\frac{\partial}{\partial r}(r\phi_r)\right] - \frac{1}{2}c_\theta = m_2 \ddot{\phi}_r. \end{aligned} \tag{5.28c}$$

From Eqs. (5.28a-c), it can be seen that the radial displacement (stretching) *u*(*r*, *t*) is uncoupled with the deflection *w*(*r*, *t*) and rotation angle $\phi_r(r,t)$. Therefore, *u*(*r*, *t*) can be obtained from solving Eq. (5.28a) subject to prescribed boundary conditions of the form in Eq. (5.25a) and suitable initial conditions. Note that the material length scale parameter *l* is not involved in Eq. (5.28a) or (5.25a). As a result, the radial displacement *u*(*r*, *t*) will not be affected by the microstructure of the plate material.

When $l = 0$ and $c_\theta = 0$ (i.e., with the microstructure effect ignored), Eqs. (5.28a-c) reduce to

$$\left[(\lambda + 2\mu)h + 2(\lambda_0 + 2\mu_0)\right](-\frac{u}{r^2} + \frac{1}{r}\frac{\partial u}{\partial r} + \frac{\partial^2 u}{\partial r^2}) + f_r = m_0 \ddot{u}, \tag{5.29a}$$

$$K_s \mu h \frac{1}{r}\frac{\partial}{\partial r}\left[r\left(\frac{\partial w}{\partial r}-\phi_r\right)\right]+2\tau_0\frac{1}{r}\frac{\partial}{\partial r}\left(r\frac{\partial w}{\partial r}\right)+f_z=m_0\ddot{w}, \tag{5.29b}$$

$$\left[\frac{(\lambda+2\mu)h^3}{12}+\frac{(\lambda_0+2\mu_0)h^2}{2}\right]\frac{\partial}{\partial r}\left[\frac{1}{r}\frac{\partial}{\partial r}(r\phi_r)\right]+K_s\mu h\left(\frac{\partial w}{\partial r}-\phi_r\right)=m_2\ddot{\phi}_r, \tag{5.29c}$$

which are the governing equations for the circular Mindlin plate with the surface energy effect alone.

When $\lambda_0 = \mu_0 = \tau_0 = 0$ (i.e., with the surface energy effect neglected), Eqs. (5.28a-c) become

$$(\lambda+2\mu)h\frac{\partial}{\partial r}\left[\frac{1}{r}\frac{\partial(ru)}{\partial r}\right]+f_r=m_0\ddot{u}, \tag{5.30a}$$

$$\frac{K_s\mu h}{r}\frac{\partial}{\partial r}\left[r\left(\frac{\partial w}{\partial r}-\phi_r\right)\right]-\frac{l^2\mu h}{4r}\frac{\partial}{\partial r}\left\{r\frac{\partial}{\partial r}\left[\frac{1}{r}\frac{\partial}{\partial r}\left(r\phi_r+r\frac{\partial w}{\partial r}\right)\right]\right\}+\frac{1}{2r}\frac{\partial(rc_\theta)}{\partial r}+f_z=m_0\ddot{w}, \tag{5.30b}$$

$$\begin{aligned}&\frac{(\lambda+2\mu)h^3}{12}\frac{\partial}{\partial r}\left[\frac{1}{r}\frac{\partial}{\partial r}(r\phi_r)\right]+K_s\mu h\left(\frac{\partial w}{\partial r}-\phi_r\right)+\frac{l^2\mu h}{4}\frac{\partial}{\partial r}\left\{\frac{1}{r}\frac{\partial}{\partial r}\left[r\left(\phi_r+\frac{\partial w}{\partial r}\right)\right]\right\}\\&-\frac{1}{2}c_\theta=m_2\ddot{\phi}_r.\end{aligned} \tag{5.30c}$$

Equations (5.30a-c) are the governing equations for the circular Mindlin plate incorporating the microstructure effect alone, which are identical to those derived in Zhou and Gao (2014) using the modified couple stress theory.

When $l = 0$, $c_\theta = 0$ and $\lambda_0 = \mu_0 = \tau_0 = 0$ (i.e., with both the microstructure and surface energy effects suppressed), Eqs. (5.28a-c) simplifies to

$$(\lambda+2\mu)h\frac{\partial}{\partial r}\left[\frac{1}{r}\frac{\partial(ru)}{\partial r}\right]+f_r=m_0\ddot{u}, \tag{5.31a}$$

$$K_s\mu h\frac{1}{r}\frac{\partial}{\partial r}\left[r\left(\frac{\partial w}{\partial r}-\phi_r\right)\right]+f_z=m_0\ddot{w}, \tag{5.31b}$$

$$\frac{(\lambda+2\mu)h^3}{12}\frac{\partial}{\partial r}\left[\frac{1}{r}\frac{\partial}{\partial r}(r\phi_r)\right]+K_s\mu h\left(\frac{\partial w}{\partial r}-\phi_r\right)=m_2\ddot{\phi}_r. \tag{5.31c}$$

Equations (5.31a-c) are the classical elasticity-based equations of motion for the circular Mindlin plate. That is, the classical Kirchhoff plate model is included in the current model as a special case. Note that the three-dimensional Hooke's law in Eq. (5.2a) used here is different from the two-dimensional Hooke's law for the plane stress state employed in classical Mindlin plates theories (e.g., Reddy, 2002).

When $\phi_r=\partial w/\partial r$ (i.e., with the normality assumption reinstated), Eqs. (5.1a-c) reduce to the displacement field in a thin circular Kirchhoff plate undergoing axisymmetric deformations, and Eqs. (5.28a-c) become

$$\left[(\lambda+2\mu)h+2(\lambda_0+2\mu_0)\right]\left(-\frac{u}{r^2}+\frac{1}{r}\frac{\partial u}{\partial r}+\frac{\partial^2 u}{\partial r^2}\right)+f_r=m_0\ddot{u}, \tag{5.32a}$$

$$\begin{aligned}&-\left[\frac{(\lambda+2\mu)h^3}{12}+\mu l^2h+\frac{(\lambda_0+2\mu_0)h^2}{2}\right]\frac{1}{r}\frac{\partial}{\partial r}\left\{r\frac{\partial}{\partial r}\left[\frac{1}{r}\frac{\partial}{\partial r}\left(r\frac{\partial w}{\partial r}\right)\right]\right\}\\&\quad+2\tau_0\frac{1}{r}\frac{\partial}{\partial r}\left(r\frac{\partial w}{\partial r}\right)+\frac{1}{r}\frac{\partial(rc_\theta)}{\partial r}+f_z=m_0\ddot{w}-m_2\left(\frac{1}{r}\frac{\partial\ddot{w}}{\partial r}+\frac{\partial^2\ddot{w}}{\partial r^2}\right).\end{aligned} \tag{5.32b}$$

Equations (5.32a) and (5.32b) are the equations of motion of the circular Kirchhoff plate derived in Zhang and Gao (2015) based on the modified couple stress theory and the surface elasticity theory, which is included in the current circular Mindlin plate model as a special case.

5.3 Example

To further demonstrate the new circular Mindlin plate model developed in Section 5.2, the static bending problem of a clamped circular plate subjected to a uniformly distributed normal load $f_z = -q$ (with the negative sign here indicating that the normal load q (>0) is pointing downward) by directly applying the new model.

In view of the general boundary conditions (BCs) in Eqs. (5.24a–d), the BCs for the current solid circular Mindlin plate (with $a = 0$) clamped at its edge $r = b$ can be identified as

$$u\big|_{r=b} = 0, \quad w\big|_{r=b} = 0, \quad \left.\frac{\partial w}{\partial r}\right|_{r=b} = 0, \quad \phi_r\big|_{r=b} = 0. \tag{5.33a-d}$$

In addition, the following symmetry conditions need to be satisfied at $r = 0$:

$$u\big|_{r=0} = 0, \quad \left.\frac{\partial w}{\partial r}\right|_{r=0} = 0, \quad \phi_r\big|_{r=0} = 0. \tag{5.34a-c}$$

For static bending problems, u, w and ϕ_r are independent of time t so that all of the time derivatives involved in Eqs. (5.27a-c) vanish. The governing equations for static problems with $f_r = 0 = c_\theta$ are given by

$$\left[(\lambda + 2\mu)h + 2(\lambda_0 + 2\mu_0)\right]\left(-\frac{u}{r^2} + \frac{1}{r}\frac{\partial u}{\partial r} + \frac{\partial^2 u}{\partial r^2}\right) = 0, \tag{5.35a}$$

$$\begin{aligned} &\frac{K_s \mu h}{r}\frac{\partial}{\partial r}\left[r\left(\frac{\partial w}{\partial r} - \phi_r\right)\right] - \frac{l^2 \mu h}{4r}\frac{\partial}{\partial r}\left\{r\frac{\partial}{\partial r}\left[\frac{1}{r}\frac{\partial}{\partial r}\left(r\phi_r + r\frac{\partial w}{\partial r}\right)\right]\right\} \\ &+ \frac{2\tau_0}{r}\frac{\partial}{\partial r}\left(r\frac{\partial w}{\partial r}\right) + f_z = 0, \end{aligned} \tag{5.35b}$$

$$\left[\frac{(\lambda+2\mu)h^3}{12}+\frac{(\lambda_0+2\mu_0)h^2}{2}\right]\frac{\partial}{\partial r}\left[\frac{1}{r}\frac{\partial}{\partial r}(r\phi_r)\right]+K_s\mu h\left(\frac{\partial w}{\partial r}-\phi_r\right)$$
$$+\frac{l^2\mu h}{4}\frac{\partial}{\partial r}\left\{\frac{1}{r}\frac{\partial}{\partial r}\left[r\left(\phi_r+\frac{\partial w}{\partial r}\right)\right]\right\}=0. \tag{5.35c}$$

As mentioned in Section 5.2, the radial displacement u is uncoupled with w and ϕ_r. It can be obtained from solving the boundary value problem (BVP) defined by Eqs. (5.33a), (5.34a) and (5.35a). The solution of this BVP gives $u(r) = 0$ for any $(r, \theta) \in R$.

The deflection w and the rotation angle ϕ_r can be obtained from solving the BVP defined by Eqs. (5.33b–d), (5.34b,c) and (5.35b,c).

Consider the following Fourier-Bessel series solutions for w and ϕ_r:

$$\frac{\partial w}{\partial r}=\sum_{n=1}^{\infty}W_n J_1(\bar{\lambda}_{1n}r), \tag{5.36a}$$

$$\phi_r=\sum_{n=1}^{\infty}\Phi_n J_1(\bar{\lambda}_{1n}r), \tag{5.36b}$$

where J_1 is the Bessel function of the first kind of the first order, $\bar{\lambda}_{1n}=\lambda_{1n}/b$, λ_{1n} is the nth positive root of $J_1(r) = 0$, and W_n and Φ_n are coefficients to be determined. It can be readily shown that the expressions in Eqs. (5.36a,b) automatically satisfy the boundary conditions in Eqs. (5.33c,d) and the symmetry conditions in Eqs. (5.34b,c) for any W_n and Φ_n.

Integrating Eq. (5.36a) with respect to r yields, upon using Eq. (5.33b) (the only remaining boundary condition),

$$w=\sum_{n=1}^{\infty}\frac{1}{\bar{\lambda}_{1n}}W_n[J_0(\lambda_{1n})-J_0(\bar{\lambda}_{1n}r)], \tag{5.37}$$

where J_0 is the Bessel function of the first kind of the zeroth order.

The axisymmetrically distributed force $f_z\,(r)$ involved in Eq. (5.34b) can also be expanded in a Fourier–Bessel series as

$$f_z = \sum_{n=1}^{\infty} F_n J_0(\bar{\lambda}_{1n} r), \tag{5.38}$$

where the coefficient F_n can be determined as (e.g., Zhou and Gao, 2014)

$$F_n = -\frac{q}{J_2(\lambda_{1n})}, \tag{5.39}$$

for $f_z\,(r) = -\,q$, where J_2 is the Bessel function of the first kind of the second order.

Using Eqs. (5.36a,b)–(5.38) in Eq. (5.35b,c) results in

$$\begin{bmatrix} C_{11} & C_{12} \\ C_{21} & C_{22} \end{bmatrix} \begin{Bmatrix} W_n \\ \Phi_n \end{Bmatrix} = \begin{Bmatrix} q / J_2(\lambda_{1n}) \\ 0 \end{Bmatrix}, \tag{5.40}$$

where

$$\begin{aligned} C_{11} &= \frac{1}{4} l^2 \mu h \bar{\lambda}_{1n}^3 + K_s \mu h \bar{\lambda}_{1n} + 2\tau_0 \bar{\lambda}_{1n}, \\ C_{12} &= \frac{1}{4} l^2 \mu h \bar{\lambda}_{1n}^3 - K_s \mu h \bar{\lambda}_{1n}, \\ C_{21} &= K_s \mu h - \frac{1}{4} l^2 \mu h \bar{\lambda}_{1n}^2, \\ C_{22} &= -\frac{(\lambda + 2\mu) h^3}{12} \bar{\lambda}_{1n}^2 - K_s \mu h - \frac{1}{4} l^2 \mu h \bar{\lambda}_{1n}^2 - \frac{h^2}{2} (\lambda_0 + 2\mu_0) \bar{\lambda}_{1n}^2. \end{aligned} \tag{5.41}$$

Solving the linear algebraic equation system in Eq. (5.40) then yields

$$W_n = \frac{C_{22}}{C_{11}C_{22} - C_{12}C_{21}} \frac{q}{J_2(\lambda_{1n})}, \quad \Phi_n = -\frac{C_{21}}{C_{11}C_{22} - C_{12}C_{21}} \frac{q}{J_2(\lambda_{1n})}. \tag{5.42a, b}$$

Then, substituting W_n and Φ_n obtained in Eqs. (5.42a) and (5.42b), respectively, into Eqs. (5.37) and (5.36b) will give the exact solutions of the deflection w and the rotation angle ϕ_r based on the current non-classical circular Mindlin plate model for the clamped plate subjected to the axisymmetrically distributed load, while the classical elasticity-based exact deflection w^c and the rotation angle ϕ_r^c solution are computed using the same equations but with $l = 0$, $\lambda_0 = \mu_0 = \tau_0 = 0$ (i.e., with both the microstructure and surface energy effects suppressed).

To illustrate the newly derived solution for the clamped solid circular Mindlin plate, some numerical results are shown in Figs 5.2 and 5.3. Figure 5.2 displays the variation of the plate deflection w along the radial direction, and Figure 5.3 shows the change of the rotation angle ϕ_r with the radial coordinate r for the clamped circular Mindlin plate. The numerical results predicted by the new model are obtained from Eqs. (5.36b), (5.37), (5.41) and (5.42a, b), while those by the classical model are determined using the same equations with $l = 0$, $\lambda_0 = \mu_0 = \tau_0 = 0$.

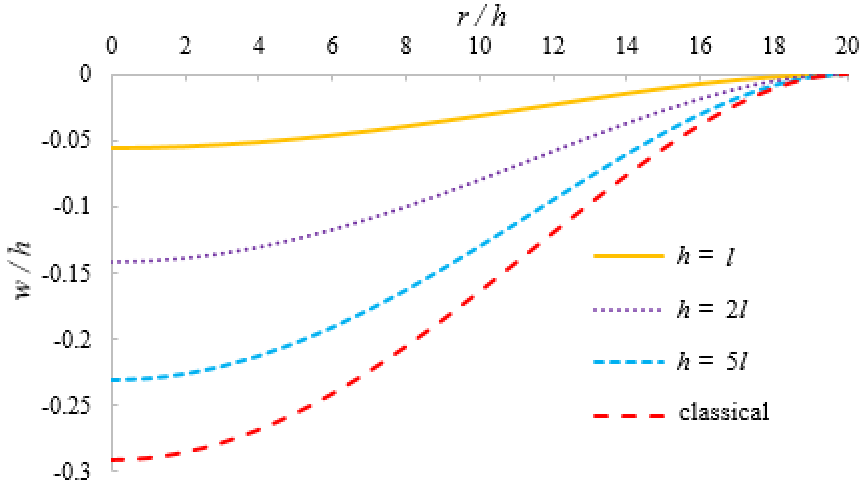

Fig. 5.2 Deflection of the clamped circular Mindlin plate

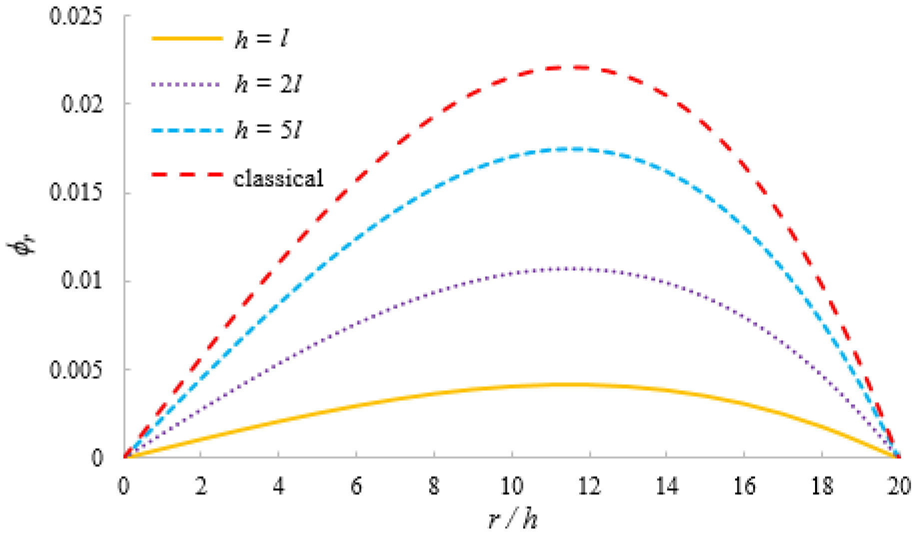

Fig. 5.3 Rotation angle of the clamped circular Mindlin plate

In generating the numerical results shown in Figs 5.2 and 5.3, the radius of the circular plate is fixed at $b = 20h$, while the plate thickness h is varying. The circular plate material is taken to be aluminum with the following properties (e.g., Liu and Rajapakse, 2010; Gao, 2015): $E = 90$ GPa, $v = 0.23$, $l = 6.58$ μm for the bulk, and $\mu_0 = -5.4251$ N/m, $\lambda_0 = 3.4939$ N/m, $\tau_0 = 0.5689$ N/m for the surface layers. Note that the Lamé constants λ and μ involved in Eq. (5.41) can be calculated from the identified Young's modulus E and Poisson's ratio v using the following relations (e.g., Timoshenko and Goodier, 1970):

$$\lambda = \frac{Ev}{(1+v)(1-2v)}, \quad \mu = \frac{E}{2(1+v)}. \tag{5.43}$$

The shear correction factor K_s used here is 0.8 (e.g., Liu and Soh, 2007; Ma et al., 2011). In addition, the uniform, downward-pointing normal load is taken to be $q = 1$ MPa.

From Figs 5.2 and 5.3, it is clearly seen that both the deflection w and rotation angle ϕ_r predicted by the current non-classical circular Mindlin model are always smaller than those predicted by the classical model in all cases considered. It also shows that the differences in the deflection and rotation values predicted by the new model and the classical model are very large when the thickness of the plate h is small (with $h = l = 6.58$ μm here), but the differences are diminishing when the thickness of the plate h increases. This predicted size effect agrees with the general trend observed experimentally (e.g., McFarland and Colton, 2005).

5.4 Summary

A new non-classical circular Mindlin plate model is provided, which is based on a modified couple stress theory, a surface elasticity theory and Hamilton's principle. The equations of motion and the boundary conditions are derived simultaneously by using a variational formulation. The newly developed model includes the circular Mindlin plate models considering the microstructure effect only or the surface energy effect alone as special cases. In addition, the current Mindlin plate model recovers the classical elasticity-based circular Mindlin plate model when both the microstructure and surface energy effects are ignored. As an example, the static bending problem of a clamped circular Mindlin plate subjected to a uniform normal load is analytically solved by directly applying the new plate model.

Chapter

6. BAND GAPS FOR FLEXURAL ELASTIC WAVE PROPAGATION IN PERIODIC COMPOSITE PLATE STRUCTURES USING A NON-CLASSICAL KIRCHHOFF PLATE MODEL INCORPORATING MICROSTRUCTURE, SURFACE ENERGY AND FOUNDATION EFFECTS

6.1 Introduction

Band gaps for elastic wave propagation in periodic composite beam and plate structures have received increasing attention (e.g., Sigalas and Economou, 1994; Hsu and Wu, 2006; Liu and Hussein, 2012; Xiao et al., 2012; Yu et al., 2012; Han et al., 2013; Piccolroaz and Movchan, 2014; Trainiti et al., 2015; Liu et al., 2016; Zhang and Parnell, 2017; Piccolroaz et al., 2017; Chen et al., 2017; Zhang et al., 2018a). Such periodic composite structures can attenuate or stop wave propagation in certain frequency ranges (i.e., band gaps) and are finding important applications in wave filtering, vibration isolating and energy harvesting. Two major mechanisms responsible for band gaps, Bragg scattering and local resonance (e.g., Liu and Hussein, 2012; Chen and Wang, 2014; Madeo et al., 2016), can both be present in such composite structures. At the micron and nanometer scales, thin beams and plates often exhibit size effects (e.g., Lam et al., 2003; McFarland and Colton, 2005). Hence, band gaps for elastic wave propagation in micro- or nano-structured composite beams and plates are also size-dependent, which cannot be described using the classical elasticity-based wave equations due to a lack of any material length scale parameter. As a result, wave equations based on higher-order continuum theories that contain microstructure-dependent material constants are needed to determine band gaps at small length scales.

Wave equations built upon higher-order elasticity theories have been derived and applied to study band gaps. Liu et al. (2012) investigated surface energy effects on band gaps for 2-D phononic crystals using the wave equations satisfying the surface elasticity theory of Gurtin and Murdoch (1975, 1978). Li et al. (2016) analyzed band gaps in 1-D phononic crystals applying the equation of motion based on the dipolar gradient elasticity theory, which is also known as the simplified strain gradient elasticity theory (e.g., Gao and Park, 2007; Gao and Ma, 2010). Madeo et al. (2016) employed the wave equations built upon a relaxed micromorphic elasticity theory to explore frequency band gaps in metamaterials. Bacigalupo and Gambarotta (2017) analyzed dispersion functions of wave propagation to detect band gaps for periodic materials through a micropolar continuum theory. Band gaps for flexural elastic wave propagation in periodic composite beam structures were recently studied in Zhang et al. (2018a) and Gao et al. (2018) by using non-classical Bernoulli–Euler and Timoshenko beam models based on a modified couple stress theory (Yang et al., 2002; Park and Gao, 2008) and a surface elasticity theory (Gurtin and Murdoch, 1975, 1978). However, wave equations for plates built upon such higher-order elasticity theories have not been utilized to determine band gaps in periodic composite plate structures. This motivated the present work.

In this chapter, band gaps for flexural elastic wave propagation in a periodic composite plate structure resting on a Winkler-Pasternak elastic foundation are studied by directly using the non-classical model for Kirchhoff plates presented in Chapter 2. The rest of Chapter 6 is organized as follows. In Section 6.2, the equations of motion for a Kirchhoff plate incorporating the microstructure, surface energy and foundation effects derived in Gao and Zhang (2016) are applied to study flexural elastic wave propagation in a periodic composite plate structure. The plane wave expansion method and Bloch's theorem for periodic structures are used in the formulation. In Section 6.3, numerical results are provided to quantitatively illustrate the band gaps for flexural elastic wave propagation predicted by the current non-classical model and those by its classical elasticity-based counterpart. The effects of the foundation moduli, plate thickness, unit cell length and volume fraction on the band gaps are studied there. The chapter concludes in Section 6.4 with a summary.

6.2 Formulation

Based on the modified couple stress theory (Yang et al., 2002; Park and Gao, 2008), the surface elasticity theory (Gurtin and Murdoch, 1975, 1978) and a two-parameter Winkler-Pasternak elastic foundation model (e.g., Selvadurai, 1979; Yokoyama, 1996), the equations of motion for a Kirchhoff plate are derived in Chapter 2 (i.e., Eqs. (2.36a-c)), which incorporate the microstructure, surface energy and elastic foundation effects. When only the deflection is considered (i.e., $w = w(x, y, t)$, $u = 0$, $v = 0$), the equations of motion reduce to

$$\begin{aligned}&-\left[\frac{1}{12}(\lambda+2\mu)h^3+\mu l^2 h+\frac{1}{2}(\lambda_0+2\mu_0)h^2\right](w_{,xxxx}+2w_{,xxyy}+w_{,yyyy})\\&\quad+(2\tau_0+k_p)(w_{,xx}+w_{,yy})-k_w w+f_z-c_{x,y}+c_{y,x}=m_0\ddot{w}-m_2\frac{\partial^2\ddot{w}}{\partial x^2}-m_2\frac{\partial^2\ddot{w}}{\partial y^2},\end{aligned} \tag{6.1a}$$

which can be rewritten as

$$\begin{gathered}-\frac{\partial^2}{\partial x^2}\left(D\frac{\partial^2 w}{\partial x^2}+C\frac{\partial^2 w}{\partial y^2}\right)-\frac{\partial^2}{\partial y^2}\left(D\frac{\partial^2 w}{\partial y^2}+C\frac{\partial^2 w}{\partial x^2}\right)-\frac{\partial^2}{\partial x\partial y}\left(B\frac{\partial^2 w}{\partial x\partial y}\right)+\frac{\partial}{\partial x}\left(S\frac{\partial w}{\partial x}\right)+\frac{\partial}{\partial y}\left(S\frac{\partial w}{\partial y}\right)\\ -k_w w+k_p\left(\frac{\partial^2 w}{\partial x^2}+\frac{\partial^2 w}{\partial y^2}\right)+f_z-c_{x,y}+c_{y,x}=\frac{\partial^2}{\partial t^2}\left(P_1 w\right)-\frac{\partial^2}{\partial t^2}\left(P_2\frac{\partial^2 w}{\partial x^2}\right)-\frac{\partial^2}{\partial t^2}\left(P_2\frac{\partial^2 w}{\partial y^2}\right),\end{gathered} \tag{6.1b}$$

where $w = w(x, y, t)$ is the deflection (or z-displacement) of point $(x, y, 0)$ on the plate mid-plane at time t (see Fig. 6.1(a)), and

$$D=\frac{1}{12}(\lambda+2\mu)h^3+\mu l^2 h+\frac{1}{2}(\lambda_0+2\mu_0)h^2,\quad C=\frac{1}{12}h^3\lambda-\mu l^2 h+\frac{h^2}{2}(\lambda_0+\tau_0), \tag{6.2a,b}$$

$$B=\frac{1}{3}\mu h^3+4\mu l^2 h+h^2(2\mu_0-\tau_0),\quad S=2\tau_0,\quad P_1=\rho h,\quad P_2=\frac{\rho h^3}{12}. \tag{6.2c-f}$$

In Eqs. (6.1a,b) and (6.2a-f), λ and μ are the Lamé constants in classical elasticity, l is a material length scale parameter measuring the couple stress effect (e.g., Mindlin, 1963; Park and Gao, 2006), μ_0, λ_0 and τ_0 are the surface elastic constants, ρ is the mass density of the plate material, h is the uniform thickness of the plate, f_z is the z-component of the body force resultant (force per unit area) through the plate thickness acting on the plate mid-plane occupying the area R, c_x and c_y are, respectively, the x- and y- components of the body couple resultant (moment per unit area) through the plate thickness acting in the area R, k_w is the Winkler foundation modulus, and k_p is the Pasternak foundation modulus (e.g., Selvadurai, 1979; Yokoyama, 1996). The plate on the two-parameter elastic foundation is schematically shown in Fig. 6.1(b).

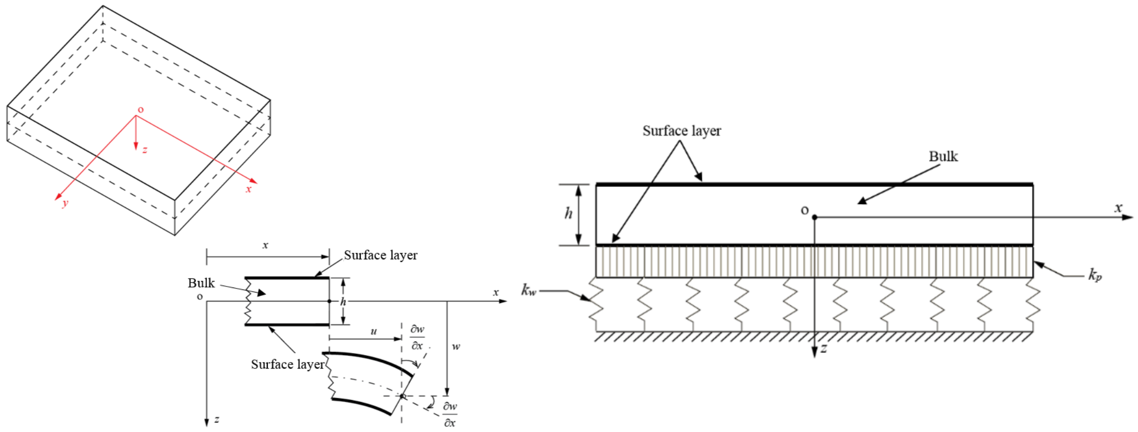

(a) (b)

Fig. 6.1 (a) Plate configuration and coordinate system; (b) plate on a two-parameter elastic foundation

Note that Eq. (6.1a) is obtained using the Cartesian coordinate system (x, y, z) shown in Fig. 6.1(a). The lower and upper surface layers (with zero-thickness) are taken to be perfectly bonded to the bulk plate material at $z = \pm h/2$, respectively. The bulk material satisfies the modified couple stress theory (Yang et al., 2002; Park and Gao, 2008), while the surface layers have distinct material properties and are governed by the surface elasticity theory (Gurtin and Murdoch, 1975, 1978).

Consider a periodic two-phase composite plate structure containing through-thickness square inclusions (as Phase I) embedded periodically in a host matrix (as Phase II) which is infinitely large in the xy-plane, as shown in Fig. 6.2. The unit cell for this periodic composite plate structure with a uniform thickness h is taken to be a square of edge length a containing a square inclusion of edge length d at its center, as illustrated in Fig. 6.3, where the corresponding irreducible first Brillouin zone is also provided.

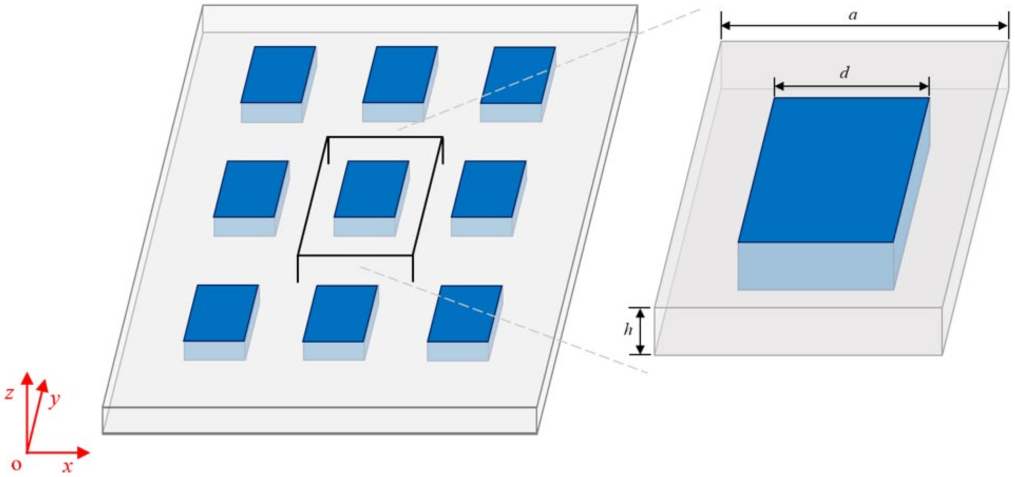

(a) (b)

Fig. 6.2 Periodic two-phase composite plate structure with a through-thickness square inclusion phase and a matrix phase: (a) the composite plate structure; (b) the unit cell.

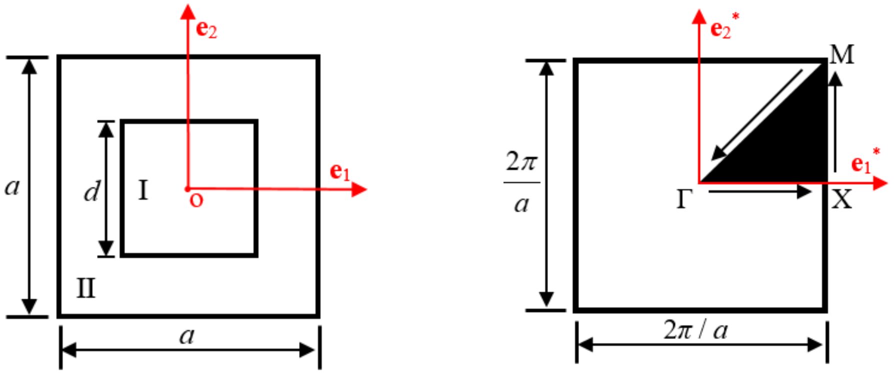

(a) (b)

Fig. 6.3 (a) Unit cell of the periodic composite plate with a square inclusion (phase I); (b) the irreducible first Brillouin zone in the reciprocal lattice.

Based on the plane-wave expansion method and Bloch theorem for periodic media, the deflection w can be written as a Fourier series of the following form (e.g., Kittel, 1986; Sigalas, 1997; Suzuki and Yu, 1998; Zhang et al., 2018b; Zhang and Gao, 2018):

$$w(\mathbf{r},t)=e^{i\mathbf{k}\cdot\mathbf{r}}\left[\sum_{\mathbf{G}'_{(m,n)}} w_{\mathbf{G}'_{(m,n)}} e^{i\mathbf{G}'_{(m,n)}\cdot\mathbf{r}}\right]e^{-i\omega t}, \tag{6.3}$$

where $w_{\mathbf{G}'_{(m,n)}}$ are the Fourier coefficients, $\mathbf{r} = (x, y)$ is the position vector, $\mathbf{k} = (k_x, k_y)$ is the

2-D Bloch wave vector, $\mathbf{G}'_{(m,n)} = (2\pi m / a, 2\pi n / a) = (G'_x, G'_y)$ is the 2-D reciprocal lattice vector for a square lattice with *m* and *n* being integers ranging from –∞ to +∞ and *a* being the lattice constant which is equal to the unit cell edge length here (see Fig. 6.3), ω is the angular frequency (in rad/s), and *i* is the imaginary unit satisfying $i^2 = -1$.

Due to the periodicity of the composite plate structure, each of the material parameters $D(\mathbf{r})$, $C(\mathbf{r})$, $B(\mathbf{r})$, $S(\mathbf{r})$, $P_1(\mathbf{r})$, $P_2(\mathbf{r})$, $k_w(\mathbf{r})$ and $k_p(\mathbf{r})$ involved in the wave equation given in Eq. (6.1b) can also be expanded in a Fourier series as

$$\alpha(\mathbf{r}) = \sum_{\mathbf{G}_{(M,N)}} \alpha_{\mathbf{G}_{(M,N)}} e^{i\mathbf{G}_{(M,N)}\cdot\mathbf{r}}, \tag{6.4}$$

where α represents *D*, *C*, *B*, *S*, P_1, P_2, k_w or k_p, $\mathbf{G}_{(M,N)} = (2\pi M / a,\ 2\pi N / a) = (G_x, G_y)$ is the 2-D reciprocal lattice vector with *M* and *N* being integers ranging from –∞ to +∞, and $\alpha_{\mathbf{G}}$ is the Fourier coefficient given by

$$\alpha_{\mathbf{G}_{(M,N)}} = \frac{1}{A}\iint_{\Omega} \alpha(\mathbf{r}) e^{-i\mathbf{G}_{(M,N)}\cdot\mathbf{r}} d\mathbf{r}, \tag{6.5}$$

where Ω denotes the 2-D domain on the plate mid-plane occupied by the unit cell, and *A* is the area of Ω. For a two-phase composite, $\alpha_{\mathbf{G}}$ can be shown to have the form:

$$\alpha_{\mathbf{G}} = \begin{cases} V_f^{(\mathrm{I})}\alpha_{\mathrm{I}} + (1 - V_f^{(\mathrm{I})})\alpha_{\mathrm{II}} & \text{for } \mathbf{G}_{(M,N)} = 0, \\ (\alpha_{\mathrm{I}} - \alpha_{\mathrm{II}}) F(\mathbf{G}_{(M,N)}) & \text{for } \mathbf{G}_{(M,N)} \neq 0, \end{cases} \tag{6.6}$$

where α_{I} and α_{II} are, respectively, the property values for materials I and II (see Fig. 6.3), $V_f^{(\mathrm{I})} = A^{(\mathrm{I})} / A$ is the volume fraction of material I, with $A^{(\mathrm{I})}$ being the area of material I on the plate mid-plane in the unit cell, and $F(\mathbf{G}_{(M,N)})$ is the shape function defined by

$$F(\mathbf{G}_{(M,N)}) = \frac{1}{A}\iint_{\Omega_{\mathrm{I}}} e^{-i\mathbf{G}_{(M,N)}\cdot\mathbf{r}} d\mathbf{r}, \tag{6.7}$$

where Ω_I is the domain occupied by material I (the inclusion phase) on the plate mid-plane in the unit cell.

For a square domain Ω_I (see Fig. 6.3(a)), the shape function $\mathrm{F}(\mathbf{G}_{(M,N)})$ is given by (e.g., Susa, 2002):

$$\mathrm{F}(\mathbf{G}_{(M,N)}) = \begin{cases} \dfrac{2d}{a^2 G_x}\sin(\dfrac{G_x d}{2}) \text{ for } G_x \neq 0,\ G_y = 0; \\ \dfrac{2d}{a^2 G_y}\sin(\dfrac{G_y d}{2}) \text{ for } G_x = 0,\ G_y \neq 0; \\ \dfrac{4}{a^2 G_x G_y}\sin(\dfrac{G_x d}{2})\sin(\dfrac{G_y d}{2}) \text{ for } G_x \neq 0,\ G_y \neq 0, \end{cases} \tag{6.8}$$

where d is the edge length of the square region Ω_I, and a is the edge length of the square unit cell Ω (see Fig. 6.3(a)).

Using Eqs. (6.3) and (6.4) in Eq. (6.1b) (with $f_z = c_x = c_y = 0$) results in, with the help of Laurent's rule for finding the Fourier coefficients of a product of two periodic functions (e.g., Li, 1996; Cao et al., 2004),

$$\left(M\right)_{\mathbf{G}_{(M,N)}-\mathbf{G}'_{(m,n)}} w_{\mathbf{G}'_{(m,n)}} = \omega^2 \left(R\right)_{\mathbf{G}_{(M,N)}-\mathbf{G}'_{(m,n)}} w_{\mathbf{G}'_{(m,n)}} \tag{6.9}$$

Where

$$\begin{aligned} \left(M\right)_{\mathbf{G}_{(M,N)}-\mathbf{G}'_{(m,n)}} &= D_{\mathbf{G}-\mathbf{G}'}(k_x+G_x)^2(k_x+G'_x)^2 + C_{\mathbf{G}-\mathbf{G}'}(k_x+G_x)^2(k_y+G'_y)^2 \\ &+ D_{\mathbf{G}-\mathbf{G}'}(k_y+G_y)^2(k_y+G'_y)^2 + C_{\mathbf{G}-\mathbf{G}'}(k_y+G_y)^2(k_x+G'_x)^2 + B_{\mathbf{G}-\mathbf{G}'}(k_x+G_x)(k_y+G_y)(k_x+G'_x)(k_y+G'_y) \\ &+ S_{\mathbf{G}-\mathbf{G}'}(k_x+G_x)(k_x+G'_x) + S_{\mathbf{G}-\mathbf{G}'}(k_y+G_y)(k_y+G'_y) + \left(k_w\right)_{\mathbf{G}-\mathbf{G}'} + \left(k_p\right)_{\mathbf{G}-\mathbf{G}'}(k_x+G'_x)^2 + \left(k_p\right)_{\mathbf{G}-\mathbf{G}'}(k_y+G'_y)^2, \end{aligned} \tag{6.10}$$

$$\left(R\right)_{\mathbf{G}_{(M,N)}-\mathbf{G}'_{(m,n)}} = \left(P_1\right)_{\mathbf{G}-\mathbf{G}'} + \left(P_2\right)_{\mathbf{G}-\mathbf{G}'}(k_x+G'_x)^2 + \left(P_2\right)_{\mathbf{G}-\mathbf{G}'}(k_y+G'_y)^2, \tag{6.11}$$

$$w_{\mathbf{G}'_{(m,n)}} = \frac{1}{A}\iint_{\Omega} w e^{-i\left(\mathbf{G}'_{(m,n)}+\mathbf{k}\right)\cdot\mathbf{r}} d\mathbf{r}, \tag{6.12}$$

in which

$$\alpha_{\mathbf{G}-\mathbf{G}'} = \frac{1}{A}\iint_{\Omega} \alpha e^{-i\left(\mathbf{G}_{(M,N)}-\mathbf{G}'_{(m,n)}\right)\cdot\mathbf{r}} d\mathbf{r}, \tag{6.13}$$

where $\alpha_{\mathbf{G}-\mathbf{G}'}$ represents $D_{\mathbf{G}-\mathbf{G}'}, C_{\mathbf{G}-\mathbf{G}'}, B_{\mathbf{G}-\mathbf{G}'}, S_{\mathbf{G}-\mathbf{G}'}, \left(P_1\right)_{\mathbf{G}-\mathbf{G}'}, \left(P_2\right)_{\mathbf{G}-\mathbf{G}'}, \left(k_w\right)_{\mathbf{G}-\mathbf{G}'}$ or $\left(k_p\right)_{\mathbf{G}-\mathbf{G}'}$.

When w and α (representing D, C, B, S, P_1, P_2, k_w or k_p) are approximated by truncated Fourier series expansions with m, n, M and N ranging from $-L$ to L, with L being an integer, Eq. (6.9) gives $(2L+1)^2$ equations, which can be assembled to yield the following system:

$$\left[(M)_{\mathbf{G}-\mathbf{G}'}\right]\left\{w_{\mathbf{G}'}\right\} = \omega^2\left[(R)_{\mathbf{G}-\mathbf{G}'}\right]\left\{w_{\mathbf{G}'}\right\}, \tag{6.14}$$

Where

$$\left[(M)_{\mathbf{G}-\mathbf{G}'}\right] = \begin{bmatrix} M_{\left(\mathbf{G}_{(-L,-L)}-\mathbf{G}'_{(-L,-L)}\right)} & M_{\left(\mathbf{G}_{(-L,-L)}-\mathbf{G}'_{(-L,-L+1)}\right)} & \cdots & M_{\left(\mathbf{G}_{(-L,-L)}-\mathbf{G}'_{(L,L-1)}\right)} & M_{\left(\mathbf{G}_{(-L,-L)}-\mathbf{G}'_{(L,L)}\right)} \\ M_{\left(\mathbf{G}_{(-L,-L+1)}-\mathbf{G}'_{(-L,-L)}\right)} & M_{\left(\mathbf{G}_{(-L,-L+1)}-\mathbf{G}'_{(-L,-L+1)}\right)} & \cdots & M_{\left(\mathbf{G}_{(-L,-L+1)}-\mathbf{G}'_{(L,L-1)}\right)} & M_{\left(\mathbf{G}_{(-L,-L+1)}-\mathbf{G}'_{(L,L)}\right)} \\ \vdots & \vdots & & \vdots & \vdots \\ M_{\left(\mathbf{G}_{(L,L-1)}-\mathbf{G}'_{(-L,-L)}\right)} & M_{\left(\mathbf{G}_{(L,L-1)}-\mathbf{G}'_{(-L,-L+1)}\right)} & \cdots & M_{\left(\mathbf{G}_{(L,L-1)}-\mathbf{G}'_{(L,L-1)}\right)} & M_{\left(\mathbf{G}_{(L,L-1)}-\mathbf{G}'_{(L,L)}\right)} \\ M_{\left(\mathbf{G}_{(L,L)}-\mathbf{G}'_{(-L,-L)}\right)} & M_{\left(\mathbf{G}_{(L,L)}-\mathbf{G}'_{(-L,-L+1)}\right)} & \cdots & M_{\left(\mathbf{G}_{(L,L)}-\mathbf{G}'_{(L,L-1)}\right)} & M_{\left(\mathbf{G}_{(L,L)}-\mathbf{G}'_{(L,L)}\right)} \end{bmatrix}, \tag{6.15}$$

$$\left[(R)_{\mathbf{G}-\mathbf{G}'}\right] = \begin{bmatrix} R_{\left(\mathbf{G}_{(-L,-L)}-\mathbf{G}'_{(-L,-L)}\right)} & R_{\left(\mathbf{G}_{(-L,-L)}-\mathbf{G}'_{(-L,-L+1)}\right)} & \cdots & R_{\left(\mathbf{G}_{(-L,-L)}-\mathbf{G}'_{(L,L-1)}\right)} & R_{\left(\mathbf{G}_{(-L,-L)}-\mathbf{G}'_{(L,L)}\right)} \\ R_{\left(\mathbf{G}_{(-L,-L+1)}-\mathbf{G}'_{(-L,-L)}\right)} & R_{\left(\mathbf{G}_{(-L,-L+1)}-\mathbf{G}'_{(-L,-L+1)}\right)} & \cdots & R_{\left(\mathbf{G}_{(-L,-L+1)}-\mathbf{G}'_{(L,L-1)}\right)} & R_{\left(\mathbf{G}_{(-L,-L+1)}-\mathbf{G}'_{(L,L)}\right)} \\ \vdots & \vdots & & \vdots & \vdots \\ R_{\left(\mathbf{G}_{(L,L-1)}-\mathbf{G}'_{(-L,-L)}\right)} & R_{\left(\mathbf{G}_{(L,L-1)}-\mathbf{G}'_{(-L,-L+1)}\right)} & \cdots & R_{\left(\mathbf{G}_{(L,L-1)}-\mathbf{G}'_{(L,L-1)}\right)} & R_{\left(\mathbf{G}_{(L,L-1)}-\mathbf{G}'_{(L,L)}\right)} \\ R_{\left(\mathbf{G}_{(L,L)}-\mathbf{G}'_{(-L,-L)}\right)} & R_{\left(\mathbf{G}_{(L,L)}-\mathbf{G}'_{(-L,-L+1)}\right)} & \cdots & R_{\left(\mathbf{G}_{(L,L)}-\mathbf{G}'_{(L,L-1)}\right)} & R_{\left(\mathbf{G}_{(L,L)}-\mathbf{G}'_{(L,L)}\right)} \end{bmatrix} \tag{6.16}$$

are two $(2L+1)^2 \times (2L+1)^2$ matrices, and

$$\{w_{\mathbf{G}'}\} = \begin{Bmatrix} w_{\mathbf{G}'_{(-L,-L)}} \\ w_{\mathbf{G}'_{(-L,-L+1)}} \\ \vdots \\ w_{\mathbf{G}'_{(L,L-1)}} \\ w_{\mathbf{G}'_{(L,L)}} \end{Bmatrix} \tag{6.17}$$

is a $(2L+1)^2 \times 1$ column matrix.

Note that for a non-trivial solution of $w_{\mathbf{G}'_{(m,n)}} \neq 0$, it is required that the determinant of the coefficient matrix vanish, i.e.,

$$\left| [\mathbf{T}] - \omega^2 [\mathbf{I}] \right| = 0, \tag{6.18}$$

where

$$[\mathbf{T}] = \left[(R)_{\mathbf{G}-\mathbf{G}'} \right]^{-1} \left[(M)_{\mathbf{G}-\mathbf{G}'} \right], \tag{6.19}$$

and $\mathbf{I}$ is the $(2L+1)^2 \times (2L+1)^2$ identity (unit) matrix. Equation (6.18) is the characteristic equation of the eigenvalue problem defined in Eq. (6.14), which is a polynomial equation in ω^2 of degree $(2L+1)^2$. By increasing the value of the integer L, the convergent solution can be obtained. For a given wave vector $\mathbf{k} = (k_x, k_y)$ in the first Brillouin zone shown in Fig. 6.3, the corresponding eigen-frequencies ω can be obtained from the roots of Eq. (6.18). The ranges of ω over which there exists no real-valued wave vector $\mathbf{k}$ will give band gaps. It is seen from Eqs. (6.18), (6.19), (6.15), (6.16), (6.10), (6.11), (6.13), (6.6), (6.8) and (6.2a-f) that the value of ω depends on the material constants λ, μ, l, λ_0, μ_0, τ_0 and ρ, the foundation moduli k_w and k_p, and the geometrical parameters a, d and h.

The classical elasticity-based band gaps for flexural elastic wave propagation in the periodic composite plate structure resting on the Winkler-Pasternak elastic foundation can be obtained as a special case by setting $l = 0$ and $\lambda_0 = \mu_0 = \tau_0 = 0$ in the relevant equations (i.e., with both the microstructure and surface energy effects suppressed).

6.3 Numerical Results and Discussion

To quantitatively illustrate the new non-classical model developed in Section 6.2, some numerical results are presented in this section. In generating these results, material I is taken to be iron with the following properties (e.g., Gurtin and Murdoch, 1978): $E^{(\mathrm{I})}$ = 177.33 GPa, $\nu^{(\mathrm{I})} = 0.27$, $l^{(\mathrm{I})}$ = 6.76 μm, ρ = 7 g/cm^3 for the bulk, and $\mu_0^{(\mathrm{I})}$ = 2.5 N/m, $\lambda_0^{(\mathrm{I})}$ = −8 N/m, $\tau_0^{(\mathrm{I})}$ = 1.7 N/m for the surface layer. Note that the value of the length scale parameter $l^{(\mathrm{I})}$ listed above is computed using $l = b_h / \sqrt{3(1-\nu)}$ (e.g., Lam et al., 2003; Park and Gao, 2006) with Poisson's ratio $\nu^{(\mathrm{I})} = 0.27$ and the higher-order bending parameter $b_h^{(\mathrm{I})}$ = 10 μm (e.g., Wang, 2010). Material II is chosen to be epoxy with the following properties (Chen and Wang, 2014): $E^{(\mathrm{II})}$ = 3.3 GPa, $\nu^{(\mathrm{II})} = 0.33$, $l^{(\mathrm{II})}$ = 16.93 μm, $\rho^{(\mathrm{II})}$ = 1.18 g/cm^3 for the bulk, and $\mu_0^{(\mathrm{II})}$ = 0.12406 N/m, $\lambda_0^{(\mathrm{II})} = 0.16376$ N/m, $\tau_0^{(\mathrm{II})}$ = 0.045 N/m for the surface layer. Note that the value of the length scale parameter $l^{(\mathrm{II})}$ given here is also computed using $l = b_h / \sqrt{3(1-\nu)}$ but with Poisson's ratio $\nu^{(\mathrm{II})} = 0.33$ and the higher-order bending parameter $b_h^{(\mathrm{II})}$ = 24 μm (e.g., Lam et al., 2003). The values of the surface elastic constants $\mu_0^{(\mathrm{II})}$ and $\lambda_0^{(\mathrm{II})}$ listed above are estimated using $\mu_0^{(\mathrm{II})} = \mu^{(\mathrm{II})} h^S$ and $\lambda_0^{(\mathrm{II})} = 2\lambda^{(\mathrm{II})}\mu^{(\mathrm{II})} h^S / (\lambda^{(\mathrm{II})} + \mu^{(\mathrm{II})})$ (Sharma and Ganti, 2004), where h^S is the thickness of transition zone and is taken to be 1 Angstrom (e.g., Miller and Shenoy, 2000), and $\lambda^{(\mathrm{II})}$, $\mu^{(\mathrm{II})}$ are the Lamé constants of the bulk epoxy given by $\lambda^{(\mathrm{II})} = E^{(\mathrm{II})}\nu^{(\mathrm{II})} / [(1+\nu^{(\mathrm{II})})(1-2\nu^{(\mathrm{II})})]$, $\mu^{(\mathrm{II})} = E^{(\mathrm{II})} / [2(1+\nu^{(\mathrm{II})})]$. In addition, $\tau_0^{(\mathrm{II})}$ is the surface tension for epoxy having a value of 45 mN/m (e.g., George, 1993; Lewin et al., 2005). The foundation moduli k_w and k_p are non-dimensionalized to obtain $\bar{K}_w \equiv k_w a^4 / D_C^{(\mathrm{I})}$, $\bar{K}_p \equiv k_p a^2 / D_C^{(\mathrm{I})}$, with $D_C^{(\mathrm{I})} = E^{(\mathrm{I})} h^3 / \{12[1-(\nu^{(\mathrm{I})})^2]\}$ being the plate flexural rigidity of material I. Moreover, the edge length of the square inclusion is taken to be $d = 0.4a$ (i.e., $V_f^{\mathrm{I}} = d^2 / a^2 = 0.16$) in all the calculations for simplicity. In Figs. 6.4-6.7, the blue dot lines represent the wave frequency curves obtained from solving Eq. (6.18). In all the cases, the convergent solutions are reached with $L = 7$.

Note that in the numerical analysis presented here, the first band gap in each case is defined to be that between the fourth and fifth frequency curves, which is first observed for the periodic composite plate structure without the elastic foundation (see Fig. 6.4(a)). This corresponds to the lowest range of ω that prohibits flexural wave propagation in the periodic composite plate structure without including the foundation effect. In addition, the first band gap for the composite plate structure with the elastic foundation, called the first foundation band gap, is identified and discussed. The other band gaps for each periodic composite plate structure with specified geometrical and material parameters can be found by following the same procedure.

6.3.1 Effects of the elastic foundation on band gaps

Figure 6.4 shows the band gaps for the periodic composite plate structure with square inclusions (see Fig. 6.2), where $f = \omega/(2\pi)$ is the wave frequency. The unit cell length a is taken to be 1 mm and the plate thickness $h = 15$ μm.

Figure 6.4(a) illustrates the first band gap frequency range predicted by the current non-classical model without the foundation (i.e., $\bar{K}_w = 0,\ \bar{K}_p = 0$), which is 175.42−190.50 kHz (marked in orange). Figures 6.4(c) and 6.4(e) display the band gap frequency ranges predicted by the new non-classical model with the Winkler foundation (i.e., $k_p = 0$): the first band gap and the first foundation band gap of 177.33−192.17 kHz and 0−20.66 kHz for the case with $\bar{K}_w = 10$ and $\bar{K}_p = 0$; 193.67−206.85 kHz and 0−62.97 kHz for the case with $\bar{K}_w = 100$ and $\bar{K}_p = 0$. Figures 6.4(b), 6.4(d) and 6.4(f) show the band gap frequency ranges predicted by the current non-classical model with the Winkler-Pasternak foundation: the first band gap and the first foundation band gap of 186.82−199.32 kHz and 0−20.69 kHz for the case with $\bar{K}_w = 10$ and $\bar{K}_p = 1$; 202.33−213.52 kHz and 0−63.18 kHz for the case with $\bar{K}_w = 100$ and $\bar{K}_p = 1$. For the case with $\bar{K}_w = 100$ and $\bar{K}_p = 10$, the first foundation band gap frequency range is 0−64.17 kHz, but there is no band gap existing between the fourth and fifth frequency curves (which would be called the first band gap to be consistent with that in the other cases), even though a band gap appears at a lower frequency (between the first and second frequency curves, as indicated in green in Fig. 6.4(f). This is called the second foundation band gap, which also exists in the cases with $\bar{K}_w = 100,\ \bar{K}_p = 1$ and $\bar{K}_w = 100,\ \bar{K}_p = 0$, as shown in Figs. 6.4(d) and 6.4(e). The band gaps calculated from these frequency ranges are listed in Table 6.1.

Table 6.1 Band gaps for the periodic composite plate structure with different values of the foundation moduli $\bar{K}_w$ and $\bar{K}_p$ predicted by the current model (with a = 1 mm, h = 15 μm)

Foundation moduli		First band gap (kHz)	First foundation band gap (kHz)	Second foundation band gap (kHz)
$\bar{K}_w$	$\bar{K}_p$			
0	0	15.08	NA	NA
10	0	14.84	20.66	NA
10	1	12.50	20.69	NA
100	0	13.18	62.97	14.85
100	1	11.19	63.18	14.89
100	10	NA	64.17	16.76

From Fig. 6.4 and Table 6.1, it is observed that the first band gap frequency ranges predicted by the current non-classical model decrease with the increase of either $\bar{K}_w$ or $\bar{K}_p$. However, the first foundation band gap frequency ranges predicted by the new non-classical model increase with these two foundation moduli. In addition, it is observed from Fig. 6.4 that the presence of the Winkler-Pasternak foundation reduces the first band gap size, and this effect is more significant than that of the Winkler foundation (i.e., $k_p = 0$).

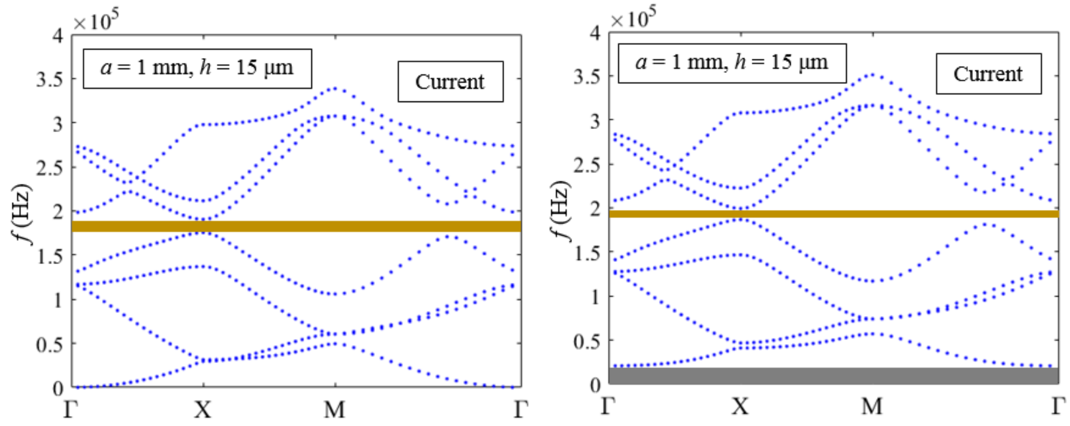

(a) (b)

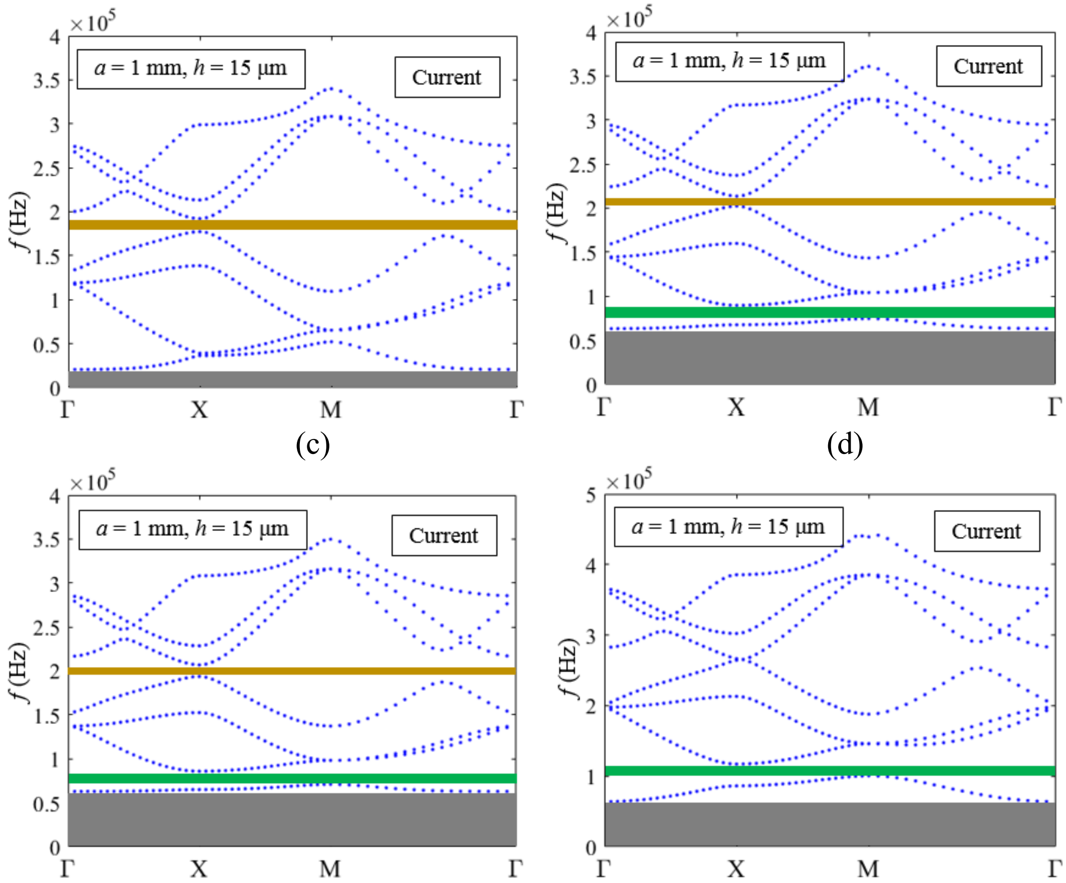

(c) (d)

(e) (f)

Fig. 6.4 Band gaps for the periodic composite plate structure predicted by the current model with: (a) $\bar{K}_w = 0,\ \bar{K}_p = 0$ (i.e., without foundation), (b) $\bar{K}_w = 10,\ \bar{K}_p = 1$, (c) $\bar{K}_w = 10,\ \bar{K}_p = 0$, (d) $\bar{K}_w = 100,\ \bar{K}_p = 1$, (e) $\bar{K}_w = 100,\ \bar{K}_p = 0$, and (f) $\bar{K}_w = 100,\ \bar{K}_p = 10$. The Bloch wave vector **k** = (k_x, k_y) at Γ, X and M is, respectively, (0, 0), (π/a, 0) and (π/a, π/a) (see Fig. 6.3(b)).

6.3.2 Effects of the microstructure and surface energy on band gaps

Figure 6.5 displays the band gaps for the periodic composite plate structure predicted by the current model with a = 1 mm and $\bar{K}_w = 10,\ \bar{K}_p = 1$. Figures 6.5(a), 6.5(c), 6.5(e) and 6.5(g) show the first band gap frequency ranges (in orange) and the first foundation band gap frequency ranges (in grey) predicted by the current non-classical model for different values of the plate thickness: 186.82−199.32 kHz and 0−20.69 kHz for h = 15 μm;

322.81−355.31 kHz and 0−55 kHz for h = 40 μm; 581.07−638.05 kHz and 0−109.86 kHz for h = 80 μm; and 841.20−923.78 kHz and 0−164.73 kHz for h = 120 μm.

Figures 6.5(b), 6.5(d), 6.5(f) and 6.5(h) illustrate the first band gap frequency ranges (in orange) and the first foundation band gap frequency ranges (in grey) predicted by the classical elasticity-based model for different values of the plate thickness: 106.28−116.50 kHz and 0−20.59 kHz for h = 15 μm: 282.65−309.87 kHz and 0−54.9 kHz for h = 40 μm; 560.00−614.20 kHz and 0−109.8 kHz for h = 80 μm; 827.20−907.90 kHz and 0−164.68 kHz for h = 120 μm. The band gaps calculated from these frequency ranges are listed in Tables 6.2 and 6.3 respectively, where the relative difference is defined to be the difference between the two band gap values over the value based on the classical model in each case.

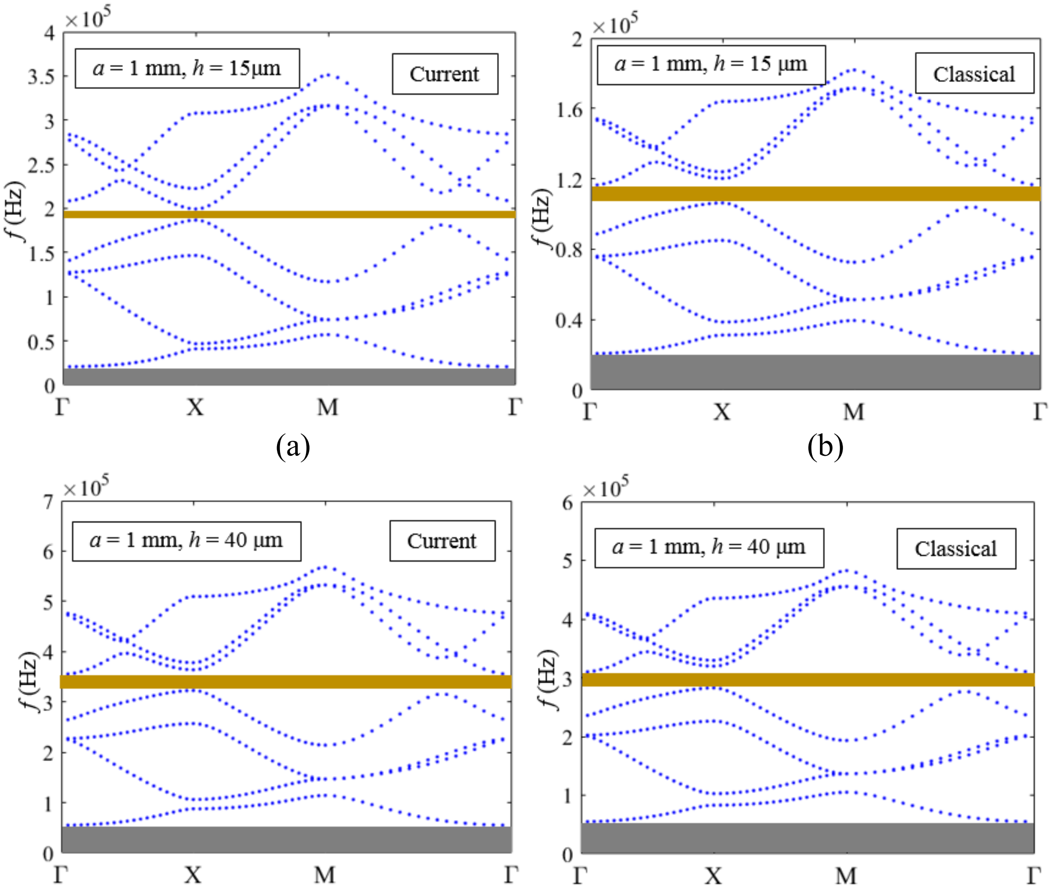

(a) (b)

(c) (d)

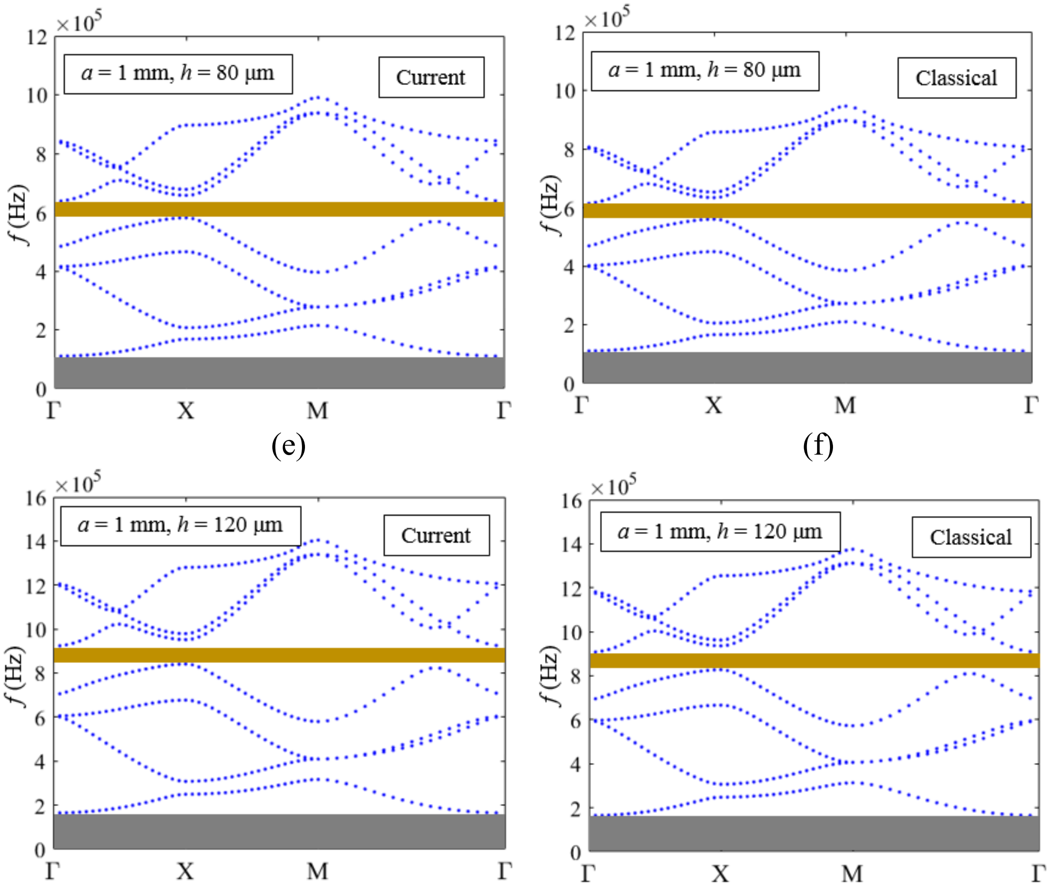

(e) (f)

(g) (h)

Fig. 6.5 Band gaps for the periodic composite plate structure (with $a = 1$ mm, $\bar{K}_w = 10$, $\bar{K}_p = 1$) predicted by: (a) the current model with $h = 15$ μm, (b) the classical model with $h = 15$ μm, (c) the current model with $h = 40$ μm, (d) the classical model with $h = 40$ μm, (e) the current model with $h = 80$ μm, (f) the classical model with $h = 80$ μm, (g) the current model with $h = 120$ μm, and (h) the classical model with $h = 120$ μm. The Bloch wave vector $\mathbf{k} = (k_x, k_y)$ at Γ, X and M is, respectively, (0, 0), (π/a, 0) and (π/a, π/a) (see Fig. 6.3(b)).

Table 6.2 First band gaps for the periodic composite plate structure with different values of the plate thickness h

h (μm)	Band gap (kHz) Current model	Band gap (kHz) Classical model	Relative difference (%)
15	12.50	10.22	22.31
40	32.50	27.22	19.40
80	56.98	54.20	5.13
120	82.58	80.70	2.33

Table 6.3 First foundation band gaps for the periodic composite plate structure with different values of the plate thickness *h*

h (μm)	Band gap (kHz) Current model	Band gap (kHz) Classical model	Relative difference (%)
15	20.69	20.59	0.49
40	55.00	54.90	0.18
80	109.86	109.80	0.05
120	164.73	164.68	0.03

It is observed from Fig. 6.5 and Table 6.2 that the first band gap predicted by the current non-classical model is always larger than that predicted by the classical model. Also, when the plate thickness *h* is small (with *h* = 15 μm here), the difference between the two band gap values is large, with the band gap predicted by the current non-classical model being 1.22 times as large as that predicted by the classical model (giving a relative difference of 22.31%). However, the difference is diminishing with the increase of the plate thickness *h*. When *h* = 120 μm, the band gap predicted by the current model is only 1.02 times of that predicted by the classical model, with the relative difference being only 2.33%. This indicates that the microstructure and surface energy effects on the first band gap are significant only when the plate thickness is very small.

From Fig. 6.5 and Table 6.3, it is clearly seen that the first foundation band gap predicted by the current non-classical model is always larger than that predicted by the classical model. However, the difference decreases with the increase of the plate thickness *h*. In addition, this difference is negligibly small compared to the difference between the two first band gap values. This shows that the microstructure and surface energy effects on the first foundation band gap are insignificant.

6.3.3 Effect of the unit cell length on band gaps

Figure 6.6 displays the first band gap (in orange) and the first foundation band gap (in grey) for the periodic composite plate structure predicted by the current model for different values of the unit cell length *a*. The plate thickness is *h* = 15 μm, and the elastic foundation moduli are $\bar{K}_w = 10$, $\bar{K}_p = 1$ in all cases.

The first band gap frequency range and the first foundation band gap frequency range are, respectively, 2065.9−2204.6 kHz and 0−229.89 kHz for the case with *a* = 20*h* shown in Fig. 6.6(a); 518.45−553.19 kHz and 0−57.48 kHz for the case with *a* = 40*h* displayed in Fig. 6.6(b); 83.07−88.63 kHz and 0−9.20 kHz for the case with *a* = 100*h* depicted in Fig. 6.6(c); and 20.80−22.18 kHz and 0−2.30 kHz for the case with *a* = 200*h* illustrated in Fig. 6.6(d). The band gaps calculated from these frequency ranges are listed in Table 6.4.

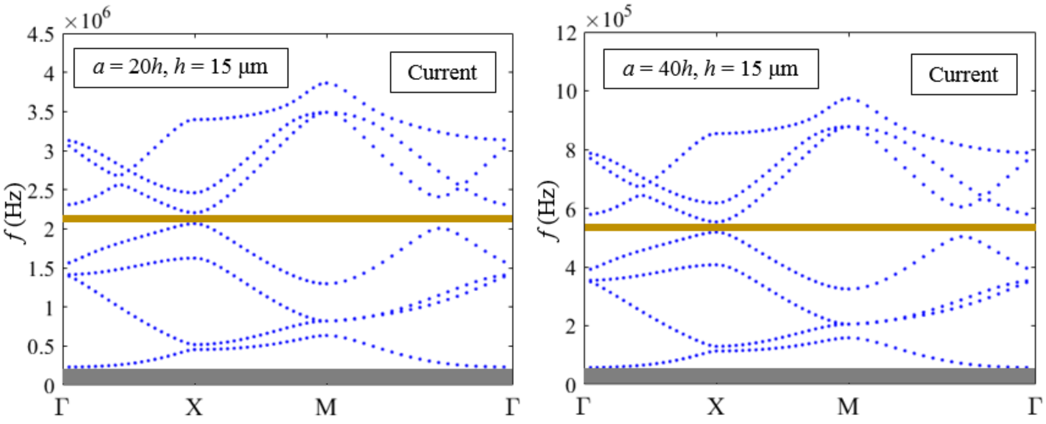

(a) (b)

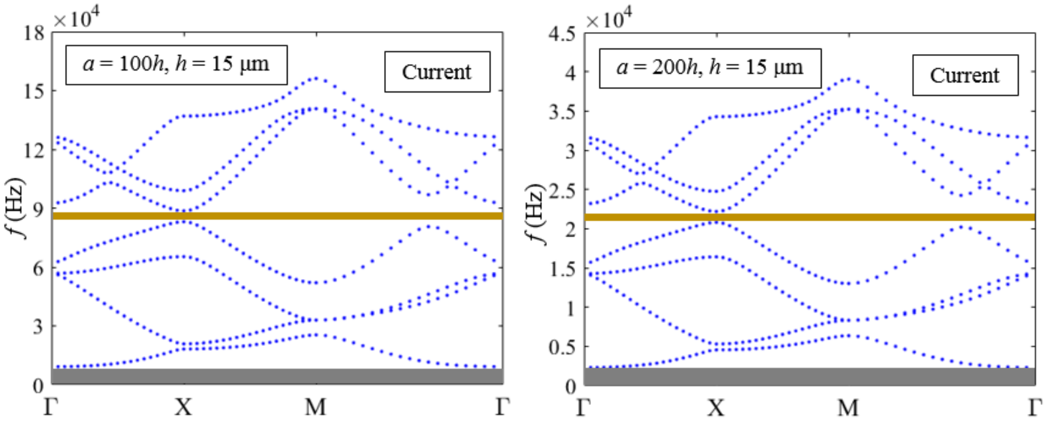

(c) (d)

Fig. 6.6 Band gaps for the periodic composite plate structure with h = 15 μm, $\bar{K}_w = 10$, $\bar{K}_p = 1$ predicted by the current model for (a) $a = 20h$, (b) $a = 40h$, (c) $a = 100h$, and (d) $a = 200h$. The Bloch wave vector $\mathbf{k} = (k_x, k_y)$ at Γ, X and M is, respectively, (0, 0), (π/a, 0) and (π/a, π/a) (see Fig. 6.3(b)).

Table 6.4 Band gaps for the periodic composite plate structure with different values of the unit cell length a predicted by the current model (with h = 15 μm, $\bar{K}_w = 10$ and $\bar{K}_p = 1$)

a	First band gap (kHz)	First foundation band gap (kHz)
$20h$	138.7	229.89
$40h$	34.74	57.48
$100h$	5.56	9.20
$200h$	1.38	2.30

From Fig. 6.6 and Table 6.4, it is seen that the frequency for producing the first band gap or the first foundation band gap becomes lower as the unit cell length a gets larger and the band gap size decreases with the increase of a. To further illustrate the effect of the unit cell length on band gaps, Fig. 6.7 shows that the first band gap for the periodic composite plate structure with h = 1 mm, which is much larger than h = 12 μm used in getting the results shown in Fig. 6.6 or h = 120 μm identified in Section 6.3.2 to be a plate thickness above which the microstructure and surface energy effects on band gaps are negligible.

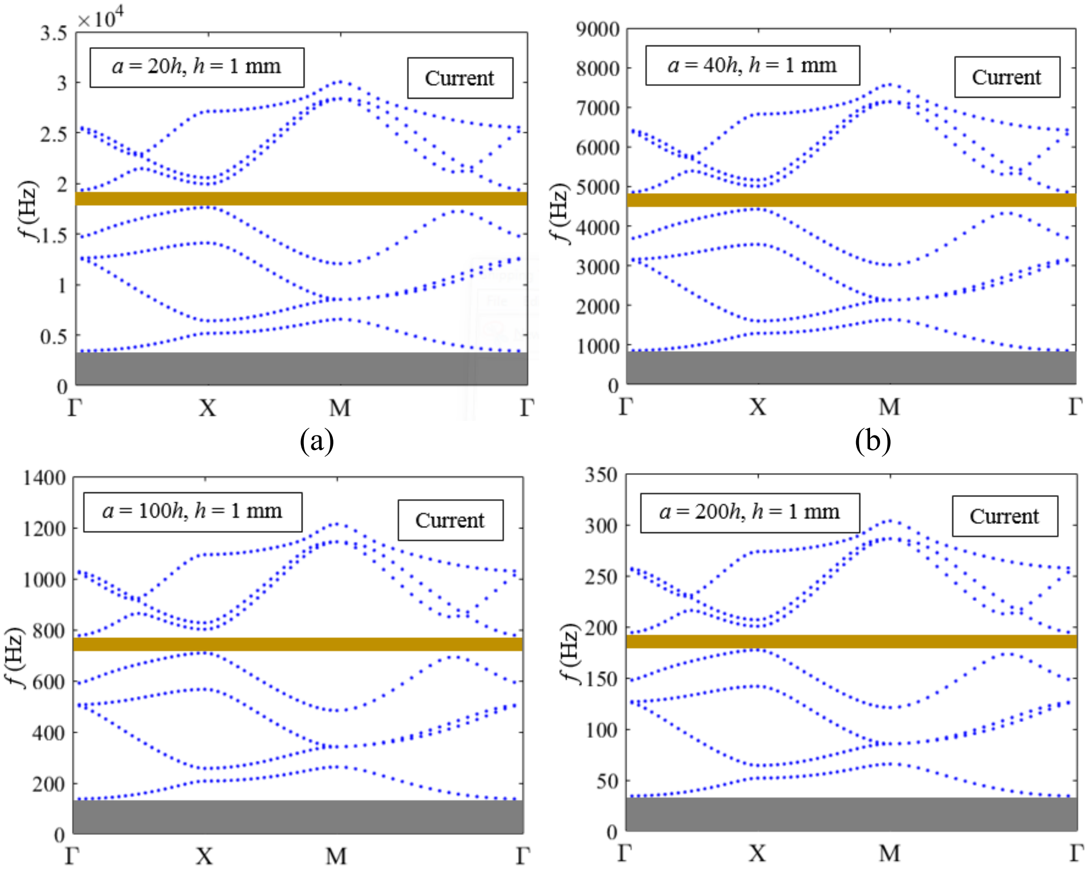

(a) (b)

(c) (d)

Fig. 6.7 Band gaps for the periodic composite plate structure with h = 1mm, $\overline{K}_w = 10$, $\overline{K}_p = 1$ predicted by the current model for (a) a = 20h, (b) a = 40h, (c) a = 100h, and (d) a = 200h. The Bloch wave vector $\mathbf{k} = (k_x, k_y)$ at Γ, X and M is, respectively, (0, 0), (π/a, 0) and (π/a, π/a) (see Fig. 6.3(b)).

Figure 6.7 illustrates the first band gap frequency ranges (in orange) predicted by the current model for the composite plate structure with h = 1 mm, $\overline{K}_w = 10$, $\overline{K}_p = 1$ and different values of the unit cell length: 17639−19339 Hz for a = 20h, 4426.1−4851.9 Hz for a = 40h, 708.93−777.08 Hz for a = 100h, and 177.27−194.30 Hz for a = 200h. Also, Figure 6.7 displays the first foundation band gap frequency ranges for different values of the unit cell length: 0−3431 MHz, 0−857.9 MHz, 0−137.26 MHz and 0−34.32 MHz for the cases with a = 20h, 40h, 100h and 200h, respectively. The band gaps calculated from these frequency ranges are listed in Table 6.5. It is found that for this plate thickness of h = 1 mm the band gap frequency ranges and band gap sizes predicted by the classical elasticity-based model are the same as the corresponding ones predicted by the current non-classical model and shown in Figs. 6.7(a)–(d).

Table 6.5 Band gaps for the periodic composite plate structure with different values of the unit cell length a predicted by the current model (with h = 1mm and $\bar{K}_w = 10,\ \bar{K}_p = 1$)

a	First band gap (Hz)	First foundation band gap (Hz)
$20h$	1700	3431
$40h$	425.8	857.9
$100h$	68.15	137.26
$200h$	17.03	34.32

It is clear from comparing the numerical values shown in Fig. 6.7 and Table 6.5 that both the frequency for producing the first band gap and the sizes of the first band gap and the first foundation band gap decrease with the increase of the unit cell length a, which is the same as that observed from Fig. 6.6 for the cases with h = 15 μm. Moreover, the fact that the trends of both the first band gap and the first foundation band gap changing with the unit cell length predicted by the classical model are the same as those predicted by the non-classical model indicates that the effect of the unit cell length on band gaps is present at all length scales.

6.3.4 Effects of the volume fraction on band gaps

The variations of the first band gap and the first foundation band gap with the volume fraction of material I are shown in Figs. 6.8 and 6.9, respectively. For comparison purposes, the first band gap and the first foundation band gap variations predicted by the classical elasticity-based model are also plotted in Figs. 6.8 and 6.9. The numerical values for wave frequency shown in Figs. 6.8 and 6.9 are obtained from solving Eq. (6.18). In all the cases, the convergent solutions are reached with $L = 7$. The properties for materials I and II used here are the same as those employed earlier to obtain the numerical results shown in Figs. 6.4–6.7. Here the unit cell length a is taken to be 1 mm, the plate thickness h is chosen to be 15 μm, and the foundation moduli are specified as $\bar{K}_w = 10$ and $\bar{K}_p = 1$.

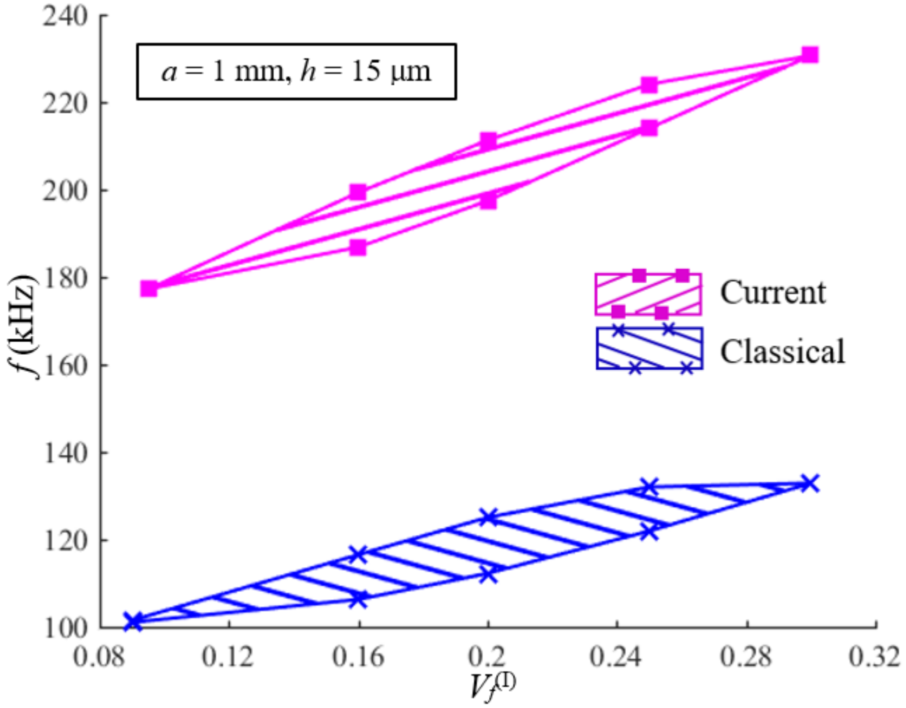

Fig. 6.8 First band gap changing with $V_f^{(\mathrm{I})}$ predicted by the current and classical models for the periodic composite plate structure (with $a = 1$ mm, $h = 15$ μm, $\bar{K}_w = 10$ and $\bar{K}_p = 1$).

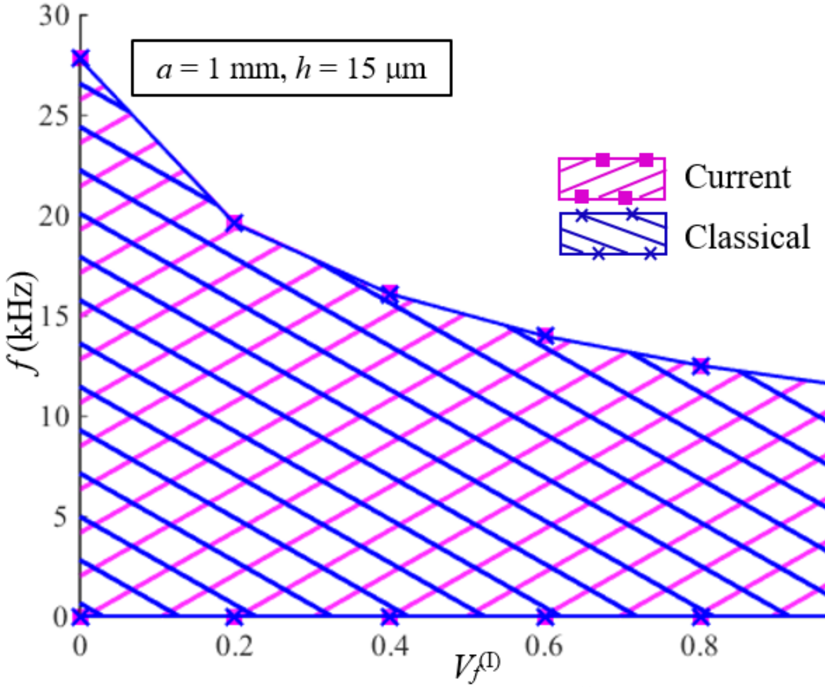

Fig. 6.9 First foundation band gap changing with $V_f^{(\mathrm{I})}$ predicted by the current and classical models for the periodic composite plate structure (with $a = 1$ mm, $h = 15$ μm, $\bar{K}_w = 10$ and $\bar{K}_p = 1$).

From Fig. 6.8, it is clearly seen that the first band gap predicted by the current model for the periodic composite plate structure starts at $V_f^{(\mathrm{I})} = 9.5\%$ and gradually increases with the increase of $V_f^{(\mathrm{I})}$ before reaching its maximum of 13.82 kHz at $V_f^{(\mathrm{I})} = 20\%$, after which the first band gap decreases with $V_f^{(\mathrm{I})}$ until it disappears at $V_f^{(\mathrm{I})} = 30\%$. Also, the first band gap predicted by the classical elasticity-based model increases from zero to its maximum value 13.31 kHz as the volume fraction $V_f^{(\mathrm{I})}$ increases from 9% to 21%, then it decreases with the increase of $V_f^{(\mathrm{I})}$ until it vanishes at $V_f^{(\mathrm{I})} = 30\%$.

From Fig. 6.9, it is observed that the first foundation band gap predicted by the current non-classical model or the classical elasticity-based model gradually decreases with the increase of $V_f^{(\mathrm{I})}$ from 0% to 100%, and the first foundation band gap values predicted by the current non-classical model and the classical elasticity-based model are very close.

Once again, these indicate that the microstructure and surface energy effects on the first foundation band gap are not significant.

From Figs. 6.8 and 6.9, it is clear that the volume fraction does have a significant effect on the first band gap and the first foundation band gap for the periodic composite plate structure according to both the current non-classical model and its classical elasticity-based counterpart. These results indicate that large band gaps can be attained by tailoring the volume fraction.

6.4 Summary

A new model for predicting band gaps for elastic wave propagation in a periodic composite plate structure is provided by employing a non-classical Kirchhoff plate model, the plane wave expansion method and the Bloch theorem. The current non-classical model recovers the classical elasticity-based model when the microstructure and surface energy effects are both suppressed. The band gaps predicted by the new model incorporate the microstructure, surface energy and elastic foundation effects and vary with the unit cell size and volume fraction of the inclusion phase.

Numerical results are included to illustrate the newly developed model and compare it with the classical elasticity-based model. It is found that the first band gap predicted by the current model with the foundation is smaller than that without the foundation, and the first foundation band gap increases with the elastic foundation moduli. In addition, the first band gap predicted by the new non-classical model is seen to be always larger than that based on the classical model, with the difference being significant for very thin plates. It is also observed that the first band gap frequency and the band gap size decrease with the increase of the unit cell length for both the first band gap and the first foundation band gap. Finally, the numerical results reveal that the band gap size varies significantly with the volume fraction of the inclusion phase, indicating that large band gaps can be achieved by tailoring the volume fraction and constituent properties.

Chapter

7. BAND GAPS FOR FLEXURAL ELASTIC WAVE PROPAGATION IN PERIODIC COMPOSITE PLATE STRUCTURES USING A NON-CLASSICAL MINDLIN PLATE MODEL INCORPORATING MICROSTRUCTURE AND SURFACE ENERGY EFFECTS

7.1 Introduction

Band gaps for elastic waves propagating in periodic composite plate structures have been extensively studied using classical elasticity (e.g., Sigalas and Economou, 1994; Hsu and Wu, 2006; El-Naggar et al., 2012; Cheng et al., 2015; Liu et al., 2016). Such composite plate structures can stop elastic wave propagation in certain frequency ranges (known as band gaps) and are finding applications in elastic wave filters, vibration isolators and energy harvesters. Band gaps for wave propagation in these periodic composite structures arise from Bragg scattering and local resonance (e.g., Chen and Wang, 2014) and are inherently microstructure-dependent, which cannot be accurately described using the classical elasticity-based wave equations due to a lack of any material length scale parameter. Hence, non-classical, higher-order elasticity theories containing microstructure-dependent material parameters need to be employed in studying band gaps.

Wave equations based on several higher-order elasticity theories have been applied to determine band gaps. Liu et al. (2012) used wave equations built upon a surface elasticity theory (Gurtin and Murdoch, 1975, 1978; Steigmann and Ogden, 1997, 1999; Altenbach et al., 2010; Eremeyev and Lebedev, 2016) to investigate surface energy effects on band gaps. Madeo et al. (2015) employed the wave equations based on a relaxed micromorphic elasticity theory (Neff et al., 2014) to study band gaps in metamaterials. Li et al. (2016) studied band gaps in 1-D phononic crystals by using the equation of motion built upon the dipolar gradient elasticity theory (e.g., Gourgiotis and Georgiadis, 2009), which is also known as the simplified strain gradient elasticity theory (e.g., Gao and Park, 2007; Gao and Ma, 2010). Bacigalupo and Gambarotta (2017) utilized a micropolar continuum theory (e.g., Eremeyev et al., 2013) to determine band gaps in periodic materials. Zhang et al. (2018a) and Gao et al. (2018) investigated band gaps for flexural elastic wave propagation in periodic composite beam structures by using non-classical Bernoulli–Euler and Timoshenko beam models based on a modified couple stress theory (Yang et al., 2002; Park and Gao, 2008) and a surface elasticity theory (Gurtin and Murdoch, 1975, 1978). Band gaps for elastic wave propagation in 2-D and 3-D periodic composite materials were studied in Zhang et al. (2018b) and Zhang and Gao (2018) by employing the wave equations built upon the modified couple stress theory. However, band gaps in periodic composite plate structures have not been explored through applying non-classical elasticity-based wave equations for plates that include both the microstructure and surface energy effects.

In Chapter 7, the band gaps of flexural elastic wave propagation in periodic composite plate structures are studied by using the non-classical Mindlin plate model formulated in Chapter 4. The rest of this chapter is organized as follows. In Section 7.2, the non-classical equations of motion for a Mindlin plate are reduced from the general equations derived in Gao and Zhang (2016) and applied to investigate flexural elastic wave propagation in periodic composite plate structures. The plane wave expansion method and Bloch's theorem for periodic media are used to determine the band gaps. In Section 7.3, numerical results are provided to quantitatively illustrate the band gaps for flexural elastic wave propagation predicted by the current model and those by its classical elasticity-based counterpart. The effects of plate thickness, unit cell length, and volume fraction on the band gaps are studied there. The chapter concludes in Section 7.4 with a summary.

7.2 Formulation

Based on the modified couple stress theory (Yang et al., 2002; Park and Gao, 2008), the surface elasticity theory (Gurtin and Murdoch, 1975, 1978) and a two-parameter Winkler–Pasternak elastic foundation model, the equations of motion for a Mindlin plate incorporating the microstructure, surface energy and elastic foundation effects have been derived in Chapter 4 (i.e., Eqs. (4.39a-e)). When the stretching is not considered (i.e., $u = 0$, $v = 0$) and the foundation effect is suppressed (i.e., $k_w = k_p = 0$), the equations of motion for the Mindlin plate of uniform thickness h and mid-plane area R reduce to

$$\begin{aligned}
&\frac{\partial}{\partial x}\left[K(\frac{\partial w}{\partial x}-\phi_x)\right]+\frac{\partial}{\partial y}\left[K(\frac{\partial w}{\partial y}-\phi_y)\right]-\frac{1}{2}\frac{\partial^2}{\partial x\partial y}\left[C(2\frac{\partial^2 w}{\partial x\partial y}+\frac{\partial\phi_x}{\partial y}+\frac{\partial\phi_y}{\partial x})\right]\\
&+\frac{1}{4}\frac{\partial^2}{\partial x^2}\left[C(-\frac{\partial^2 w}{\partial x^2}+\frac{\partial^2 w}{\partial y^2}-\frac{\partial\phi_x}{\partial x}+\frac{\partial\phi_y}{\partial y})\right]-\frac{1}{4}\frac{\partial^2}{\partial y^2}\left[C(-\frac{\partial^2 w}{\partial x^2}+\frac{\partial^2 w}{\partial y^2}-\frac{\partial\phi_x}{\partial x}+\frac{\partial\phi_y}{\partial y})\right] \quad (7.1a)\\
&+\frac{\partial}{\partial x}\left(S\frac{\partial w}{\partial x}\right)+\frac{\partial}{\partial y}\left(S\frac{\partial w}{\partial y}\right)+f_z-\frac{1}{2}c_{x,y}+\frac{1}{2}c_{y,x}=\frac{\partial^2}{\partial t^2}\left(P_1 w\right)
\end{aligned}$$

$$\begin{aligned}
&-K(\frac{\partial w}{\partial x}-\phi_x)-\frac{\partial}{\partial x}\left(D\frac{\partial \phi_x}{\partial x}\right)-\frac{\partial}{\partial x}\left(D_1\frac{\partial \phi_y}{\partial y}\right)-\frac{\partial}{\partial y}\left[D_2(\frac{\partial \phi_x}{\partial y}+\frac{\partial \phi_y}{\partial x})\right]\\
&+\frac{1}{4}\frac{\partial}{\partial x}\left[C(-\frac{\partial^2 w}{\partial x^2}+\frac{\partial^2 w}{\partial y^2}-\frac{\partial \phi_x}{\partial x}+\frac{\partial \phi_y}{\partial y})\right]-\frac{1}{2}\frac{\partial}{\partial y}\left[C(\frac{\partial^2 w}{\partial x\partial y}+2\frac{\partial \phi_x}{\partial y}-\frac{\partial \phi_y}{\partial x})\right]\\
&+\frac{1}{2}\frac{\partial^2}{\partial x\partial y}\left[C_1(\frac{\partial^2 \phi_x}{\partial x\partial y}-\frac{\partial^2 \phi_y}{\partial x^2})\right]+\frac{1}{2}\frac{\partial^2}{\partial y^2}\left[C_1(\frac{\partial^2 \phi_x}{\partial y^2}-\frac{\partial^2 \phi_y}{\partial x\partial y})\right]\\
&-h\frac{\partial}{\partial x}\left(B_1\frac{\partial \phi_x}{\partial x}+B_2\frac{\partial \phi_y}{\partial y}\right)-h\frac{\partial}{\partial y}\left[B_3\left(\frac{\partial \phi_x}{\partial y}+\frac{\partial \phi_y}{\partial x}\right)\right]+\frac{1}{2}c_y=-\frac{\partial^2}{\partial t^2}\left(P_2\phi_x\right)
\end{aligned}\tag{7.1b}$$

$$\begin{aligned}
&-K(\frac{\partial w}{\partial y}-\phi_y)-\frac{\partial}{\partial y}\left(D\frac{\partial \phi_y}{\partial y}\right)-\frac{\partial}{\partial y}\left(D_1\frac{\partial \phi_x}{\partial x}\right)-\frac{\partial}{\partial x}\left[D_2(\frac{\partial \phi_x}{\partial y}+\frac{\partial \phi_y}{\partial x})\right]\\
&-\frac{1}{2}\frac{\partial}{\partial x}\left[C(\frac{\partial^2 w}{\partial x\partial y}+2\frac{\partial \phi_y}{\partial x}-\frac{\partial \phi_x}{\partial y})\right]-\frac{1}{4}\frac{\partial}{\partial y}\left[C(-\frac{\partial^2 w}{\partial x^2}+\frac{\partial^2 w}{\partial y^2}-\frac{\partial \phi_x}{\partial x}+\frac{\partial \phi_y}{\partial y})\right]\\
&-\frac{1}{2}\frac{\partial^2}{\partial x^2}\left[C_1(\frac{\partial^2 \phi_x}{\partial x\partial y}-\frac{\partial^2 \phi_y}{\partial x^2})\right]-\frac{1}{2}\frac{\partial^2}{\partial x\partial y}\left[C_1(\frac{\partial^2 \phi_x}{\partial y^2}-\frac{\partial^2 \phi_y}{\partial x\partial y})\right]\\
&-h\frac{\partial}{\partial y}\left(B_2\frac{\partial \phi_x}{\partial x}+B_1\frac{\partial \phi_y}{\partial y}\right)-h\frac{\partial}{\partial x}\left[B_3\left(\frac{\partial \phi_x}{\partial y}+\frac{\partial \phi_y}{\partial x}\right)\right]-\frac{1}{2}c_x=-\frac{\partial^2}{\partial t^2}\left(P_2\phi_y\right)
\end{aligned}\tag{7.1c}$$

for any $(x, y) \in R$, where $w = w(x, y, t)$ is the z-displacement (or deflection) of point $(x, y, 0)$ on the plate mid-plane at time t, ϕ_x and ϕ_y are, respectively, the rotation angles of a transverse normal about the y- and x-axes (see Fig. 7.1), and

$$D=\frac{1}{12}(\lambda+2\mu)h^3\,,D_1=\frac{1}{12}\lambda h^3\,,D_2=\frac{1}{12}\mu h^3\,,\ K=k_s\mu h\,,\tag{7.2a-d}$$

$$C=\mu l^2 h\,,C_1=\frac{1}{24}\mu l^2 h^3\,,\ S=2\tau_0\,,\ P_1=\rho h,\quad P_2=\frac{\rho h^3}{12}\,,\tag{7.2e-i}$$

$$B_1=\frac{h}{2}(\lambda_0+2\mu_0)\,,B_2=\frac{h}{2}(\lambda_0+\tau_0)\,,\ B_3=\frac{h\left(2\mu_0-\tau_0\right)}{4}\tag{7.2j-l}$$

In Eqs. (7.1a-c)-(7.2a-l), λ and μ are the Lamé constants in classical elasticity, l is a material length scale parameter measuring the couple stress effect (e.g., Park and Gao, 2006), μ_0 and λ_0 are the surface elastic constants, τ_0 is the residual surface stress (i.e., the surface stress at zero strain), ρ is the density of the plate material, h is the thickness of the plate, f_z is the z-component of the body force resultant (force per unit area) through the plate thickness acting in the plate mid-plane area R, c_x and c_y are, respectively, the x- and y-components of the body couple resultant (moment per unit area) through the plate thickness acting in the area R.

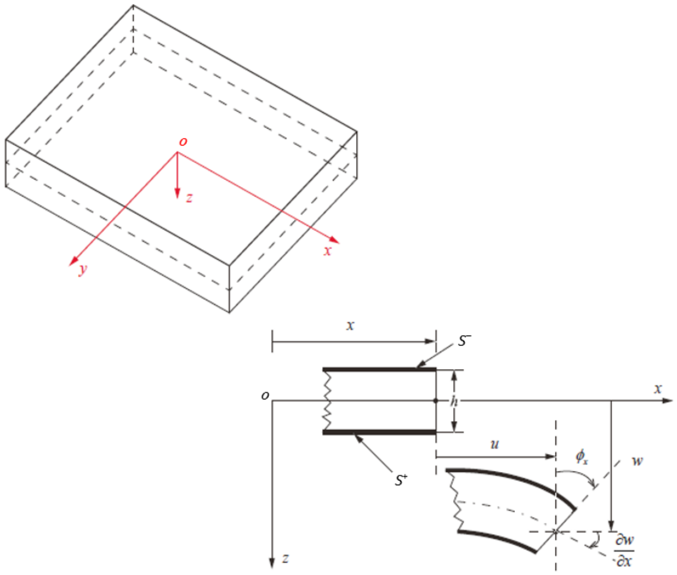

Fig. 7.1 Plate configuration and coordinate system

Note that Eqs. (7.1a-c) are obtained using the Cartesian coordinate system (x, y, z) shown in Fig. 7.1, where the xy-plane is coincident with the geometrical mid-plane of the undeformed plate. The lower S^+ and upper S^- surface layers (with zero-thickness) are taken to be perfectly bonded to the bulk plate material at $z = \pm h/2$, respectively. The bulk material satisfies the modified couple stress theory (Yang et al., 2002; Park and Gao, 2008), while the surface layers are governed by the surface elasticity theory (Gurtin and Murdoch, 1975, 1978).

Consider a periodic two-phase composite plate structure containing inclusions (as Phase I) in the shape of a square or a square with connecting rods embedded periodically in a host matrix (as Phase II) which is infinitely large in the *xy*-plane, as shown in Fig. 7.2. The latter represents a co-continuous or interpenetrating phase composite (e.g., Ai and Gao, 2016, 2017; Zhang and Gao, 2018). The unit cell for this periodic composite plate structure is taken to be a square of edge length *a* containing a square inclusion of edge length *d* at its center or a center square inclusion of edge length *d* with connecting rods of rectangular cross section having a width *g* and a height *h*, as illustrated in Fig. 7.3, where the corresponding irreducible first Brillouin zone is also provided. For brevity, the second type of inclusion is called a cruciform inclusion hereafter.

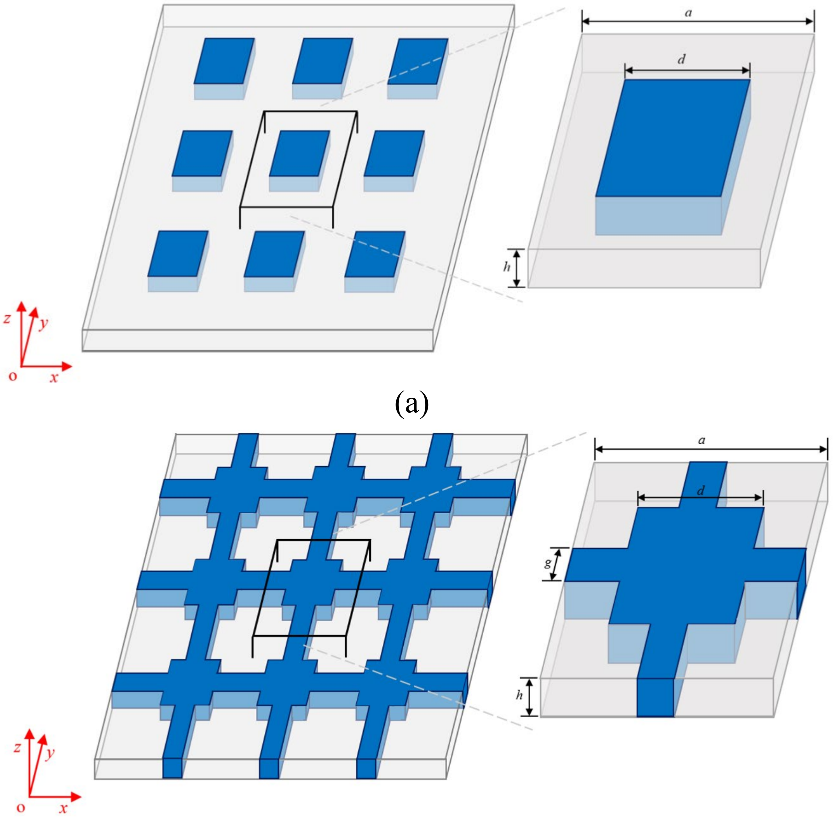

(a)

(b)

Fig. 7.2 Periodic two-phase composite plate structure with an inclusion phase and a matrix phase: (a) square inclusions; (b) cruciform inclusions.

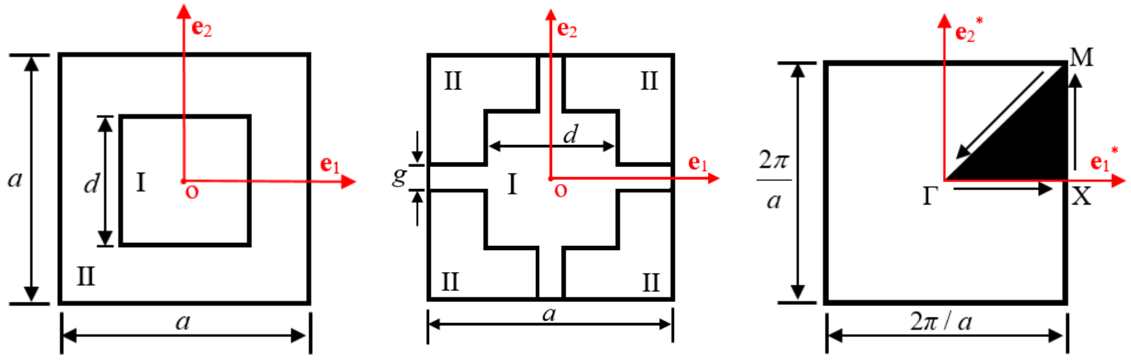

(a) (b) (c)

Fig. 7.3 Unit cell of the periodic composite plate structure: (a) square inclusion; (b) cruciform inclusion; (c) irreducible first Brillouin zone in the reciprocal lattice.

Based on the plane-wave expansion method and Bloch theorem for periodic media, w, ϕ_x and ϕ_y can each be written as a Fourier series (e.g., Kittel, C., 1986; Hsu and Wu, 2006):

$$w(\mathbf{r},t)=e^{i\mathbf{k}\cdot\mathbf{r}}\left[\sum_{\mathbf{G}'_{(m,n)}} w_{\mathbf{G}'_{(m,n)}}e^{i\mathbf{G}'_{(m,n)}\cdot\mathbf{r}}\right]e^{-i\omega t}, \tag{7.3a}$$

$$\phi_x(\mathbf{r},t)=e^{i\mathbf{k}\cdot\mathbf{r}}\left[\sum_{\mathbf{G}'_{(m,n)}} (\phi_x)_{\mathbf{G}'_{(m,n)}}e^{i\mathbf{G}'_{(m,n)}\cdot\mathbf{r}}\right]e^{-i\omega t}, \tag{7.3b}$$

$$\phi_y(\mathbf{r},t)=e^{i\mathbf{k}\cdot\mathbf{r}}\left[\sum_{\mathbf{G}'_{(m,n)}} (\phi_y)_{\mathbf{G}'_{(m,n)}}e^{i\mathbf{G}'_{(m,n)}\cdot\mathbf{r}}\right]e^{-i\omega t} \tag{7.3c}$$

where $w_{\mathbf{G}'_{(m,n)}}$, $(\phi_x)_{\mathbf{G}'_{(m,n)}}$ and $(\phi_y)_{\mathbf{G}'_{(m,n)}}$ are the Fourier coefficients, **r** = (x, y) is the position vector, **k** = (k_x, k_y) is the 2-D Bloch wave vector which is confined to the first Brillouin zone shown in Fig. 7.3(c), $\mathbf{G}'_{(m,n)}=(2\pi m/a, 2\pi n/a)=(G'_x, G'_y)$ is the 2-D reciprocal lattice vector for a square lattice with m and n being integers ranging from –∞ to +∞ and a being the lattice constant which is equal to the unit cell edge length here (see Fig. 7.3), ω

is the angular wave frequency, and *i* is the imaginary unit satisfying $i^2 = -1$.

Due to the periodicity of the composite plate structures under consideration, each of the material parameters $D(\mathbf{r})$, $D_1(\mathbf{r})$, $D_2(\mathbf{r})$, $K(\mathbf{r})$, $C(\mathbf{r})$, $C_1(\mathbf{r})$, $S(\mathbf{r})$, $P_1(\mathbf{r})$, $P_2(\mathbf{r})$, $B_1(\mathbf{r})$, $B_2(\mathbf{r})$ and $B_3(\mathbf{r})$, defined in Eqs. (7.2a-l) and involved in the wave equations given in Eqs. (7.1a-c), can also be expanded in a Fourier series as

$$\alpha(\mathbf{r}) = \sum_{\mathbf{G}_{(M,N)}} \alpha_{\mathbf{G}_{(M,N)}} e^{i\mathbf{G}_{(M,N)}\cdot\mathbf{r}}, \tag{7.4}$$

where α represents D, D_1, D_2, K, C, C_1, S, P_1, P_2, B_1, B_2 or B_3, $\mathbf{G}_{(M,N)} = (2\pi M / a,\ 2\pi N / a) = (G_x, G_y)$ is the 2-D reciprocal lattice vector with M and N being integers also ranging from −∞ to +∞, and $\alpha_{\mathbf{G}_{(M,N)}}$ is the Fourier coefficient given by

$$\alpha_{\mathbf{G}_{(M,N)}} = \frac{1}{A}\iint_{\Omega} \alpha(\mathbf{r}) e^{-i\mathbf{G}_{(M,N)}\cdot\mathbf{r}} d\mathbf{r}, \tag{7.5}$$

where Ω denotes the 2-D domain on the plate mid-plane by the unit cell, and A is the area of Ω. For a two-phase composite, $\alpha_{\mathbf{G}_{(M,N)}}$ has the form (e.g., Zhang et al., 2018b)

$$\alpha_{\mathbf{G}_{(M,N)}} = \begin{cases} V_f^{\mathrm{I}}\alpha_{\mathrm{I}} + (1 - V_f^{\mathrm{I}})\alpha_{\mathrm{II}} & \text{for } \mathbf{G}_{(M,N)} = 0, \\ (\alpha_{\mathrm{I}} - \alpha_{\mathrm{II}}) F(\mathbf{G}_{(M,N)}) & \text{for } \mathbf{G}_{(M,N)} \neq 0, \end{cases} \tag{7.6}$$

where α_{I} and α_{II} are the property values for materials I and II (see Fig. 7.3) respectively, $V_f^{\mathrm{I}} = A^{\mathrm{I}} / A$ is the volume fraction of material I, with A^{I} being the area of material I on the plate mid-plane in the unit cell, and $F(\mathbf{G}_{(M,N)})$ is the shape function defined by

$$F(\mathbf{G}_{(M,N)}) = \frac{1}{A}\iint_{\Omega_{\mathrm{I}}} e^{-i\mathbf{G}_{(M,N)}\cdot\mathbf{r}} d\mathbf{r}, \tag{7.7}$$

where Ω_{I} is the domain on the plate mid-plane occupied by material I on the plate mid-plane in the unit cell.

For a square domain Ω_I (see Fig. 7.3(a)), the shape function $\mathrm{F}(\mathbf{G}_{(M,N)})$ is given by (e.g., Susa, 2002; Zhang et al., 2018b):

$$\mathrm{F}(\mathbf{G}_{(M,N)}) = \begin{cases} \dfrac{2d}{a^2 G_x}\sin(\dfrac{G_x d}{2}) \text{ for } G_x \neq 0,\ G_y = 0; \\ \dfrac{2d}{a^2 G_y}\sin(\dfrac{G_y d}{2}) \text{ for } G_x = 0,\ G_y \neq 0; \\ \dfrac{4}{a^2 G_x G_y}\sin(\dfrac{G_x d}{2})\sin(\dfrac{G_y d}{2}) \text{ for } G_x \neq 0,\ G_y \neq 0, \end{cases} \tag{7.8}$$

where d is the edge length of the square region Ω_{I}, and a is the edge length of the square unit cell Ω (see Fig. 7.3(a)).

For the cruciform inclusion shown in (see Fig. 7.3(b)), the shape function $\mathrm{F}(\mathbf{G}_{(M,N)})$ has been obtained as (see Appendix A for derivations)

$$\mathrm{F}(\mathbf{G}_{(M,N)}) = \frac{g}{a}(A_x F_y + F_x A_y) + \frac{d^2}{a^2} f_x f_y - \frac{dg}{a^2}(f_x F_y + F_x f_y), \tag{7.9}$$

where

$$F_\beta = \begin{cases} 1, & G_\beta = 0, \\ \dfrac{2}{G_\beta g}\sin\left(\dfrac{G_\beta g}{2}\right), & G_\beta \neq 0; \end{cases} \tag{7.10a}$$

$$f_\beta = \begin{cases} 1, & G_\beta = 0, \\ \dfrac{2}{G_\beta d}\sin\left(\dfrac{G_\beta d}{2}\right), & G_\beta \neq 0; \end{cases} \tag{7.10b}$$

$$A_\beta = \begin{cases} 1, & G_\beta = 0, \\ 0, & G_\beta \neq 0. \end{cases} \tag{7.10c}$$

Note that the subscript β in Eqs. (7.10a-c) represents x and y, respectively.

Using Eqs. (7.3a-c) and (7.4) in Eqs. (7.1a-c) yields, with $f_z = 0$, $c_x = c_y = 0$ and upon using Laurent's rule for finding the Fourier coefficients of a product of two periodic functions (e.g., Li, 1996; Cao et al., 2004),

$$\begin{bmatrix} (M_{11})_{\mathbf{G}_{(M,N)}-\mathbf{G}'_{(m,n)}} & (M_{12})_{\mathbf{G}_{(M,N)}-\mathbf{G}'_{(m,n)}} & (M_{13})_{\mathbf{G}_{(M,N)}-\mathbf{G}'_{(m,n)}} \\ (M_{21})_{\mathbf{G}_{(M,N)}-\mathbf{G}'_{(m,n)}} & (M_{22})_{\mathbf{G}_{(M,N)}-\mathbf{G}'_{(m,n)}} & (M_{23})_{\mathbf{G}_{(M,N)}-\mathbf{G}'_{(m,n)}} \\ (M_{31})_{\mathbf{G}_{(M,N)}-\mathbf{G}'_{(m,n)}} & (M_{32})_{\mathbf{G}_{(M,N)}-\mathbf{G}'_{(m,n)}} & (M_{33})_{\mathbf{G}_{(M,N)}-\mathbf{G}'_{(m,n)}} \end{bmatrix} \begin{Bmatrix} w_{\mathbf{G}'_{(m,n)}} \\ \left(\phi_x\right)_{\mathbf{G}'_{(m,n)}} \\ \left(\phi_y\right)_{\mathbf{G}'_{(m,n)}} \end{Bmatrix}$$

$$= \omega^2 \begin{bmatrix} -\left(P_1\right)_{\mathbf{G}_{(M,N)}-\mathbf{G}'_{(m,n)}} & 0 & 0 \\ 0 & \left(P_2\right)_{\mathbf{G}_{(M,N)}-\mathbf{G}'_{(m,n)}} & 0 \\ 0 & 0 & \left(P_2\right)_{\mathbf{G}_{(M,N)}-\mathbf{G}'_{(m,n)}} \end{bmatrix} \begin{Bmatrix} w_{\mathbf{G}'_{(m,n)}} \\ \left(\phi_x\right)_{\mathbf{G}'_{(m,n)}} \\ \left(\phi_y\right)_{\mathbf{G}'_{(m,n)}} \end{Bmatrix} \tag{7.11}$$

where

$$\begin{aligned} (M_{11})_{\mathbf{G}_{(M,N)}-\mathbf{G}'_{(m,n)}} &= -K_{\mathbf{G}-\mathbf{G}'}(k_x+G_x)(k_x+G'_x) - K_{\mathbf{G}-\mathbf{G}'}(k_y+G_y)(k_y+G'_y) \\ &-C_{\mathbf{G}-\mathbf{G}'}(k_x+G_x)(k_y+G_y)(k_x+G'_x)(k_y+G'_y) - \frac{1}{4}C_{\mathbf{G}-\mathbf{G}'}(k_x+G_x)^2(k_x+G'_x)^2 \\ &+\frac{1}{4}C_{\mathbf{G}-\mathbf{G}'}(k_x+G_x)^2(k_y+G'_y)^2 + \frac{1}{4}C_{\mathbf{G}-\mathbf{G}'}(k_y+G_y)^2(k_x+G'_x)^2 \\ &-\frac{1}{4}C_{\mathbf{G}-\mathbf{G}'}(k_y+G_y)^2(k_y+G'_y)^2 - S_{\mathbf{G}-\mathbf{G}'}(k_x+G_x)(k_x+G'_x) \\ &-S_{\mathbf{G}-\mathbf{G}'}(k_y+G_y)(k_y+G'_y), \end{aligned} \tag{7.12a}$$

$$\begin{aligned} (M_{12})_{\mathbf{G}_{(M,N)}-\mathbf{G}'_{(m,n)}} &= -iK_{\mathbf{G}-\mathbf{G}'}(k_x+G_x) + \frac{1}{2}iC_{\mathbf{G}-\mathbf{G}'}(k_x+G_x)(k_y+G_y)(k_y+G'_y) \\ &+\frac{1}{4}iC_{\mathbf{G}-\mathbf{G}'}(k_x+G_x)^2(k_x+G'_x) - \frac{1}{4}iC_{\mathbf{G}-\mathbf{G}'}(k_y+G_y)^2(k_x+G'_x), \end{aligned} \tag{7.12b}$$

$$\begin{aligned} (M_{13})_{\mathbf{G}_{(M,N)}-\mathbf{G}'_{(m,n)}} &= -iK_{\mathbf{G}-\mathbf{G}'}(k_y+G_y) + \frac{1}{2}iC_{\mathbf{G}-\mathbf{G}'}(k_x+G_x)(k_y+G_y)(k_x+G'_x) \\ &-\frac{1}{4}iC_{\mathbf{G}-\mathbf{G}'}(k_x+G_x)^2(k_y+G'_y) + \frac{1}{4}iC_{\mathbf{G}-\mathbf{G}'}(k_y+G_y)^2(k_y+G'_y), \end{aligned} \tag{7.12c}$$

$$\begin{aligned}(M_{21})_{\mathbf{G}_{(M,N)}-\mathbf{G}'_{(m,n)}} &= -iK_{\mathbf{G}-\mathbf{G}'}(k_x+G'_x)+\frac{1}{4}iC_{\mathbf{G}-\mathbf{G}'}(k_x+G_x)(k_x+G'_x)^2\\ &-\frac{1}{4}iC_{\mathbf{G}-\mathbf{G}'}(k_x+G_x)(k_y+G'_y)^2+\frac{1}{2}iC_{\mathbf{G}-\mathbf{G}'}(k_y+G_y)(k_x+G'_x)(k_y+G'_y),\end{aligned}\tag{7.12d}$$

$$\begin{aligned}(M_{22})_{\mathbf{G}_{(M,N)}-\mathbf{G}'_{(m,n)}} &= K_{\mathbf{G}-\mathbf{G}'}+D_{\mathbf{G}-\mathbf{G}'}(k_x+G_x)(k_x+G'_x)+\left(D_2\right)_{\mathbf{G}-\mathbf{G}'}(k_y+G_y)(k_y+G'_y)\\ &+\frac{1}{4}C_{\mathbf{G}-\mathbf{G}'}(k_x+G_x)(k_x+G'_x)+C_{\mathbf{G}-\mathbf{G}'}(k_y+G_y)(k_y+G'_y)\\ &+\frac{1}{2}\left(C_1\right)_{\mathbf{G}-\mathbf{G}'}(k_x+G_x)(k_y+G_y)(k_x+G'_x)(k_y+G'_y)\\ &+\frac{1}{2}\left(C_1\right)_{\mathbf{G}-\mathbf{G}'}(k_y+G_y)^2(k_y+G'_y)^2+h\left(B_1\right)_{\mathbf{G}-\mathbf{G}'}(k_x+G_x)(k_x+G'_x)\\ &+h\left(B_3\right)_{\mathbf{G}-\mathbf{G}'}(k_y+G_y)(k_y+G'_y),\end{aligned}\tag{7.12e}$$

$$\begin{aligned}(M_{23})_{\mathbf{G}_{(M,N)}-\mathbf{G}'_{(m,n)}} &= \left(D_1\right)_{\mathbf{G}-\mathbf{G}'}(k_x+G_x)(k_y+G'_y)+\left(D_2\right)_{\mathbf{G}-\mathbf{G}'}(k_y+G_y)(k_x+G'_x)\\ &-\frac{1}{4}C_{\mathbf{G}-\mathbf{G}'}(k_x+G_x)(k_y+G'_y)-\frac{1}{2}C_{\mathbf{G}-\mathbf{G}'}(k_y+G_y)(k_x+G'_x)\\ &-\frac{1}{2}\left(C_1\right)_{\mathbf{G}-\mathbf{G}'}(k_x+G_x)(k_y+G_y)(k_x+G'_x)^2-\frac{1}{2}\left(C_1\right)_{\mathbf{G}-\mathbf{G}'}(k_y+G_y)^2(k_x+G'_x)(k_y+G'_y)\\ &+h\left(B_2\right)_{\mathbf{G}-\mathbf{G}'}(k_x+G_x)(k_y+G'_y)+h\left(B_3\right)_{\mathbf{G}-\mathbf{G}'}(k_y+G_y)(k_x+G'_x),\end{aligned}\tag{7.12f}$$

$$\begin{aligned}(M_{31})_{\mathbf{G}_{(M,N)}-\mathbf{G}'_{(m,n)}} &= -iK_{\mathbf{G}-\mathbf{G}'}(k_y+G'_y)+\frac{1}{2}iC_{\mathbf{G}-\mathbf{G}'}(k_x+G_x)(k_x+G'_x)(k_y+G'_y)\\ &-\frac{1}{4}iC_{\mathbf{G}-\mathbf{G}'}(k_y+G_y)(k_x+G'_x)^2+\frac{1}{4}iC_{\mathbf{G}-\mathbf{G}'}(k_y+G_y)(k_y+G'_y)^2,\end{aligned}\tag{7.12g}$$

$$\begin{aligned}(M_{32})_{\mathbf{G}_{(M,N)}-\mathbf{G}'_{(m,n)}} &= \left(D_1\right)_{\mathbf{G}-\mathbf{G}'}(k_y+G_y)(k_x+G'_x)+\left(D_2\right)_{\mathbf{G}-\mathbf{G}'}(k_x+G_x)(k_y+G'_y)\\ &-\frac{1}{2}C_{\mathbf{G}-\mathbf{G}'}(k_x+G_x)(k_y+G'_y)-\frac{1}{4}C_{\mathbf{G}-\mathbf{G}'}(k_y+G_y)(k_x+G'_x)\\ &-\frac{1}{2}\left(C_1\right)_{\mathbf{G}-\mathbf{G}'}(k_x+G_x)^2(k_x+G'_x)(k_y+G'_y)-\frac{1}{2}\left(C_1\right)_{\mathbf{G}-\mathbf{G}'}(k_x+G_x)(k_y+G_y)(k_y+G'_y)^2\\ &+h\left(B_2\right)_{\mathbf{G}-\mathbf{G}'}(k_y+G_y)(k_x+G'_x)+h\left(B_3\right)_{\mathbf{G}-\mathbf{G}'}(k_x+G_x)(k_y+G'_y),\end{aligned}\tag{7.12h}$$

$$\begin{aligned}(M_{33})_{\mathbf{G}_{(M,N)}-\mathbf{G}'_{(m,n)}} &= K_{\mathbf{G}-\mathbf{G}'}+D_{\mathbf{G}-\mathbf{G}'}(k_y+G_y)(k_y+G'_y)+\left(D_2\right)_{\mathbf{G}-\mathbf{G}'}(k_x+G_x)(k_x+G'_x)\\ &+C_{\mathbf{G}-\mathbf{G}'}(k_x+G_x)(k_x+G'_x)+\frac{1}{4}C_{\mathbf{G}-\mathbf{G}'}(k_y+G_y)(k_y+G'_y)\\ &+\frac{1}{2}\left(C_1\right)_{\mathbf{G}-\mathbf{G}'}(k_x+G_x)^2(k_x+G'_x)^2+\frac{1}{2}\left(C_1\right)_{\mathbf{G}-\mathbf{G}'}(k_x+G_x)(k_y+G_y)(k_x+G'_x)(k_y+G'_y)\\ &+h\left(B_1\right)_{\mathbf{G}-\mathbf{G}'}(k_y+G_y)(k_y+G'_y)+h\left(B_3\right)_{\mathbf{G}-\mathbf{G}'}(k_x+G_x)(k_x+G'_x),\end{aligned}\tag{7.12i}$$

$$w_{\mathbf{G}'_{(m,n)}}=\frac{1}{A}\iint_{\Omega}we^{-i\left(\mathbf{G}'_{(m,n)}+\mathbf{k}\right)\cdot\mathbf{r}}d\mathbf{r},\tag{7.13}$$

$$\left(\phi_x\right)_{\mathbf{G}'_{(m,n)}}=\frac{1}{A}\iint_\Omega \phi_x e^{-i\left(\mathbf{G}'_{(m,n)}+\mathbf{k}\right)\cdot\mathbf{r}}d\mathbf{r}, \tag{7.14}$$

$$\left(\phi_y\right)_{\mathbf{G}'_{(m,n)}}=\frac{1}{A}\iint_\Omega \phi_y e^{-i\left(\mathbf{G}'_{(m,n)}+\mathbf{k}\right)\cdot\mathbf{r}}d\mathbf{r}, \tag{7.15}$$

in which

$$\alpha_{\mathbf{G}-\mathbf{G}'}=\frac{1}{A}\iint_\Omega \alpha e^{-i\left(\mathbf{G}_{(M,N)}-\mathbf{G}'_{(m,n)}\right)\cdot\mathbf{r}}d\mathbf{r}, \tag{7.16}$$

where $\alpha_{\mathbf{G}-\mathbf{G}'}$ represents $D_{\mathbf{G}-\mathbf{G}'}$, $\left(D_1\right)_{\mathbf{G}-\mathbf{G}'}$, $\left(D_2\right)_{\mathbf{G}-\mathbf{G}'}$, $K_{\mathbf{G}-\mathbf{G}'}$, $C_{\mathbf{G}-\mathbf{G}'}$, $\left(C_1\right)_{\mathbf{G}-\mathbf{G}'}$, $S_{\mathbf{G}-\mathbf{G}'}$, $\left(P_1\right)_{(\mathbf{G}-\mathbf{G}')}$, $\left(P_2\right)_{(\mathbf{G}-\mathbf{G}')}$, $\left(B_1\right)_{\mathbf{G}-\mathbf{G}'}$, $\left(B_2\right)_{\mathbf{G}-\mathbf{G}'}$ or $\left(B_3\right)_{\mathbf{G}-\mathbf{G}'}$.

When w, ϕ_x, ϕ_y and α (representing D, D_1, D_2, K, C, C_1, S, P_1, P_2, B_1, B_2 or B_3) are approximated by truncated Fourier series expansions with m, n, M and N ranging from $-L$ to L, with L being an integer, Eq. (7.11) gives $3(2L+1)^2$ equations, which can be assembled to obtain

$$\begin{bmatrix} \left[(M_{11})_{\mathbf{G}-\mathbf{G}'}\right] & \left[(M_{12})_{\mathbf{G}-\mathbf{G}'}\right] & \left[(M_{13})_{\mathbf{G}-\mathbf{G}'}\right] \\ \left[(M_{21})_{\mathbf{G}-\mathbf{G}'}\right] & \left[(M_{22})_{\mathbf{G}-\mathbf{G}'}\right] & \left[(M_{23})_{\mathbf{G}-\mathbf{G}'}\right] \\ \left[(M_{31})_{\mathbf{G}-\mathbf{G}'}\right] & \left[(M_{32})_{\mathbf{G}-\mathbf{G}'}\right] & \left[(M_{33})_{\mathbf{G}-\mathbf{G}'}\right] \end{bmatrix} \begin{Bmatrix} \left\{w_{\mathbf{G}'}\right\} \\ \left\{\left(\phi_x\right)_{\mathbf{G}'}\right\} \\ \left\{\left(\phi_y\right)_{\mathbf{G}'}\right\} \end{Bmatrix} = \omega^2 \begin{bmatrix} -\left[\left(P_1\right)_{\mathbf{G}-\mathbf{G}'}\right] & 0 & 0 \\ 0 & \left[\left(P_2\right)_{\mathbf{G}-\mathbf{G}'}\right] & 0 \\ 0 & 0 & \left[\left(P_2\right)_{\mathbf{G}-\mathbf{G}'}\right] \end{bmatrix} \begin{Bmatrix} \left\{w_{\mathbf{G}'}\right\} \\ \left\{\left(\phi_x\right)_{\mathbf{G}'}\right\} \\ \left\{\left(\phi_y\right)_{\mathbf{G}'}\right\} \end{Bmatrix} \tag{7.17}$$

where

$$\left[(M_{ij})_{\mathbf{G}-\mathbf{G}'}\right]=\begin{bmatrix} (M_{ij})_{\mathbf{G}_{(-L,-L)}-\mathbf{G}'_{(-L,-L)}} & (M_{ij})_{\mathbf{G}_{(-L,-L)}-\mathbf{G}'_{(-L,-L+1)}} & \cdots & (M_{ij})_{\mathbf{G}_{(-L,-L)}-\mathbf{G}'_{(L,L-1)}} & (M_{ij})_{\mathbf{G}_{(-L,-L)}-\mathbf{G}'_{(L,L)}} \\ (M_{ij})_{\mathbf{G}_{(-L,-L+1)}-\mathbf{G}'_{(-L,-L)}} & (M_{ij})_{\mathbf{G}_{(-L,-L+1)}-\mathbf{G}'_{(-L,-L+1)}} & \cdots & (M_{ij})_{\mathbf{G}_{(-L,-L+1)}-\mathbf{G}'_{(L,L-1)}} & (M_{ij})_{\mathbf{G}_{(-L,-L+1)}-\mathbf{G}'_{(L,L)}} \\ \vdots & \vdots & \ddots & \vdots & \vdots \\ (M_{ij})_{\mathbf{G}_{(L,L-1)}-\mathbf{G}'_{(-L,-L)}} & (M_{ij})_{\mathbf{G}_{(L,L-1)}-\mathbf{G}'_{(-L,-L+1)}} & \cdots & (M_{ij})_{\mathbf{G}_{(L,L-1)}-\mathbf{G}'_{(L,L-1)}} & (M_{ij})_{\mathbf{G}_{(L,L-1)}-\mathbf{G}'_{(L,L)}} \\ (M_{ij})_{\mathbf{G}_{(L,L)}-\mathbf{G}'_{(-L,-L)}} & (M_{ij})_{\mathbf{G}_{(L,L)}-\mathbf{G}'_{(-L,-L+1)}} & \cdots & (M_{ij})_{\mathbf{G}_{(L,L)}-\mathbf{G}'_{(L,L-1)}} & (M_{ij})_{\mathbf{G}_{(L,L)}-\mathbf{G}'_{(L,L)}} \end{bmatrix}$$

(7.18)

is a $(2L+1)^2 \times (2L+1)^2$ matrix representing, respectively, $[M_{11}]$, $[M_{12}]$, $[M_{13}]$, $[M_{21}]$, $[M_{22}]$, $[M_{23}]$, $[M_{31}]$, $[M_{32}]$ and $[M_{33}]$ for each (i, j) combination (with $i, j \in \{1, 2, 3\}$),

$$\left[(P_i)_{\mathbf{G}-\mathbf{G}'}\right]=\begin{bmatrix} (P_i)_{\mathbf{G}_{(-L,-L)}-\mathbf{G}'_{(-L,-L)}} & (P_i)_{\mathbf{G}_{(-L,-L)}-\mathbf{G}'_{(-L,-L+1)}} & \cdots & (P_i)_{\mathbf{G}_{(-L,-L)}-\mathbf{G}'_{(L,L-1)}} & (P_i)_{\mathbf{G}_{(-L,-L)}-\mathbf{G}'_{(L,L)}} \\ (P_i)_{\mathbf{G}_{(-L,-L+1)}-\mathbf{G}'_{(-L,-L)}} & (P_i)_{\mathbf{G}_{(-L,-L+1)}-\mathbf{G}'_{(-L,-L+1)}} & \cdots & (P_i)_{\mathbf{G}_{(-L,-L+1)}-\mathbf{G}'_{(L,L-1)}} & (P_i)_{\mathbf{G}_{(-L,-L+1)}-\mathbf{G}'_{(L,L)}} \\ \vdots & \vdots & \ddots & \vdots & \vdots \\ (P_i)_{\mathbf{G}_{(L,L-1)}-\mathbf{G}'_{(-L,-L)}} & (P_i)_{\mathbf{G}_{(L,L-1)}-\mathbf{G}'_{(-L,-L+1)}} & \cdots & (P_i)_{\mathbf{G}_{(L,L-1)}-\mathbf{G}'_{(L,L-1)}} & (P_i)_{\mathbf{G}_{(L,L-1)}-\mathbf{G}'_{(L,L)}} \\ (P_i)_{\mathbf{G}_{(L,L)}-\mathbf{G}'_{(-L,-L)}} & (P_i)_{\mathbf{G}_{(L,L)}-\mathbf{G}'_{(-L,-L+1)}} & \cdots & (P_i)_{\mathbf{G}_{(L,L)}-\mathbf{G}'_{(L,L-1)}} & (P_i)_{\mathbf{G}_{(L,L)}-\mathbf{G}'_{(L,L)}} \end{bmatrix}$$

(7.19)

is a $(2L+1)^2 \times (2L+1)^2$ matrix representing, respectively, $[P_1]$, $[P_2]$ and $[P_3]$ (with $i \in \{1, 2, 3\}$),, and

$$\left\{w_{\mathbf{G}'}\right\}=\left\{\begin{matrix} w_{\mathbf{G}'_{(-L,-L)}} \\ w_{\mathbf{G}'_{(-L,-L+1)}} \\ \vdots \\ w_{\mathbf{G}'_{(L,L-1)}} \\ w_{\mathbf{G}'_{(L,L)}} \end{matrix}\right\},\quad \left\{(\phi_x)_{\mathbf{G}'}\right\}=\left\{\begin{matrix} (\phi_x)_{\mathbf{G}'_{(-L,-L)}} \\ (\phi_x)_{\mathbf{G}'_{(-L,-L+1)}} \\ \vdots \\ (\phi_x)_{\mathbf{G}'_{(L,L-1)}} \\ (\phi_x)_{\mathbf{G}'_{(L,L)}} \end{matrix}\right\},\ \left\{(\phi_y)_{\mathbf{G}'}\right\}=\left\{\begin{matrix} (\phi_y)_{\mathbf{G}'_{(-L,-L)}} \\ (\phi_y)_{\mathbf{G}'_{(-L,-L+1)}} \\ \vdots \\ (\phi_y)_{\mathbf{G}'_{(L,L-1)}} \\ (\phi_y)_{\mathbf{G}'_{(L,L)}} \end{matrix}\right\} \qquad (7.20\text{a-c})$$

are three $(2L+1)^2 \times 1$ column matrices.

Note that for a non-trivial solution of $w_{\mathbf{G}'_{(m,n)}} \neq 0$, $(\phi_x)_{\mathbf{G}'_{(m,n)}} \neq 0$ and $(\phi_y)_{\mathbf{G}'_{(m,n)}} \neq 0$, it is required that the determinant of the coefficient matrix vanish, i.e.,

$$\left|[\mathbf{T}] - \omega^2 [\mathbf{I}]\right| = 0, \tag{7.21}$$

where

$$[\mathbf{T}] = \begin{bmatrix} -\left[(P_1)_{\mathbf{G}-\mathbf{G}'}\right] & 0 & 0 \\ 0 & \left[(P_2)_{\mathbf{G}-\mathbf{G}'}\right] & 0 \\ 0 & 0 & \left[(P_2)_{\mathbf{G}-\mathbf{G}'}\right] \end{bmatrix}^{-1} \begin{bmatrix} \left[(M_{11})_{\mathbf{G}-\mathbf{G}'}\right] & \left[(M_{12})_{\mathbf{G}-\mathbf{G}'}\right] & \left[(M_{13})_{\mathbf{G}-\mathbf{G}'}\right] \\ \left[(M_{21})_{\mathbf{G}-\mathbf{G}'}\right] & \left[(M_{22})_{\mathbf{G}-\mathbf{G}'}\right] & \left[(M_{23})_{\mathbf{G}-\mathbf{G}'}\right] \\ \left[(M_{31})_{\mathbf{G}-\mathbf{G}'}\right] & \left[(M_{32})_{\mathbf{G}-\mathbf{G}'}\right] & \left[(M_{33})_{\mathbf{G}-\mathbf{G}'}\right] \end{bmatrix}$$

(7.22)

and **I** is the $[3(2L+1)^2] \times [3(2L+1)^2]$ identity (unit) matrix. Equation (7.21) is the characteristic equation of the eigenvalue problem defined in Eq. (7.17), which is a polynomial equation in ω^2 of degree $3 \times (2L+1) \times (2L+1)$. By increasing the value of the integer L, the convergent solution can be obtained. For a given wave vector $\mathbf{k} = (k_x, k_y)$ in the first Brillouin zone, the corresponding eigen-frequencies ω can be obtained from the roots of Eq. (7.21). The band gaps are the ranges of ω over which there exists no real-valued wave vector **k**.

The classical elasticity-based band gaps of the flexural elastic wave propagation in the periodic composite plate structure can be obtained as a special case by setting $l = 0$ and $\lambda_0 = \mu_0 = \tau_0 = 0$ in the relevant equations (i.e., with both the microstructure and surface energy effects suppressed).

7.3 Numerical Results and Discussion

To quantitatively illustrate the current non-classical model, numerical results for sample cases are presented in this section. In generating these results, material I is taken to be iron with the following properties (e.g., Gurtin and Murdoch, 1978; Gao and Zhang, 2016): $E^{(\mathrm{I})}$ = 177.33 GPa, $\nu^{(\mathrm{I})}$ = 0.27, $l^{(\mathrm{I})}$ = 6.76 μm, ρ = 7 g/cm^3 for the bulk, and $\mu_0^{(\mathrm{I})}$ = 2.5 N/m, $\lambda_0^{(\mathrm{I})} = -8$ N/m, $\tau_0^{(\mathrm{I})}$ = 1.7 N/m for the surface layer. Note that the value of the length scale parameter $l^{(\mathrm{I})}$ listed above is computed using $l = b_h / \sqrt{3(1-\nu)}$ (e.g., Lam et al., 2003; Park and Gao, 2006) with Poisson's ratio $\nu^{(\mathrm{I})}$ = 0.27 and the higher-order bending parameter $b_h^{(\mathrm{I})}$ = 10 μm (e.g., Wang, 2010). Material II is chosen to be epoxy with the following properties (Chen and Wang, 2014; Lam et al., 2003; Sharma and Ganti, 2004): $E^{(\mathrm{II})}$ = 3.3 GPa, $\nu^{(\mathrm{II})}$ = 0.33, $l^{(\mathrm{II})}$ = 16.93 μm, $\rho^{(\mathrm{II})}$ = 1.18 g/cm^3 for the bulk, and $\mu_0^{(\mathrm{II})}$ = 0.12406 N/m, $\lambda_0^{(\mathrm{II})} = 0.16376$ N/m, $\tau_0^{(\mathrm{II})}$ = 0.045 N/m for the surface layer. Note that the value of $l^{(\mathrm{II})}$ is also computed using $l = b_h / \sqrt{3(1-\nu)}$ but with $\nu^{(\mathrm{II})}$ = 0.33 and $b_h^{(\mathrm{II})}$ = 24 μm for epoxy (e.g., Lam et al., 2003). The values of the surface elastic constants $\mu_0^{(\mathrm{II})}$ and $\lambda_0^{(\mathrm{II})}$ listed above are computed using $\mu_0^{(\mathrm{II})} = \mu^{(\mathrm{II})} h^S$ and $\lambda_0^{(\mathrm{II})} = 2\lambda^{(\mathrm{II})}\mu^{(\mathrm{II})} h^S / (\lambda^{(\mathrm{II})} + \mu^{(\mathrm{II})})$ (Sharma and Ganti, 2004), where h^S is the thickness of transition zone and is taken to be 1 Angstrom (e.g., Miller and Shenoy, 2000), and $\lambda^{(\mathrm{II})}$ and $\mu^{(\mathrm{II})}$ are the Lamé constants of the bulk epoxy given by $\lambda^{(\mathrm{II})} = E^{(\mathrm{II})}\nu^{(\mathrm{II})} / [(1+\nu^{(\mathrm{II})})(1-2\nu^{(\mathrm{II})})]$, $\mu^{(\mathrm{II})} = E^{(\mathrm{II})} / [2(1+\nu^{(\mathrm{II})})]$. In addition, the value of the surface elastic constant $\tau_0^{(\mathrm{II})}$ for epoxy is 45 mN/m (e.g., George, 1993; Lewin et al., 2005).

Note that in the numerical analysis presented herein, only the first band gap (marked in orange) is identified and discussed in each case, which corresponds to the lowest range of ω that prohibits flexural wave propagation. The other band gaps for each periodic composite plate structure with specified geometrical and material parameters can be found by following the same procedure. In all the cases, the convergent solutions are reached with $L = 7$.

7.3.1 Effects of the microstructure and surface energy on band gaps

Figure 7.4 shows the band gaps for the periodic composite plate structure with square inclusions (see Fig. 7.3(a)), where $f = \omega/(2\pi)$ is the wave frequency. In obtaining the numerical results shown in Fig. 7.4, the unit cell length a = 1mm and the volume fraction V_f^{I} = 16% are used. Figures 7.4(a), 7.4(c) and 7.4(e) display the first band gap frequency ranges predicted by the current non-classical model for different values of the plate thickness h: 189.14−213.27 kHz for h = 20 μm, 344.70−391.68 kHz for h = 60 μm and 557.27−617.63 kHz for h = 120 μm. Figures 7.4(b), 7.4(d) and 7.4(f) show the first band gap frequency ranges predicted by the classical elasticity-based model: 110.44−127.19 kHz for h = 20 μm, 311.39−355.64 kHz for h = 60 μm, and 541.40−599.50 kHz for h = 120 μm. The first band gaps calculated from these frequency ranges are listed in Table 7.1, where the relative difference is defined to be the difference between the two band gap values over the value based on the classical model in each case.

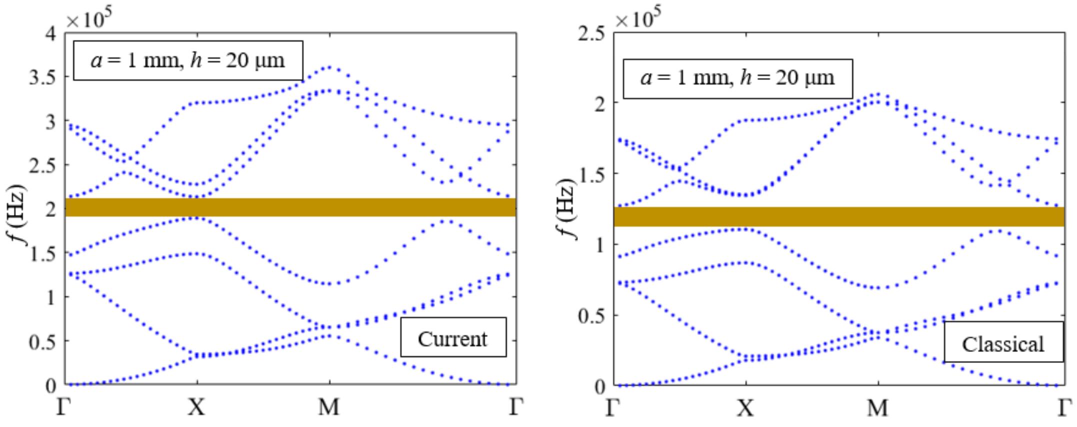

(a) (b)

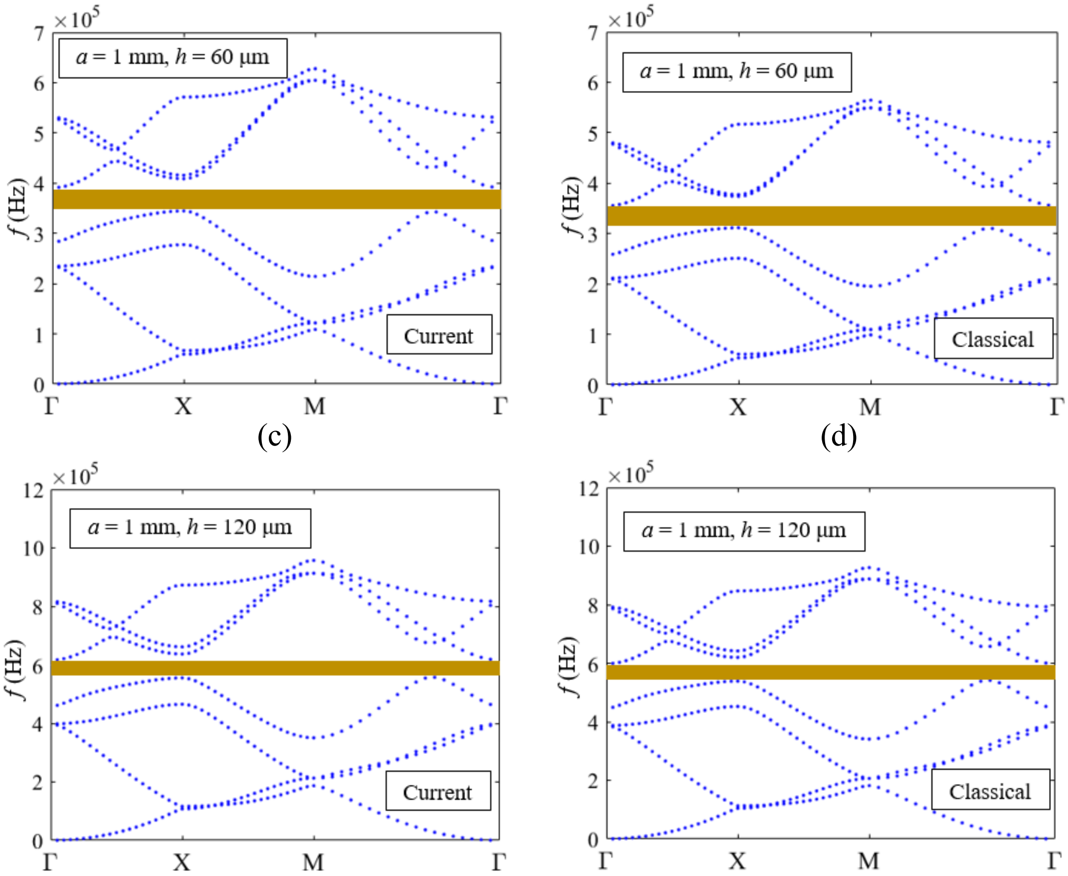

(e) (f)

Fig. 7.4 First band gaps for the periodic composite plate structure with square inclusions predicted by the current model with: (a) $h = 20$ μm, (c) $h = 60$ μm, (e) $h = 120$ μm, and by the classical model with: (b) $h = 20$ μm, (d) $h = 60$ μm, (f) $h = 120$ μm. The Bloch wave vector $\mathbf{k} = (k_x, k_y)$ at Γ, X and M is, respectively, (0, 0), $(\pi/a, 0)$ and $(\pi/a, \pi/a)$ (see Fig. 7.3(c)).

Table 7.1 First band gaps for the periodic composite plate structure containing square inclusions with different values of the plate thickness h

h (μm)	Band Gap (kHz) Current Model	Band Gap (kHz) Classical Model	Relative difference (%)
20	24.13	16.75	44.06
60	46.98	44.25	6.17
120	60.36	58.1	3.89

It is observed from Fig. 7.4 and Table 7.1 that the first band gap value increases with the increase of the plate thickness h according to both the current non-classical and classical models. In addition, when h is smaller, the difference between the two first band gap values is significantly larger. However, the difference is diminishing with the increase of h. This indicates that the microstructure effect on the band gap as measured by h is significant only when the plate is very thin.

Figure 7.5 shows the band gaps for the periodic co-continuous composite plate structure with cruciform inclusions (see Fig. 7.3(b)). The values of a and $V_f^{(I)}$ used here are the same as those employed earlier to obtain the numerical results displayed in Fig. 7.4. Note that in the numerical analysis presented herein and in the sequel, the width of the rectangular cross section of each connecting rod is taken to be $g = d/10$ for the periodic co-continuous composite plate structure.

Figures 7.5(a), 7.5(c) and 7.5(e) display the first band gap frequency ranges predicted by the current non-classical model for different values of the plate thickness h: for $h = 20$ μm, 60 μm and 120 μm, the first band gap frequency range is 195.54−201.49 kHz, 388.94−405.13 kHz and 647.34−654.72 kHz, respectively. Figures 7.5(b), 7.5(d) and 7.5(f) show the first band gap frequency ranges predicted by the classical elasticity-based model: for $h = 20$ μm, 60 μm and 120 μm, the first band gap frequency range is 127.62−131.97 kHz, 359.05−371.85 kHz and 624.72−632.01 kHz, respectively. The first band gaps calculated from these frequency ranges are listed in Table 7.2.

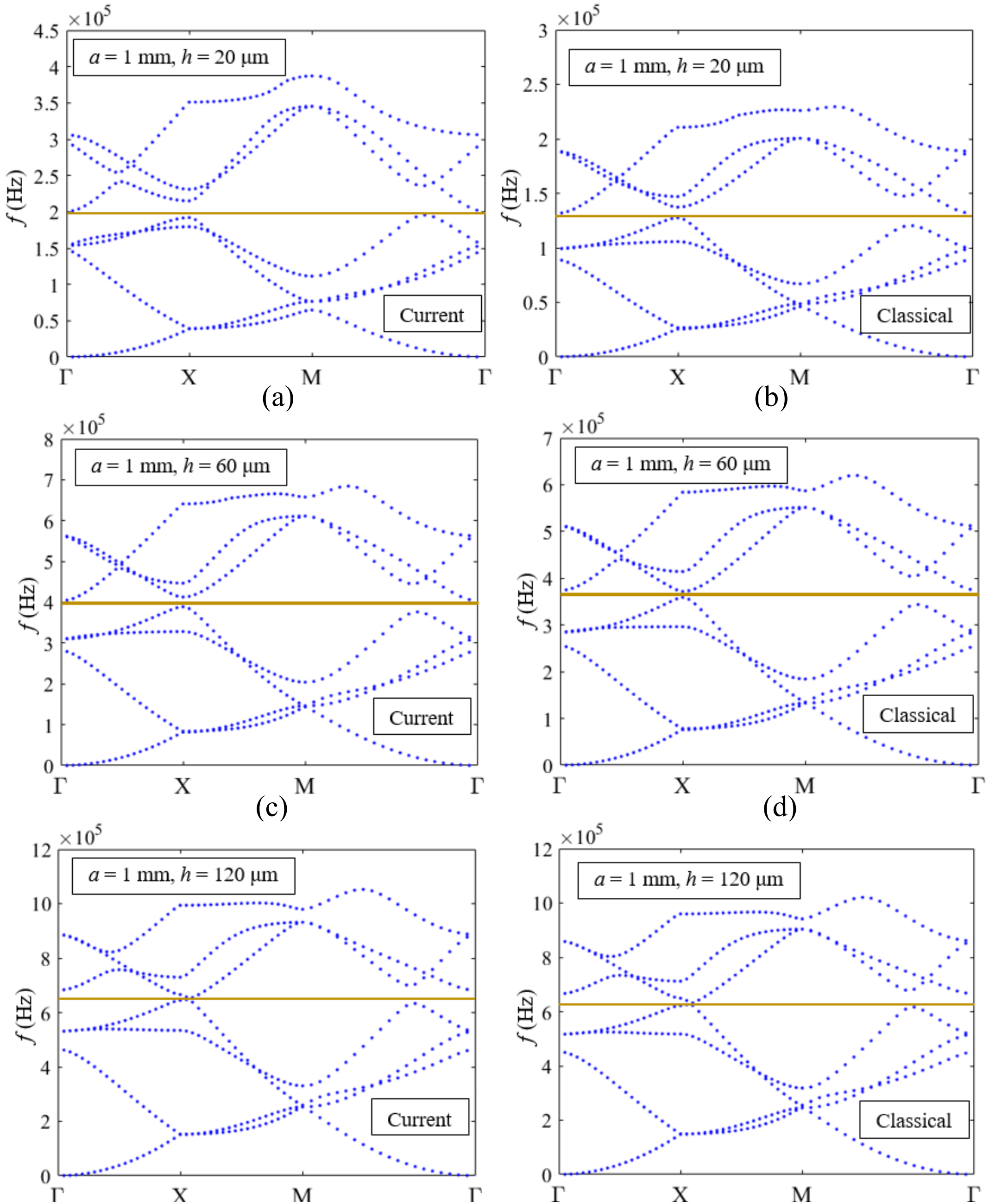

Fig. 7.5 First band gaps for the periodic co-continuous composite plate structure with cruciform inclusions predicted by the current model with: (a) h = 20 μm, (c) h = 60 μm, (e) h = 120 μm, and by the classical model with: (b) h = 20 μm, (d) h = 60 μm, (f) h = 120 μm. The Bloch wave vector $\mathbf{k} = (k_x, k_y)$ at Γ, X and M is, respectively, (0, 0), (π/a, 0) and (π/a, π/a) (see Fig. 7.3(c)).

Table 7.2 First band gaps for the periodic co-continuous composite plate structure containing cruciform inclusions with different values of the plate thickness h

h (μm)	Band Gap (kHz) Current Model	Band Gap (kHz) Classical Model	Relative difference (%)

20	5.95	4.35	36.78
60	16.19	12.8	26.48
120	7.38	7.29	1.23

From Fig. 7.5 and Table 7.2, it is observed that the relative difference between the two band gap values predicted by the current non-classical and classical models is large when the plate is thin (with h = 20 μm here). However, the difference is diminishing with the increase of the plate thickness (with h > 120 μm here).

In addition, it is seen from Tables 7.1 and 7.2 that the band gap size predicted by both the current and classical models depends on the inclusion shape. For each plate thickness considered, the first band gap size for the composite plate with square inclusions is always larger than that for the co-continuous composite with cruciform inclusions for the same value of $V_f^{(\mathrm{I})}$ according to both the current non-classical model and its classical elasticity-based counterpart.

7.3.2 Effect of the unit cell length on band gaps

Figure 7.6 displays the first band gap for the periodic composite plate structure with square inclusions (see Fig. 7.3(a)) predicted by the current model for different values of the unit cell length a. The values of h = 20 μm and $V_f^{(\mathrm{I})} = 16\%$ are used in obtaining the numerical results presented here.

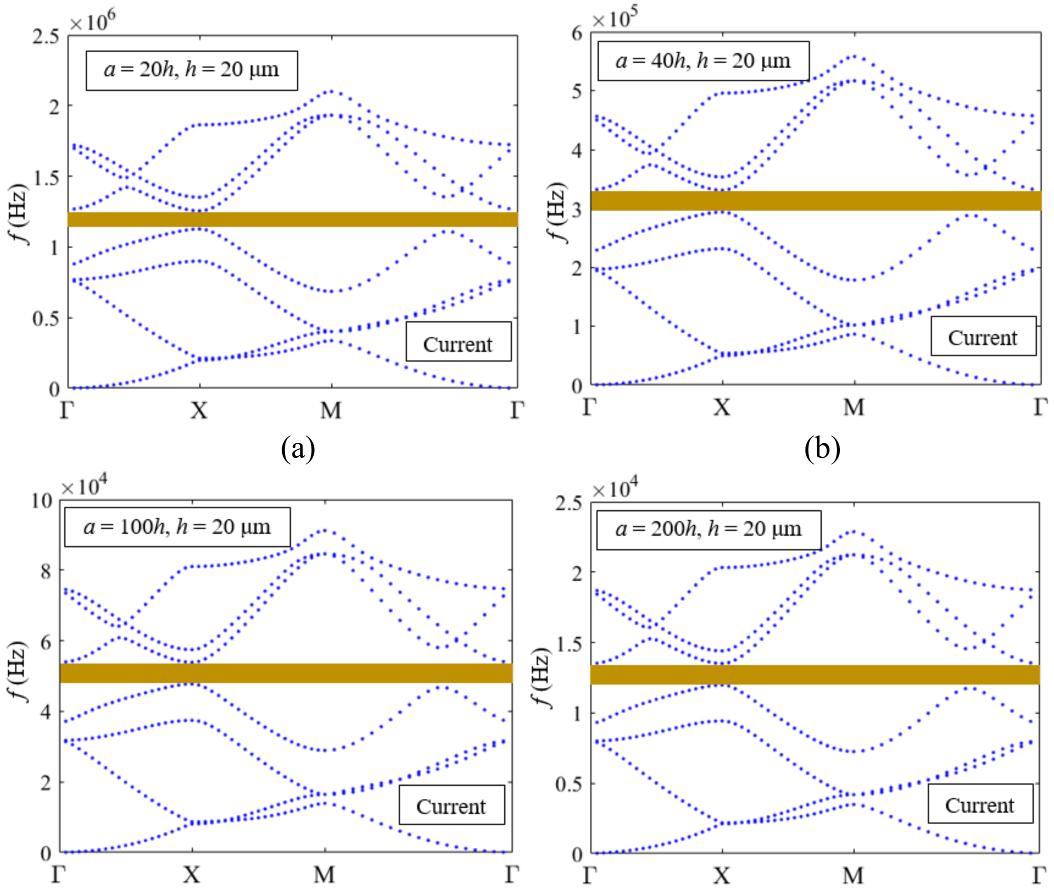

(a) (b)

(c) (d)

Fig. 7.6 Band gaps for the periodic composite plate structure (with h = 20 μm and $V_f^{(\mathrm{I})} = 16\%$) containing square inclusions predicted by the current model for (a) a = 20h, (b) a = 40h, (c) a = 100h, and (d) a = 200h. The Bloch wave vector $\mathbf{k} = (k_x, k_y)$ at Γ, X and M is, respectively, (0, 0), (π/a, 0) and (π/a, π/a) (see Fig. 7.3(c)).

For the cases with a = 20h, 40h, 100h and 200h, the first band gap frequency range is 1126.7−1255.5 kHz, 293.74−330.85 kHz, 47.713−53.861 kHz and 11.977−13.512 kHz, respectively. The first band gaps calculated from these frequency ranges are listed in Table 7.3.

Table 7.3 First Band gaps for the periodic composite plate structure with square inclusions for different values of the unit cell length *a* predicted by the current model (with $h = 20$ μm)

a	Band Gap (kHz)
20*h*	128.8
40*h*	37.11
100*h*	6.148
200*h*	1.535

From Fig. 7.6 and Table 7.3, it is seen that the first frequency for producing the band gap becomes lower as the unit cell length *a* gets larger and the band gap size decreases with the increase of *a*.

Figure 7.7 displays the first band gap for the periodic co-continuous composite plate structure (with $h = 20$ μm and $V_f^{(\mathrm{I})} = 16\%$) containing cruciform inclusions (see Fig. 7.3(b)) predicted by the current model for different values of the unit cell length *a*.

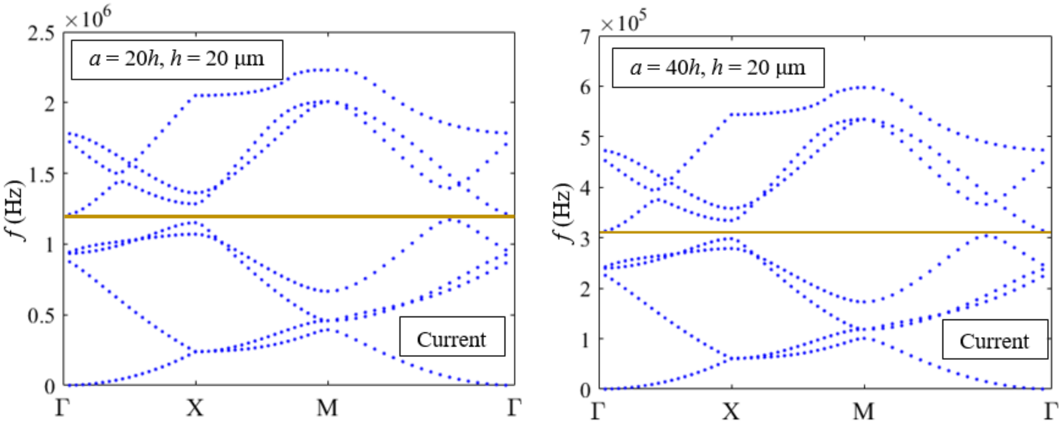

(a) (b)

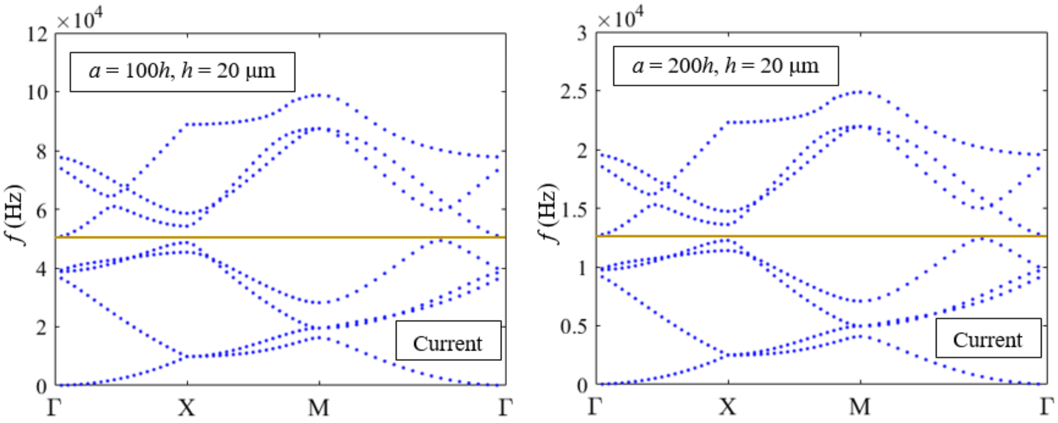

(c) (d)

Fig. 7.7 Band gaps for the periodic co-continuous composite plate structure containing cruciform inclusions with $h = 20$ µm predicted by the current model for (a) $a = 20h$, (b) $a = 40h$, (c) $a = 100h$, and (d) $a = 200h$. The Bloch wave vector $\mathbf{k} = (k_x, k_y)$ at Γ, X and M is, respectively, (0, 0), (π/a, 0) and (π/a, π/a) (see Fig. 7.3(c)).

For the cases with $a = 20h$, $40h$, $100h$ and $a = 200h$, the first band gap frequency range is 1171.2−1209.3 kHz, 303.81−313.09 kHz, 49.331−50.811 kHz and 12.395−12.749 kHz, respectively. The first band gaps calculated from these frequency ranges are listed in Table 7.4.

Table 7.4 First Band gaps for the periodic co-continuous composite plate structure with cruciform inclusions predicted by the current model (with $h = 20$ µm) for different values of the unit cell length a

a	Band Gap (kHz)
$20h$	38.1
$40h$	9.28
$100h$	1.48
$200h$	0.354

From Fig. 7.7 and Table 7.4, it is seen that the band gap size for the periodic co-continuous composite plate structure decreases with the increase of unit cell length a. From Tables 7.3 and 7.4, it is observed that for each unit cell length considered, the first band gap size for the composite plate with square inclusions is always larger than that for the composite plate with cruciform inclusions.

To further illustrate the effect of the unit cell length on band gaps, Fig. 7.8 displays the first band gap for the periodic composite plate structure containing square inclusions with $h = 2$ mm, which is much larger than $h = 20$ μm used in getting the results shown in Fig. 7.6 or $h = 120$ μm identified in Section 7.3.1 to be a plate thickness above which the microstructure and surface energy effects on band gaps are negligible. The volume fraction $V_f^{(\mathrm{I})}$ remains to be 16%.

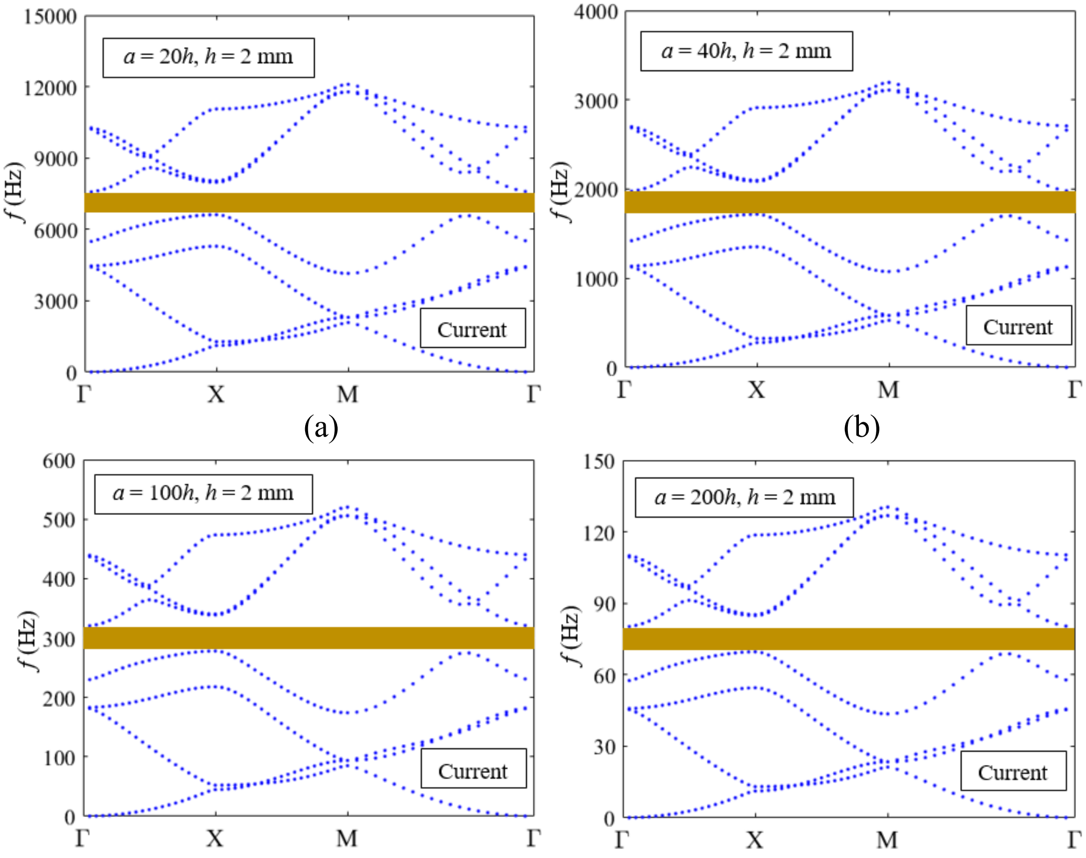

(a) (b)

(c) (d)

Fig. 7.8 Band gaps for the periodic composite plate structure containing square inclusions with $h = 2$ mm predicted by the current model for (a) $a = 20h$, (b) $a = 40h$, (c) $a = 100h$, and (d) $a = 200h$. The Bloch wave vector $\mathbf{k} = (k_x, k_y)$ at Γ, X and M is, respectively, (0, 0), (π/a, 0) and (π/a, π/a) (see Fig. 7.3(c)).

Figure 7.8 show the first band gap frequency ranges predicted by the current model for the periodic composite plate structure (with $h = 2$ mm) containing square inclusions with different values of the unit cell length: 6616.1−7579.2 Hz for $a = 20h$, 1717.3−1976.7 Hz for $a = 40h$, 278.04−320.40 Hz for $a = 100h$, and 69.63−80.25 Hz for $a = 200h$. The band gaps calculated from these frequency ranges are listed in Table 7.5.

Table 7.5 First Band gaps for the periodic composite plate structure with square inclusions for different values of the unit cell length a predicted by the current model (with $h = 2$ mm)

a	Band Gap (Hz)
$20h$	963.1
$40h$	259.4
$100h$	42.36
$200h$	10.62

It is clear from comparing the numerical values shown in Fig. 7.8 and Table 7.5 that both the first frequency for producing the band gap and the band gap size decrease with the increases of the unit cell length a, which is the same as that observed from Fig. 7.6 for the cases with $h = 20$ μm. Moreover, as the band gap frequency ranges and band gap sizes predicted by the classical elasticity-based model are found to be the same as the corresponding ones predicted by the current non-classical model and shown in Figs. 7.8(a)–(d), which indicates that the effect of the unit cell length on band gaps is present at both micro- and macro-length scales.

7.3.3 Effects of the volume fraction on band gaps

The variations of the first band gap size with the volume fraction of material I are shown in Fig. 7.9 for the two different inclusion shapes. For comparison purposes, the first band gap variations predicted by the classical elasticity-based model are also plotted in Fig. 7.9. The materials I and II used here are the same as those employed earlier to obtain the numerical results displayed in Figs. 7.4-7.8.

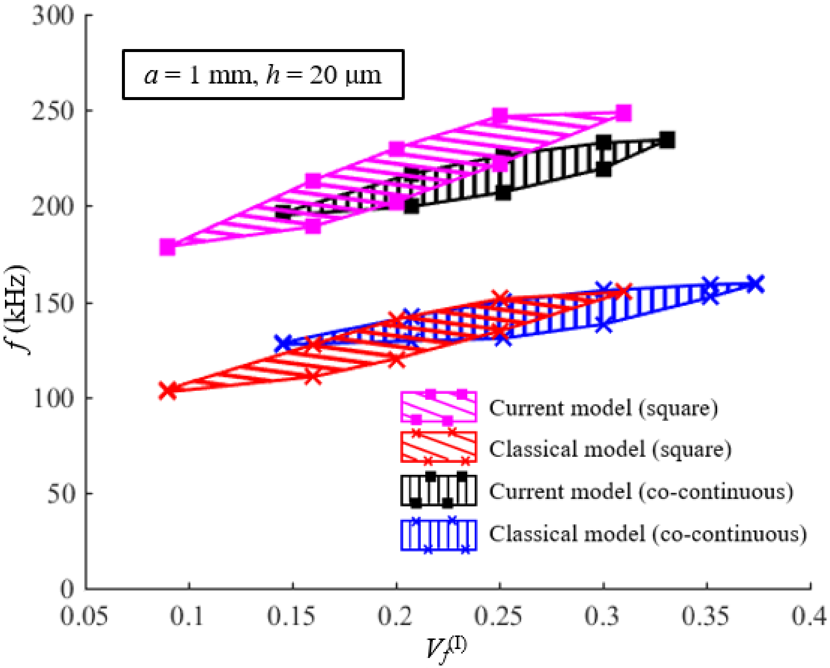

Fig. 7.9 First band gap size changing with $V_f^{(\mathrm{I})}$ predicted by the current and classical models for the periodic composite plate structures with square and cruciform inclusions (with $a = 1$ mm, $h = 20$ μm).

From Fig. 7.9, it is clearly seen that the first band gap size for the periodic composite plate structure with square inclusions predicted by the current non-classical model (i.e., the pink area) gradually increases with the increase of $V_f^{(\mathrm{I})}$ from 9% before reaching its maximum of 27.94 kHz at $V_f^{(\mathrm{I})} = 20\%$, after which the first band gap size decreases with $V_f^{(\mathrm{I})}$ until it disappears at $V_f^{(\mathrm{I})} = 31\%$. Similarly, the first band gap size for the periodic composite plate structure with square inclusions predicted by the classical elasticity-based model (i.e., the red area) increases from zero to its maximum of 20.99 kHz as $V_f^{(\mathrm{I})}$ increases from 9% to 20% and then decreases with the increase of $V_f^{(\mathrm{I})}$ until it vanishes at $V_f^{(\mathrm{I})} = 31\%$. For the periodic co-continuous composite plate structure with cruciform inclusions, the size of the first band gap predicted by the current model (i.e., the black area) is gradually increasing with $V_f^{(\mathrm{I})}$ from 14.5% until reaching the maximum value of 19.39 MHz at $V_f^{(\mathrm{I})} =$ 24%, and it then decreases with $V_f^{(\mathrm{I})}$ until it vanishes at $V_f^{(\mathrm{I})} =$ 33%. However, the first band gap predicted by the classical model (i.e., the blue area) increases with $V_f^{(\mathrm{I})}$ from 14.5% to its maximum value of 20.74 MHz at $V_f^{(\mathrm{I})} =$ 27%, and it is then decreasing with the increase of $V_f^{(\mathrm{I})}$ until it disappears when $V_f^{(\mathrm{I})}$ becomes 37.5%. These variation trends are similar for the periodic composite plate structures with square and cruciform inclusions. However, the ranges of the first band gap are different for these two composite plate structures. The maximum first band gap size for the composite plate structure with square inclusions is larger than that for the co-continuous composite plate structure with cruciform inclusions according to both the current and classical models.

From Fig. 7.9, it is clearly seen that the volume fraction does have a significant effect on the first band gap for the two periodic composite plate structures as predicted by both the current non-classical model and its classical elasticity-based counterpart. In addition, the inclusion shape has a large influence on the band gap. These indicate that large band gaps can be attained by tailoring the volume fraction and shape of the inclusion phase.

7.4 Summary

A new model for predicting band gaps for elastic wave propagation in periodic composite plate structures is provided, which is based on the modified couple stress theory and surface elasticity theory. The wave equations including the microstructure and surface energy effects are solved by using the plane wave expansion method and Bloch theorem to determine band gaps. The current non-classical model reduces to its classical elasticity-based counterpart when the microstructure and surface energy effects are both suppressed.

Numerical results are included to illustrate the new model and compare it with the classical model for periodic composite plate structures with square or cruciform inclusions. It is found that for both the composite structures the microstructure and surface energy effects are significant for very thin plates. In addition, the first band gap frequency and the band gap size are seen to decrease with the increase of the unit cell length for both the inclusion shapes at all length scales. Moreover, the numerical results reveal that the band gap size varies significantly with the volume fraction and inclusion shape.

Appendix A

It is shown here that the shape function $\mathrm{F}(\mathbf{G}_{(M,N)})$ for the cruciform inclusions displayed in Fig. 7.3(b) has the form:

$$\mathrm{F}(\mathbf{G}_{(M,N)}) = \frac{g}{a}(A_x F_y + F_x A_y) + \frac{d^2}{a^2} f_x f_y - \frac{dg}{a^2}(f_x F_y + F_x f_y), \tag{A.1}$$

where

$$F_\beta = \begin{cases} 1, & G_\beta = 0, \\ \dfrac{2}{G_\beta g}\sin\left(\dfrac{G_\beta g}{2}\right), & G_\beta \neq 0; \end{cases} \tag{A2a}$$

$$f_\beta = \begin{cases} 1, & G_\beta = 0, \\ \dfrac{2}{G_\beta d}\sin\left(\dfrac{G_\beta d}{2}\right), & G_\beta \neq 0; \end{cases} \tag{A2b}$$

$$A_\beta = \begin{cases} 1, & G_\beta = 0, \\ 0, & G_\beta \neq 0. \end{cases} \tag{A2c}$$

These are listed in Eqs. (7.9) and (7.10a-c) in Section 7.2.

Proof. Note that the unit cell of the cruciform inclusion (see Fig. 7.3(b)) can be divided into three parts: a large cross structure (part I), a center square inclusion (part II) and a small cross structure 3 (part III), as shown in Fig. 7.10.

When $\mathbf{G}_{(M,N)} \neq \mathbf{0}$, the shape function for the cruciform inclusion can be obtained from Eq. (7.7) as, with the help of the decomposition shown in Fig. 7.10,

$$F(\mathbf{G}_{(M,N)}) = \frac{1}{A}\left[\iint_{A^{(\mathrm{I})}} e^{-i\mathbf{G}_{(M,N)}\cdot\mathbf{r}}d\mathbf{r} + \iint_{A^{(\mathrm{II})}} e^{-i\mathbf{G}_{(M,N)}\cdot\mathbf{r}}d\mathbf{r} - \iint_{A^{(\mathrm{III})}} e^{-i\mathbf{G}_{(M,N)}\cdot\mathbf{r}}d\mathbf{r}\right] = F^{(\mathrm{I})} + F^{(\mathrm{II})} + F^{(\mathrm{III})}, \tag{A3}$$

where

$$\begin{aligned} F^{(\mathrm{I})} &= \frac{1}{A}\iint_{A^{(\mathrm{I})}} e^{-i\mathbf{G}_{(M,N)}\cdot\mathbf{r}}d\mathbf{r} \\ &= \frac{1}{A}\left(\int_{-a/2}^{a/2} e^{-iG_x x}dx\int_{-g/2}^{g/2} e^{-iG_y y}dy + \int_{-g/2}^{g/2} e^{-iG_x x}dx\int_{-a/2}^{a/2} e^{-iG_y y}dy - \int_{-g/2}^{g/2} e^{-iG_x x}dx\int_{-g/2}^{g/2} e^{-iG_y y}dy\right) \\ &= \frac{1}{A}\left[ag\frac{\sin(\frac{G_x a}{2})}{\frac{G_x a}{2}}\frac{\sin(\frac{G_y g}{2})}{\frac{G_y g}{2}} + ag\frac{\sin(\frac{G_x g}{2})}{\frac{G_x g}{2}}\frac{\sin(\frac{G_y a}{2})}{\frac{G_y a}{2}} - g^2\frac{\sin(\frac{G_x g}{2})}{\frac{G_x g}{2}}\frac{\sin(\frac{G_y g}{2})}{\frac{G_y g}{2}}\right], \end{aligned} \tag{A4}$$

$$F^{(\mathrm{II})} = \frac{1}{A}\iint_{A^{(\mathrm{II})}} e^{-i\mathbf{G}_{(M,N)}\cdot\mathbf{r}}d\mathbf{r} = \frac{1}{A}\left(\int_{-d/2}^{d/2} e^{-iG_x x}dx\int_{-d/2}^{d/2} e^{-iG_y y}dy\right) = \frac{d^2}{A}\frac{\sin(\frac{G_x d}{2})}{\frac{G_x d}{2}}\frac{\sin(\frac{G_y d}{2})}{\frac{G_y d}{2}}, \tag{A5}$$

$$\begin{aligned} F^{(\mathrm{III})} &= \frac{1}{A}\iint_{A^{(\mathrm{III})}} e^{-i\mathbf{G}_{(M,N)}\cdot\mathbf{r}}d\mathbf{r} \\ &= \frac{1}{A}\left(\int_{-d/2}^{d/2} e^{-iG_x x}dx\int_{-g/2}^{g/2} e^{-iG_y y}dy + \int_{-g/2}^{g/2} e^{-iG_x x}dx\int_{-d/2}^{d/2} e^{-iG_y y}dy - \int_{-g/2}^{g/2} e^{-iG_x x}dx\int_{-g/2}^{g/2} e^{-iG_y y}dy\right) \\ &= \frac{1}{A}\left[dg\frac{\sin(\frac{G_x d}{2})}{\frac{G_x d}{2}}\frac{\sin(\frac{G_y g}{2})}{\frac{G_y g}{2}} + dg\frac{\sin(\frac{G_x g}{2})}{\frac{G_x g}{2}}\frac{\sin(\frac{G_y d}{2})}{\frac{G_y d}{2}} - g^2\frac{\sin(\frac{G_x g}{2})}{\frac{G_x g}{2}}\frac{\sin(\frac{G_y g}{2})}{\frac{G_y g}{2}}\right]. \end{aligned} \tag{A6}$$

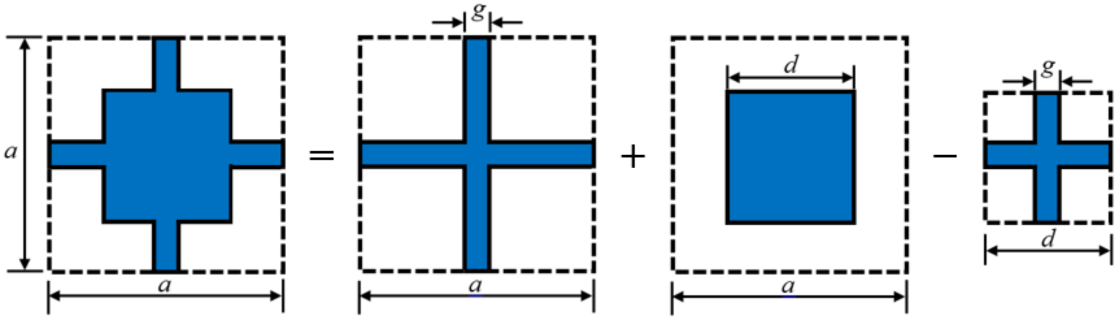

(I) (II) (III)

Fig. 7.10 Decomposition of the cruciform inclusion into three parts

Using Eqs. (A4)–(A6) in (A3) then gives, noting that $\mathbf{G}_{(M,N)} = (G_x, G_y) = (\frac{2\pi M}{a}, \frac{2\pi N}{a})$ and $M \neq 0$, $N \neq 0$ needed for $\mathbf{G}_{(M,N)} \neq \mathbf{0}$,

$$F_{\mathbf{G}_{(M,N)}} = \frac{1}{A}\left[d^2 \frac{\sin(\frac{G_x d}{2})}{\frac{G_x d}{2}} \frac{\sin(\frac{G_y d}{2})}{\frac{G_y d}{2}} - dc \frac{\sin(\frac{G_x d}{2})}{\frac{G_x d}{2}} \frac{\sin(\frac{G_y c}{2})}{\frac{G_y c}{2}} - dc \frac{\sin(\frac{G_x c}{2})}{\frac{G_x c}{2}} \frac{\sin(\frac{G_y d}{2})}{\frac{G_y d}{2}} \right].$$

(A7)

When $\mathbf{G}_{(M,N)} = \mathbf{0}$, Eq. (7.7) yields

$$F(\mathbf{G}_{(M,N)}) = \frac{A^{(\mathrm{I})}}{A} = V_f^{(\mathrm{I})}. \qquad \text{(A8)}$$

Combining Eqs. (A7) and (A8) then leads to the shape function listed in Eqs. (A1) and (A2a-c), thereby completing the proof.

REFERENCES

Ai, L. and Gao, X.-L., 2016, Evaluation of effective elastic properties of 3-D printable interpenetrating phase composites using the meshfree radial point interpolation method. *Mech. Adv. Mater. Struct.* (published on-line on September 20, 2016) (DOI: 10.1080/15376494.2016.1143990)

Ai, L. and Gao, X.-L., 2017, Micromechanical modeling of 3-D printable interpenetrating phase composites with tailorable effective elastic properties including negative Poisson's ratio, *J. Micromech. Molecular Phys.* **2**, 1750015-1~21.

Akgöz, B. and Civalek, Ö., 2013, Modeling and analysis of micro-sized plates resting on elastic medium using the modified couple stress theory, *Meccanica* **48**, 863-873.

Altenbach, H., Eremeyev, V. A. and Lebedev, L. P., 2010, On the existence of solution in the linear elasticity with surface stresses, *Z. Angew. Math. Mech.* **90**, 231–240.

Bacigalupo, A. and Gambarotta, L., 2017, Dispersive wave propagation in two-dimensional rigid periodic blocky materials with elastic interfaces, *Journal of the Mechanics and Physics of Solids* **102**, 165-186.

Cammarata, R. C., 1994, Surface and interface stress effects in thin films, *Prog. Surf. Sci.* **46**, 1-38.

Cao, Y., Hou, Z. and Liu, Y., 2004, Convergence problem of plane-wave expansion method for phononic crystals, *Physics Letters A* **327**(2), 247-253.

Chen, A. L. and Wang, Y. S., 2011, Size-effect on band structures of nanoscale phononic crystals, *Physica E* **44**, 317-321.

Chen, Y. and Wang, L., 2014, Periodic co-continuous acoustic metamaterials with overlapping locally resonant and Bragg band gaps, *Appl. Phys. Lett.* **105**, 191907-1~5.

Chen, Y. Y., Li, T. T., Scarpa, F. and Wang, L. F., 2017, Lattice metamaterials with mechanically tunable Poisson's ratio for vibration control, *Physical Review Applied* **7**, 024012-1~11.

Cheng, Z. B., Xu, Y. G. and Zhang, L. L., 2015, Analysis of flexural wave bandgaps in periodic plate structures using differential quadrature element method. *International Journal of Mechanical Sciences*, **100**, 112-125.

El-Naggar, S. A., Mostafa, S. I. and Rafat, N. H., 2012, Complete band gaps of phononic crystal plates with square rods, *Ultrasonics*, **52**, 536-542.

Eremeyev, V. A. and Lebedev, L. P., 2016, Mathematical study of boundary-value problems within the framework of Steigmann–Ogden model of surface elasticity, *Contin. Mech. Thermodyn.* **28**, 407-422.

Eremeyev, V. A., Lebedev, L. P. and Altenbach, H., 2013, *Foundations of Micropolar Mechanics*, Springer, Berlin.

Eringen, A. C., 1983, On differential equations of nonlocal elasticity and solutions of screw dislocation and surface waves, *J. Appl. Phys.* **54**, 4703-4710.

Eringen, A. C., 1999, *Foundations and Solids, Microcontinuum Field Theories*, Springer-Verlag, New York.

Gao, R. Z., Zhang, G. Y., Ioppolo, T. and Gao, X.-L., 2018, Elastic wave propagation in a periodic composite beam structure: a new model for band gaps incorporating surface energy, transverse shear and rotational inertia effects, *J. Micromech. Molecular Phys.*

3, 1840005-1~22.

Gao, X.-L., 2015, A new Timoshenko beam model incorporating microstructure and surface energy effects, *Acta Mech.* **226**, 457-474.

Gao, X.-L., Huang, J. X. and Reddy, J. N., 2013, A non-classical third-order shear deformation plate model based on a modified couple stress theory, *Acta Mech.* **224**, 2699-2718.

Gao, X.-L. and Ma, H. M., 2010, Solution of Eshelby's inclusion problem with a bounded domain and Eshelby's tensor for a spherical inclusion in a finite spherical matrix based on a simplified strain gradient elasticity theory, *Journal of the Mechanics and Physics of Solids* **58**, 779-797.

Gao, X.-L. and Mahmoud, F. F., 2014, A new Bernoulli-Euler beam model incorporating microstructure and surface energy effects, *Z. Angew. Math. Phys.* **65**, 393-404.

Gao, X.-L. and Mall, S., 2001, Variational solution for a cracked mosaic model of woven fabric composites, *Int. J. Solids Struct.* **38**, 855-874.

Gao, X.-L. and Park, S. K., 2007, Variational formulation of a simplified strain gradient elasticity theory and its application to a pressurized thick-walled cylinder problem, *Int. J. Solids Struct.* **44**, 7486-7499.

Gao, X.-L. and Zhang, G. Y., 2015, A microstructure- and surface energy-dependent third-order shear deformation beam model, *Z. Angew. Math. Phys.* **66**, 1871-1894.

Gao, X.-L. and Zhang, G. Y., 2016, A non-classical Kirchhoff plate model incorporating microstructure, surface energy and foundation effects, *Continuum Mech. Thermodyn*. **28**, 195-213.

Gao, X.-L. and Zhang, G. Y., 2016b, A non-classical Mindlin plate model incorporating microstructure, surface energy and foundation effects, *Proceedings of the Royal* ***Society*** *A* **472**, 20160275-1~25.

Gao, X.-L. and Zhou, S.-S., 2013, Strain gradient solutions of half-space and half-plane contact problems, *Z. Angew. Math. Phys.* **64**, 1363-1386.

Gao, R. Z., Zhang, G. Y., Ioppolo, T. and Gao, X.-L., 2018, Elastic wave propagation in a periodic composite beam structure: a new model for band gaps incorporating surface energy, transverse shear and rotational inertia effects, *Journal of Micromechanics and Molecular Physics* **3**, 1840005-1~22.

George, G. A., 1993, Surface modification and analysis of ultra-high-modulus polyethylene fibres for composites, Chapter 7, *Polymer Surfaces and Interfaces II*, Feast, W. J., Munro H. S. and Richards, R. W., eds., Wiley, Hoboken, NJ, pp. 161-201.

Gourgiotis, P. A., Georgiadis, H. G., 2009, Plane-strain crack problems in microstructured solids governed by dipolar gradient elasticity, *J. Mech. Phys. Solids* **57**, 1898–1920.

Gurtin, M. E. and Murdoch, A. I., 1975, A continuum theory of elastic material surfaces, *Arch. Ration. Mech. Anal.* **57**, 291-323.

Gurtin, M. E. and Murdoch, A. I., 1978, Surface stress in solids, *Int. J. Solids Struct*. **14**, 431-440.

Han, L., Zhang, Y., Jiang, L.H. and Zhang, Z.M., 2013. Free transverse vibration in periodically hinged identical beams on elastic foundations: a single material phononic crystal, *Physica Status Solidi –Rapid Research Letters* **7**, 514-517.

Hsu, J.-C. and Wu, T-T., 2006, Efficient formulation for band-structure calculations of two-dimensional phononic-crystal plates, *Phys. Rev. B* **74**, 144303-1~8.

Jing, G. Y., Duan, H. L., Sun, X. M., Zhang, Z. S., Xu, J., Li, Y. D., Wang, J. X. and Yu,

D. P., 2006, Surface effects on elastic properties of silver nanowires: contact atomic-force microscopy, *Phy. Rev. B* **73**, 235409-1~6.

Jomehzadeh, E., Noori, H. R. and Saidi, A. R., 2011, The size-dependent vibration analysis of micro-plates based on a modified couple stress theory, *Physica E.* **43**, 877-883.

Khajeansari A., Baradaran G. H. and Yvonnet J., 2012, An explicit solution for bending of nanowires lying on Winkler-Pasternak elastic substrate medium based on the Euler-Bernoulli beam theory, *Int. J. Eng. Sci.* **52**, 115-128.

Kittel, C., 1986, *Introduction to Solid State Physics*, Wiley, New York.

Lam, D. C. C., Yang, F., Chong, A. C. M., Wang, J. and Tong, P., 2003, Experiments and theory in strain gradient elasticity. *J. Mech. Phys. Solids.* **51**, 1477-1508.

Lazopoulos, K. A., 2004, On the gradient strain elasticity theory of plates, *Euro. J. Mech. A/Solids* **23**, 843–852.

Lazopoulos, K. A., 2009, On bending of strain gradient elastic micro-plates, *Mech. Res. Commun.* **36**, 777-783.

Lewin, M., Mey-Marom, A. and Frank, R., 2005, Surface free energies of polymeric materials, additives and minerals, *Polymers for Advanced Technologies* **16**, 429-441.

Li, C., Bando, Y., Zhi, C., Huang, Y. and Golberg, D., 2009, Thickness-dependent bending modulus of hexagonal boron nitride nanosheets, *Nanotechnology* **20**, 385707-1 – 385707-6.

Li, L., 1996, Use of Fourier series in the analysis of discontinuous periodic structures, *Journal of the Optical* ***Society*** *of America A* **13**(9), 1870-1876.

Li, Y., Wei, P. and Zhou, Y., 2016, Band gaps of elastic waves in 1-D phononic crystal with dipolar gradient elasticity, *Acta Mechanica* **227**, 1005-1023.

Lim, C. W. and He, L. H., 2004, Size-dependent nonlinear response of thin elastic films with nano-scale thickness, *Int. J. Mech. Sci.* **46**, 1715-1726.

Limkatanyu, S., Ponbunyanon, P., Prachasaree, W., Kuntiyawichai, K. and Kwon, M., 2014, Correlation between beam on Winkler-Pasternak foundation and beam on elastic substrate medium with inclusion of microstructure and surface effects. *J. Mech. Sci. Tech.* **28**, 3653-3665.

Liu, C. and Rajapakse, R. K. N. D., 2010, Continuum models incorporating surface energy for static and dynamic response of nanoscale beams, *IEEE Trans. Nanotech.* **9**, 422-431.

Liu, C. and Rajapakse, R. K. N. D., 2013, A size-dependent continuum model for nanoscale circular plates, *IEEE Trans. Nanotech.* **12**, 13-20.

Liu, L. and Hussein, M. I., 2012, Wave motion in periodic flexural beams and characterization of the transition between Bragg scattering and local resonance, *Journal of Applied Mechanics* **79**, 011003-1~17.

Liu, W., Chen, J., Liu, Y. and Su, X., 2012, Effect of interface/surface stress on the elastic wave band structure of two-dimensional phononic crystals, *Phys. Lett. A* **376**, 605-609.

Liu, X., Shi, Z. and Mo, Y. L., 2016, Attenuation zones of initially stressed periodic Mindlin plates on an elastic foundation. *International Journal of Mechanical Sciences*, **115**, 12-23.

Liu, Y. and Soh, C.-K., 2007, Shear correction for Mindlin type plate and shell elements. *Int. J. Numer. Meth. Eng.* **69**, 2789–2806.

Lu, P., He, L. H., Lee, H. P. and Lu, C., 2006, Thin plate theory including surface effects, *Int. J. Solids Struct.* **43**, 4631-4647.

Lu, P., Zhang, P. Q., Lee, H. P., Wang, C. M. and Reddy, J. N., 2007, Non-local elastic plate theories, *Proc. R. Soc.* A **463**, 3225-3240.

Lü, C. F., Wu, D. Z and Chen, W. Q., 2011, Nonlinear responses of nanoscale FGM films including the effects of surface energies, *IEEE Trans. Nanotech.* **10**, 1321-1327.

Ma, H. M., Gao, X.-L. and Reddy, J. N., 2008, A microstructure-dependent Timoshenko beam model based on a modified couple stress theory, *J. Mech. Phys. Solids* **56**, 3379-3391.

Ma, H. M., Gao, X.-L. and Reddy, J. N., 2010, A non-classical Reddy-Levinson beam model based on a modified couple stress theory, *Int. J. Multiscale Comput. Eng.* **8**, 167-180.

Ma, H. M., Gao, X.-L. and Reddy, J. N., 2011, A non-classical Mindlin plate model based on a modified couple stress theory, *Acta Mech.* **220**, 217-235.

Madeo, A., Barbagallo, G., d'Agostino, M. V., Placidi, L. and Neff, P., 2016, First evidence of non-locality in real band-gap metamaterials: determining parameters in the relaxed micromorphic model, *Proc. R. Soc. A* **472**, 20160169-1~21.

Madeo, A., Neff, P., Ghiba, I.-D., Placidi, L. and Rosi, G., 2015, Band gaps in the relaxed linear micromorphic continuum, *Z. Angew. Math. Mech.* **95**, 880-887.

McFarland, A. W. and Colton, J. S., 2005, Role of material microstructure in plate stiffness with relevance to microcantilever sensors, *J. Micromech. Microeng.* **15**, 1060-1067.

Miller, R. E. and Shenoy, V. B., 2000, Size-dependent elastic properties of nanosized structural elements, *Nanotech.* **11**, 139-147.

Mindlin, R. D., 1963, Influence of couple-stresses on stress concentrations, *Exp. Mech.* **3**, 1-7.

Mindlin, R. D., 1964, Micro-structure in linear elasticity, *Arch. Ration. Mech. Anal.* **16**, 51-

78.

Neff, P., Ghiba, I.-D., Madeo, A., Placidi, L. and Rosi, G, 2014, A unifying perspective: the relaxed linear micromorphic continuum, *Contin. Mech. Thermodyn.* **26**, 639-681.

Papargyri-Beskou, S. and Beskos, D. E., 2008, Static, stability and dynamic analysis of gradient elastic flexural Kirchhoff plates, *Arch. Appl. Mech.* **78**, 625–635.

Papargyri-Beskou, S., Giannakopoulos, A. E. and Beskos, D. E., 2010, Variational analysis of gradient elastic flexural plates under static loading, *Int. J. Solids Struct.* **47**, 2755-2766.

Park, S. K. and Gao, X.-L., 2006, Bernoulli-Euler beam model based on a modified couple stress theory, *J. Micromech. Microeng.* **16**, 2355-2359.

Park, S. K. and Gao, X.-L., 2008, Variational formulation of a modified couple stress theory and its application to a simple shear problem, *Z. Angew. Math. Phys.* **59**, 904-917.

Piccolroaz, A. and Movchan, A. B., 2014, Dispersion and localisation in structured Rayleigh beams, *International Journal of Solids and Structures* **51**, 4452-4461.

Piccolroaz, A., Movchan, A. B. and Cabras, L., 2017, Rotational inertia interface in a dynamic lattice of flexural beams, *International Journal of Solids and Structures* **112**, 43-53.

Reddy, J. N., 2002, Energy Principles and Variational Methods in Applied Mechanics, 2nd ed., Wiley, Hoboken, New Jersey.

Reddy, J. N. and Berry, J., 2012, Nonlinear theories of axisymmetric bending of functionally graded circular plates with modified couple stress. *Composite Structures*, **94**, 3664-3668.

Ru, C. Q., 2010, Simple geometrical explanation of Gurtin-Murdoch model of surface elasticity with clarification of its related versions, *Sci. China Phys. Mech. Astron.* **53**, 536-544.

Selvadurai, A. P. S., 1979, *Elastic Analysis of Soil-Foundation Interaction*, Elsevier, Amsterdam.

Shaat, M., Mahmoud, F. F., Gao, X.-L. and Faheem, A. F., 2014, Size-dependent bending analysis of Kirchhoff nano-plates based on a modified couple-stress theory including surface effects, *Int. J. Mech. Sci.* **79**, 31-37.

Sharma, P. and Ganti, S., 2004, Size-dependent Eshelby's tensor for embedded nano-inclusions incorporating surface/interface energies, *ASME Journal of Applied Mechanics* **71**, 663-671.

Shenoy, V. B., 2005, Atomistic calculations of elastic properties of metallic fcc crystal surfaces, *Phys. Rev. B* **71**, 094104-1~11.

Sigalas, M. M. and Economou, E. N., 1994, Elastic waves in plates with periodically placed inclusions. *Journal of Applied Physics* **75**, 2845-2850.

Sigalas, M. M., 1997, Elastic wave band gaps and defect states in two-dimensional composites, *The Journal of the Acoustical Society of America* **101**, 1256-1261.

Şimşek M. and Reddy J. N., 2013, A unified higher order beam theory for buckling of a functionally graded microbeam embedded in elastic medium using modified couple stress theory, *Compos. Struct.* **101**, 47-58.

Steigmann, D. J., 1996, The variational structure of a nonlinear theory for spatial lattices, *Meccanica* **31**, 441-455.

Steigmann, D. J., 2007, Thin-plate theory for large elastic deformations, *Int. J. Non-Linear Mech.* **42**, 233-240.

Steigmann, D. J. and Ogden, R. W., 1997, Plane deformations of elastic solids with intrinsic boundary elasticity, *Proc. R. Soc. Lond. A* **453**, 853-877.

Steigmann, D. J. and Ogden, R. W., 1999, Elastic surface-substrate interactions, *Proc. R. Soc. Lond. A* **455**, 437-474.

Susa, N., 2002, Large absolute and polarization-independent photonic band gaps for various lattice structures and rod shapes, *Journal of Applied Physics* **91**, 3501-3510.

Suzuki, T. and Yu, P. K. L., 1998, Complex elastic wave band structures in three-dimensional periodic elastic media, *Journal of the Mechanics and Physics of Solids* **46**, 115-138.

Timoshenko, S. P. and Goodier, J. N., 1970, *Theory of Elasticity*, 3rd edition, McGraw-Hill, New York.

Trainiti, G., Rimoli, J. J. and Ruzzene, M., 2015, Wave propagation in periodically undulated beams and plates, *International Journal of Solids and Structures* **75**, 260-276.

Tsiatas, G. C., 2009, A new Kirchhoff plate model based on a modified couple stress theory, *Int. J. Solids Struct.* **46**, 2757-2764.

Wang, C.M., Lim, G.T., Reddy, J.N. and Lee, K.H., 2001, Relationships between bending solutions of Reissner and Mindlin plate theories. *Eng. Struct.* **23**, 838–849.

Wang, K. F. and Wang, B. L., 2012, Effects of residual surface stress and surface elasticity on the nonlinear free vibration of nanoscale plates, *J. Appl. Phys.* **112**, 013520-1~6.

Wang, L., 2010, Size-dependent vibration characteristics of fluid-conveying microtubes, *Journal of Fluids and Structures* **26**, 675-684.

Xiao, Y., Wen, J. and Wen, X., 2012, Flexural wave band gaps in locally resonant thin plates with periodically attached spring–mass resonators, *Journal of Physics D: Applied Physics* **45**, 195401-1~12.

Yang, F., Chong, A. C. M., Lam, D. C. C. and Tong, P., 2002, Couple stress based strain gradient theory for elasticity, *Int. J. Solids Struct.* **39**, 2731-2743.

Yokoyama, T., 1996, Vibration analysis of Timoshenko beam-columns on two-parameter elastic foundations, *Comput. Struct.* **6**1, 995-1007.

Yu, D., Wen, J., Shen, H., Xiao, Y. and Wen, X., 2012, Propagation of flexural wave in periodic beam on elastic foundations, *Phys. Lett. A* **376**, 626-630.

Zhang, G. Y. and Gao, X.-L., 2018, Elastic wave propagation in 3-D periodic composites: band gaps incorporating microstructure effects, *Composite Structures* **204**, 920-932.

Zhang, G. Y., Gao, X.-L. and Wang, J. Z., 2015, A non-classical model for circular Kirchhoff plates incorporating microstructure and surface energy effects, *Acta Mech.* **226**, 4073-4085.

Zhang, G. Y., Gao, X.-L., Bishop, J. E. and Fang, H. E., 2018a, Band gaps for elastic wave propagation in a periodic composite beam structure incorporating microstructure and surface energy effects, *Composite Structures*, **189**, 263-272.

Zhang, G. Y., Gao, X.-L. and Ding, S. R., 2018b, Band gaps for wave propagation in 2-D periodic composite structures incorporating microstructure effects, *Acta Mechanica* **229**, 4199-4214.

Zhang, P. and Parnell, W. J., 2017, Band gap formation and tunability in stretchable serpentine interconnects, *ASME J. Appl. Mech.* **84**, 091007-1~7.

Zhang, Y., Zhuo, L. J. and Zhao, H. S., 2013, Determining the effects of surface elasticity and surface stress by measuring the shifts of resonant frequencies, *Proc. Roy. Soc. A* **469**, 20130449-1 ~14.

Zhou, S.-S. and Gao, X.-L., 2013, Solutions of half-space and half-plane contact problems based on surface elasticity, *Z. Angew. Math. Phys.* **64**, 145-166.

Zhou, S.-S. and Gao, X.-L., 2014, A non-classical model for circular Mindlin plates based on a modified couple stress theory, *ASME J. Appl. Mech.* **81**, 051014-1~8.

Zhou, S.-S. and Gao, X.-L., 2015, Solutions of the generalized half-plane and half-space Cerruti problems with surface effects, *Z. Angew. Math. Phys.* **66**. 1125-1142.

PUBLICATIONS

Journal papers:

Zhang, G. Y. and Gao, X.-L., 2018, Elastic wave propagation in 3-D periodic composites: band gaps incorporating microstructure effects. *Compos. Struct.* **204**, 920-932.

Gao, R. Z., Zhang, G. Y., Ioppolo, T. and Gao, X.-L., 2018, Elastic wave propagation in a periodic composite beam structure: a new model for band gaps incorporating surface energy, transverse shear and rotational inertia effects. *J. Micromech. Molecular Phys.* **3**, 1840005-1~22.

Zhang, G. Y. and Gao, X.-L., 2018, A non-classical Kirchhoff rod model based on the modified couple stress theory. *Acta Mech.* (in press) (DOI: 10.1007/s00707-018-2279-z)

Zhang, G. Y., Gao, X.-L. and Ding, S. R., 2018, Band gaps for wave propagation in 2-D periodic composite structures incorporating microstructure effects. *Acta Mech.* **229**, 4199-4214.

Zhang, G. Y., Gao, X.-L., Bishop, J. E. and Fang, H. E., 2018, Band gaps for elastic wave propagation in a periodic composite beam structure incorporating microstructure and surface energy effects. *Compos. Struct.* **189**, 263-272.

Zhang, G. Y., Gao, X.-L. and Guo, Z. Y., 2017, A non-classical model for an orthotropic Kirchhoff plate embedded in a viscoelastic medium. *Acta Mech.* **228**, 3811–3825.

Zhang, G. Y., Gao, X.-L. and Tang, S., 2017, A non-classical model for circular Mindlin plates incorporating microstructure and surface energy effects. *Procedia IUTAM* **21**, 48-55.

Gao, X.-L. and Zhang, G. Y., 2016, A non-classical Mindlin plate model incorporating microstructure, surface energy and foundation effects. *Proc. Royal Soc. A* **472**, 20160275-1~25.

Gao, X.-L. and Zhang, G. Y., 2016, A non-classical Kirchhoff plate model incorporating microstructure, surface energy and foundation effects. *Continuum Mech. Thermodynamics* **28**, 195-213.

Zhang, G. Y., Gao, X.-L. and Wang, J. Z., 2015, A non-classical model for circular Kirchhoff plates incorporating microstructure and surface energy effects. *Acta Mech.* **226**, 4073-4085.

Gao, X.-L. and Zhang, G. Y., 2015, A microstructure- and surface energy-dependent third-order shear deformation beam model. *Z. angew. Math. Phys.* **66**, 1871-1894.